

Doctoral Dissertation

博士論文

Dynamics of Magnetized Prestellar Cores

(磁化された前恒星コアのダイナミクス)

A Dissertation Submitted for the Degree of Doctor of Philosophy

December 2023

令和5年12月博士（理学）申請

Department of Astronomy, Graduate School of Science,

The University of Tokyo

東京大学大学院理学系研究科天文学専攻

Shinichi Kinoshita

木下 真一

Doctoral Dissertation

Dynamics of Magnetized Prestellar Cores

SHINICHI KINOSHITA

Supervised by Assoc Prof. Fumitaka Nakamura

Department of Astronomy, the University of Tokyo
Division of Science, National Astronomical Observatory of Japan

Abstract

Stars are formed in dense cores within molecular clouds. The prestellar core is the gravitationally bound but starless core that precedes the formation of a protostar. The properties of prestellar cores determine the local environment of protostellar disks, outflows, and multiplicity of protostars. Investigating and characterizing the prestellar core is thus crucial for understanding the stages of the star formation process.

Angular momentum \mathbf{L}_{core} and magnetic fields \mathbf{B}_{core} within cores are considered key agents in affecting the formation of protostellar disks and driving outflow. The characteristics of \mathbf{L}_{core} and \mathbf{B}_{core} vary, particularly in relation to the larger scale dynamics from region to region. This variation suggests that their characteristics may reflect the physical state of the clumps, which are parental bodies of cores. Recent observational studies have suggested that clumps could rotate strongly or collide with other clumps. Assessing the effects of these dynamic environments of clumps on prestellar core properties is essential. Our study utilized three-dimensional, turbulent magnetohydrodynamic (MHD) simulations to investigate the nature of prestellar cores formed within single rotating clumps and colliding clumps, focusing on the extent to which angular momentum and magnetic fields are inherited from clumps. The novelty of this study lies in expanding the initial conditions that were limited in previous simulation studies and in considering the rotation and collision of clumps using MHD simulations. We found that cores efficiently inherit angular momentum from the clump, showing the alignment of \mathbf{L}_{core} only if the single clump rotates and its rotational energy exceeds its turbulent energy. On the other hand, clear alignment of \mathbf{L}_{core} does not occur in colliding clumps, regardless of the initial turbulence strength. As to \mathbf{B}_{core} , we found that a stronger magnetic field in the parent clump tends to imprint its orientation onto \mathbf{B}_{core} , especially in colliding clumps where the field aligns with the compressed layer. Our intriguing finding is that the angle between \mathbf{L}_{core} and \mathbf{B}_{core} is random in most cases regardless of initial conditions. This general misalignment between \mathbf{L}_{core} and \mathbf{B}_{core} has significant implications for resolving the "magnetic braking catastrophe" and explaining the protostellar disk formation without contradiction.

Furthermore, previous observations have also suggested that cores can collide with each other within their lifetimes. Collision between cores can significantly alter their physical state and subsequent evolutions. We conducted three-dimensional MHD simulations of

collisions between stable isothermal Bonnor-Ebert spheres modeling cores. We mainly investigated the influence of strength and orientations of large-scale magnetic fields. The novelty of this study is that it considers magnetic field effects, which have been ignored in previous simulations of core-scale collisions. We found that stronger magnetic fields can suppress gas motion through magnetic pressure, diminishing fragmentation, and accretion rates. The resulting multiplicity of stars and structural outcomes depend significantly on the angle between the collision axis and the large-scale magnetic field.

Acknowledgements

I would like to express my deepest gratitude to my supervisor, Fumitaka Nakamura, for his meticulous and detailed instruction on the star formation, engaging in passionate discussions, and arranging numerous opportunities for interaction with other researchers. His guidance has been priceless in my academic journey.

I also would like to thank Wu Benjamin for his technical support on simulations. A special acknowledgment goes to Yasushi Suto, who served as a co-supervisor in IGPEES. My heartfelt thanks to the anonymous referees of my published works for their constructive feedback and insights. I extend my appreciation to Kazunari Iwasaki, Yoshiaki Misugi, and Sota Arakawa for their fruitful discussions. I would also like to express my gratitude to Hideaki Takemura for being an excellent role model to me and teaching me a lot.

My sincere thanks are due to the referees of this doctoral dissertation, Seiichi Sakamoto, Katsukawa Yukio, Michiko Fujii, Mami Machida, and Hidenobu Yajima, for their detailed review and constructive criticism on the draft of this thesis and the presentation for the Ph.D. defense.

I owe immense gratitude to my peers, Ikki Mitsuhashi, Jin Beniyama, Raiga Kashiwagi, Takaho Masai, and Yuki Yoshida, with whom I spent fruitful and fun times at NAOJ. They have been a significant emotional support to me.

Above all, I am most grateful to my parents, who have supported me warmly. Their kindness is essential for the completion of this dissertation and my fulfilling life.

Computations described in this work were performed using the publicly-available **Enzo** code (<http://enzo-project.org>), which is the product of a collaborative effort of many independent scientists from numerous institutions around the world. Their commitment to open science has helped make this work possible. Numerical computations were performed on the Cray XC50 at Center for Computational Astrophysics, National Astronomical Observatory of Japan, with subsequent analyses conducted on analysis servers. This work was supported by Grant-in-Aid for JSPS Research Fellow.

Contents

Abstract	i
Acknowledgements	iii
List of Figures	xii
List of Tables	xiii
Abbreviations and Symbols	xiv
Publication List	xix
1 General Introduction	1
1.1 Star Formation in the Molecular Cloud	1
1.2 Angular Momentum within Cores	4
1.3 Magnetic Fields within Cores	7
1.4 Rotation-Magnetic Field Relation	11
1.5 Collision between Prestellar Cores	14
1.6 Purpose of this Thesis	15
1.7 Content of this Thesis	17
2 Dynamics of Prestellar Cores in Cluster-Forming Clumps	18
2.1 Introduction of this Chapter	18
2.1.1 Importance of Angular Momentum and Magnetic Fields within Prestellar Cores	18
2.1.2 Observed Dynamics of Cluster-forming Clumps	19
2.1.3 Content of this Chapter	20
2.2 Method	21
2.2.1 Numerical Code	21
2.2.2 Initial Conditions and Parameters	22

2.2.2.1	Rotation Setup	23
2.2.2.2	Collision Setup	26
2.2.3	Measuring Core Properties	28
2.3	Results	32
2.3.1	Rotation Setup	32
2.3.1.1	Angular Momentum of the Rotation Setup	32
2.3.1.2	Magnetic Field of the Rotation Setup	35
2.3.1.3	Rotation-Magnetic Field Relation of the Rotation Setup	38
2.3.2	Collision Setup	39
2.3.2.1	Angular Momentum of the Collision Setup	40
2.3.2.2	Magnetic Field of the Collision Setup	40
2.3.2.3	Rotation-Magnetic Field Relation of the Collision Setup	47
2.4	Discussion	50
2.4.1	Alignment of Core Angular Momentum	50
2.4.2	Misalignment between the Angular Momentum and the Magnetic Field	55
2.4.3	Core Shape	57
2.4.4	Energies	59
2.4.5	Specific Angular Momentum	64
2.4.6	Caveats	67
2.5	Summary of this Chapter	68
3	Collision between Prestellar Cores	70
3.1	Introduction of this Chapter	70
3.1.1	Collisions at Core-Scale	70
3.1.2	Content of this Chapter	71
3.2	Methods	72
3.2.1	Numerical Code	72
3.2.2	Initial Conditions	72
3.2.3	Analysis	74
3.2.3.1	Color Variable	74
3.2.3.2	Derivation of Polarized Emissions	74

3.3	Results	76
3.3.1	Head-On Collisions	76
3.3.1.1	Head-On Collision Overview	77
3.3.1.2	$\mathcal{M}_c = 1$ and $\theta = 0^\circ$	77
3.3.1.3	$\mathcal{M}_c = 1$ and $\theta = 90^\circ$	80
3.3.1.4	$\mathcal{M}_c = 3$ and $\theta = 0^\circ$	80
3.3.1.5	$\mathcal{M}_c = 3$ and $\theta = 90^\circ$	80
3.3.2	Off-Center Collisions	81
3.3.2.1	$\mathcal{M}_c = 1$, and $\theta = 0^\circ$	81
3.3.2.2	$\mathcal{M}_c = 1$, and $\theta = 90^\circ$	83
3.3.2.3	$\mathcal{M}_c = 1$, and $\theta = 45^\circ$	83
3.3.2.4	$\mathcal{M}_c = 3$	84
3.4	Discussion	90
3.4.1	Discussion of Head-On Collision	90
3.4.2	Discussion of Off-Center Collision	92
3.4.2.1	Effect of the Initial Magnetic Field Strength	92
3.4.2.2	Effect of Initial Magnetic Field Orientation	93
3.4.3	Mixing of Gas	96
3.4.4	Caveats	101
3.5	Summary of this Chapter	102
4	Conclusions and Future Prospects	104
4.1	Summary of this Dissertation	104
4.2	Discussion and Conclusions throughout this Dissertation	106
4.3	Future Prospects	109
A	Key Terms and Concepts	111
A.1	Bonnor-Ebert Sphere	111
A.2	Mach number	114
A.3	Alfven Mach Number	115
A.4	Mass-to-Flux Ratio	115
A.5	Magnetic Field-Density Relation	116

A.6	The Timescale of Magnetic Braking	117
A.7	Triaxiality	119
A.8	Position-Position-Velocity Data Cube	119
A.9	Shock-Compression Ratio for the Isothermal MHD equations	121
B	Appendix of Chapter 2	123
B.1	Verification of Prograde Rotation	123
B.2	Dispersion of the Magnetic Field within Cores	124
B.3	Energies within Cores.	124
B.4	Mass-to-Flux Ratio	125
B.5	Rotation-Magnetic Field Relation and Energies	125
B.6	Shape of identified cores	129
B.7	Core-Scale and Clump-Scale Field Relation and Energies of Cores. . . .	131
B.8	Magnetic Field-Density Relation for Simulated Cluster-Forming Clumps	135
B.9	High-Resolution Runs	137
B.9.1	Angular Momentum for High-Resolution Runs	137
B.9.2	Magnetic Field for High-resolution Runs	141
B.9.3	Rotation-Magnetic Field Relation for High-Resolution Runs . .	141
C	Appendix of Chapter 3	146
C.1	Estimation of Collision Rate	146
C.2	Comparison with Observed Magnetic Spirals	148
	Bibliography	152

List of Figures

1.1	A schematic plot in the temperature and number density domain showing the locations of multiphases of the interstellar medium	2
1.2	A schematic of a molecular cloud showing hierarchical structures inside the cloud	3
1.3	The specific angular momentum-radius ($j - r$) correlation measured in both previous observations and simulations.	5
1.4	Projected stellar-spin inclinations of the 48 red giants of NGC 6791 and NGC 6819.	6
1.5	Magnetic fields in the Orion molecular cloud region.	8
1.6	Multiscale projections of simulated data in Hull et al. (2017).	10
1.7	The cumulative distribution function of the projected angles between the mean magnetic field and outflow directions.	13
2.1	Sample map from simulations considered in this study.	24
2.2	Time evolution of column density along the x -axis for the Rot-M5-B10P and Rot-M5-B10D model.	25
2.3	Time evolution of column density along the x -axis for the Col-M5-B10P and Col-M5-B10D model.	27
2.4	Histograms of the cosine of the relative angles between $\mathbf{\Omega}_0$ and \mathbf{L}_{core} in models of Rotation Setup	33
2.5	Histograms of the cosine of the relative angles between \mathbf{B}_0 and \mathbf{L}_{core} in models of w/o Setup	35
2.6	The cosine of relative orientation angles of \mathbf{L}_{core} pairs as a function of their separation distances in models of Rotation Setup.	36

2.7	Histograms of the cosine of the relative angle between \mathbf{B}_0 and \mathbf{B}_{core} in models of Rotation Setup.	37
2.8	The cosine of relative orientation angles of \mathbf{B}_{core} pairs as a function of their separation distances in models of Rotation Setup.	38
2.9	The cumulative distribution function of the cosine of the relative angle between \mathbf{B}_{core} and \mathbf{L}_{core} in models of Rotation Setup.	39
2.10	Same as Figure 2.4 except for Collision Setup models.	41
2.11	Same as Figure 2.6 except for Collision Setup models.	42
2.12	Same as Figure 2.7 except for Collision Setup models.	43
2.13	Slice plots of the gas density in a plane through the center of the simulation box at $t = 0.2$ Myr in Col-M1.5-B10P and Col-M1.5-B10D models.	44
2.14	Histograms of the cosine of the relative angle between \mathbf{B}_{core} and $\mathbf{\Omega}_{\text{col}}$ for fast collision models with $\theta_0 = 45^\circ$	45
2.15	Same as Figure 2.8 except for Collision Setup models.	46
2.16	Same as Figure 2.9 except for Collision Setup models.	47
2.17	Evolution of total angular momentum of dense gas in the z-direction, L_z	52
2.18	Slice map of ρj_z for the Col-M1.5-B10P and Col-M1.5-B100P models.	53
2.19	Column densities and momentum structure around the most massive dense core for the Rot-M1.5-B10P model and Col-M1.5-B10P model.	54
2.20	Histograms of the ratio of the free fall time t_{ff} to the magnetic braking timescale $\tau_{\text{b},\parallel} \equiv \rho_{\text{cl}} Z / \rho_{\text{ext}} v_{\text{A}}$	55
2.21	Same as Figure 2.20 except for the ratio of the free fall time t_{ff} to the magnetic braking timescale $\tau_{\text{b,col}} \equiv (8/5)^{1/3} \lambda_{\text{J}} / v_{\text{A}}$	56
2.22	The a_3/a_1 vs. a_2/a_1 plot.	59
2.25	$E_{\text{kin}}/ E_{\text{grav}} $ and $E_{\text{mag}}/ E_{\text{grav}} $, as a function of core radius.	63
2.26	Rotational parameter β and $E_{\text{rot}}/E_{\text{kin}}$, as a function of bound core radius.	64
2.27	Specific angular momentum, $j \equiv L_{\text{core}}/M_{\text{core}}$, plotted against the core radius.	66
3.1	Initial conditions with the mass surface density.	73
3.2	Column density, magnetic field, and velocity distributions of the model b0-M1-Bz10.	78

3.3	Temporal evolution of mass accretion rate of sink particles for head-on ($b = 0$) cases.	79
3.4	Temporal evolution of the maximum density normalized to the initial central core density for head-on ($b = 0$) cases.	79
3.5	As in Figure 3.2 except for the model b1-M1-By10	84
3.6	As in Figure 3.2 except for the model b1-M1-By30	85
3.7	As in Figure 3.2 except for the model b1-M1-Bz10	86
3.8	As in Figure 3.2 except for the model b1-M1-Bz30	87
3.9	Temporal evolution of the mass accretion rate of sink particles for off-center ($b = 1$) cases.	87
3.10	As in Figure 3.2 except for the model b1-M1-Bz50	88
3.11	As in Figure 3.4 except for off-center ($b = 1$) cases.	88
3.12	As in Figure 3.2 except for the model b1-M3-Bz10	89
3.13	Phase plot of the magnetic field strength and gas density for models b1-M1-By10 , b1-M1-By30 , and b1-M1-By50 at t_{sink} for each model. . . .	92
3.14	Simulation results in the B_0 vs. θ plane for models with $b = 1$ and $\mathcal{M}_c = 1$	94
3.15	Histogram of the relative angle between the magnetic field B and the velocity of dense gas ($> 10^5 \text{ cm}^{-3}$) pixel-by-pixel in models b1-M1-By50 , b1-M1-Bz50 , and b1-M1-Bob50	96
3.16	Integration of color variable in the line of sight.	98
3.17	As in Figure 3.2 except for the collision of unequal-mass cores.	99
3.18	Evolution of mass and mass accretion rate of the sink particle for the collision of unequal-mass cores.	100
3.19	Results for all models shown in a 3D parameter space.	102
4.1	The position and discoveries of this paper.	105
4.2	Comparison between classical views and pictures obtained from our study and recent research.	106
A.1	The density profile of Bonnor-Ebert sphere.	113
A.2	Dimensionless mass as a function of ρ_c/ρ_0	114
A.3	The geometries employed for discussing the magnetic braking of aligned and perpendicular rotators.	117

A.4	Schematic depiction of prolate, oblate, and triaxial ellipsoids.	120
A.5	The geometry of a plane parallel MHD shock.	122
B.1	Histograms of the cosine of the relative angles between $\mathbf{\Omega}_0$ and \mathbf{L}_{core} in the range of -1 to 1 for $\mathcal{M} = 1.5$ models.	123
B.2	Histograms of $\langle \theta_B \rangle$ for various models.	125
B.3	Energies of the gravitationally bound cores for models of Rotation Setups and w/o Setups.	126
B.4	Same as Figure B.3 except for models of Collision Setups.	127
B.5	Histograms of the estimated mass-to-flux ratio $\mu_\Phi = (M/\Phi)/(M/\Phi)_{\text{crit}}$ for each model.	128
B.6	$E_{\text{mag}}/ E_{\text{grav}} $ and $E_{\text{kin}}/ E_{\text{grav}} $, as functions of the cosine of the relative angle between \mathbf{L}_{core} and \mathbf{B}_{core}	129
B.7	Same as Figure B.6 except for Collision Setup models.	130
B.8	The a_3/a_2 vs. a_2/a_1 plot.	131
B.9	$E_{\text{mag}}/ E_{\text{grav}} $ and $E_{\text{kin}}/ E_{\text{grav}} $, as functions of the cosine of the relative angle between \mathbf{B}_{core} and \mathbf{B}_0	133
B.10	Same as Figure B.9 except for Collision Setup models.	134
B.11	Phase plots of B versus n_H among models with $\mathcal{M} = 5$, $B_0 = 10\mu G$, and $\theta = 0^\circ$	135
B.12	Same as Figure B.11 except for models with $\mathcal{M} = 5$, $B_0 = 100\mu G$, and $\theta = 0^\circ$	136
B.13	Same as Figure B.11 except for models with $\mathcal{M} = 1.5$, $B_0 = 10\mu G$, and $\theta = 0^\circ$	136
B.14	Same as Figure B.11 except for models with $\mathcal{M} = 1.5$, $B_0 = 100\mu G$, and $\theta = 0^\circ$	136
B.15	Same as Figure 2.4 except for high-resolution runs of Rotation Setup models.	139
B.16	Same as Figure 2.10 except for high-resolution runs of Collision Setup models.	140
B.17	Same as Figure 2.7 except for high-resolution runs of Rotation Setup models.	142
B.18	Same as Figure 2.12 except for high-resolution runs of Collision Setup models.	143

B.19	Same as Figure 2.14 except for high-resolution runs.	144
B.20	Same as Figure 2.9 except for high-resolution runs of Rotation Setup models.	145
B.21	Same as Figure 2.16 except for high-resolution runs of Collision Setup models.	145
C.1	Time evolution of the column density and position-velocity diagrams for the collision of unequal-mass cores.	150
C.2	Evolution of mass and mass accretion rate of the sink particle for the collision of unequal-mass cores.	151

List of Tables

1	List of abbreviations	xiv
2	List of symbols	xv
2.1	Summary of simulations and explored parameter space	31
2.2	Properties of identified bound cores	48
2.2	Properties of identified bound cores	49
2.3	Geometry of identified cores	61
2.4	Energetic properties of bound and unbound cores	65
3.1	Explored parameter space	75
3.2	Simulation results	82
B.1	Shape of identified cores	132
B.2	Summary of simulation results and explored parameter space for high-resolution runs	138
C.1	Properties of cores in models of w/o Setups	147

Abbreviations and Symbols

The following tables list the abbreviations and symbols used in this paper. Table 1 provides abbreviations. Table 2 lists symbols.

Table 1: List of abbreviations

Abbreviation	
AAS	American Astronomical Society
AD	Ambipolar diffusion
ALMA	Atacama Large Millimeter/submillimeter Array
AMR	Adaptive mesh refinement
BE	Bonnor-Ebert
CARMA	Combined Array for Research in Millimeter-wave Astronomy
CDF	Cumulative distribution function
CMF	Core mass function
DCF	Davis-Chandrasekhar-Fermi
GMC	Giant molecular cloud
HD	Hydrodynamics
HLL	Harten-Lax-van Leer
HLLD	Harten-Lax-Van Leer with multiple discontinuities
ISM	Interstellar medium
IMF	Initial mass function
IRAS	Infrared Astronomical Satellite
K-H	Kelvin-Helmholtz
K-S	Kolmogorov-Smirnov
MHD	Magnetohydrodynamics
MST	Minimum spanning tree
MUSCL	Monotonic Upstream-centered Scheme for Conservation Laws
NGC	New General Catalogue of Nebulae and Clusters of Stars
NRO	Nobeyama Radio Observatory
ONC	Orion Nebula Cluster
PLM	Piecewise linear model
SFE	Star formation efficiency
SIS	Singular isothermal sphere
SPH	Smoothed particle hydrodynamics
PPV	Position-positon-velocity
PV	Position-velocity
UV	Ultraviolet

Table 2: List of symbols

Symbol	Description
a_1, a_2, a_3	Axis lengths of cores
$\mathbf{a}_1, \mathbf{a}_2, \mathbf{a}_3$	Directions of core axis
α	$(E_{\text{clump,tur}} + E_{\text{clump,mag}} + E_{\text{clump,rot}} + E_{\text{clump,therm}})/ E_{\text{clump,grav}} $
b	Impact Parameter
b	Ratio of the impact parameter of the collision to r_c (in Chapter 3)
B	Magnetic field
B_0	Strength of initial large-scale uniform magnetic field
B_{los}	Line-of-sight components of magnetic field
B_{pos}	Plane-of-sky components of magnetic field
\mathbf{B}_0	Initial large-scale uniform magnetic field
\mathbf{B}_{core}	Mean magnetic field within the identified core
β	Thermal-to-magnetic pressure ratio
β	Ratio between the rotational energy and the gravitational potential energy (in Chapter 2)
β	Thermal-to-magnetic pressure ratio of the initial core surface (in Chapter 3)
C_i	Lagrangian tracers
c_A	Alfven velocity
c_s	Sound speed
c_s	Isothermal sound speed within the initial clump (in Chapter 2)
c_s	Isothermal sound speed within the initial core (in Chapter 3)
χ	Angle
χ	Polarization angle (in Chapter 3)
χ_c	Density contrast between the cloud surface and ambient ISM
Δx	Resolution of the simulation cell
Δx_{min}	Finest Resolution of the simulation cell
$E_{\text{clump,col}}$	Kinetic energy due to the overall motion of the clump for Collision Setup models
$E_{\text{clump,grav}}$	Gravitational energy of the initial clump
$E_{\text{clump,mag}}$	Magnetic energy of the initial clump
$E_{\text{clump,rot}}$	Rotational energy of the initial clump for Rotation Setup models
$E_{\text{clump,turb}}$	Turbulent energy of the initial clump
E_{grav}	Gravitational energy of the identified core
E_{kin}	Kinetic energy of the identified core
E_{mag}	Magnetic energy of the identified core
E_{rot}	Rotational energy of the identified core
E_{thermal}	Thermal energy of the identified core
γ	Adiabatic index
I	The total rotational inertia of the core
I_{ij}	Momentum of inertia within cores
j	Specific angular momentum

j_z	z component of the specific angular momentum
k	Boltzmann constant
k	Wavenumber
k_B	Boltzmann constant
L	Angular momentum
L_{box}	Length of one side of the simulation box
L_{core}	Magnitude of the net angular momentum of the identified core
L_{total}	Total angular momentum within simulation box around the center
L_z	Total angular momentum of gas in the z -direction around the center
\mathbf{L}_{core}	Net angular momentum of the identified core
$\hat{\mathbf{L}}_{\text{core}}$	The rotational axis for the core
l_{core}	Core MST separations
λ	Cores mean free path for a geometrical encounter
λ_J	Jeans length
M	Mass
M_c	Mass of the BE sphere
M_{clump}	Mass of the initial clump
M_{core}	Mass of the identified core
M_{total}	Total clump mass within the simulation box
M_J	Thermal Jeans mass
$M_{J,\text{mag}}$	Magnetic Jeans mass
\dot{M}	Mass accretion rate
m	Mass
m_H	Mass of hydrogen
\mathcal{M}	Mach number
\mathcal{M}	Mach number of turbulence within the clump (in Chapter 2)
\mathcal{M}_A	Alfven Mach number
$\mathcal{M}_{A,0}$	Alfven Mach number within the initial clump
\mathcal{M}_c	v_c/c_s
μ	Mean molecular weight
μ_Φ	Normalized mass-to-flux ratio
N_{core}	Total number of identified bound cores
n	Number density
n_{amb}	Number density of ambient gas
n_c	Number density of cores
n_{clump}	Number density of the initial clump
n_{crit}	Number density when refinement reaches maximum resolution
n_H	Hydrogen number density
n_{max}	Maximum number density within identified cores
n_{th}	Number density threshold above which gas is identified as cores
Ω_0	Rotational angular velocity of the clump for Rotation Setup models
Ω_{core}	Mean angular velocity of the identified core
Ω_{turb}	Total initial angular velocities of the clump purely from turbulence

$\mathbf{\Omega}_0$	Axis of rotation of the clump for Rotation Setup models
$\mathbf{\Omega}_{\text{col}}$	Axis of rotation generated by the collision for Collision Setup models
P	Pressure
P_{col}	Collision probability
p	Polarization fraction
\mathbf{p}	Polarized emissions
Φ	Magnetic Flux
ϕ	Relative angle between the magnetic field and velocity of dense gas
R_{clump}	Radius of the initial clump
R_{core}	Radius of the identified core
r	Radius
r_c	Radius of cores
r_c	Radius of BE sphere (in Chapter3)
\mathbf{r}_{CM}	Center of mass
ρ	Density
ρ_c	Central density of the BE sphere
ρ_{cen}	Central density of the core
ρ_{cl}	Density of the core
ρ_{clump}	Density of the initial clump
ρ_{crit}	Density when refinement reaches maximum resolution
ρ_{ext}	Density in the ambient medium
ρ_{th}	Density threshold above which gas is identified as cores
S	Orientation parameter
S_{B,a_1}	$(3\langle \cos^2 \angle[\mathbf{B}_{\text{core}}, \mathbf{a}_1] \rangle - 1)/2$
S_{B,a_3}	$(3\langle \cos^2 \angle[\mathbf{B}_{\text{core}}, \mathbf{a}_3] \rangle - 1)/2$
S_{B,B_0}	$(3\langle \cos^2 \angle[\mathbf{B}_{\text{core}}, \mathbf{B}_0] \rangle - 1)/2$
$S_{B,\Omega}$	$(3\langle \cos^2 \angle[\mathbf{B}_{\text{core}}, \mathbf{\Omega}_{\text{col}}] \rangle - 1)/2.$
S_{L,a_1}	$(3\langle \cos^2 \angle[\mathbf{L}_{\text{core}}, \mathbf{a}_1] \rangle - 1)/2$
S_{L,a_3}	$(3\langle \cos^2 \angle[\mathbf{L}_{\text{core}}, \mathbf{a}_3] \rangle - 1)/2$
$S_{L,B}$	$(3\langle \cos^2 \angle[\mathbf{L}_{\text{core}}, \mathbf{B}_{\text{core}}] \rangle - 1)/2.$
S_{L,B_0}	$(3\langle \cos^2 \angle[\mathbf{L}_{\text{core}}, \mathbf{B}_0] \rangle - 1)/2$
$S_{L,\Omega}$	$(3\langle \cos^2 \angle[\mathbf{L}_{\text{core}}, \mathbf{\Omega}_0] \rangle - 1)/2$ (for Rotation Setup)
$S_{L,\Omega}$	$(3\langle \cos^2 \angle[\mathbf{L}_{\text{core}}, \mathbf{\Omega}_{\text{col}}] \rangle - 1)/2$ (for Collision Setup)
σ	Collision cross section
σ_v	Velocity dispersion within the clump
T	Temperature
T	Triaxiality (in Chapter 2)
t	Time
t_{ff}	Free-fall time
t_{sink}	Sink formation time
$\tau_{\text{b},\parallel}, \tau_{\text{b,col}}$	Magnetic braking timescale
τ_{coll}	Collision time scale

θ	Angle between the initial uniform magnetic field relative to the collision axis of the cores
θ_0	Angle between \mathbf{B}_0 relative to the $\mathbf{\Omega}_0$ (for Rotation Setup)
θ_0	Angle between \mathbf{B}_0 relative to the $\mathbf{\Omega}_{\text{col}}$ (for Collision Setup)
$\theta_{B,B}$	Relative angle between \mathbf{B}_{core} pairs
$\theta_{L,L}$	Relative angle between \mathbf{L}_{core} pairs
V	Volume
V_0	Initial velocity of the clumps for Collision Setup models
V_{core}	Volume of the identified core
V_{rel}	Relative collision velocity for Collision Setup models
v	Velocity
v_A	Alfven velocity
$v_{A,\text{clump}}$	Alfven velocity within the initial clump
v_c	Velocity of the core with respect to the parent cloud
v_c	Pre-collision speeds of cores (in Chapter 3)
\mathbf{v}_{mean}	Mean velocity of the core
v_{rot}	Rotation velocity
ξ	Dimensionless radius of BE sphere
ξ_{crit}	Critical dimensionless radius of BE sphere
Z	Half of core height

Publication List

This doctoral dissertation is based on

Chapter 2: Shinichi. W. Kinoshita and Fumitaka Nakamura, 2023, ApJ, 955, 122, doi: [10.3847/1538-4357/acf1f9](https://doi.org/10.3847/1538-4357/acf1f9)

Chapter 3: Shinichi W. Kinoshita and Fumitaka Nakamura, 2022, ApJ, 937, 69, doi: [10.3847/1538-4357/ac8c95](https://doi.org/10.3847/1538-4357/ac8c95)

Some methodology and discussions are related to works in the master's course,

Shinichi W. Kinoshita, Fumitaka Nakamura and Benjamin Wu, 2021, ApJ, 921, 150, doi: [10.3847/1538-4357/ac1d4b](https://doi.org/10.3847/1538-4357/ac1d4b)

The dissertation's author, Shinichi Kinoshita, is responsible for the entire scope of the work, from its conception to the simulation, analysis, and discussion, with the cooperation of the supervisor, Fumitaka Nakamura.

Chapter 1

General Introduction

1.1 Star Formation in the Molecular Cloud

A galaxy comprises stars and interstellar medium (ISM). ISM is the material that fills the space between the stars and consists mainly of gas and dust. The chemical composition of interstellar gas is close to the cosmic composition, namely, 90.8 % by the number of hydrogen, 9.1 % of helium, and 0.12 % of heavier elements (Ferrière, 2001). ISM is dynamic and found with a wide range of temperatures and densities (Myers, 1978). Figure 1.1 shows the temperature and number density of the ISM in the Milky Way. Pressures of intercloud gas (partially ionized H) and diffuse cloud (HI cloud) are in the range of $10^2 \text{ K cm}^{-3} \lesssim P/k \lesssim 10^4 \text{ K cm}^{-3}$ and they are approximately in pressure equilibrium. HII region and molecular clouds are out of pressure equilibrium. HII regions are ionized by the Lyman continuum photons from the early-type stars. Molecular clouds are a high-density gravitationally bound gas where star formation takes place. If the conditions are right, star clusters containing many thousands of stars will form in giant molecular clouds (GMCs).

GMCs have a predominantly hierarchical structure with higher density as the scale decreases (see Figure 1.2). The typical radius, density, mass, and temperature of the GMC are $\sim 10 \text{ pc}$, $\sim 10^3 \text{ cm}^{-3}$, $\sim 10^5 M_\odot$, and $\sim 10 \text{ K}$. GMCs exhibit turbulence with supersonic motions at size scales $\gtrsim 0.1 \text{ pc}$; the bulk of their volume is characterized by gas motion that exceed the thermal sound speed. Within these clouds are clumps at intermediate densities with sizes $\sim 0.1 - 1 \text{ pc}$. Clumps generally contain a number of

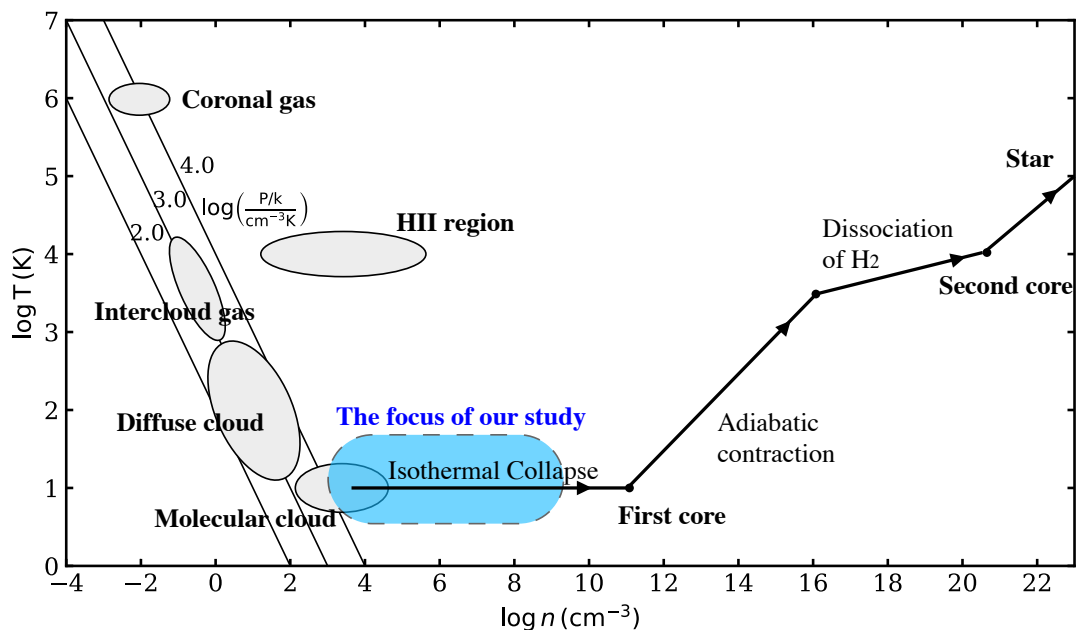


Figure 1.1: A schematic plot in the temperature and number density domain showing the locations of multiphases of the interstellar medium. The three diagonal lines indicate constant pressure domains. The diagram in the range of $n \lesssim 10^{10} \text{ cm}^{-3}$ is originally made by [Myers \(1978\)](#). In the higher density range, a theoretical path from the molecular cloud core to the star is also shown ([Bhandare et al., 2018](#)). Blue shaded area indicates the focus of our study (see § 1.6).

cores, the objects from which new stars are born ([Shu et al., 1987](#)). Cores are self-gravitating density peaks, which have a typical size of $\sim 0.1 \text{ pc}$, density of $10^5 - 10^7 \text{ cm}^{-3}$ and a mass of order $0.3 - 10 M_{\odot}$. Unlike in molecular clouds, in cores, the velocity dispersion tends to be subsonic (e.g., [Barranco & Goodman, 1998](#); [Hacar & Tafalla, 2011](#)).

The dynamical stability of a core is determined by the relative importance of thermal, non-thermal (turbulent), and magnetic pressure against its own gravity. A gravitationally bound starless core with temperatures typically of order a few Kelvin is called a prestellar core ([Ward-Thompson et al., 1994, 1999](#)). Prestellar cores are generally not spherical, but it has been found to be a Bonnor-Ebert (BE) sphere (see Appendix A.1). In combination with turbulence and gas gravity, magnetic effects and angular momentum are considered important factors affecting the dynamics within prestellar cores and subsequent star formation (see § 1.2 - 1.4).

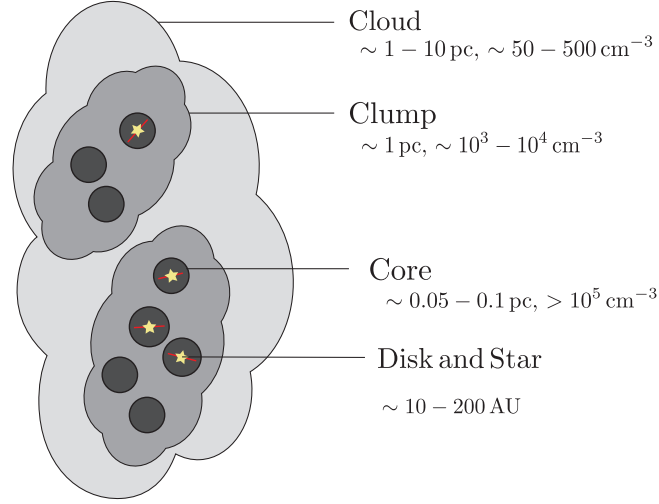


Figure 1.2: A schematic figure showing hierarchical structures within the cloud. The image is not drawn to scale. The figure shows the cloud, clumps, cores, and protostellar systems. Properties of them is taken from [Bergin & Tafalla \(2007\)](#).

There have been detailed numerical investigations of core-collapse (see review by [Young, 2023](#)). Figure 1.1 shows a theoretical path from the prestellar core to the star. During the initial stage of core-collapse ($10^4 \text{ cm}^{-3} \lesssim n \lesssim 10^{10} \text{ cm}^{-3}$), radiative cooling in molecular lines and thermal emission from dust grains keep the gas almost isothermal. As a result, the gas pressure is not important at this stage, and the gas material moves inward in a nearly free-fall state. Therefore, the timescale of star formation is roughly determined by the free-fall time¹:

$$t_{\text{ff}} = \sqrt{\frac{3\pi}{32G\rho}} = 0.44 \left(\frac{n_{\text{H}}}{10^4 \text{ cm}^{-3}} \right)^{-1/2} \text{ Myr}, \quad (1.1)$$

where G is the gravitational constant, ρ is the density, n_{H} is the number density of the core.

When the core central density increases as $\sim 10^{11} \text{ cm}^{-3}$, the optical depth becomes greater than unity, and radiative cooling becomes inefficient. As gas pressure rises,

¹Theoretical models indicate that the lifetimes of the cores vary between ~ 1 to ~ 10 times of t_{ff} , with the latter representing the characteristic timescale of ambipolar diffusion ([McKee, 1989](#)).

it decelerates the contraction, eventually forming the hydrostatic object, known as "first core" at the center. The first core eventually contracts adiabatically. Once the central temperature reaches ~ 2000 K, the hydrostatic core becomes unstable due to H_2 dissociation and initiates the second collapse phase. The second hydrostatic core, i.e., the protostar, is formed after most of the H_2 is dissociated and eventually undergoes a phase of adiabatic contraction.

The protostar is surrounded by the infalling envelope, which is called the protostellar core. As the system evolves further, the conservation of angular momentum leads to forming a circumstellar disk around the protostar, which can eventually host planets. Once the core center reaches the ignition temperatures of nuclear hydrogen burning ($\geq 10^6$ K), a star is born.

1.2 Angular Momentum within Cores

In the core collapse process, the angular momentum of dense cores, L , is important, leading to the creation of protostellar systems within dense cores. Due to the angular momentum of the dense core, the accretion material cannot directly fall onto the central protostar, which results in the formation of a rotationally-supported disk. In addition, large angular momentum causes fragmentation in the collapsing core, which then leads to the formation of binary or multiple systems (e.g., [Miyama et al., 1984](#); [Tsuribe & Inutsuka, 1999](#)).

It is known that some dense cores show a clear gradient in line-of-sight velocity. This velocity gradient can be attributed to the rotation of clouds/cores ². In observational studies, linear fitting of the velocity gradient is commonly used to estimate the angular momentum. Previous observations and numerical simulations confirmed a power-law relationship between the specific angular momentum j and radius r for dense cores and clumps with radii $\sim 0.005 - 10$ pc, such that $j \propto r^\alpha$, with $\alpha \approx 1.5 - 2$ (see [Figure 1.3](#)). Recently, [Gaudel et al. \(2020\)](#) found $j \propto r^{1.6}$ above 1600 au and $j \approx \text{constant}$ between 50-1600 au in 12 Class 0 protostellar envelopes. [Pandhi et al. \(2023\)](#) found $j \propto r^{1.82 \pm 0.10}$ for cores in some star forming regions. The power-law $j - r$ correlation in wide spatial scales suggest that rotational motion in cores originates at scales much larger than the core size.

²Velocity gradients can also be attributed to other ordered flows like accretion or collapse

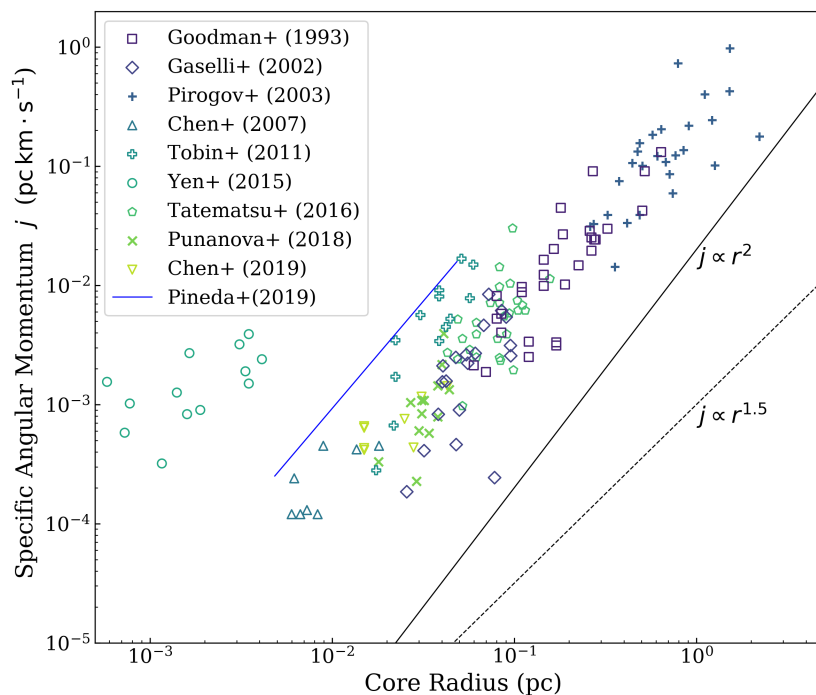


Figure 1.3: The specific angular momentum-radius ($j - r$) correlation measured in previous observations (Goodman et al., 1993; Caselli et al., 2002; Pirogov et al., 2003; Chen et al., 2007; Tobin et al., 2011; Yen et al., 2015; Tatematsu et al., 2016; Punanova et al., 2018; Chen et al., 2019). The blue line indicates the specific angular momentum radial profile shown in Pineda et al. (2019). The black solid and dashed lines are $j \propto r^2$ and $j \propto r^{1.5}$ respectively.

There are some proposals for the origin of angular momentum within cores. Burkert & Bodenheimer (2000) claimed that observed angular momentum within cores could simply be from the sampling of turbulence at a range of scales. Since, $j = L/M \sim r \cdot v_{\text{rot}}$, the power-law relation $j \propto r^{1.5}$ suggest that $v_{\text{rot}} \propto r^{0.5}$ (Chen & Ostriker, 2018). Such a relation is consistent with the Larson relation that turbulent velocities increase roughly $\propto r^{0.5}$ in supersonic turbulence. Thus, the observed relation $j \propto r^{1.5}$ may suggest that the rotational velocity in cores is inherited from the overall turbulent cascade (Chen & Ostriker, 2018, see also Offner et al., 2008; Dib et al., 2010; Ntormousi & Hennebelle, 2019). Alternatively, Kuznetsova et al. (2019) claimed that the angular momentum is generated by local torques from other cores and density concentrations.

The large-scale rotation in the parent body of cores is also a candidate for the origin of angular momentum. Observations have shown the spin alignment of stars in some open clusters (Corsaro et al., 2017; Kovacs, 2018). Figure 1.4 shows the distribution of the

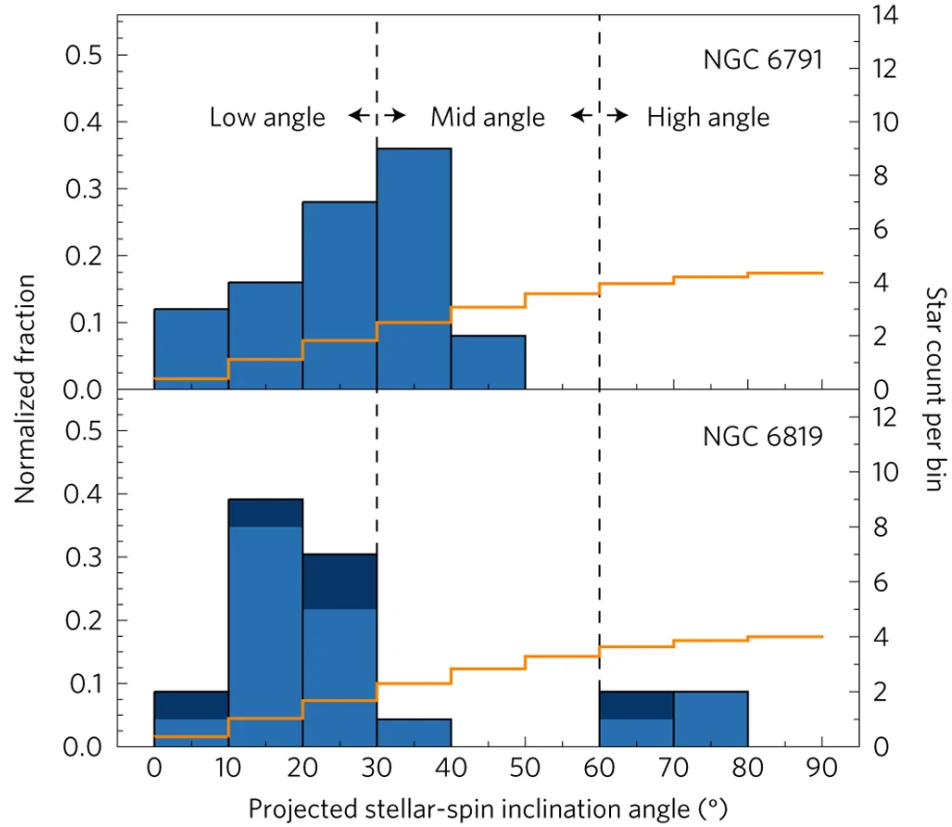


Figure 1.4: Projected stellar-spin inclinations of the 48 red giants of NGC 6791 and NGC 6819. The top panel shows the distribution of the inclination angle from the line of sight for NGC 6791. The orange histogram shows the expected distribution for a three-dimensional uniform orientation of the spin vectors. The bottom panel is the same as the top panel but for NGC 6819. Figure taken from [Corsaro et al. \(2017\)](#), reproduced by permission of Springer Nature.

spin inclinations in 48 stars from the two open clusters NGC 6791 and NGC 6819. The distributions are far from random; the stars within each cluster show strong alignment. This result indicates that the global angular momentum of the parental clouds was efficiently transferred to each star. Hydrodynamical simulations by [Corsaro et al. \(2017\)](#) also indicated that the stellar spin alignment happens unless the global rotation of the star-forming clump is weak compared to the turbulence. In contrast, [Jackson & Jeffries \(2010\)](#) indicated mostly random distributions of spin axes in young open clusters. The spin alignment is not universal. The origin of the angular momentum is not clearly understood and subject to ongoing research.

1.3 Magnetic Fields within Cores

Molecular clouds are weakly ionized by UV photons and cosmic rays ([McKee & Ostriker, 1977](#)). Therefore, the magnetic field and mass should be well coupled (flux freezing). Figure 1.6 illustrates the examples of ordered magnetic fields that pervade the star forming region from cloud-scale to core-scale in the Orion molecular cloud region. These magnetic fields can affect the dynamics of star formation in molecular clouds at all physical scales and throughout different evolutionary stages ([Shu et al., 1987](#); [McKee & Ostriker, 2007](#); [Crutcher, 2012](#)). While cloud-scale magnetic fields in clouds could restrict compression caused by turbulence-driven shocks and restrict gas movement, the core-scale magnetic field is important in regulating the gas dynamics within cores via removing angular momentum and transporting feedback (see § 1.4).

Magnetic fields within prestellar cores are generally considered to act to resist the gravitational collapse ([Mestel & Spitzer, 1956](#)), while debate continues over whether magnetic fields play a significant role in the process of star formation or negligible. Line-of-sight components (B_{los}) can be directly measured through Zeeman splitting of spectral lines of paramagnetic species (e.g., [Crutcher & Kemball, 2019](#)). According to Zeeman measurement, mass-to-flux ratios (see Appendix A.4) are estimated to be mildly supercritical with typical values $\mu_{\Phi} \sim 2 - 3$ ([Crutcher, 2012](#)). The average Alfvén Mach number (see Appendix A.3) estimated by Zeeman measurement is found to be $\mathcal{M}_A \sim 1.5$, suggesting the approximate equipartition between the turbulent and magnetic energies ([Falgarone et al., 2008](#); [Girart et al., 2009](#)). While Zeeman measurement is used to estimate the strength of B_{los} , near-IR starlight polarization and sub-mm polarized dust emission provide the features of magnetic fields in the plane of

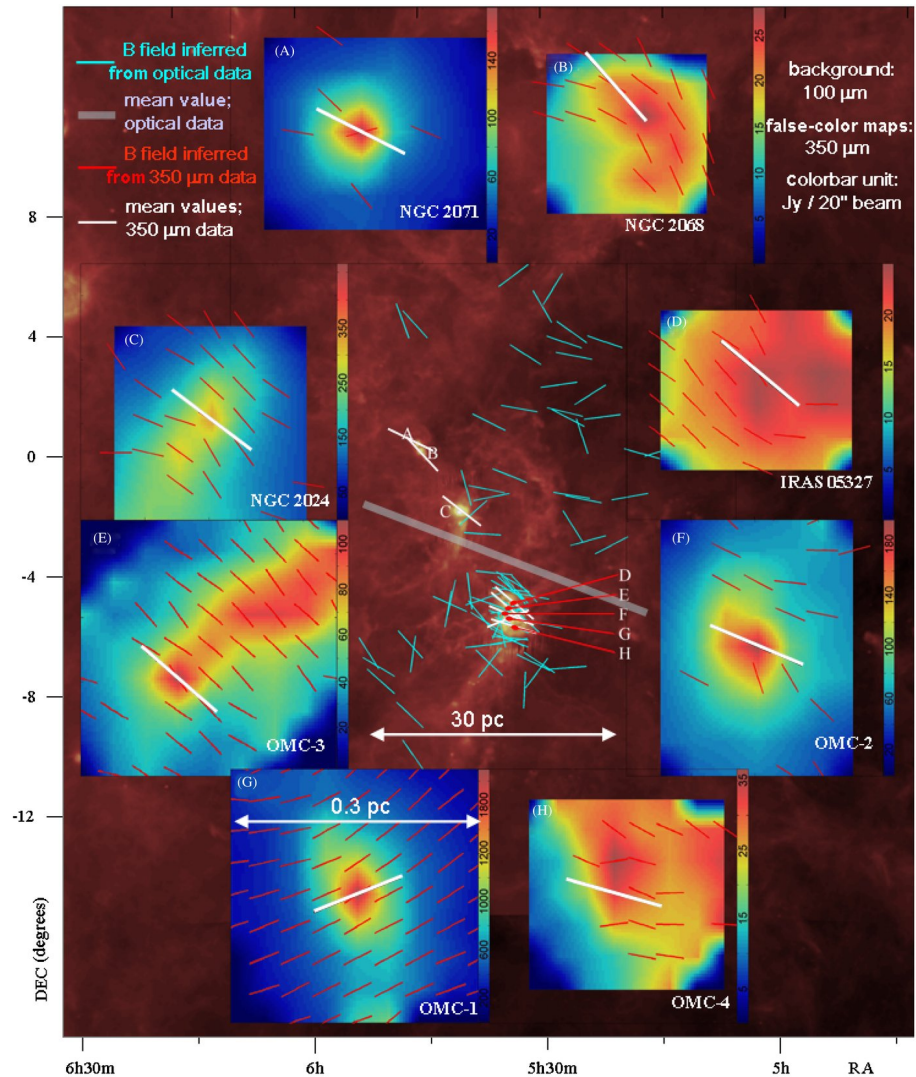


Figure 1.5: Magnetic fields in the Orion molecular cloud region. Light blue lines show optical data, and red lines show 350 μ m Hertz Caltech Submillimeter Observatory data that sample the polarization of dust emission in each of the cores (see labels A through H). Thick white lines show the mean field directions over the extended region and in each core. The background image shows the IRAS 100 μ m map. Figure taken from (Li et al., 2009), and reproduced by permission of the AAS.

the sky, B_{pos} , as oblong dust grains tend to be aligned by magnetic fields (e.g., [Lazarian, 2007](#)). The strength of B_{pos} can be estimated by the Davis-Chandrasekhar-Fermi (DCF) method ([Davis, 1951](#); [Chandrasekhar & Fermi, 1953](#)). The DCF measurements of magnetic field strength in cores range from $\sim 10\mu G$ (e.g., [Kirk et al., 2006](#)) to a few $100\mu G$ (e.g., [Karoly et al., 2020](#)). Corresponding mass-to-flux ratios range from moderate supercritical (e.g., $\mu_{\Phi} \sim 2 - 3$; [Kirk et al., 2006](#)) to subcritical (e.g., $\mu_{\Phi} \sim 0.1 - 0.4$; [Karoly et al., 2020](#)).

These measurements indicate that magnetic pressure alone is not sufficient to balance gravity and prevent contraction, but magnetic fields are dynamically important in most cores. Field strengths vary considerably from cloud to cloud, so some cores may be magnetically supported. However, [Sanhueza et al. \(2019\)](#) found $\mu_{\Phi} > 8$ in the high mass star-forming regions IRAS 18089-1732, suggesting that, in at least some cases, cores may be highly gravitationally-dominated.

The correlation between core- and cloud-scale fields is a crucial topic. Observations of magnetic fields in cores are still limited in number, so it's uncertain whether discrepancies exist between large-scale and core-scale fields. However, there have been several recent observational efforts on this front. For instance, [Pattle et al. \(2021\)](#) observed magnetic fields of the L1689 Molecular Cloud and core/clumps inside it. In two of the core/clump inside L1689, the core-scale field morphologies are consistent with the cloud-scale field, but in one, there were discrepancies between the large and core/clump scale fields. In other regions, the large and small fields agree in some cores, while in others, they are perpendicular (e.g., [Alves et al., 2014](#); [Chen et al., 2020](#); [Doi et al., 2020](#); [Karoly et al., 2020](#)). [Hull et al. \(2017\)](#) conducted magnetohydrodynamic (MHD) simulations to study the magnetic field's orientation. Figure 1.6 compares their simulations. Only in the very strongly magnetized case (sub-Alfvenic), the field direction is preserved from cloud to protostar scales. When the cloud-scale magnetic field is weak, turbulence shapes the field on small scales, divorcing it from the mean large-scale magnetic field. This result suggests that the relationship between core- and cloud-scale fields highly depends on the magnetic field strength. [Chen et al. \(2020\)](#) conducted MHD simulations of plane-parallel converging flows resulting in a strongly magnetized post-shock layer (plasma $\beta \sim 0.1$). They found that the local field in the post-shock layer is generally aligned with the large-scale field. Further analysis involving simulations with various levels of magnetization and simulations will better quantify this correlation.

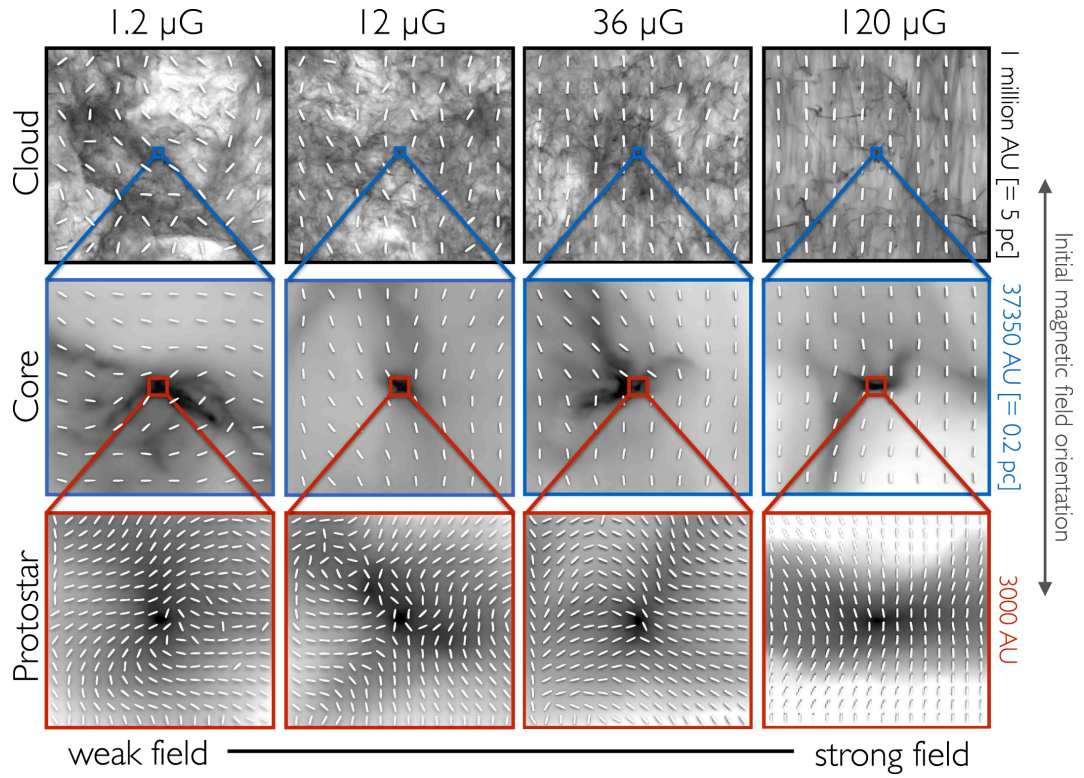


Figure 1.6: Multiscale column densities and the magnetic field orientation of protostellar cores that formed in simulations in [Hull et al. \(2017\)](#). The initial magnetic field strength increases from the left to the right columns, corresponding to $\mathcal{M}_A = 35, 3.5, 1.2$, and 0.35 . Figure taken from [Hull et al. \(2017\)](#), and reproduced by permission of the AAS.

1.4 Rotation-Magnetic Field Relation

A well-known problem is that cores have much larger angular momentum than is measured in individual stars. For example, the specific angular momentum $j \equiv L/M$ of the classical T Tauri stars is observed to be $j \sim 10^{16} \text{ cm}^2 \text{ s}^{-1}$ (Bouvier et al., 1993). On the other hand, in observed NH_3 cores, j is approximately $\sim 10^{21} \text{ cm}^2 \text{ s}^{-1}$ (Goodman et al., 1993). If momentum conservation holds, the interstellar gas cannot shrink to the size of a stellar object. In order to overcome this angular momentum barrier and contract to protostar, the core must lose nearly all of its angular momentum. One of the mechanisms to lose angular momentum is "magnetic braking" during the collapse of prestellar cores and the formation of disks. In ideal MHD, magnetic braking can be simply understood as removing the angular momentum of inner material via transport along the magnetic field lines to the ambient medium (Mouschovias & Paleologou, 1979, 1980).

Numerical simulations, however, showed "magnetic braking catastrophe", i.e., magnetic braking should prevent disks from forming unless the dense cores are weakly magnetized to an unrealistic level (Allen et al., 2003; Hennebelle & Fromang, 2008; Mellon & Li, 2008; Hennebelle et al., 2011). As described in § 1.3, the observed dense core has a typical of $\mu_\Phi \sim 2 - 3$. Such a strong magnetic field, if not sufficiently decoupled from collapsing gas, can transport most angular momentum away via magnetic braking, suppressing the formation of the rotationally supported disc.

Nonideal MHD effects, including ambipolar diffusion (AD), Ohmic dissipation, and Hall effect, have been proposed to enable the decoupling between core material and magnetic field, allowing the formation of rotationally supported proto-planetary disks (Shu et al., 2006; Krasnopolsky et al., 2011; Machida et al., 2011; Dapp et al., 2012; Tomida et al., 2012). Zhao et al. (2016, 2018) showed that a moderate grain could greatly promote AD and help the formation of rotationally supported disks.

The classical theory suggests that the magnetic axis of cores should be parallel to their rotational axis, as perpendicular configuration allows for faster magnetic braking compared to parallel configurations (Mouschovias, 1979; Mouschovias & Paleologou, 1979, see also Appendix A.6). Therefore, many analytical models of star formation have, for simplicity, assumed that the rotation axis of the core, its magnetic field direction, and its outflow direction are all parallel (Shu et al., 2000; Konigl & Pudritz, 2000).

However, [Hennebelle & Ciardi \(2009\)](#) (see also [Price & Bate, 2007](#)) pointed out that the disk formation process is significantly affected by misalignment between the magnetic field and rotation axis. In non-collapsing prestellar cores, whose density is not centrally condensed and fanning-out of magnetic fields is weak, magnetic braking is more efficient when the magnetic field is initially misaligned with the rotation axis rather than when it is aligned. On the other hand, for collapsing cores where magnetic field lines are strongly squeezed toward the center, aligned rotators are more efficiently braked than misaligned ones (for details, see [Joos et al., 2012](#) and [Tsukamoto et al., 2018](#)). Many researchers have emphasized the significance of magnetic field-rotation misalignment in the formation of disks ([Ciardi & Hennebelle, 2010](#); [Joos et al., 2012](#); [Boss & Keiser, 2013](#); [Krumholz et al., 2013](#); [Hirano et al., 2020](#)). They indicated that a rotationally supported disk can form in prestellar cores where the rotation axis is not initially aligned with the global magnetic field. The magnetic field-rotation misalignment appears to be the promising solution to magnetic braking catastrophe.

The interplay between magnetic field and rotation is also responsible for launching outflows, and their misalignment is critical for outflow formation. [Ciardi & Hennebelle \(2010\)](#) found that mass ejection is less efficient for increasing the angle between the rotation axis and large-scale magnetic field. Several numerical simulations also suggest that there is a correlation among the disk size, outflow activity, and misalignment (e.g., [Li et al., 2013](#); [Hirano et al., 2020](#)). [Hirano et al. \(2020\)](#) showed that the misalignment promotes disk formation and suppresses outflow driving in the gas accretion phase unless the initial cloud is highly gravitationally unstable.

[Hull et al. \(2013\)](#) and [Hull & Zhang \(2019, and references therein\)](#) showed the random orientations of the core rotation and magnetic fields within protostellar cores in various regions in the whole sky. Figure 1.3 shows the cumulative distribution function (CDF) of the projected angles between the magnetic fields and outflows derivable from interferometric observations of low-mass protostellar cores. The observed CDF is similar to that expected for random alignment, shown by the solid curve. If one assumes that outflows are launched parallel to the angular momentum of the core ([Tomisaka, 2002](#); [Matsumoto & Tomisaka, 2004](#); [Launhardt et al., 2009](#)), then this result implies that the rotation axes do not align with the magnetic fields. [Doi et al. \(2020\)](#) also find no correlation between the magnetic field angles and the rotation axes in NGC 1333. On the other hand, there are observations suggesting the preference for weak alignment of them in some regions ([Yen et al., 2021](#); [Xu et al., 2022](#)). [Kong et al. \(2019\)](#) indicated

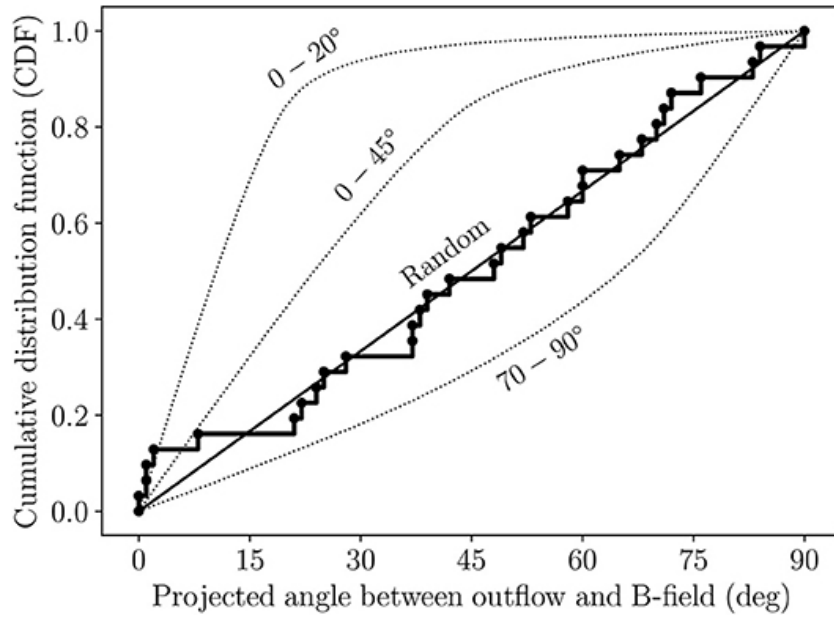


Figure 1.7: The thick solid curve represents the cumulative distribution function (CDF) of the projected angles between the mean magnetic field and the outflow directions derivable from interferometric observations of low-mass protostellar cores. The dashed curves are the CDF from a Monte Carlo simulation where outflow and magnetic field directions are constrained to within 20° , 45° , and $70 - 90^\circ$ of one another, respectively. The straight line represents the CDF for random orientation. Figure taken from [Hull & Zhang \(2019\)](#).

outflow axes being mostly orthogonal to their parent filament in G28.37+0.07, which may suggest a preferred alignment between the core rotation and bulk field.

Previous simulations have also implied the misalignment between the magnetic field and the rotation axes. Core-scale simulations with turbulence have shown that turbulence could produce an angle difference between the magnetic field and rotation vector of the collapsing core (Joos et al., 2013; Matsumoto et al., 2017). In cloud/clump-scale, Chen & Ostriker (2018) looked at 3D MHD simulations of plane-parallel converging flows and showed no preferred alignment between the magnetic field and core angular momentum orientation. Using MHD simulations of weakly magnetized clouds, Kuznetsova et al. (2020) found that the relative angle between the angular momentum of the core and the local core-scale magnetic field is consistent with being randomly distributed. Such simulations probing the rotation-magnetic field relation at the cloud/clump scale are few, and the parameters that have been investigated are limited. Further investigation of the rotation-magnetic field relation is necessary.

1.5 Collision between Prestellar Cores

A velocity dispersion of approximately a few $\text{km} \cdot \text{s}^{-1}$ is often found in star forming regions and in the interiors of giant molecular clouds (see § 1.1). In such turbulent clouds, collisions between dense cores are possible because of the velocity dispersion between them. Some theoretical studies (e.g., Inutsuka & Miyama, 1997) have also suggested that coalescence among dense cores can occur after the fragmentation of their parental filamentary cloud.

We can roughly estimate the geometrical collision timescale for dense cores. Cores mean free path for a geometrical encounter is given by

$$\lambda = \frac{1}{\sigma n_c}. \quad (1.2)$$

Here, we assume that cores with a collision cross-section of σ are distributed uniformly in the cloud with a core number density of n_c . Then, the collision time scale can be estimated as:

$$\tau_{\text{coll}} = \frac{\lambda}{v} = \frac{1}{4\pi r_c^2 n_c v_c}. \quad (1.3)$$

In the above estimation, we assumed the collision of identical cores and replaced σ with $4\pi r_c^2$, where r_c is the radius of the core that experiences collisions; v_c is the velocity of

the core with respect to that of the parent cloud; and τ_{coll} is expressed as follows:

$$\tau_{\text{coll}} \sim 0.15 \left(\frac{r_c}{0.05 \text{ pc}} \right)^{-2} \left(\frac{n_c}{200 \text{ pc}^{-3}} \right)^{-1} \left(\frac{v_c}{\text{km s}^{-1}} \right)^{-1} \text{ Myr}, \quad (1.4)$$

As an observational example, we use the core sample of the Orion Nebula Cluster (ONC) region to estimate the collision timescale, τ_{coll} , in GMCs. This area was recently observed by CARMA-NRO (Kong et al., 2018). Using CARMA-NRO C¹⁸O ($J = 1 - 0$) data, Takemura et al. (2021) identified approximately 200 dense cores in the filamentary region of ONC ($\sim 1 \text{ pc}^{-3}$ area), which gives a number density of $n_c \sim 200 \text{ pc}^{-3}$. If we adopt $r_c = 0.05 \text{ pc}$ and $v_c = 1 \text{ km s}^{-1}$ as representative values, we can derive the collision time $\tau_{\text{coll}} \sim 0.15 \text{ Myr}$ using Equation 1.4. Takemura et al. (2021) derived the core lifetime in Orion A of $\sim 5 t_{\text{ff}} \simeq 0.5 - 1.5 \text{ Myr} > \tau_{\text{coll}}$ for starless cores with densities $\sim 10^4 - 10^5 \text{ cm}^{-3}$. Therefore, the typical core would experience collisions before a star is created. In the denser region or flowing along the filamentary structures, more frequent collisions can be expected. Virtually, Tokuda et al. (2020) found the internal substructures with a size scale of $\sim 1000 \text{ au}$ in prestellar cores, and proposed core-core collision as one possible origin of its formation. Their estimation indicated that the coalescence of dense cores can occur within their lifetime.

Huang et al. (2013) suggested that core coagulation is one of the dominant physical processes to determine the form of dense cores mass function (CMF). They have reproduced the observed CMF among the starless cores using a numerical method to consider the coalescence between cores and their ablation induced by their relative motion through ambient gas. Dib (2023) showed that the increased efficiency of the core coalescence process leads to shallower slopes of the initial mass function (IMF) in agreement with the observations of young clusters. These studies have indicated that the interaction between cores is crucial in determining the initial states of stars/clusters. However, these theoretical models ignore the effects of magnetic fields and phenomena at the local scale during collisions. Understanding and organizing the specific depiction of the collision between prestellar cores is important.

1.6 Purpose of this Thesis

This thesis aims to explore the properties of prestellar cores. Prestellar cores, as immediate precursors of stars, are the initial conditions of star formation and determine

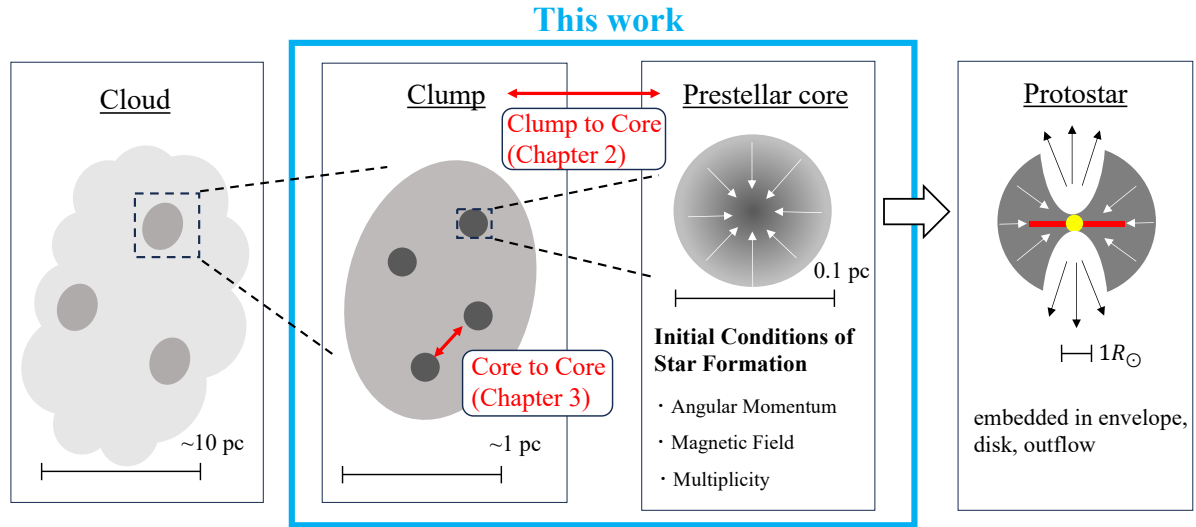


Figure 1.8: Schematic view of the focus of this paper. In Chapter 2, we explore the link between the dynamics of prestellar cores and clump physical states. In Chapter 3, we investigate the properties of prestellar cores after interaction with neighboring cores. Throughout this paper, we study properties of prestellar cores, i.e., initial conditions of star formation. See also Figure 1.1.

the local environment of protostellar disks, outflows, and multiplicity of stars. Therefore, understanding their properties is essential for comprehensively grasping the star formation process.

Figure 1.8 provides the schematic view of the approach of this thesis. Recent observations imply that prestellar cores' properties vary from region to region, indicating a dependence on the local environment. For example, as described in § 1.2, some studies indicate mostly random distributions of spin axes in young open clusters, while others have found strong spin alignment of stars within specific open clusters. That is to say, in some regions, the large-scale rotation of the parent structure (clump/cloud) is the origin of angular momentum, whereas, in other regions, this large-scale rotation is not reflected in the core rotation. Also, as explained in § 1.3, the correlation between the magnetic field within cores and the large-scale magnetic field varies by region. Therefore, it is essential to systematically investigate the relationship between the prestellar cores and their encompassing external environment. Top-down simulations of clump-scale provide a powerful tool for studying the formation and evolution of star clusters (e.g., Klessen et al., 2000; Bate et al., 2003; Nakamura & Li, 2007; Vázquez-Semadeni

et al., 2011; Padoan et al., 2014). In light of the advantages of simulations, in Chapter 2, we show clump-scale simulation to explore the link between the dynamics of prestellar cores and clump physical states. The novelty of this work lies in its initial conditions of simulations, including clump motion, magnetic fields, and turbulence intensity on the basis of observed cluster-forming clumps.

Furthermore, as described in § 1.5, in areas where cores are densely distributed, collisions between cores can occur, which can significantly alter the physical state of the prestellar cores. In Chapter 3, we show core-scale simulation to explore the prestellar cores after interaction with neighboring cores. The novelty of this study is that it considers the magnetic field effect, which is ignored in previous studies of core interaction.

1.7 Content of this Thesis

In Chapter 2, we perform MHD simulation of dense clumps and follow dense core formation. We investigate the properties of magnetized prestellar cores with a particular focus on the angular momentum and magnetic field. In Chapter 3, we present the MHD simulation of core-core collision. We explore magnetized cores' physical properties and evolution after a collision event. The conclusions and future prospects of this paper are presented in Chapter 4.

Chapter 2

Dynamics of Prestellar Cores in Cluster-Forming Clumps

2.1 Introduction of this Chapter

2.1.1 Importance of Angular Momentum and Magnetic Fields within Prestellar Cores

The angular momentum of dense cores is a crucial factor in creating protostellar systems, as it plays a key role in forming protoplanetary disks (see § 1.2). As the core collapse progresses, the interplay between a rotating accretion disk and a magnetic field is responsible for launching protostellar outflows. In addition, the magnetic field within collapsing cores is the primary means for the gas to lose angular momentum through magnetic braking, which could inhibit protoplanetary disk formation (see § 1.4). Therefore, the initial structures and distributions of angular momentum, magnetic fields, and their relationship within dense cores are critical parameters in protostellar evolution.

By simulating the collapse of cluster-forming clumps and the subsequent formation of dense cores, previous studies can shed light on the origin and properties of the angular momentum and magnetic fields of cores, as well as their implications for protostellar outflows and disk formation (Chen & Ostriker, 2018; Kuznetsova et al., 2020). Chen & Ostriker (2018) investigated the properties of dense cores in MHD simulations of

large-scale converging flows. They suggested that the internal and external magnetic fields are correlated, and the angular momentum of cores is acquired from ambient turbulence. [Kuznetsova et al. \(2020\)](#) investigated the weakly magnetized clouds and evolution of angular momentum and magnetic fields in dense cores. These studies highlight the importance of the interplay between dense regions and their environments in determining core properties.

2.1.2 Observed Dynamics of Cluster-forming Clumps

Generally, many dense cores are harbored by clumps. Therefore, the environment of clumps may significantly influence the core's angular momentum and magnetic fields.

The velocity fields of massive cluster-forming clumps ($\sim 1000M_{\odot}$), traced by high-density tracers (e.g., H^{13}CO^+ , C^{18}O , etc.) are often complex, exhibiting several velocity components. Some hypotheses have been proposed to explain such complex velocity fields of cluster-forming clumps. One of the leading interpretations is that the complex velocity fields represent the collision of clumps and/or filaments (e.g., [Higuchi et al., 2010](#); [Torii et al., 2011](#); [Dobashi et al., 2014](#)). [Higuchi et al. \(2010\)](#) conducted $\text{H}^{13}\text{CO}^+(J = 1 - 0)$ survey observations toward embedded clusters and found some H^{13}CO^+ clumps have distinct velocity gradients at their central parts. Assuming that the velocity gradients represent the rigid-like rotation of the clumps, these clumps are estimated to be gravitationally unbound. Since cluster formation occurring in a gravitational unbound dense clump is puzzling, [Higuchi et al. \(2010\)](#) proposed a clump-clump collision model to explain the velocity gradients.

On the other hand, [Shimoikura et al. \(2016\)](#) investigated the velocity structure of the cluster-forming clump S235AB, and suggested that cluster-forming clump S235AB is infalling with rotation toward the clump center. They made a simple model of an infalling, rotating clump and demonstrated that it fits well with observed data. Furthermore, statistical studies by [Shimoikura et al. \(2018, 2022\)](#) found that some molecular clumps are characterized by a velocity structure representing gravitational contraction with rotation. They suggested that such infall motion with rotation is a common phenomenon for clumps in an early stage.

There can also be various gas motions in cluster-forming clumps such as outflows, expansion of compact H_{ii} regions (e.g., [Shimoikura et al., 2015](#)), or oscillation of the

clumps as suggested for the Bok globule B68 ([Lada et al., 2003](#)).

Consequently, the various gas motions within cluster-forming clumps can influence the physical properties of the dense cores and, by extension, the stars/clusters.

2.1.3 Content of this Chapter

In this Chapter, we perform a MHD simulation of cluster-forming clumps with adaptive mesh refinement (AMR) by employing the **Enzo** code ([Bryan et al., 2014](#)). The simulation ingredients include turbulence and gas self-gravity. We investigated the properties of bound cores under different environmental conditions, including single rotating clumps, colliding clumps, and non-rotating/non-colliding clumps implied by previous observations. Evaluating and comparing the angular momentum and magnetic fields of the identified cores under these initial conditions is the novelty of this work.

Mainly, we will discuss the following three topics.

1. The transfer of the global angular momentum of the clump to each core (related to § [1.2](#))
2. The correlation between magnetic fields at the clump-scale and the core-scale (related to § [1.3](#))
3. Relative angle between the angular momentum of the core and core-scale magnetic field (related to § [1.4](#))

Below, § [2.2](#) describes the method of our simulations and analyses. Results are presented in § [2.3](#), including analysis of core angular momentum, magnetic fields, and dynamics. In § [2.4](#), we discuss the implications of our results. We summarize our results in § [2.5](#).

2.2 Method

2.2.1 Numerical Code

We use the numerical code **Enzo**¹, a MHD adaptive mesh refinement (AMR) code (Bryan et al., 2014). The ideal MHD equations were solved using a Runge-Kutta second-order-based MUSCL solver utilizing the Dedner MHD solver and hyperbolic divergence cleaning method (Dedner et al., 2002; Wang et al., 2008). The Riemann problem was solved using the Harten-Lax-van Leer (HLL) method, while the reconstruction method for the MUSCL solver was a piecewise linear model (PLM). The self-gravity of the gas is included in our simulations.

The hydrodynamical equations are solved for MHD conditions. The mass, momentum, energy, and induction equation coupled with the Poisson equation for gravity, are given by

$$\frac{\partial \rho}{\partial t} + \nabla \cdot (\rho \mathbf{v}) = 0, \quad (2.1)$$

$$\frac{\partial}{\partial t}(\rho \mathbf{v}) + \nabla \cdot \left(\rho \mathbf{v} \otimes \mathbf{v} + P_{\text{tot}} \mathbb{I} - \frac{1}{4\pi} \mathbf{B} \otimes \mathbf{B} \right) = \rho \mathbf{g}, \quad (2.2)$$

$$\frac{\partial E_{\text{tot}}}{\partial t} + \nabla \cdot \left((E_{\text{tot}} + P_{\text{tot}}) \mathbf{v} - \frac{1}{4\pi} \mathbf{B} (\mathbf{B} \cdot \mathbf{v}) \right) = \rho \mathbf{g} \cdot \mathbf{v}, \quad (2.3)$$

$$\frac{\partial \mathbf{B}}{\partial t} = \nabla \times (\mathbf{v} \times \mathbf{B}), \quad (2.4)$$

where ρ is the mass density, \mathbf{v} is the fluid velocity vector, \mathbf{B} is the magnetic field vector, \mathbf{g} is the gravitational acceleration vector, P_{tot} is the total pressure, E_{tot} is the total specific energy. P_{tot} is defined as the sum of the thermal pressure and the magnetic pressure:

$$P_{\text{tot}} = P + \frac{1}{8\pi} B^2. \quad (2.5)$$

E_{tot} is defined as the sum of the kinetic energy, the internal energy and magnetic energy:

¹<http://enzo-project.org> (v.2.6)

$$E_{\text{tot}} = \frac{1}{2}\rho v^2 + e + \frac{1}{8\pi}B^2. \quad (2.6)$$

The fluid equation of state is given by the ideal gas equation of state:

$$P = (\gamma - 1)e. \quad (2.7)$$

The Poisson equation is given by

$$\nabla^2\phi = 4\pi G\rho \quad \Rightarrow \quad g = -\nabla\phi. \quad (2.8)$$

Note that we work here in *cgs* units.

We assumed a mean molecular weight $\mu = 2.3$, and an adiabatic index was set to $\gamma = 1.00001$ for an approximate isothermal assumption.

2.2.2 Initial Conditions and Parameters

We choose initial conditions to match the properties of observed clumps (e.g., [Shimoikura et al., 2018](#)). As an initial clump, we set a magnetized gas sphere with uniform density $n_{\text{clump}} = \rho_{\text{clump}}/\mu m_{\text{H}} = 1.2 \times 10^4 \text{ cm}^{-3}$, isothermal sound speed $c_s = 0.27 \text{ km} \cdot \text{s}^{-1}$, and radii $R_{\text{clump}} = 0.7 \text{ pc}$, giving a mass $M_{\text{clump}} \sim 10^3 M_{\odot}$. The clump is embedded within ambient gas of 10 times lower density, $n_{\text{amb}} = \rho_{\text{amb}}/\mu m_{\text{H}} = 1.2 \times 10^3 \text{ cm}^{-3}$.

The simulation box is initialized with a large-scale uniform magnetic field \mathbf{B}_0 , parallel to the z axis. Following crutcher relation (see Appendix [A.5](#)), the magnetic field strength is approximately $100 \mu\text{G}$ when the density is around n_{clump} . In our simulation, we explored initial magnetic field strengths of $B_0 = 10 \mu\text{G}$ (weak) and $100 \mu\text{G}$ (strong). Then, the ratios of magnetic energy $E_{\text{clump,mag}} \equiv B_0^2 R_{\text{clump}}^3 / 6$ with respect to the gravitational energy $E_{\text{clump,grav}} \equiv -3GM_{\text{clump}}^2 / 5R_{\text{clump}}$ are $E_{\text{clump,mag}}/|E_{\text{clump,grav}}| \approx 2.3 \times 10^{-3}$ and 0.23, respectively.

We generated turbulent velocities within the clump material at $t = 0 \text{ Myr}$ to approximate the velocity and density fluctuations in observed clumps. This velocity field chosen for our simulations follows a power spectrum of the Larson law $v_k^2 \propto k^{-4}$ ([Larson,](#)

1981), with a pure solenoidal component, where k is the wavenumber for an eddy diameter. We limit our k -modes to be $4 < \frac{k}{\pi/L_{\text{box}}} < 20$. We select two turbulence Mach number $\mathcal{M} \equiv \sigma_v/c_s$, $\mathcal{M} = 1.5$ (weak) and $\mathcal{M} = 5$ (strong), where σ_v is the velocity dispersion in the clump. From which, the ratios of turbulent energy $E_{\text{clump,turb}} \equiv M_{\text{clump}}\sigma_v^2/2$ with respect to the gravitational energy are $E_{\text{clump,turb}}/|E_{\text{clump,grav}}| \approx 0.02$ and 0.25 , respectively. Turbulent velocity generates some base level of clump angular momentum. The total initial angular velocities purely from turbulence for $\mathcal{M} = 1.5$ and $\mathcal{M} = 5$ are respectively $\Omega_{\text{turb}} \sim 1.0 \times 10^{-15} \text{ rad s}^{-1}$ and $\sim 3.0 \times 10^{-15} \text{ rad s}^{-1}$. Our initial clumps do not have enough kinetic and magnetic support to prevent gravitational collapse at the beginning.

As described in § 2.1, previous observations have indicated that clump velocity structures can be attributed to either infall with rotation or clump collision. To investigate these scenarios, we used two different setups in our simulations: “Rotation Setup” where a single clump contracts with rotation, and the “Collision Setup” where two clumps collide (see Section 2.2.2.1 and 2.2.2.2). For comparison, we also examine clumps that are neither rotating nor colliding, which we call “w/o Setup”. Table 2.1 lists the models for both setups and illustrates the parameter space explored. Throughout our subsequent discussion, we will refer to the model names as shown in Table 2.1.

The numerical domain is set to $L_{\text{box}} = 2.8 \text{ pc}$ cubic. We use a root grid of 256^3 with five levels of refinement, corresponding to an effective resolution of 8192^3 . To avoid artificial fragmentation (Truelove et al., 1997), we base our refinement criterion on resolving the Jeans length by eight cells: $\Delta x \leq \lambda_J/8$, where $\lambda_J = \pi^{1/2}c_s/(G\rho)^{1/2}$ is the Jeans length. Refinement is allowed until the finest resolution reaches $\Delta x_{\text{min}} = L_{\text{box}}/8192 \simeq 3.4 \times 10^{-4} \text{ pc}$, where the local number density reaches $n_{\text{crit}} = \rho_{\text{crit}}/\mu m_{\text{H}} \simeq 1.2 \times 10^8 \text{ cm}^{-3}$ in some region. In Appendix B.9, we have also conducted higher-resolution runs and validated our results.

2.2.2.1 Rotation Setup

In the Rotation Setup, besides the initial turbulent velocity field, we add an angular momentum with constant velocity to the entire clump. The rotational angular velocity is $\Omega_0 = 1.0 \times 10^{-13} \text{ rad s}^{-1}$, from which the ratios of rotational energy $E_{\text{clump,rot}} \equiv M_{\text{clump}}R_{\text{clump}}^2\Omega_0^2/5$ with respect to the gravitational energy is $E_{\text{clump,rot}}/|E_{\text{clump,grav}}| \approx 0.25$. This value is based on some previous observational

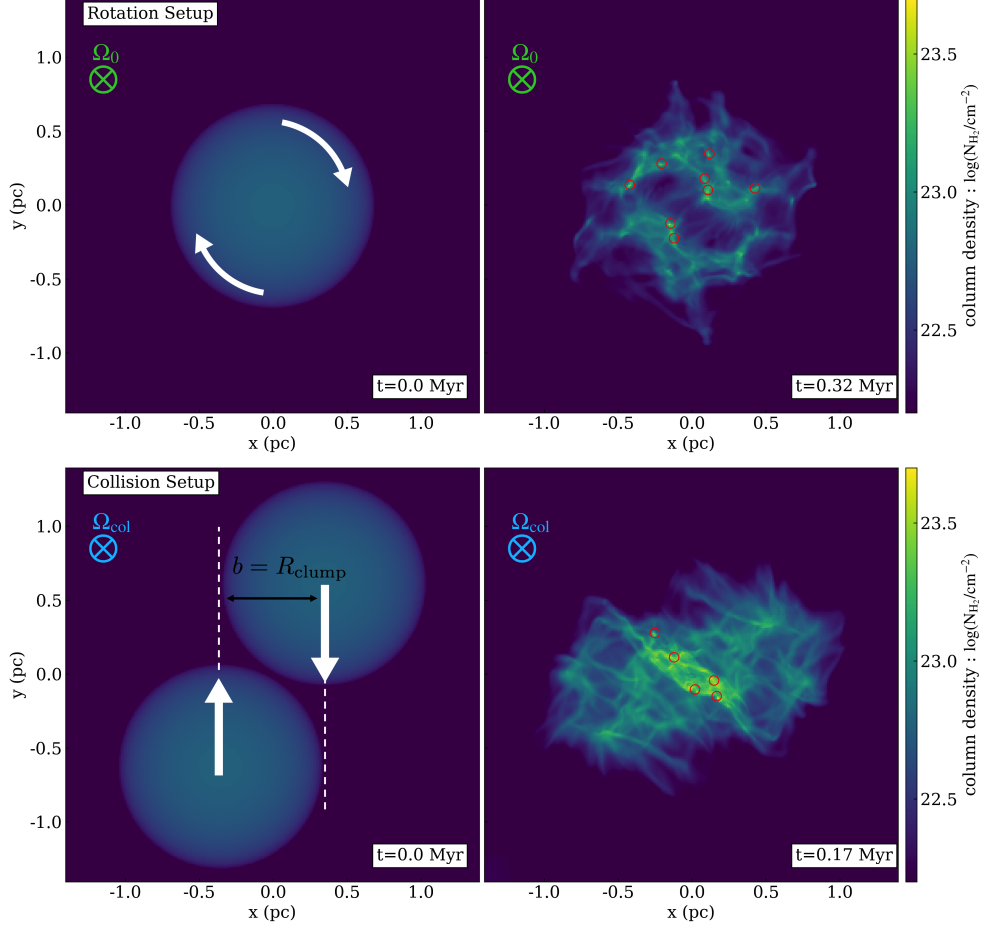


Figure 2.1: Sample map from simulations considered in this study. The column density, as viewed along the z axis, is shown. The top two rows display one of the Rotation Setup models (Rot-M5-B10P) at 0.0 and 0.32 Myr. The orientation of the rotation axis of the clump is indicated by the symbol " \otimes " pointing in the direction of the z axis. The bottom two rows display one of the Collision Setup models (Co1-M5-B10P) at 0.0 and 0.17 Myr. In the Collision Setup, the initial clump does not have an overall rotational velocity. However, after the collision, the two clumps rotate around their center due to the off-center configuration. The positions of bound cores identified in simulations are additionally plotted as red open circles.

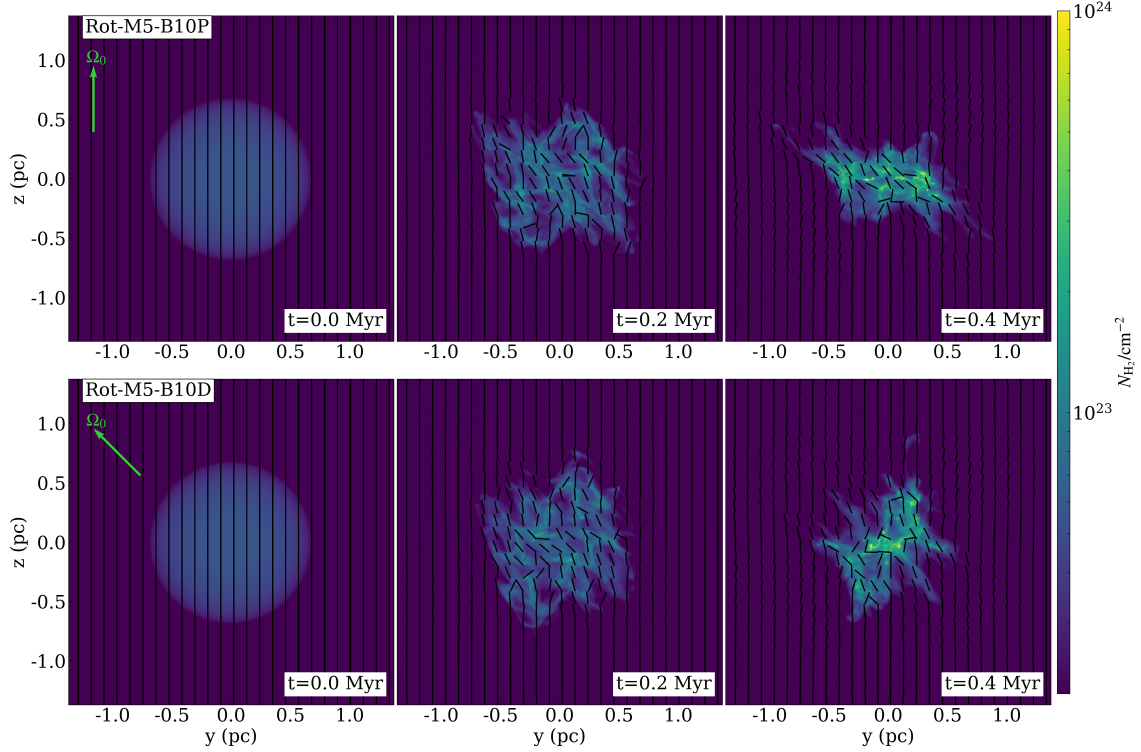


Figure 2.2: Time evolution of column density along the x -axis for the **Rot-M5-B10P** (top) and **Rot-M5-B10D** (bottom) model. Snapshots at 0.0, 0.2, and 0.4 Myr are shown. Mass-weighted magnetic field directions projected on the corresponding plane are shown as black lines. Ω_0 is indicated by green arrows. In both models, the gas forms a roughly perpendicular, disk-like structure with respect to the rotation axis. Other Rotation setup models also undergo similar temporal evolution, forming elongated structures that extend perpendicular to the rotation axis.

works (e.g., Higuchi et al., 2010; Shimoikura et al., 2018). Ω_0 is about two orders larger than Ω_{turb} and dominant for the rotational motion of the entire clump. Total magnitude of the angular momentum within the clump around the center is $|\mathbf{L}_{\text{total}}| \sim 1.9 \times 10^{16} \text{ km}^2 \text{ s}^{-1} M_{\odot}$.

To investigate the effects of the initial magnetic field direction, we consider two arrangements with respect to the rotation axis Ω_0 , namely $\theta_0 = 0^\circ$ and 45° , where θ_0 is the angle between \mathbf{B}_0 relative to the Ω_0 . In other words, $\theta_0 = 0^\circ$ means that Ω_0 and \mathbf{B}_0 are parallel, and $\theta_0 = 45^\circ$ means that the angle between them is 45° .

The upper row of Figure 2.1 shows the sample map from one of the Rotation Setup

models (**Rot-M5-B10P**) showing the simulated gas structure in column density integrated along z axis. Initially, the gas rotates around a constant rotation axis Ω_0 . Gradually, dense structures develop due to turbulence compression and local gravitational collapse, eventually forming dense cores. The red circles in the figure show the positions of identified cores (see Section 2.2.3), indicating that cores have formed at various locations within the clump. The column density along the x -axis at 0.0, 0.2, and 0.4 Myr for two Rotation Setup models, **Rot-M5-B10P** and **Rot-M5-B10D** are shown in Figure 2.2. The initial uniform magnetic field is distorted by turbulence and clump rotation. In both models, the gas forms a roughly perpendicular, disk-like structure with respect to the rotation axis (see also Figure 2.1). Other Rotation setup models also undergo similar temporal evolution, forming disk-like structures that extend perpendicular to the rotation axis.

For comparison, we also consider the setup, referred to as "w/o Setup", in which a single clump contracts without initial angular momentum with Ω_0 . All conditions in the w/o Setup are the same as in the Rotation setup, except that there is no initial angular momentum with Ω_0 in the former.

2.2.2.2 Collision Setup

In the Collision Setup, we investigate the collision of two clumps with an initial impact parameter of $b = R_{\text{clump}}$ ². Turbulent velocities are generated within the two clumps' material at $t = 0$ Myr, similar to the Rotation and w/o Setups. However, unlike the Rotation Setup, the initial two clumps are not rotating with Ω_0 . Due to the off-center collision, the shear motion is converted into the rotating motion of the compressed dense gas, whose angular momentum axis is roughly perpendicular to the collision axis. Henceforth, we refer to the axis of rotation generated by the collision as Ω_{col} . The default initial velocity of the clumps is set to be $V_0 \approx 2.8 \text{ km s}^{-1}$ (fast) by means of relative collision velocity $V_{\text{rel}} = 2V_0$. For comparison, $V_0 \approx 1.4 \text{ km s}^{-1}$ (slow) is also explored. From which, the ratios of kinetic energy due to the overall motion of the clump, $E_{\text{clump,col}} = M_{\text{clump}}V_0^2/2$ to the gravitational energy are $E_{\text{clump,col}}/|E_{\text{clump,grav}}| \approx 0.25$

²Note that this clump-clump collision is different in mass and scale from the core-core collision addressed in Chapter 3. The mass of core addressed in Chapter 3 is roughly equivalent to the Bonnor-Ebert mass M_{BE} . Without external forces, it would not fragment into multiple structures. On the other hand, the clump stated here has a mass of $10^3 M_{\odot}$, which is approximately 20 times as high as the jeans mass M_j . Within it, many dense cores form.

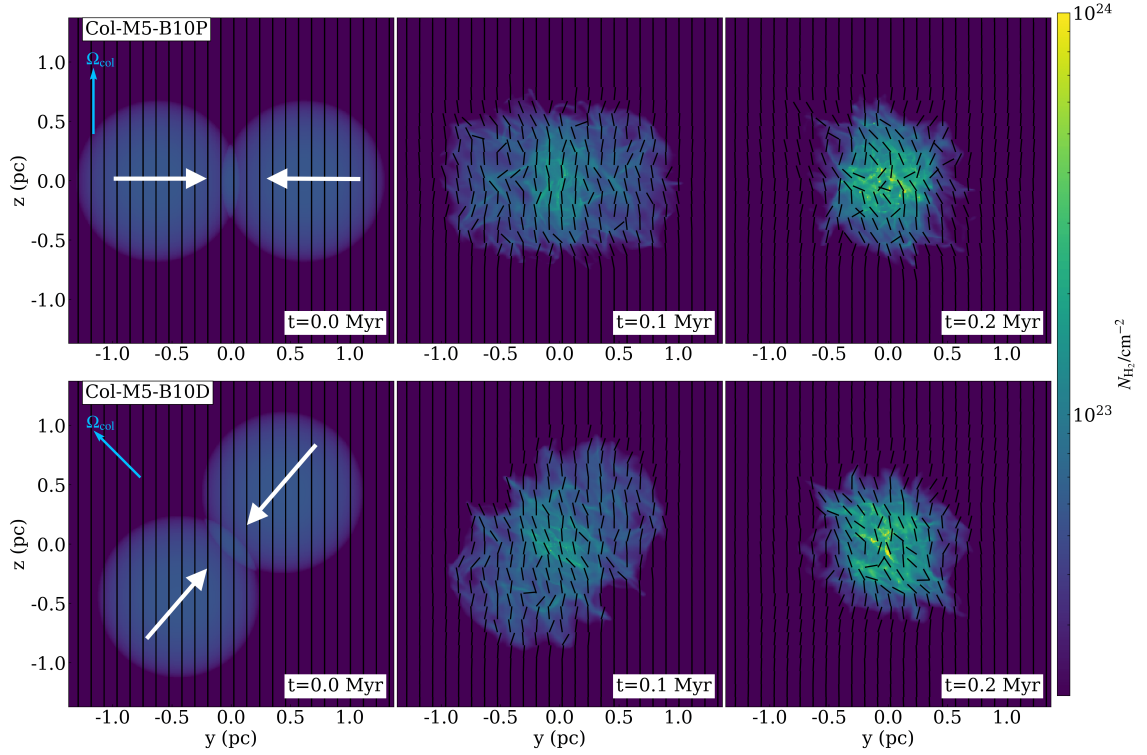


Figure 2.3: Time evolution of column density along the x -axis for the Col-M5-B10P (top) and Col-M5-B10D (bottom) model. Snapshots at 0.0, 0.1, and 0.2 Myr are shown. Mass-weighted magnetic field directions projected on the corresponding plane are shown as black lines. Ω_{col} is indicated by blue arrows. White arrows indicate the collision axis.

(slow) and 1.00 (fast), respectively. These energy ratios are consistent with observations implying possible clump-clump collisions (see Table 1 and 3 of Higuchi et al., 2010). Corresponding total magnitude of the angular momentum of the entire system around the simulation box center is $|\mathbf{L}_{\text{total}}| \sim 3.0 \times 10^{16}$ and $6.0 \times 10^{16} \text{ km}^2 \text{ s}^{-1} M_{\odot}$ (Since there are two clumps in the Collision Setup, the total angular momentum of within the single clump is half of this, $\sim 1.5 \times 10^{16}$ and $3.0 \times 10^{16} \text{ km}^2 \text{ s}^{-1} M_{\odot}$).

We select two arrangement of initial magnetic field \mathbf{B}_0 and $\mathbf{\Omega}_{\text{col}}$, $\theta_0 = 0^\circ$ and 45° . When $\theta_0 = 0^\circ$, it means that the collision axis is perpendicular to \mathbf{B}_0 ($\mathbf{B}_0 \parallel \mathbf{\Omega}_{\text{col}}$), and when $\theta_0 = 45^\circ$, it means that the angle between the collision axis and \mathbf{B}_0 is 45° .

The lower row of Figure 2.1 shows sample maps from one of the Collision Setup models (Co1-M5-B10P). At the interface of the colliding, a high-density compressed layer is formed. Dense cores primarily form inside this shock layer. Two clump gas rotates around $\mathbf{\Omega}_{\text{col}}$. The column density along the x -axis at 0.0, 0.1, and 0.2 Myr for two Collision Setup models Co1-M5-B10P and Co1-M5-B10D model are shown in Figure 2.3. The initial uniform magnetic field is distorted by the turbulence and clump moving.

2.2.3 Measuring Core Properties

For each set of model parameters, we typically conduct four simulations with different realizations of the input turbulence. We identify gravitationally bound cores at the time when the most evolved core collapses ($n_{\text{max}} \geq 10^8 \text{ cm}^{-3}$) by applying the following criteria: (i) $n \geq n_{\text{th}} = 10^6 \text{ cm}^{-3}$, (ii) cell number $> 3^3$, (iii) total mass $M_{\text{core}} > 0.1 M_{\odot}$, (iv) $E_{\text{thermal}} + E_{\text{mag}} + E_{\text{grav}} < 0$ (details below). We tested multiple values of threshold density n_{th} and verified that the following results do not strongly depend on n_{th} . We chose $n_{\text{th}} = \rho_{\text{th}}/\mu m_{\text{H}} = 10^6 \text{ cm}^{-3}$ since this is high enough to guarantee dense core formation but below n_{crit} . For some models, the total number of identified cores in the four simulations is below 20. In such cases, we perform additional simulations to ensure that the total number of cores exceeds 20, allowing for statistically meaningful discussions. In Section 2.4.4, we also discuss unbound cores that do not satisfy the criterion (iv).

For each core, we calculated its thermal energy E_{thermal} , kinetic energy E_{kin} , magnetic

energy, E_{mag} , and self-gravitational energy E_{grav} . E_{thermal} is given by

$$E_{\text{thermal}} = \sum_i \frac{3}{2} n_i k T_i \Delta V_i, \quad (2.9)$$

where i is an index of a cell in the core, n_i is the number density, k is the Boltzmann constant, T_i is the temperature, and ΔV_i is the volume of a simulation cell.

E_{kin} is given by

$$E_{\text{kin}} = \sum_i \frac{1}{2} \rho_i |\mathbf{v}_i - \mathbf{v}_{\text{mean}}|^2 \Delta V_i, \quad (2.10)$$

where ρ_i is the mass density, \mathbf{v}_i is the velocity, and \mathbf{v}_{mean} is the mean velocity of core defined by

$$\mathbf{v}_{\text{mean}} = \frac{\sum_i \rho_i \mathbf{v}_i \Delta V_i}{M_{\text{core}}}, \quad (2.11)$$

where M_{core} is the mass of the core. E_{grav} is calculated by

$$E_{\text{grav}} = -\frac{3GM_{\text{core}}^2}{5R_{\text{core}}}, \quad (2.12)$$

The core radius R_{core} is defined by

$$R_{\text{core}} = \left(\frac{3V_{\text{core}}}{4\pi} \right)^{1/3}, \quad (2.13)$$

where V_{core} is the total volume of the core.

E_{mag} is given by

$$E_{\text{mag}} = \sum_i \frac{\mathbf{B}_i^2}{8\pi} \Delta V_i, \quad (2.14)$$

where \mathbf{B}_i is the magnetic field flux density. These calculation methods are similar to those used in earlier works (e.g., [Sakre et al., 2023](#)).

We estimate the net angular momentum \mathbf{L}_{core} based on the calculation presented in [Chen & Ostriker \(2018\)](#). \mathbf{L}_{core} is defined by the integration of each cell's relative angular momentum over the entire volume:

$$\mathbf{L}_{\text{core}} = \sum_i \rho_i \Delta V_i \cdot (\mathbf{r}_i - \mathbf{r}_{\text{CM}}) \times \mathbf{v}_i, \quad (2.15)$$

where \mathbf{r}_{CM} is the center of mass. The rotational axis for the core is determined to be $\hat{\mathbf{L}}_{\text{core}} = \mathbf{L}_{\text{core}}/L_{\text{core}}$, where $L_{\text{core}} = |\mathbf{L}_{\text{core}}|$ is the magnitude of the net angular momentum of the core. The total rotational inertia of the core around this axis can be calculated by first determining the projected radius for each cell:

$$\mathbf{r}_{i,\perp} = (\mathbf{r}_i - \mathbf{r}_{\text{CM}}) - \left[(\mathbf{r}_i - \mathbf{r}_{\text{CM}}) \cdot \hat{\mathbf{L}}_{\text{core}} \right] \hat{\mathbf{L}}_{\text{core}} \quad (2.16)$$

and then integrating over the whole volume:

$$I \equiv \sum_i \rho_i \Delta V_i \cdot |\mathbf{r}_{i,\perp}|^2 \quad (2.17)$$

The mean angular velocity Ω_{core} and the rotational energy E_{rot} of the core are

$$\Omega_{\text{core}} \equiv L_{\text{core}}/I, \quad (2.18)$$

$$E_{\text{rot}} \equiv \frac{1}{2} I \Omega_{\text{core}}^2. \quad (2.19)$$

The mean magnetic field within the core is calculated by

$$\mathbf{B}_{\text{core}} = \frac{\sum_i \mathbf{B}_i \Delta V_i}{V_{\text{core}}}. \quad (2.20)$$

In the following section, we will explore the angles between various vectors, such as \mathbf{L}_{core} and $\boldsymbol{\Omega}_0(\boldsymbol{\Omega}_{\text{col}})$, \mathbf{L}_{core} and \mathbf{B}_{core} . We study the statistics using the cosine values for angles between two vectors. This is because the distribution function of random 3D angles is uniform in cosine, not degree³. To quantify the alignment level and its significance, we use the orientation parameter S :

$$S = \frac{3 \langle \cos^2 \chi \rangle - 1}{2}, \quad (2.21)$$

where χ is the angle with respect to the director. In the case of a perfect alignment, $S = 1$, while in the case of a completely random alignment, $S = 0$. When $0 < S < 1$, it denotes a partial alignment. For example, when $\langle \cos^2 \chi \rangle = \cos^2 45^\circ$, $S = 0.25$. In the following discussion, $S > 0.25$ will be referred to as strong alignment and $0.25 > S > 0$ as weak alignment.

³The probability for the 3D angle χ is proportional to the associated solid angle ($\sin \chi d\chi$). Therefore, the cumulative probability of the relative angle to be smaller than χ is $\int_0^\chi \sin \chi' d\chi' = 1 - \cos \chi$.

Table 2.1. Summary of simulations and explored parameter space

Model name	V_0 ^a (km s ⁻¹)	\mathcal{M} ^b	B_0 ^c (μG)	θ_0 ^d ($^\circ$)	$\mathcal{M}_{A,0}$ ^e	α ^f
Rotation Setup						
Rot-M1.5-B10P	...	1.5	10	0	3.1	0.30
Rot-M1.5-B100P	...	1.5	100	0	0.3	0.53
Rot-M5-B10P	...	5	10	0	10.3	0.53
Rot-M5-B100P	...	5	100	0	1.0	0.75
Rot-M1.5-B10D	...	1.5	10	45	3.1	0.30
Rot-M1.5-B100D	...	1.5	100	45	0.3	0.53
Rot-M5-B10D	...	5	10	45	10.3	0.53
Rot-M5-B100D	...	5	100	45	1.0	0.75
w/o Setup ^g						
w/o-M1.5-B10	...	1.5	10	...	3.1	0.05
w/o-M1.5-B100	...	1.5	100	...	0.3	0.28
w/o-M5-B10	...	5	10	...	10.3	0.28
w/o-M5-B100	...	5	100	...	1.0	0.50
Collision Setup						
Col-M1.5-B10P	2.8	1.5	10	0	3.1	0.05
Col-M1.5-B100P	2.8	1.5	100	0	0.3	0.28
Col-M5-B10P	2.8	5	10	0	10.3	0.28
Col-M5-B100P	2.8	5	100	0	1.0	0.50
Col-M1.5-B10D	2.8	1.5	10	45	3.1	0.05
Col-M1.5-B100D	2.8	1.5	100	45	0.3	0.28
Col-M5-B10D	2.8	5	10	45	10.3	0.28
Col-M5-B100D	2.8	5	100	45	1.0	0.50
Col-S-M1.5-B10P	1.4	1.5	10	0	3.1	0.05
Col-S-M1.5-B100P	1.4	1.5	100	0	0.3	0.28
Col-S-M5-B10P	1.4	5	10	0	10.3	0.28
Col-S-M5-B100P	1.4	5	100	0	1.0	0.50

Note. — ^a The pre-collision velocity of the clump. ^b The Mach number of turbulence. ^c The strength of initial magnetic field. ^d The angle between the initial magnetic field \mathbf{B}_0 relative to the Ω_0 (Ω_{col}). ^e The Alfvén Mach number within the initial clump: $\mathcal{M}_{A,0} \equiv \sigma_v/v_{A,\text{clump}}$, where $v_{A,\text{clump}} = B_0/\sqrt{4\pi\rho_{\text{clump}}}$. ^f Energy ratio of the sum of the turbulent, magnetic field, rotation, and thermal energies to the absolute value of self-gravitational energy for the initial clump, $(E_{\text{clump,tur}} + E_{\text{clump,mag}} + E_{\text{clump,rot}} + E_{\text{clump,therm}})/|E_{\text{clump,grav}}|$. ^g The models of the clump that has neither initial angular momentum with Ω_0 nor collide.

2.3 Results

We compare the results of 24 simulation models listed in Table 2.1. For each set of model parameters, we run multiple simulations with different realizations of the input turbulence and identify bound cores. We present analysis results of bound cores in the Rotation Setup in Section 2.3.1, and those of the Collision Setup in Section 2.3.2. Table 2.2 summarizes the physical properties measured from cores.

2.3.1 Rotation Setup

This section shows the simulation results of the Rotation Setup. For each identified core, we measured the net angular momentum \mathbf{L}_{core} and mean magnetic field \mathbf{B}_{core} . We show the correlation between \mathbf{L}_{core} and the rotational axis of the clump, $\mathbf{\Omega}_0$, in Section 2.3.1.1. In Section 2.3.1.2, we discuss the correlation between \mathbf{B}_{core} and the initial field \mathbf{B}_0 . In Section 2.3.1.3, we present the rotation-magnetic field relation ($\mathbf{L}_{\text{core}}\text{-}\mathbf{B}_{\text{core}}$) among bound cores.

2.3.1.1 Angular Momentum of the Rotation Setup

We examine the orientation of \mathbf{L}_{core} for all bound cores to determine if the cores reflect the average angular momentum of the clump. Figure 2.4 illustrates the histograms of the cosine of the angle between parental clump rotation axis $\mathbf{\Omega}_0$ and the core angular momentum \mathbf{L}_{core} . Here, the orientation parameter $S_{L,\Omega}$ is defined as $S_{L,\Omega} = (3\langle \cos^2 \angle[\mathbf{L}_{\text{core}}, \mathbf{\Omega}_0] \rangle - 1)/2$. In all models with weak turbulence (indicated by blue lines), strong alignment ($S_{L,\Omega} > 0.25$) is achieved regardless of the strength or orientation of the initial magnetic field \mathbf{B}_0 . For these models, the distribution of $\cos \angle[\mathbf{L}_{\text{core}}, \mathbf{\Omega}_0]$ deviates greatly from a uniform distribution and the null hypothesis that “the distribution is uniform” is rejected at a significance level of 5% using the Kolmogorov-Smirnov (K-S) test⁴. In models with weak turbulence, the rotation of the parental clump is passed down to the bound cores. On the other hand, in models with strong turbulence (indicated by red lines), the distribution of spin axes is found to be close to isotropic, and the null hypothesis that “the distribution is uniform” cannot

⁴We utilize the Python implementation `kstest` in the `scipy.stats` (v.1.1.0) package (Virtanen et al., 2020). In the following part, we conduct a K-S test with a significance level of 5%.

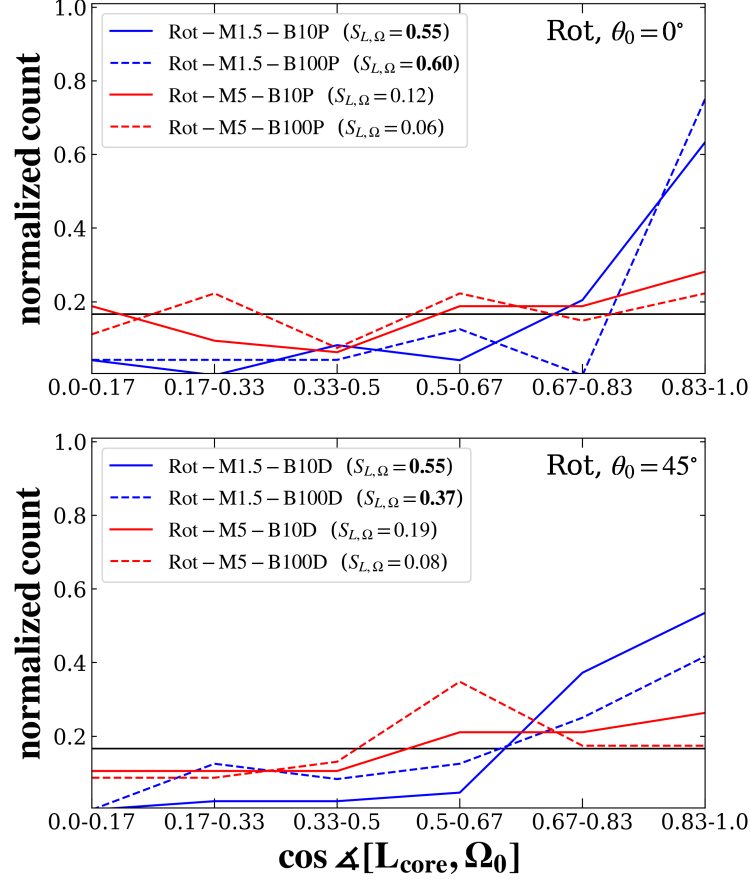


Figure 2.4: Histograms of the cosine of the relative angles between parental clump rotation axis $\mathbf{\Omega}_0$ and the integrated angular momentum \mathbf{L}_{core} , for all bound cores formed in different models. The black dashed line shows the expected distribution for an isotropic orientation of \mathbf{L}_{core} . In the legends, the orientation parameter $S_{L,\Omega} = (3\langle \cos^2 \angle[\mathbf{L}_{\text{core}}, \mathbf{\Omega}_0] \rangle - 1)/2$ for each model are shown, and values with $S_{L,\Omega} > 0.25$ are indicated in bold. $\theta_0 = 0^\circ$ cases are shown in the first row, while $\theta_0 = 45^\circ$ cases are shown in the second row. In all models with weak turbulence (indicated by blue lines), there is a clear tendency for \mathbf{L}_{core} and $\mathbf{\Omega}_0$ to align. On the other hand, in the strong turbulence models (indicated by red lines), the angles are close to being isotropically distributed, and no tendency for alignment is observed.

be rejected. This suggests that the rotational motion of the clumps is not reflected in the bound cores in strong turbulence models. In other words, there is no tendency for alignment when $E_{\text{clump,rot}}/E_{\text{clump,tur}} \sim 1$, and a strong tendency for alignment when $E_{\text{clump,rot}}/E_{\text{clump,tur}} > 1$. Therefore, the turbulence intensity is a critical parameter that determines whether the bound cores inherit the rotational motion of the parental clump. This correlation between turbulence intensity and alignment of the core rotation is consistent with Corsaro et al. (2017). Using 3D HD simulations of proto-cluster formation, Corsaro et al. (2017) indicated that the degree of alignment reflects the importance of the clouds average angular momentum. Our results newly imply that even in the presence of a magnetic field, the global angular momentum of the clump is efficiently transferred to cores when $E_{\text{clump,rot}}/E_{\text{clump,tur}} > 1$, independent of the orientation of \mathbf{B}_0 . In Appendix B.1, we show that this alignment is a prograde rotation rather than a retrograde rotation.

We also investigated the angle between \mathbf{L}_{core} and the initial magnetic field \mathbf{B}_0 in w/o Setups. The clumps in w/o Setups have no initial angular momentum with Ω_0 , allowing us to study the correlation between \mathbf{L}_{core} and \mathbf{B}_0 without the confounding effects of overall clump rotation. Figure 2.5 shows the histograms of the cosine of the angle between \mathbf{L}_{core} and \mathbf{B}_0 for w/o Setups. In all models of w/o Setups, the distribution of $\cos \angle[\mathbf{L}_{\text{core}}, \mathbf{B}_0]$ is close to uniform and the null hypothesis that “the distribution is uniform” is not rejected. We can conclude that \mathbf{B}_0 does not dictate \mathbf{L}_{core} directly. As shown later in Section 2.3.1.3, there is also little correlation between \mathbf{L}_{core} and \mathbf{B}_{core} . At least within the parameters investigated in this study, the magnetic field does not constrain the direction of \mathbf{L}_{core} .

Between all \mathbf{L}_{core} pairs in each simulation run, we calculate the cosine of the relative orientation angle, noted as $\cos \theta_{L,L}$ and their separations. Figure 2.6 displays $\cos \theta_{L,L}$ as a function of their separation distances between all pairs of \mathbf{L}_{core} . The results are binned by separation distances of pairs and presented as each bin’s mean and standard deviation. The left panel shows the results of the Rotation Setup, while the right panel shows those of w/o Setup for comparison. In the Rotation Setup, particularly with weak turbulence ($\mathcal{M} = 1.5$), $\cos \theta_{L,L}$ is generally higher close to $\cos 45^\circ$ indicating a relatively stronger alignment of \mathbf{L}_{core} pairs. Weak turbulence models exhibit relatively high $\cos \theta_{L,L}$ values over a wide range of separations from 0.2 to 1.2 pc, suggesting that \mathbf{L}_{core} pairs are generally aligned regardless of the distance between cores. As shown in Figure 2.4, in the Rotation Setup with the weak turbulence, \mathbf{L}_{core} inherits the rotation

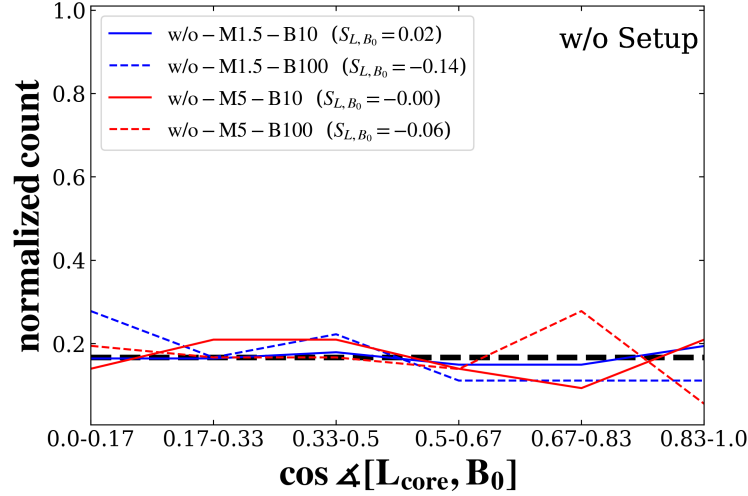


Figure 2.5: Histograms of the cosine of the relative angles between the initial magnetic field direction \mathbf{B}_0 and the integrated angular momentum \mathbf{L}_{core} . The black dashed line shows the expected distribution for an isotropic orientation of \mathbf{L}_{core} . In the legends, the orientation parameter $S_{L,B_0} = (3\langle\cos^2\angle[\mathbf{L}_{\text{core}}, \mathbf{B}_0]\rangle - 1)/2$ for each model are shown. In each model, there is no tendency for \mathbf{L}_{core} and \mathbf{B}_0 to align.

of clumps. Therefore, \mathbf{L}_{core} tends to align with similar angles between pairs. On the other hand, in Rotation Setup with the strong turbulence ($\mathcal{M} = 5$), $\cos\theta_{L,L}$ is close to ~ 0.5 , which would be expected from a uniform distribution of $\cos\theta_{L,L}$. As shown in Figure 2.4, in the case of strong turbulence, the rotation of the clump is not transferred to the core, so the pairs of \mathbf{L}_{core} did not align. In the case of w/o Setup, since the clump is not rotating globally, the direction of each \mathbf{L}_{core} is almost random, and $\cos\theta_{L,L}$ is around 0.5 at any separation, indicating no clear alignment between \mathbf{L}_{core} pairs.

2.3.1.2 Magnetic Field of the Rotation Setup

We explored the orientation of \mathbf{B}_{core} for all bound cores and investigated the correlation between \mathbf{B}_{core} and the initial magnetic field of the clump \mathbf{B}_0 . Figure 2.7 shows the histograms of cosine of the angle between \mathbf{B}_{core} and \mathbf{B}_0 . The parameter S_{B,B_0} is defined as $(3\langle\cos^2\angle[\mathbf{B}_{\text{core}}, \mathbf{B}_0]\rangle - 1)/2$. In all models with strong B_0 (indicated by dashed lines), S_{B,B_0} is larger than 0.25 indicating the strong alignment between \mathbf{B}_{core} and \mathbf{B}_0 . The null hypothesis that “the distribution is uniform” is rejected for all models with strong B_0 . Strong magnetic fields tend to maintain their coherence along the initial direction.

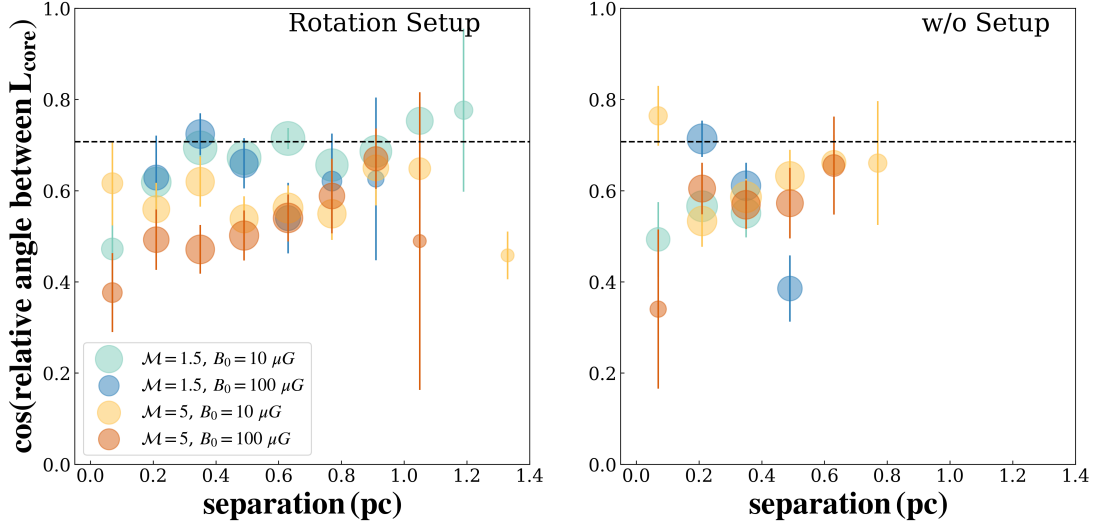


Figure 2.6: The cosine of relative orientation angles of \mathbf{L}_{core} pairs as a function of their separation distances. The data are averaged in various separation distance bins, with the size of the circle representing the number of samples in each distance bin. The black dashed line indicates $\cos 45^\circ$. The models with $\theta_0 = 0^\circ$ and 45° are presented together. Rotation Setup is shown in the left panel and w/o Setup in the right panel. In the Rotation Setup, a stronger alignment of \mathbf{L}_{core} pairs is observed, especially when the turbulence is weak ($\mathcal{M} = 1.5$).

Therefore, \mathbf{B}_{core} inherits the initial orientation of the clump’s field, which leads to a tendency for \mathbf{B}_{core} to align parallel to \mathbf{B}_0 . Also, for some models with weak B_0 , S_{B,B_0} is positive, and the null hypothesis that “the distribution is uniform” is rejected. However, the degree of alignment is weaker compared to models of strong B_0 . This is because when the magnetic field is weak, the magnetic field inside the clump is easily disturbed by turbulence or rotational motion, resulting in the misalignment of \mathbf{B}_{core} . In Appendix B.2, we show the degree of dispersion in magnetic field orientations within cores. We found that the stronger the initial magnetic field, the more aligned the magnetic fields within the core. This trend is consistent with previous simulation studies (see § 1.3).

Similar tendencies are obtained by analyzing \mathbf{B}_{core} pairs. Figure 2.8 shows the cosine of the relative orientation angle, noted as $\cos \theta_{B,B}$, between all \mathbf{B}_{core} pairs as a function of their separation distances in the same manner as Figure 2.6. In the models of Rotation Setup with a strong B_0 ($= 100 \mu G$), there is a higher degree of alignment with an average $\cos \theta_{B,B}$ around $\cos 45^\circ$ over a wide range of separations from 0.2 to

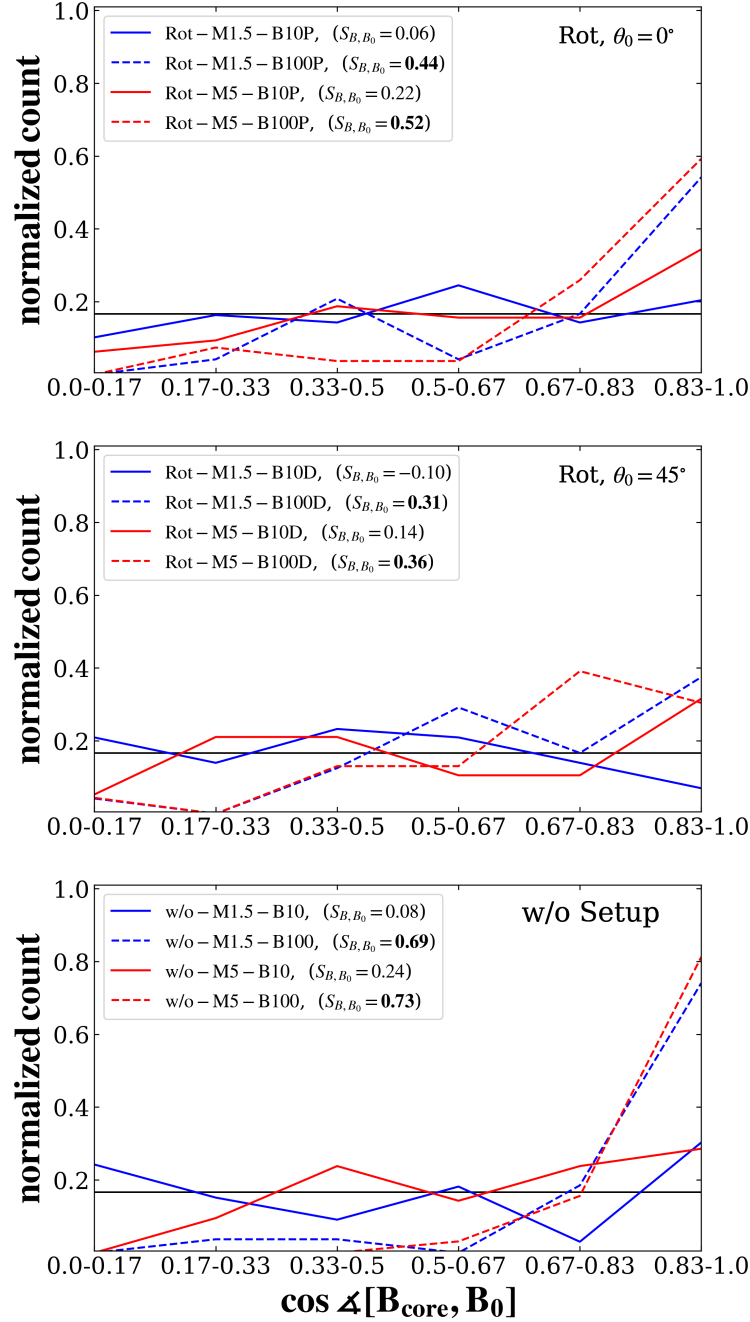


Figure 2.7: Histograms of the cosine of the relative angle between the initial magnetic field \mathbf{B}_0 and the mean magnetic field within the core, \mathbf{B}_{core} , for bound cores formed in different models. The black dashed line shows the expected distribution for an isotropic orientation of \mathbf{B}_{core} . In the legends, the orientation parameter $S_{B,B_0} = (3\langle \cos^2 \angle[\mathbf{B}_{\text{core}}, \mathbf{B}_0] \rangle - 1)/2$ for each model are shown, and values with $S_{L,B_0} > 0.25$ are indicated in bold. Rotation setup models with $\theta_0 = 0^\circ$ are shown in the top panel, while $\theta_0 = 45^\circ$ models are shown in the middle panel. w/o Setup models are shown in the bottom panel. Generally, in models with strong magnetic fields (indicated by dashed lines), the strong alignment of \mathbf{B}_{core} with \mathbf{B}_0 is observed.

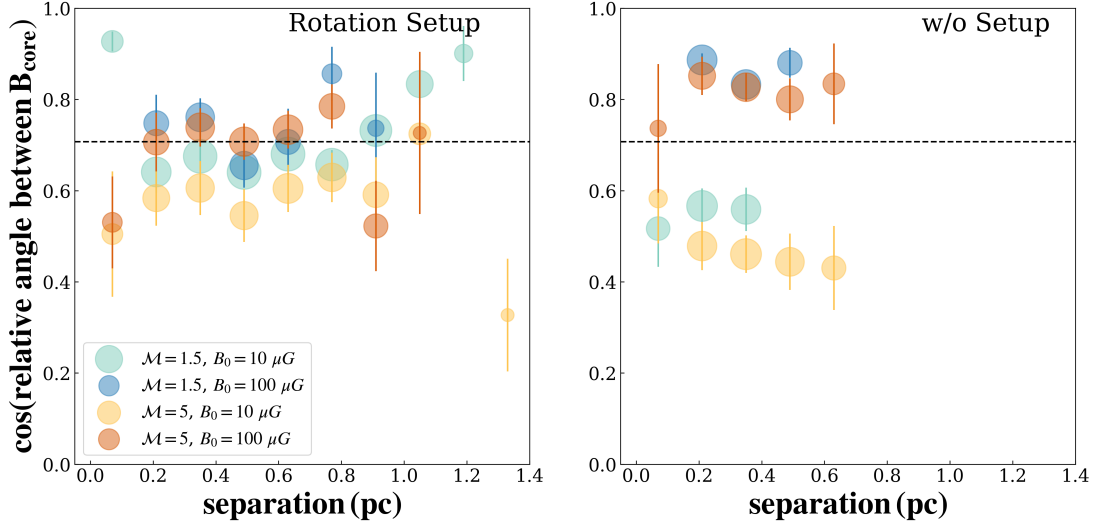


Figure 2.8: The cosine of relative orientation angles of \mathbf{B}_{core} pairs as a function of their separation distances. The presentation method is similar to Figure 2.6. Models with strong magnetic fields ($B_0 = 100 \mu G$) have a higher degree of alignment of \mathbf{B}_{core} pairs compared to models with weak magnetic fields ($B_0 = 10 \mu G$).

1.2 pc. On the other hand, in the weak B_0 ($= 10 \mu G$) models of Rotation Setup, the degree of alignment is generally lower compared to the strong B_0 models for a range of separations between 0.2 and 0.8. The strength of the initial magnetic field determines the degree of alignment of \mathbf{B}_{core} pairs.

In w/o Setup, the difference in results between strong and weak B_0 cases is significant. In the weak B_0 models, $\cos \theta_{B,B}$ is around 0.5, while in the strong B_0 cases, the degree of alignment of \mathbf{B}_{core} pairs is higher and surpasses $\cos 45^\circ$.

2.3.1.3 Rotation-Magnetic Field Relation of the Rotation Setup

We investigated the relation between \mathbf{L}_{core} and \mathbf{B}_{core} . Figure 2.9 illustrates the cumulative distribution function (CDF) of the cosine of the relative angle between \mathbf{L}_{core} and \mathbf{B}_{core} compared to a uniform distribution. The orientation parameter $S_{L,B}$ is defined as $S_{L,B} = (3\langle \cos^2 \angle[\mathbf{L}_{\text{core}}, \mathbf{B}_{\text{core}}] \rangle - 1)/2$. The CDF of most models appears to be a relatively straight line, and the null hypothesis that “the distribution is uniform” is

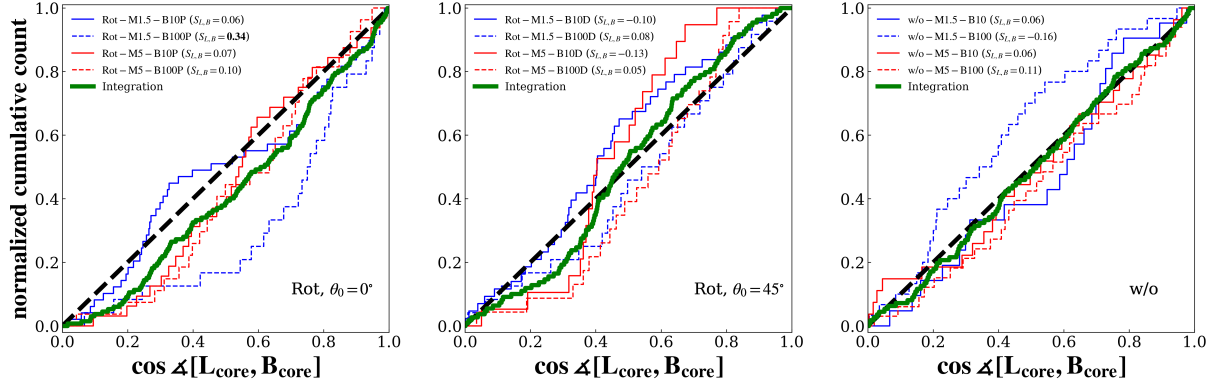


Figure 2.9: The cumulative distribution function of the cosine of the relative angle between the mean magnetic field \mathbf{B}_{core} and the angular momentum \mathbf{L}_{core} , compared to the expected CDF (black dashed lines) for a completely uniform distribution. Rotation Setup models with $\theta_0 = 0^\circ$ are shown in the left panel, while $\theta_0 = 45^\circ$ models are shown in the middle panel. The green line is the result of combining the cores of the four models in each panel. The right panel shows the results of w/o Setup. In most models, suggesting random distributions of $\angle[\mathbf{L}_{\text{core}}, \mathbf{B}_{\text{core}}]$.

not rejected at a significance level of 5 % using the K-S test except for the model Rot-M1.5-B100P.

The model Rot-M1.5-B100P has weak initial turbulence intensity ($\mathcal{M} = 1.5$), resulting in a well-aligned \mathbf{L}_{core} with Ω_0 , as shown in Section 2.3.1.1. Furthermore, the strong initial magnetic field ($B_0 = 100\mu G$) contributes to the alignment between \mathbf{B}_{core} and \mathbf{B}_0 (see Section 2.3.1.2), and as $\theta_0 = 0^\circ$ ($\Omega_0 \parallel \mathbf{B}_0$), \mathbf{L}_{core} is well aligned with \mathbf{B}_{core} . As such, due to the limited initial conditions and geometric reasons, \mathbf{L}_{core} and \mathbf{B}_{core} are aligned, resulting in a high orientation parameter $S_{L,B} = 0.34$. In models other than Rot-M1.5-B100P with such specific initial conditions, the distribution of angle between \mathbf{L}_{core} and \mathbf{B}_{core} is generally random. We can conclude that \mathbf{B}_{core} does not strongly limit \mathbf{L}_{core} . As shown in Section 2.3.1.1, the rotation of clumps and turbulence determine the property of \mathbf{L}_{core} .

2.3.2 Collision Setup

This section shows the simulation results of the Collision Setup. We show the correlation between the \mathbf{L}_{core} and Ω_{col} in Section 2.3.2.1. In Section 2.3.2.2, we discuss the

correlation between \mathbf{B}_{core} and \mathbf{B}_0 . In Section 2.3.2.3, we present the rotation-magnetic field relation ($\mathbf{L}_{\text{core}}\text{-}\mathbf{B}_{\text{core}}$) among bound cores.

2.3.2.1 Angular Momentum of the Collision Setup

In the Collision Setup, the initial clumps are set to have no initial rotational angular velocity Ω_0 . Nonetheless, due to their off-center arrangement, the two clumps begin to rotate after the collision, resulting in a dominant momentum in the plane perpendicular to the rotation axis Ω_{col} . It is therefore expected that the gas motion of the clumps would be inherited by the cores formed, with the angular momentum vector \mathbf{L}_{core} aligning with Ω_{col} . However, contrary to this expectation, the results of the analysis reveal a different outcome. Figure 2.10 illustrates the histograms of cosine of the angle between \mathbf{L}_{core} and Ω_{col} as Figure 2.4. Here, the orientation parameter $S_{L,\Omega}$ is defined as $S_{L,\Omega} = (3\langle \cos^2 \angle[\mathbf{L}_{\text{core}}, \Omega_{\text{col}}] \rangle - 1)/2$. In the Collision Setup, $S_{L,\Omega}$ is generally small regardless of turbulence strength. Also, all Collision Setup models are roughly consistent with a uniform distribution of $\cos \angle[\mathbf{L}_{\text{core}}, \Omega_{\text{col}}]$, which cannot be rejected at a significance level of 5%. In the Rotation Setup, a clear alignment tendency was observed between \mathbf{L}_{core} and Ω_0 for weak turbulence models as shown in § 2.3.1.1. However, in the Collision Setup, the clump's rotation is not transferred to the core, regardless of the initial parameters.

Figure 2.11 displays $\cos \theta_{L,L}$ as a function of their separation distances as Figure 2.6. For any models, $\cos \theta_{L,L}$ is around 0.5 for most separation ranges, indicating the random distribution of the direction of \mathbf{L}_{core} .

2.3.2.2 Magnetic Field of the Collision Setup

Figure 2.12 shows the histograms of cosine of the angle between \mathbf{B}_{core} and \mathbf{B}_0 as Figure 2.7. In fast collision models with $\theta_0 = 0^\circ$ (shown in the top panel), the alignment tendency between \mathbf{B}_{core} and \mathbf{B}_0 is strong, as indicated by a significant deviation from the uniform distribution of $\cos \angle[\mathbf{B}_{\text{core}}, \mathbf{B}_0]$, and a large S_{B,B_0} , which holds true for both strong and weak B_0 models. In Section 2.3.1.2, we showed that in Rotation Setup models with the weak B_0 , the direction of \mathbf{B}_{core} tends to be relatively random, and the degree of alignment between \mathbf{B}_{core} and \mathbf{B}_0 is lower than those of strong B_0 models. However, a strong alignment tendency is present in the Collision Setup even in weak

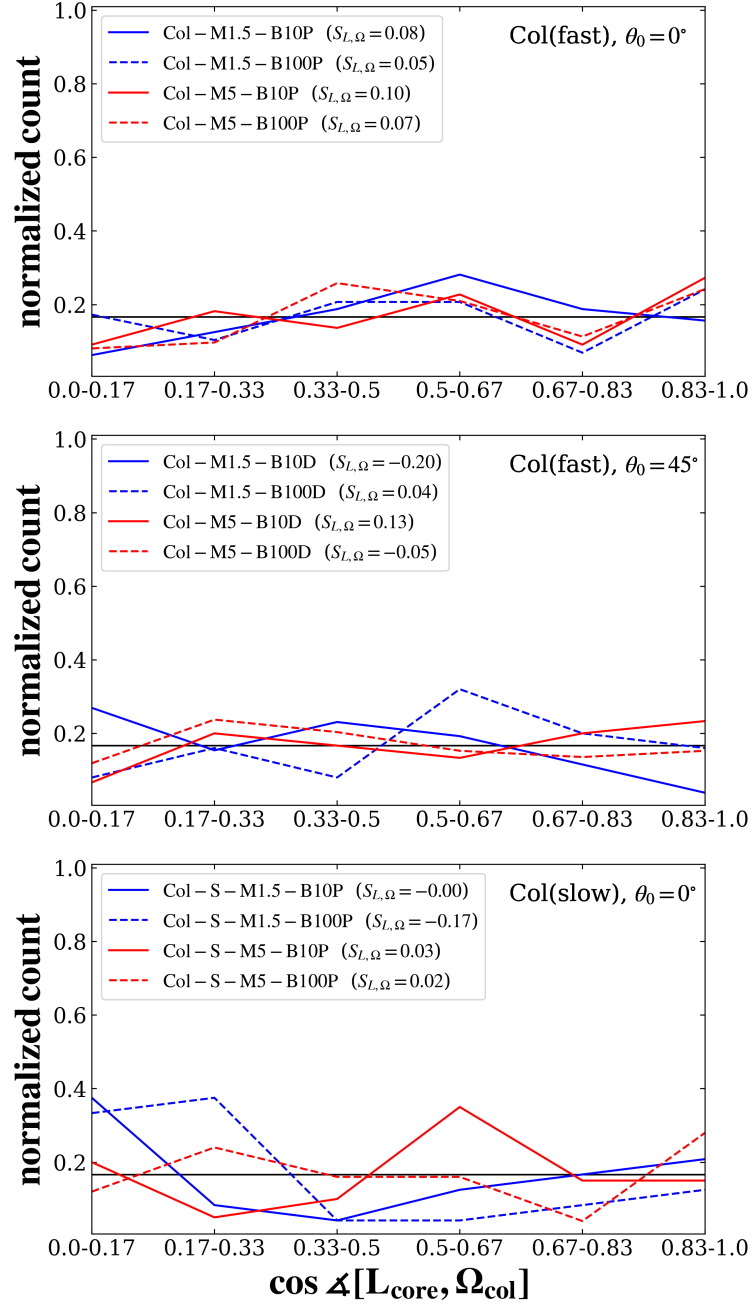


Figure 2.10: Same as Figure 2.4 except for Collision Setup models. Fast collision velocity cases with $\theta_0 = 0^\circ$ are shown in the top panel, and those of $\theta_0 = 45^\circ$ are shown in the middle panel. Slow collision velocity cases are shown in the bottom panel. For all models in the Collision Setup, the angles are close to being isotropically distributed, and no tendency for alignment is observed.

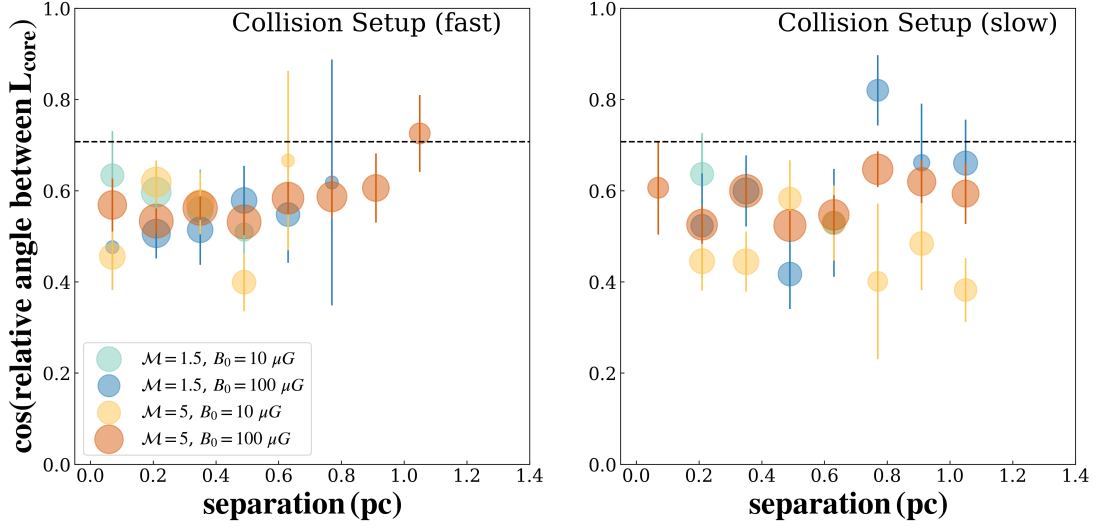


Figure 2.11: Same as Figure 2.6 except for Collision Setup models. Fast collision velocity cases are shown in the left panel, and slow collision velocity cases are shown in the right panel. Regardless of the models, $\cos \theta_{L,L}$ is close to 0.5 for most separation ranges, which suggests that the direction of \mathbf{L}_{core} is randomly distributed.

B_0 models. This strong alignment is caused by the large-scale alignment of magnetic fields due to collisions. Figure 2.13 is a density and magnetic field (black lines) in slices cut through the center of the simulation box in Collision Setup models with weak B_0 models, Co1-M1.5-B10P and Co1-M1.5-B10D. The shocked layer is formed at the interface of the two clumps. The magnetic field is amplified and aligned more efficiently along the shocked layer due to compression and bending by collisions. Most dense cores are formed within the shocked layer, inheriting this aligned magnetic field. Therefore, the degree of alignment of \mathbf{B}_{core} is high, and this trend is also evident in weak B_0 models where the magnetic field is easily bent. That is to say, in cases where clumps collide, the direction of \mathbf{B}_{core} is determined by the direction of the collision axis.

The middle panel of Figure 2.12 shows results of fast collision models with $\theta_0 = 45^\circ$. In these models with weak B_0 (indicated by solid lines), the peak of the distribution of $\cos \angle[\mathbf{B}_{\text{core}}, \mathbf{B}_0]$ is not within the range of 0.83-1.0, but rather in the range of 0.67-0.83. Compared to the weak B_0 model with $\theta_0 = 0^\circ$ in the top panel, the difference is evident, with smaller values of S_{B,B_0} . This tendency for misalignment in the $\theta_0 = 45^\circ$ model can be explained by the magnetic field distortion due to collisions. The bottom

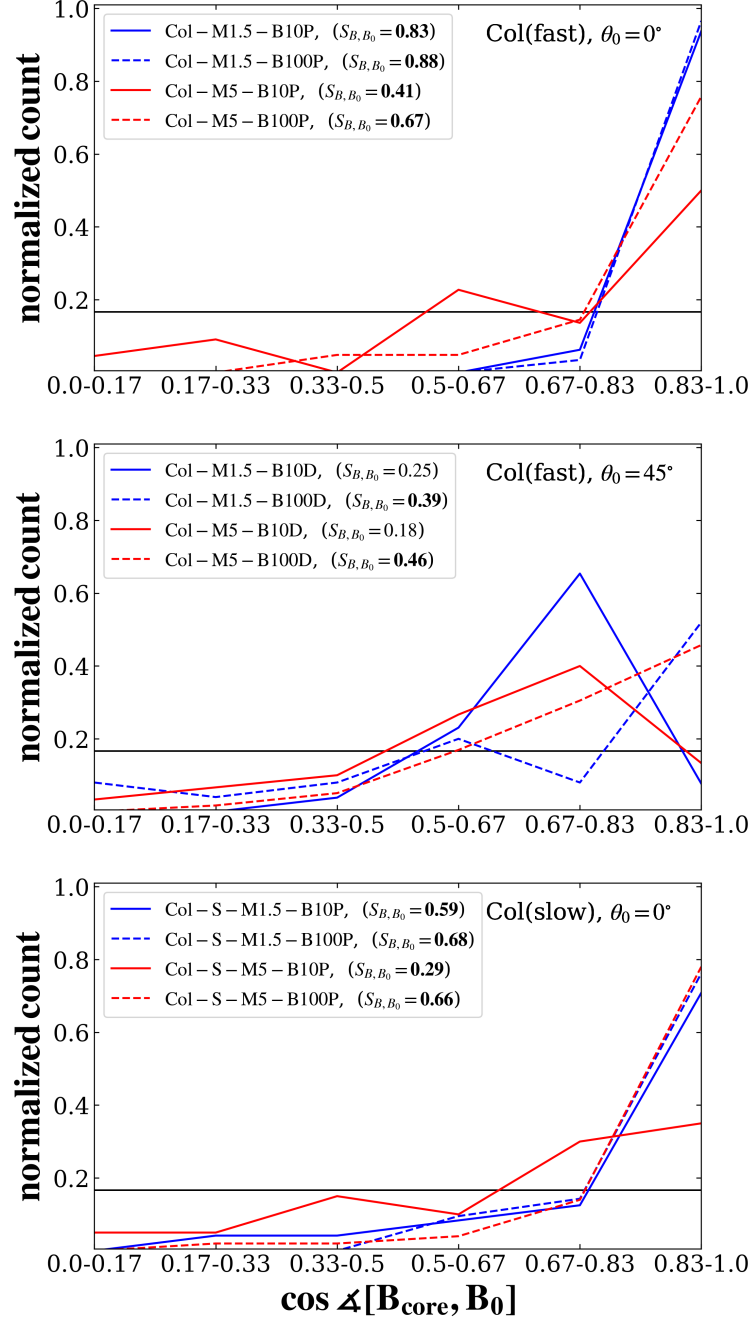


Figure 2.12: Same as Figure 2.7 except for Collision Setup models. Fast collision velocity cases with $\theta_0 = 0^\circ$ are shown in the top panel, and those of $\theta_0 = 45^\circ$ are shown in the middle panel. Slow collision velocity cases are shown in the bottom panel.

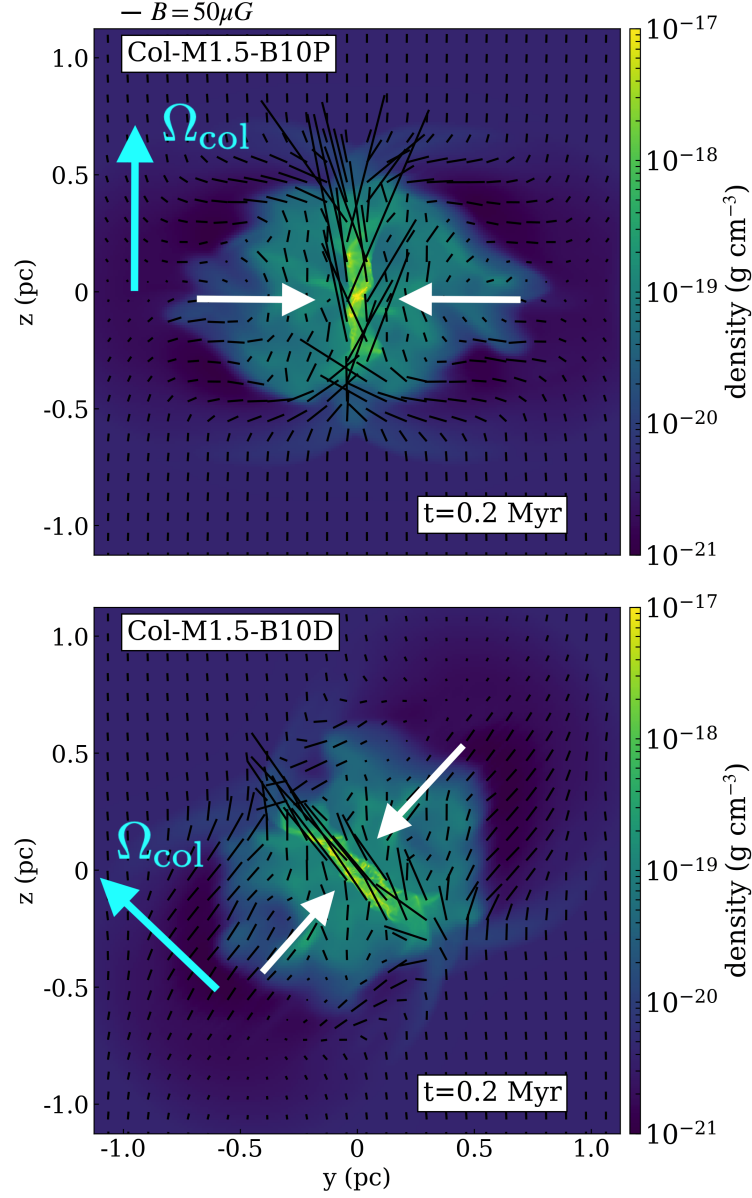


Figure 2.13: Slice plots of the gas density in a plane through the center of the simulation box at $t = 0.2$ Myr in Col-M1.5-B10P and Col-M1.5-B10D models. Black dashed lines show the magnetic field direction (\mathbf{B}_0 is parallel to the z axis). The length of lines corresponds to the magnetic field strength. White arrows indicate the collision axis. The magnetic field is amplified and aligned along the shocked layer.

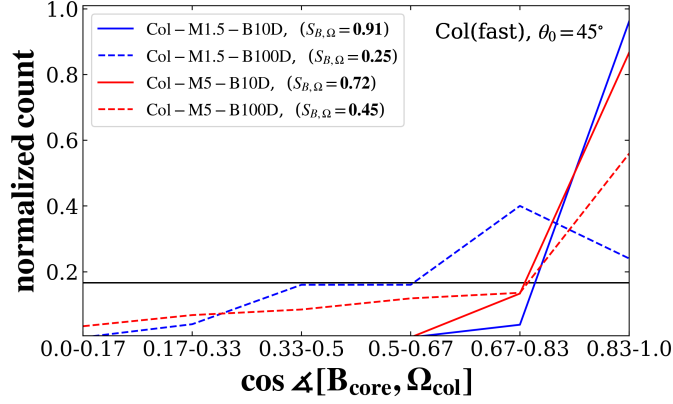


Figure 2.14: Histograms of the cosine of the relative angle between \mathbf{B}_{core} and $\mathbf{\Omega}_{\text{col}}$ for fast collision models with $\theta_0 = 45^\circ$. The black dashed line shows the expected distribution for an isotropic orientation of \mathbf{B}_{core} . In the legends, the orientation parameter $S_{B,\Omega} = (3\langle \cos^2 \angle[\mathbf{B}_{\text{core}}, \mathbf{\Omega}_{\text{col}}] \rangle - 1)/2$ for each model are shown, and values with $S_{L,B_0} > 0.25$ are indicated in bold. In models with weak magnetic fields (indicated by solid lines), the strong alignment of \mathbf{B}_{core} with $\mathbf{\Omega}_{\text{col}}$ is observed. Furthermore, in the weak magnetic field model, $S_{B,\Omega}$ is higher than S_{B,B_0} , indicating that the direction of \mathbf{B}_{core} is determined not by the direction of the initial magnetic field, but rather by the direction of collision axis.

panel of Figure 2.13 indicates the density and magnetic field in slices for the weak B_0 model with $\theta_0 = 45^\circ$. Since the collision axis is inclined at 45° to \mathbf{B}_0 , the shocked layer is oblique to \mathbf{B}_0 and parallel to $\mathbf{\Omega}_{\text{col}}$. The magnetic field inside the clump is twisted and amplified along the direction of the shock, causing the field to be tilted by 45° with respect to \mathbf{B}_0 and become parallel to $\mathbf{\Omega}_{\text{col}}$. \mathbf{B}_{core} aligns with $\mathbf{\Omega}_{\text{col}}$ rather than \mathbf{B}_0 , as it inherits the aligned magnetic field within the shocked layer. Figure 2.14 shows histograms of the cosine of the relative angle between \mathbf{B}_{core} and $\mathbf{\Omega}_{\text{col}}$ for fast collision models with $\theta_0 = 45^\circ$. For weak B_0 models, the peak of the distribution of $\cos \angle[\mathbf{B}_{\text{core}}, \mathbf{\Omega}_{\text{col}}]$ is sharp within the range of 0.83-1.0 indicating the strong alignment of \mathbf{B}_{core} with $\mathbf{\Omega}_{\text{col}}$. As $\theta_0 = 0^\circ$ models, the collision-axis determines the direction of \mathbf{B}_{core} . However, it should be noted that in cases where B_0 is strong, this may not necessarily hold. In models with strong B_0 (dashed line in Figure 2.14), the peak in the distribution is not as sharp compared to the model with weak B_0 , and the orientation parameter $S_{B,\Omega} = (3\langle \cos^2 \angle[\mathbf{B}_{\text{core}}, \mathbf{\Omega}_{\text{col}}] \rangle - 1)/2$, is smaller. When B_0 is strong, the magnetic field inside the clump is more likely to be aligned with the direction of \mathbf{B}_0 . Therefore, when $\theta_0 = 45^\circ$, the magnetic field may not align perfectly with the shocked layer. \mathbf{B}_{core} , which inherits the magnetic field inside the clump, will tilt relative to

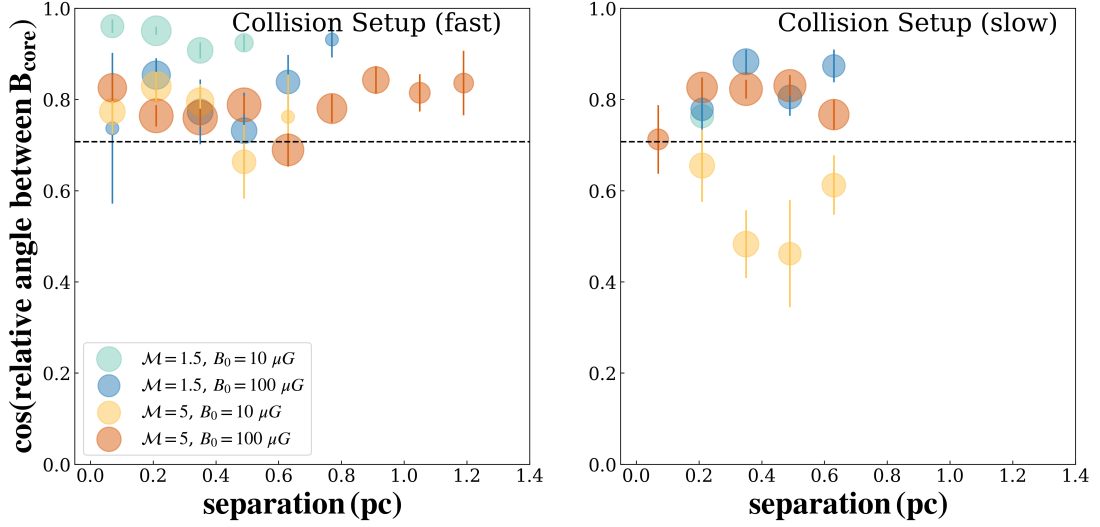


Figure 2.15: Same as Figure 2.8 except for Collision Setup models. Fast collision velocity cases are shown in the left panel, and slow collision velocity cases are shown in the right panel. The Collision Setup model has a higher degree of alignment for \mathbf{B}_{core} compared to Rotation Setup and w/o Setup models. Especially when B_0 is weak, the field aligns along the shocked layer, resulting in a significantly higher degree of alignment for \mathbf{B}_{core} .

Ω_{col} .

Figure 2.15 shows the cosine of the relative orientation angle, noted as $\cos \theta_{B,B}$, between all \mathbf{B}_{core} pairs as a function of their separation distances in the same manner as Figure 2.8. All models except for the slow collision model with $\mathcal{M} = 5$ and $B_0 = 10\mu G$ exhibit a clear tendency for alignment between \mathbf{B}_{core} pairs over a wide range of separations. A crucial characteristic is that even in weak B_0 models, $\cos \theta_{B,B}$ is large. As shown in Section 2.3.1.2, in the Rotation setup, $\cos \theta_{B,B}$ for weak B_0 models are significantly smaller than those of strong B_0 models. However, in the Collision setup, the global alignment of the fields inside the clump due to collisions causes $\cos \theta_{B,B}$ of the weak B_0 models to be even greater. In the slow collision model with $\mathcal{M} = 5$ and $B_0 = 10\mu G$, due to the strong turbulence and slow collision velocities, the magnetic field is not well aligned at the shocked layer, resulting in a random distribution of the direction of \mathbf{B}_{core} . However, in other models, if collisions compress the gas sufficiently, the \mathbf{B}_{core} pairs will align. Generally, the orientation of the collision axis (or Ω_{col}) is a crucial factor in determining the direction of \mathbf{B}_{core} .

2.3.2.3 Rotation-Magnetic Field Relation of the Collision Setup

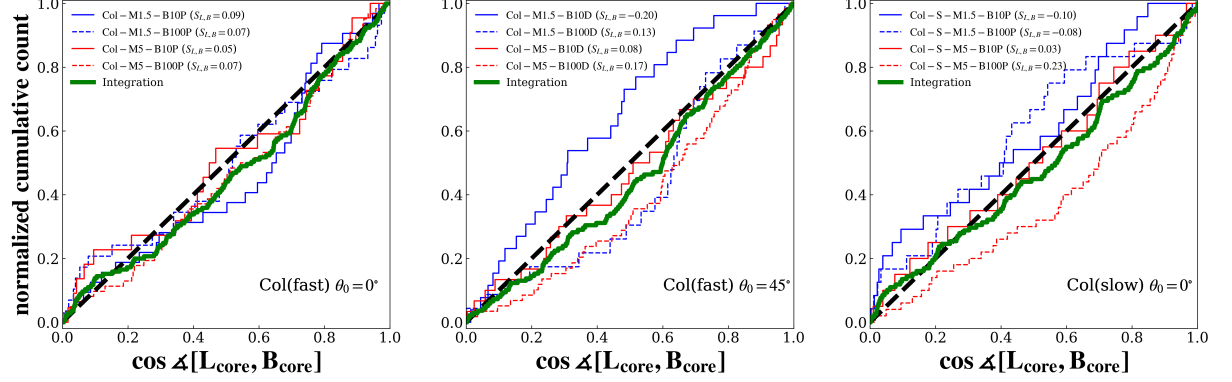


Figure 2.16: Same as Figure 2.9 except for Collision Setup models. Fast collision velocity cases with $\theta_0 = 0^\circ$ are shown in the left panel, and those of $\theta_0 = 45^\circ$ are shown in the middle panel. Slow collision velocity cases are shown in the right panel. In most models, they suggest random distributions of $\angle[\mathbf{L}_{\text{core}}, \mathbf{B}_{\text{core}}]$.

Figure 2.16 illustrates the cumulative distribution function (CDF) of the cosine of the relative angle between \mathbf{L}_{core} and \mathbf{B}_{core} compared to a uniform distribution as Figure 2.9. For most models, CDF is similar to a uniform distribution, and the null hypothesis that "the distribution is uniform" cannot be rejected at a significance level of 5% using the K-S test, except for models Col-M5-B100D and Col-S-M5-B100P. The models Col-M5-B100D and Col-S-M5-B100P with strong B_0 show a slight tendency towards alignment. However, $S_{L,B}$ is not significantly large (weak alignment), and other models of Collision Setup show almost uniform distributions.

Table 2.2. Properties of identified bound cores

Model name	$S_{L,\Omega}^a$	S_{B,B_0}^b	$S_{L,B}^c$	$\langle \cos \theta_{L,L} \rangle^d$	$\langle \cos \theta_{B,B} \rangle^e$	β^f /10 ⁻²	$E_{\text{rot}}/E_{\text{kin}}^g$ /10 ⁻²	N_{core}^h
Rotation Setup								
Rot-M1.5-B10P	0.55	0.06	0.06	0.68±0.25	0.64±0.31	4.6(2.2-8.2)	19.3(10.0-25.9)	49
Rot-M1.5-B100P	0.60	0.44	0.34	0.72±0.25	0.66±0.27	6.3(5.1-9.6)	36.8(32.2-44.3)	24
Rot-M5-B10P	0.12	0.22	0.07	0.60±0.27	0.60±0.31	3.2(2.2-6.1)	15.1(8.4-23.0)	32
Rot-M5-B100P	0.06	0.52	0.10	0.50±0.29	0.70±0.26	3.8(2.1-16.5)	24.7(7.1-55.3)	27
Rot-M1.5-B10D	0.55	-0.10	-0.10	0.69±0.28	0.75±0.24	5.3(3.5-8.4)	18.9(13.0-30.8)	43
Rot-M1.5-B100D	0.37	0.31	0.08	0.63±0.30	0.74±0.23	7.9(5.2-13.5)	28.9(24.3-37.1)	24
Rot-M5-B10D	0.19	0.14	-0.13	0.51±0.33	0.59±0.31	7.1(4.0-11.0)	26.1(8.9-36.9)	20
Rot-M5-B100D	0.08	0.36	0.05	0.55±0.32	0.73±0.24	7.0(2.4-11.3)	36.7(13.9-54.0)	23
w/o Setup								
w/o-M1.5-B10	...	0.08	0.06	0.55±0.31	0.56±0.28	1.7(0.6-3.9)	4.1(0.9-8.8)	21
w/o-M1.5-B100	...	0.69	-0.18	0.62±0.29	0.86±0.11	2.3(1.1-5.7)	10.1(3.8-19.8)	32
w/o-M5-B10	...	0.24	0.06	0.60±0.30	0.47±0.31	7.4(2.1-13.2)	20.5(7.3-33.5)	33
w/o-M5-B100	...	0.73	0.11	0.58±0.30	0.82±0.19	2.1(0.9-7.4)	11.1(3.4-30.6)	27
Collision Setup								
Col-M1.5-B10P	0.08	0.83	0.09	0.64±0.25	0.92±0.06	0.7(0.4-2.1)	1.7(0.8-2.8)	32
Col-M1.5-B100P	0.05	0.88	0.07	0.49±0.30	0.93±0.08	3.6(2.2-7.0)	15.5(10.8-24.0)	29
Col-M5-B10P	0.10	0.41	0.05	0.60±0.25	0.66±0.25	8.8(2.3-14.0)	16.3(6.0-29.5)	22
Col-M5-B100P	0.07	0.67	0.07	0.58±0.30	0.81±0.19	7.3(3.2-13.5)	19.1(9.8-37.5)	62
Col-M1.5-B10D	-0.20	0.25	-0.20	0.55±0.34	0.96±0.05	1.3(0.2-3.1)	2.0(0.7-4.1)	26
Col-M1.5-B100D	0.04	0.39	0.13	0.61±0.27	0.59±0.30	5.5(3.1-7.6)	19.6(12.0-26.6)	23
Col-M5-B10D	0.13	0.18	0.08	0.53±0.32	0.86±0.13	7.0(3.3-15.4)	10.7(7.4-20.7)	30
Col-M5-B100D	-0.05	0.46	0.17	0.54±0.29	0.71±0.27	5.2(1.8-11.7)	16.2(7.0-26.6)	59

Table 2.2 (cont'd)

Model name	$S_{L,\Omega}^a$	S_{B,B_0}^b	$S_{L,B}^c$	$\langle \cos \theta_{L,L} \rangle^d$	$\langle \cos \theta_{B,B} \rangle^e$	β^f /10 ⁻²	$E_{\text{rot}}/E_{\text{kin}}^g$ /10 ⁻²	N_{core}^h
Co1-S-M1.5-B10P	0.00	0.59	-0.10	0.58±0.31	0.79±0.21	2.3 (1.1-3.3)	4.7 (2.2-7.3)	24
Co1-S-M1.5-B100P	-0.13	0.68	-0.08	0.59±0.32	0.84±0.14	3.3 (2.2-5.7)	22.2 (11.0-26.7)	21
Co1-S-M5-B10P	0.03	0.29	0.03	0.48±0.28	0.59±0.3	4.3 (2.4-7.4)	13.0 (10.4-20.5)	20
Co1-S-M5-B100P	0.02	0.66	0.23	0.57±0.28	0.8±0.21	5.9 (2.7-12.1)	22.5 (15.7-39.3)	50

Note. — ^a The orientation parameter $S_{L,\Omega} = (3\langle \cos^2 \angle[\mathbf{L}_{\text{core}}, \mathbf{\Omega}_0(\mathbf{\Omega}_{\text{col}})] \rangle - 1)/2$. ^b The orientation parameter $S_{B,B_0} = (3\langle \cos^2 \angle[\mathbf{B}_{\text{core}}, \mathbf{B}_0] \rangle - 1)/2$. ^c The orientation parameter $S_{L,B} = (3\langle \cos^2 \angle[\mathbf{L}_{\text{core}}, \mathbf{B}_{\text{core}}] \rangle - 1)/2$. ^d Mean of the cosine of the relative angle between \mathbf{L}_{core} vectors. ^e Mean of the cosine of the relative angle between \mathbf{B}_{core} vectors ^f The median and upper/lower quartiles of the rotational parameter $\beta(\equiv E_{\text{rot}}/E_{\text{grav}})$ over all cores for each parameter set. ^g The median and upper/lower quartiles of $E_{\text{rot}}/E_{\text{kin}}$ over all cores for each parameter set. ^h The total number of identified bound cores.

2.4 Discussion

2.4.1 Alignment of Core Angular Momentum

The inheritance of global motion by dense cores from their parental clump is a significant topic of study. As described in § 1.2, previous research has yielded mixed results, with some studies indicating mostly random distributions of spin axes in young open clusters (Jackson & Jeffries, 2010), while others have found strong spin alignment of stars within specific open clusters (Corsaro et al., 2017). This variability may depend on the specific environment of the parental star-forming regions. In this subsection, we discuss the trend of the relative angle between the parental clump rotation axis and \mathbf{L}_{core} .

As shown in Section 2.3.1.1 and 2.3.2.1, for all strong turbulence models ($\mathcal{M} = 5$), we find the random distributions of $\angle[\mathbf{L}_{\text{core}}, \boldsymbol{\Omega}_0(\boldsymbol{\Omega}_{\text{col}})]$. Strong turbulence can disturb the gas feeding the core, causing a loss of memory of the clump’s global rotational motion. On the other hand, in Rotation Setups with weak turbulence ($\mathcal{M} = 1.5$), we observed the alignment between $\boldsymbol{\Omega}_0$ and \mathbf{L}_{core} . However, in Collision Setups, even with weak turbulence, the distributions of $\cos\angle[\mathbf{L}_{\text{core}}, \boldsymbol{\Omega}_{\text{col}}]$ are uniform, and the \mathbf{L}_{core} pairs are not aligned with each other. In the Collision Setup, despite the total angular momentum within a single clump being approximately equal (in the slow model) or double (in the fast model) that of the Rotation Setup, \mathbf{L}_{core} does not align with $\boldsymbol{\Omega}_{\text{col}}$.

This misalignment in the Collision setup is partly due to the failure to transfer angular momentum to the dense gas harboring cores. Figure 2.17 shows the evolution of total angular momentum of dense gas in the z-direction, L_z , as functions of dense gas mass or total core mass ΣM_{core} for $\mathcal{M} = 1.5$ models. Notably, L_z for the Rotation Setup cases is much higher than that of Collision Setup cases. For example, at $\Sigma M_{\text{core}}/M_{\text{total}} = 1.0 \times 10^{-2}$, $L_z(n > 10^6 \text{ cm}^{-3})$ for the Rotation Setup cases have increased to approximately 1% of $|\mathbf{L}_{\text{total}}|$, while in the Collision Setup cases these have been equal to or less than 0.1% of $|\mathbf{L}_{\text{total}}|$. That is, the Collision Setup cases exhibit less angular momentum transfer when comparing at the same efficiency of core formation. Moreover, in the Collision Setup, models with weak B_0 show approximately an order of magnitude lower L_z compared to strong B_0 models.

These differences in rates of angular momentum transfer across the models are at-

tributable to the processes of dense gas formation. Figure 2.17 illustrates the slice map of ρj_z for the **Col-M1.5-B10P** and **Col-M1.5-B100P** models at $\Sigma M_{\text{core}}/M_{\text{total}} = 0.01$, where j_z is the z component of the specific angular momentum around the simulation box center. The dense regions form at the center, where bound dense cores are formed mainly. These dense layers are formed by the collision of gases moving in opposite directions and are located in the central part hence they initially have little momentum. As time progresses, angular momentum is injected into the dense regions from the overall system. However, due to the intense compression from collisions, cores form promptly when the angular momentum of dense regions is still low. Therefore, little angular momentum is transported to the core, and as a result, the core does not inherit the rotational motion of the clumps. In models with strong B_0 , the magnetic pressure hinders rapid compression, so the dense gas has more angular momentum during core formation compared to models with weak B_0 . However, the majority of the total angular momentum in the system is still possessed by the gas in the outer regions.

As described in § 2.2.3, we identify gravitationally bound cores at the time when the most evolved core collapses. We note that if collisions continue to progress and cores are formed further from dense gas with enough angular momentum, it is plausible that the cores could inherit the rotation of the clumps. In this study, we have demonstrated that, at least in the initial stages, the main cores forming in the central region are less likely to inherit rotation.

In Figure 2.19, to show the direction dependency of the accretion flow toward the dense core, we illustrate the momentum structure around the most massive dense core position for two models, **Rot-M1.5-B10P** of Rotation Setup and **Col-M1.5-B10P** of Collision Setup. In the left panels, we display Column densities summed over 0.6 pc around the most massive core. In the right panels, the purple lines show the average momentum around the x -axis: $\int_S \rho(v_x - v_{x,\text{core}}) dydz / \int_S dydz$, where $v_{x,\text{core}}$ is the x -component of the center of mass velocity of the core, and $S = \{(y, z) \mid [(y - y_{\text{core}})^2 + (z - z_{\text{core}})^2]^{1/2} \leq 0.05\text{pc}\}$. The horizontal axis corresponds to $x - x_{\text{core}}$. Similarly, the green and blue lines represent the average momentum around the y -axis and z -axis, respectively. In the Rotation Setup model **Rot-M1.5-B10P**, gas with predominant momentum in the y direction can be observed around the core. We have confirmed that, similarly, gas with dominant momentum in the x or y direction can be found around many other cores. In Rotation Setup models, the velocity field of clump rotation is generally parallel to the

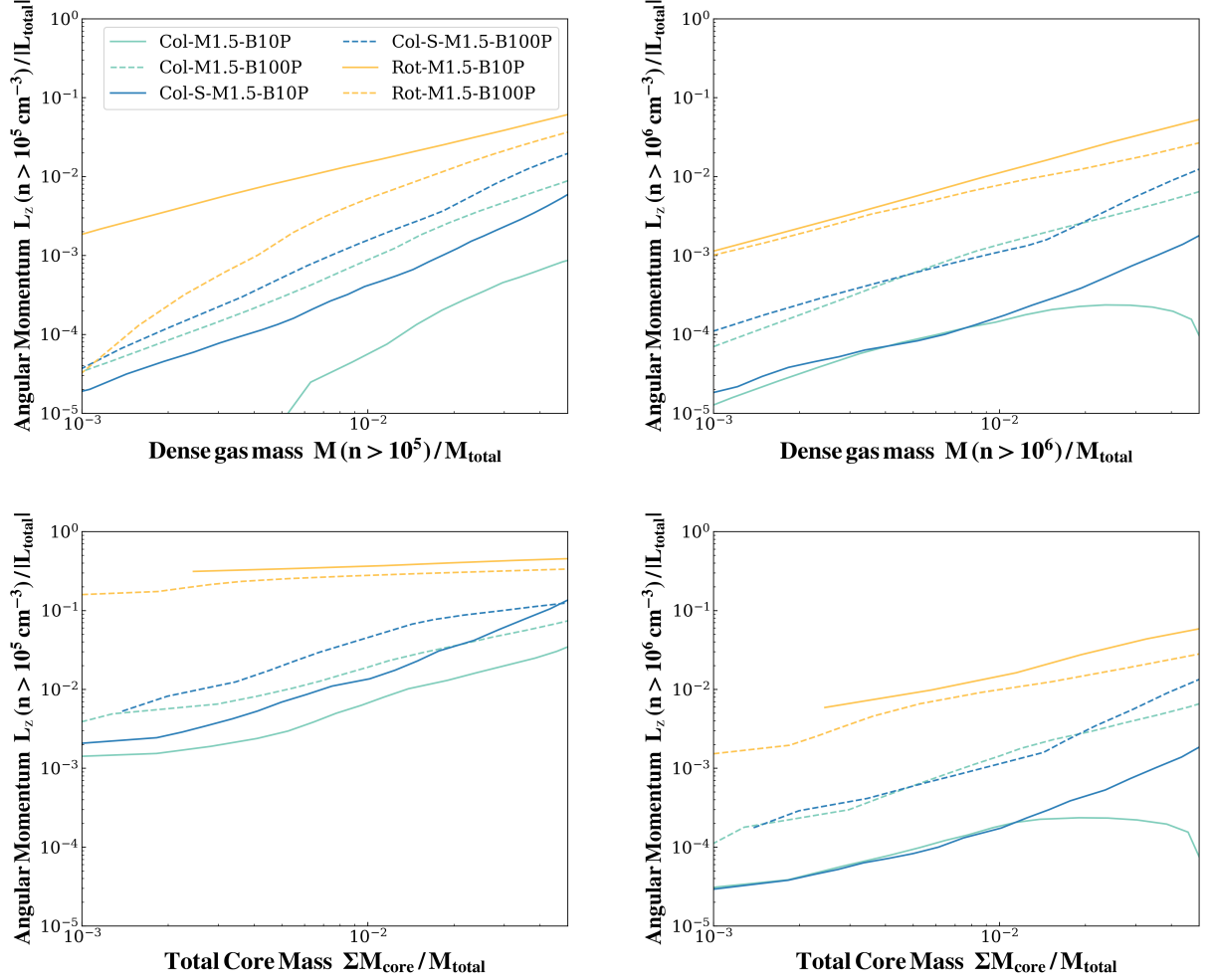


Figure 2.17: Evolution of total angular momentum of dense gas in the z -direction, L_z . We are comparing models for weak turbulence $\mathcal{M} = 1.5$ and $\theta_0 = 0^\circ$ with the same realization of the input turbulence. The top-left figure plots L_z versus total mass, both for gas above a density of 10^5 cm^{-3} . L_z is normalized by $|\mathbf{L}_{\text{total}}|$, and dense gas mass $M(n > 10^5 \text{ cm}^{-3})$ is normalized by the total clump mass $M_{\text{total}} (\equiv 2M_{\text{clump}}$ in the Collision Setup, $\equiv M_{\text{clump}}$ in the Rotation Setup). The top-right figure similarly plots L_z for a density of 10^6 cm^{-3} . The bottom figures depict L_z against the total mass of bound cores, ΣM_{core} , with ΣM_{core} normalized by M_{total} .

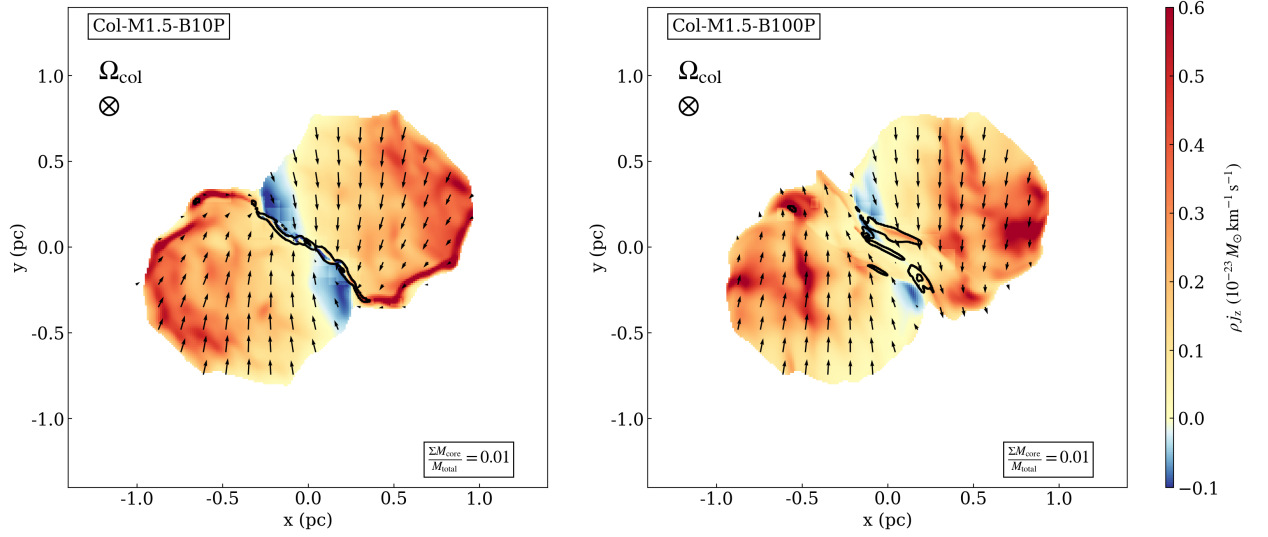


Figure 2.18: Slice map of ρj_z for the Col-M1.5-B10P and Col-M1.5-B100P models at $\Sigma M_{\text{core}}/M_{\text{total}} = 0.01$, where j_z is the z component of the specific angular momentum around the simulation box center. Black contours are drawn at $n = \rho/\mu m_{\text{H}} = 10^5 \text{ cm}^{-3}$. The angular momentum of the high-density regions in the center is low, and the majority of the total angular momentum of the system is possessed by the gas on the outer parts.

xy plane. Therefore, dense gas regions with dominant momentum in the xy direction are more likely to form, especially when turbulence is weak. As momentum in such a region is injected into the core, the dense core acquires a rotational velocity on the xy plane, with the rotation axis parallel to the z -axis. The same effect occurs even when $\theta_0 = 45^\circ$. Thus, as shown in Section 2.3.1.1, in weak turbulence Rotation Setup, \mathbf{L}_{core} aligns with $\mathbf{\Omega}_0$.

On the other hand, the bottom-right panel of Figure 2.19 shows that the momentum of the gas around the core is isotropic in the Collision Setup model Col-M1.5-B10P. Momentum is not biased in the direction of clump motion (on the xy plane), and gas flow from the direction perpendicular to the collision axis (z) is also injected into the core significantly. In Collision Setup, the rotation direction of the dense core is not biased to one side. The distributions of $\cos\angle[\mathbf{L}_{\text{core}}, \mathbf{\Omega}_{\text{col}}]$ are uniform, as shown in Section 2.3.2.1.

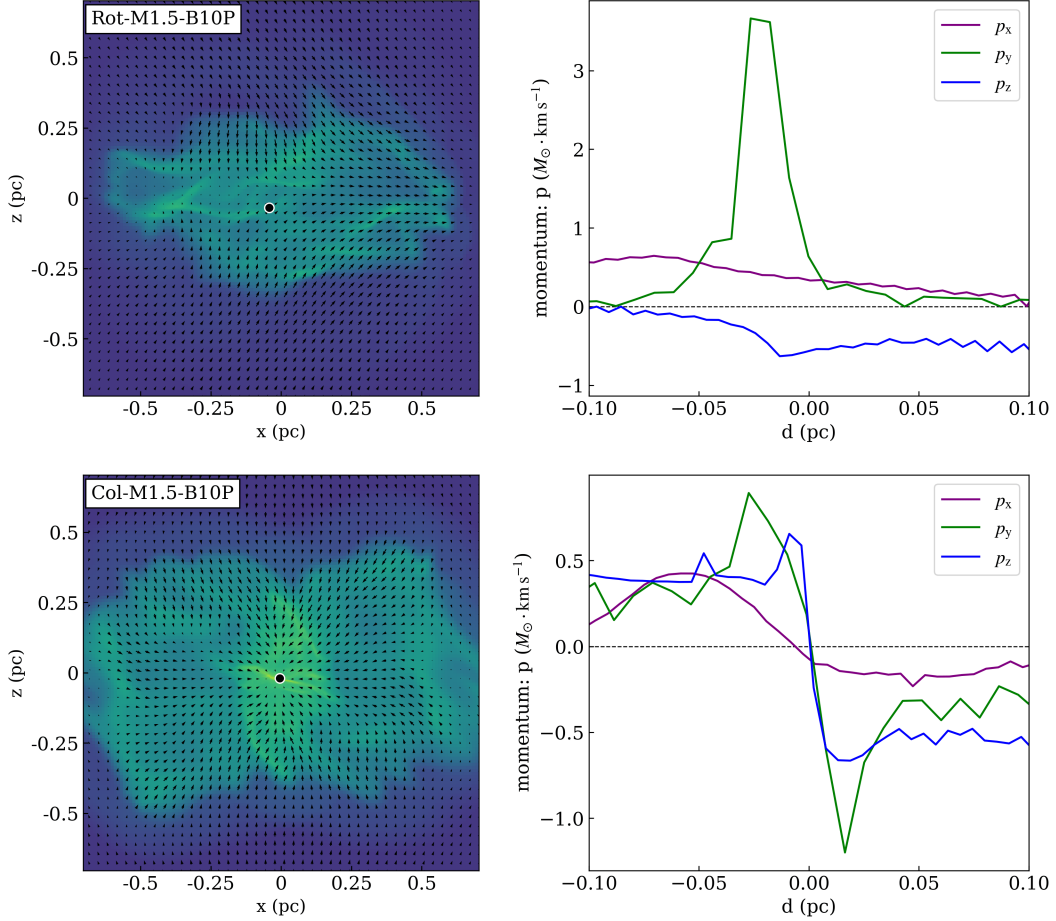


Figure 2.19: Left: Column densities summed over 0.6 pc for the **Rot-M1.5-B10P** model at 0.3 Myr (top) and **Col-M1.5-B10P** model at 0.2 Myr (bottom). The black lines show the average velocity field projected onto the plane. The position of the most massive dense core is indicated with a black circle. Right: Momentum structure around the most massive dense core corresponding to the left panel. Purple lines show the average momentum around the x -axis: $\int_S \rho(v_x - v_{x,\text{core}}) dy dz / \int_S dy dz$, where $v_{x,\text{core}}$ is the x -component of the center of mass velocity of the core, and $S = \{(y, z) \mid [(y - y_{\text{core}})^2 + (z - z_{\text{core}})^2]^{1/2} \leq 0.05 \text{ pc}\}$. The horizontal axis corresponds to $x - x_{\text{core}}$. Similarly, the green and blue lines represent the average momentum around the y -axis and z -axis, respectively. Momentum around the core is isotropic in the **Col-M1.5-B10P** model, while the y -component is dominant in the **Rot-M1.5-B10P** model.

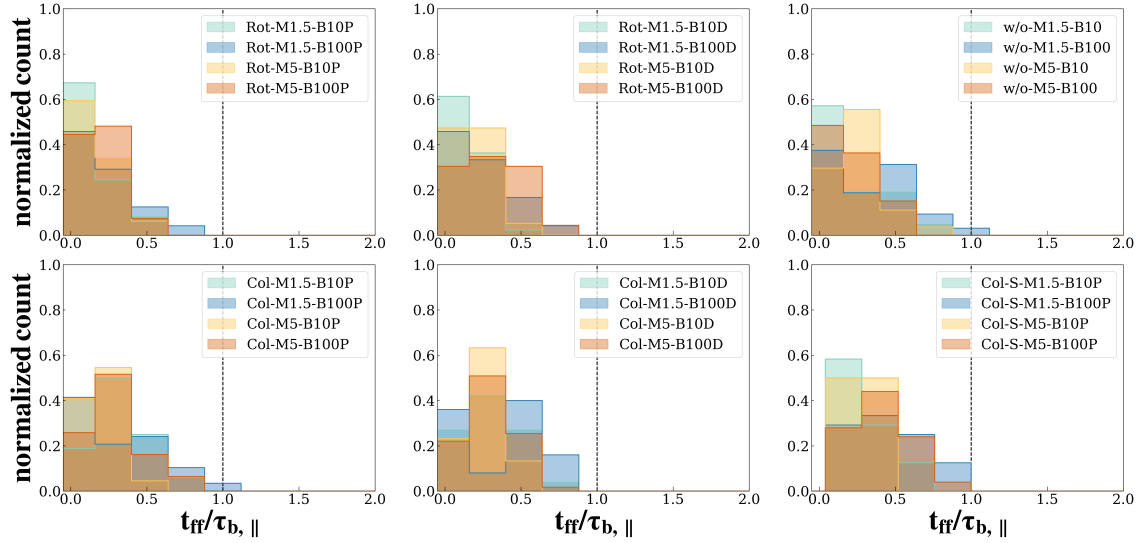


Figure 2.20: Histograms of the ratio of the free fall time t_{ff} to the magnetic braking timescale $\tau_{b,\parallel} \equiv \rho_{\text{cl}} Z / \rho_{\text{ext}} v_A$ for all bound cores in different models. Vertical dashed lines indicate the $t_{\text{ff}}/\tau_{b,\parallel} = 1.0$. For most cores, $t_{\text{ff}}/\tau_{b,\parallel}$ is lower than 1.0, suggesting that the effect of magnetic braking is not large.

2.4.2 Misalignment between the Angular Momentum and the Magnetic Field

As described in § 1.4, the relation between angular momentum and initial magnetic field within prestellar cores are important for late evolution during core collapse since they control the efficiency of the magnetic braking process. Furthermore, [Ciardi & Hennebelle \(2010\)](#) showed that the efficiency of mass ejection in the outflow depends on the angle between the rotation axis and the magnetic field.

As shown in Section 2.3.1.3 and 2.3.2.3, we find that the relative angle between \mathbf{L}_{core} and \mathbf{B}_{core} is random in most models. The alignment is strong only for the model **Rot-M1.5-B100P** due to the limited initial conditions. In some models of the Collision Setup, random distributions are rejected, but the alignment is weak. These results of general misalignment are consistent with previous numerical simulations under common initial conditions of clumps or clouds ([Chen & Ostriker, 2018](#); [Kuznetsova et al., 2020](#)). Our findings suggest that, except for exceptional cases, there is no tendency for strong alignment between \mathbf{L}_{core} and \mathbf{B}_{core} at core-scale ($\sim 0.01 - 0.1\text{pc}$) in single rotating clumps and colliding clumps.

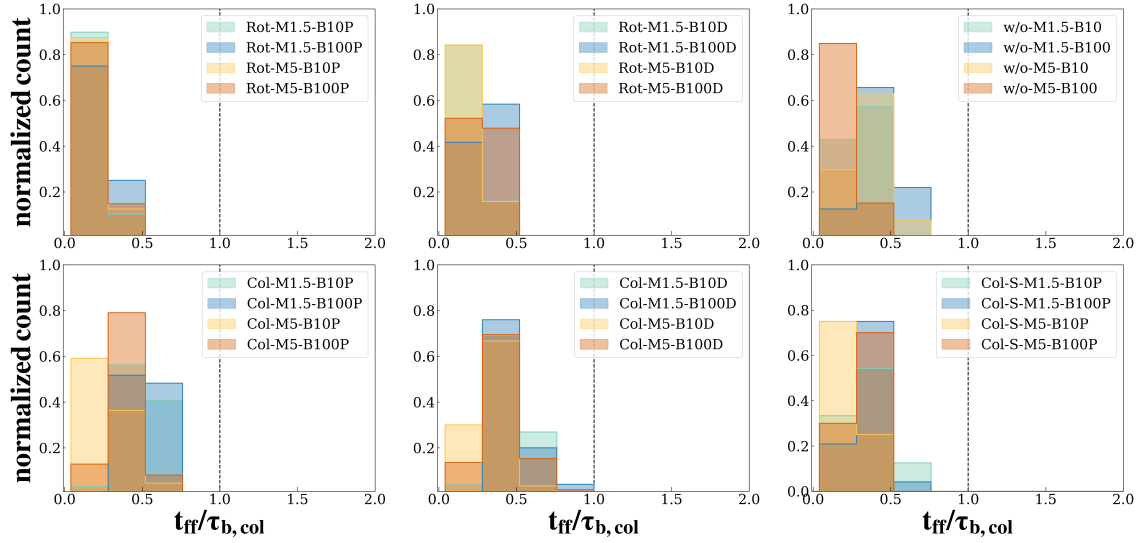


Figure 2.21: Same as Figure 2.20 except for the ratio of the free fall time t_{ff} to the magnetic braking timescale $\tau_{b,\text{col}} \equiv (8/5)^{1/3} \lambda_{J,\text{cl}}/v_A$. $t_{\text{ff}}/\tau_{b,\text{col}}$ is lower than 1.0, suggesting that the effect of magnetic braking is not large.

As described in § 1.4, the classical theory indicated that the magnetic axis of cores should be parallel to their rotational axis, as perpendicular configuration allows for faster magnetic braking compared to parallel configurations. If the effect of magnetic braking within the prestellar core is strong, the trend of strong alignment between \mathbf{L}_{core} and \mathbf{B}_{core} is expected. We use the characteristic time $\tau_{b,\parallel}$ for magnetic braking to study the effect of magnetic braking within cores quantitatively. When the mean direction of the field lines is parallel to the rotation axis, $\tau_{b,\parallel}$ is given by (see Appendix A.6):

$$\tau_{b,\parallel} = \frac{\rho_{\text{cl}}}{\rho_{\text{ext}}} \frac{Z}{v_A}, \quad (2.22)$$

where ρ_{cl} is the density of the core, Z is the half of core height, ρ_{ext} and v_A are the density and the Alfvén velocity in the ambient medium. $\tau_{b,\parallel}$ is an approximate timescale for magnetic braking to constrain the angular momentum. We calculate the column density $\rho_{\text{cl}}Z$ as $\rho_{\text{cl}}Z = M_{\text{core}}/\pi R_{\text{core}}^2$, ρ_{ext} as ρ_{th} , and v_A as $B_{\text{core}}/(4\pi\rho_{\text{ext}})^{1/2}$. Figure 2.20 shows the histogram of the ratio between the free-fall time t_{ff} and $\tau_{b,\parallel}$ for all bound cores in different models. For most cores, $t_{\text{ff}}/\tau_{b,\parallel} < 1$, indicating that the effect of magnetic braking is not significant. This is consistent with the random distribution

of $\angle[\mathbf{L}_{\text{core}}, \mathbf{B}_{\text{core}}]$ shown in Section 2.3.1.3 and 2.3.2.3. We note that $\tau_{\text{b},\parallel}$ defined in Equation 2.22 applies to the case where the magnetic field and the angular momentum are parallel. Our identified cores include those in which \mathbf{L}_{core} is not parallel to \mathbf{B}_{core} , therefore Equation 2.22 is only approximate.

We also estimate the timescale for magnetic braking using the method in Matsumoto & Tomisaka (2004) (see Appendix A.6). Matsumoto & Tomisaka (2004) assume the collapsing cloud and approximate the timescale for magnetic braking as

$$\tau_{\text{b,col}} = \left(\frac{8}{5}\right)^{1/3} \frac{\lambda_{\text{J,cl}}}{v_{\text{A}}}, \quad (2.23)$$

where $\lambda_{\text{J,cl}} = c_s (\pi/G\rho_{\text{cen}})^{1/2}$ is the jeans length within the core. We calculate ρ_{cen} as the mean density of the core. Figure 2.21 shows the histogram of the ratio between the free-fall time t_{ff} and $\tau_{\text{b,col}}$. For almost all cores, $\tau_{\text{b,col}}$ is longer than t_{ff} , showing the relative weakness of the magnetic braking as Figure 2.20. We note that our simulations are ideal MHD, but the magnetic braking can be even weaker if the non-ideal MHD effects (including ambipolar diffusion, Hall effect, and Ohmic dissipation) are considered (e.g., Mellon & Li, 2009; Kunz & Mouschovias, 2010; Tomida et al., 2015; Masson et al., 2016; Marchand et al., 2018).

The magnetic field-rotation misalignment has been proposed to solve the magnetic braking catastrophe and explain the disk formation (see § 1.4). Our results suggest that under many circumstances, the misalignment between the core’s magnetic field and rotation can be realized, and the formation of the protostellar disk could be explained without contradiction.

In Appendix B.5, we also show the correlation between $\angle[\mathbf{L}_{\text{core}}, \mathbf{B}_{\text{core}}]$ and energies of cores for all models. We found that $\angle[\mathbf{L}_{\text{core}}, \mathbf{B}_{\text{core}}]$ is independent of $E_{\text{mag}}/|E_{\text{grav}}|$ or $E_{\text{kin}}/|E_{\text{grav}}|$, and their distribution is random for our samples.

2.4.3 Core Shape

In this subsection, we discuss the geometry of bound cores. To estimate the length and direction of the core axis, we measured the momentum of inertia within cores:

$$I_{ij} = \frac{1}{M_{\text{core}}} \int (r_i - r_{\text{CM},i}) (r_j - r_{\text{CM},j}) \rho(\mathbf{r}) d\mathbf{r}, \quad (2.24)$$

where the subscripts i and j represent coordinate labels. The three-axis lengths of cores are estimated from the three principal axes ($a_1 > a_2 > a_3$) defined by the square roots of eigenvalues of I_{ij} . Corresponding eigenvectors ($\mathbf{a}_1, \mathbf{a}_2$ and \mathbf{a}_3) represents the direction of the each axis. This analysis is essentially the same as that used in [Matsumoto & Hanawa \(2004\)](#). The ration $a_3/a_2 \sim 1$ indicates a prolate core, while $a_2/a_1 \sim 1$ means an oblate core. Cores with $a_3/a_2 < 1$ and $a_2/a_1 < 1$ are triaxial (see Appendix A.7).

Figure 2.22 displays the scatter plots of axis ratios of cores in some models. Cores have a wide range of axis rations and, in general, fall in prolate populations or triaxial populations regardless of initial conditions⁵. Instead of an oblate core, as is often assumed for classical views, elongated prolate structures are more common. This tendency is consistent with previous works (e.g., [Gammie et al., 2003](#); [Offner et al., 2008](#); [Chen & Ostriker, 2018](#)). In Appendix B.6, we classify the core shape by the comparison between $a_1 a_3$ and a_2^2 . In this classification method as well, the proportion of prolate cores is higher in most models.

In classical views, prestellar cores are often assumed to have \mathbf{L}_{core} and \mathbf{B}_{core} , which are perpendicular to the major axis (\mathbf{a}_1) and parallel to the minor axis (\mathbf{a}_3), respectively. However, our identified cores have different properties than this depiction. Figure 2.23 shows histograms of the cosine of the relative angle between \mathbf{L}_{core} and its major (\mathbf{a}_1 , top) and minor (\mathbf{a}_3 , bottom) axes. Typically, \mathbf{L}_{core} tends to be perpendicular to major axis \mathbf{a}_1 as indicated by a negative $S_{L,a_1} \equiv (3\langle \cos^2 \angle[\mathbf{L}_{\text{core}}, \mathbf{a}_1] \rangle - 1)/2$. The p-values from the K-S test, listed in Table 2.3, suggest that the $\cos \angle[\mathbf{L}_{\text{core}}, \mathbf{a}_1]$ distribution significantly deviates from uniformity in most models, with p-values below 0.05. This perpendicularity of \mathbf{L}_{core} to \mathbf{a}_1 is a natural result from the definition of the angular momentum ($L_{\text{core}} \propto |\mathbf{r}_i - \mathbf{r}_{\text{CM}}|$, see Equation 2.15). Meanwhile, \mathbf{L}_{core} has no significant correlation with \mathbf{a}_3 except in Rotation Setup models with $\mathcal{M} = 1.5$. That is, \mathbf{L}_{core} is not constrained by \mathbf{a}_2 and \mathbf{a}_3 .

Similar to Figure 2.23, Figure 2.24 shows histograms of the cosine of the relative angle between \mathbf{B}_{core} and its major (\mathbf{a}_1 , top) and minor (\mathbf{a}_3 , bottom) axes. Typically, \mathbf{B}_{core}

⁵The exact boundaries of these populations are arbitrary. However, it is certainly true that oblate cores tend to occupy a smaller percentage of our identified cores.

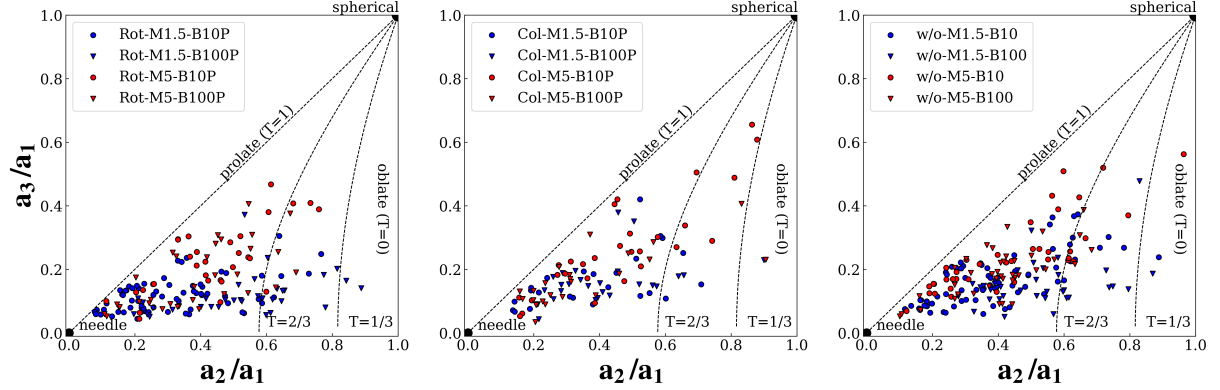


Figure 2.22: The a_3/a_1 vs. a_2/a_1 plot. The dashed lines are curves of constant triaxiality T (see Appendix A.7). Oblate spheroids have $T = 0$, prolate spheroids have $T = 1$. The separations between the prolate, triaxial, and oblate populations occur at $T = 1/3$ and $2/3$. In general, cores are close to triaxial or prolate rather than oblate.

is preferentially more perpendicular to \mathbf{a}_1 and preferentially more parallel to \mathbf{a}_3 . However, not all models exhibit this tendency; some do not reject the uniform distribution of $\cos\angle[\mathbf{B}_{\text{core}}, \mathbf{a}_1]$ or $\cos\angle[\mathbf{B}_{\text{core}}, \mathbf{a}_3]$, and there are also models where \mathbf{B}_{core} and \mathbf{a}_3 are perpendicular.

Conclusively, \mathbf{L}_{core} and \mathbf{B}_{core} are not necessarily perpendicular to \mathbf{a}_1 or parallel to \mathbf{a}_3 contradicting the simple classical pictures. Especially, non-correlation between \mathbf{L}_{core} and \mathbf{a}_3 except in Rotation Setup models with $\mathcal{M} = 1.5$ is intriguing and consistent with the randomness of the $\angle[\mathbf{L}_{\text{core}}, \mathbf{B}_{\text{core}}]$ discussed in § 2.4.2.

2.4.4 Energies

Energy analysis can reveal the dynamical properties of the cores and provide an important indicator in exploring the impact of the clump environment on the core. In this subsection, we mainly discuss the energies of dense cores.

The first row of Figure 2.25 presents the ratio between kinetic and gravitational energies, $E_{\text{kin}}/|E_{\text{grav}}|$, as a function of core radius. Unlike the other figures, this plot includes unbound cores ($E_{\text{thermal}} + E_{\text{kin}} + E_{\text{mag}} + E_{\text{grav}} > 0$). In the Rotation and w/o Setups, $E_{\text{kin}}/|E_{\text{grav}}|$ is relatively independent of the radius. In the Collision Setup, the contribution of kinetic energy is relatively large for smaller cores compared to other

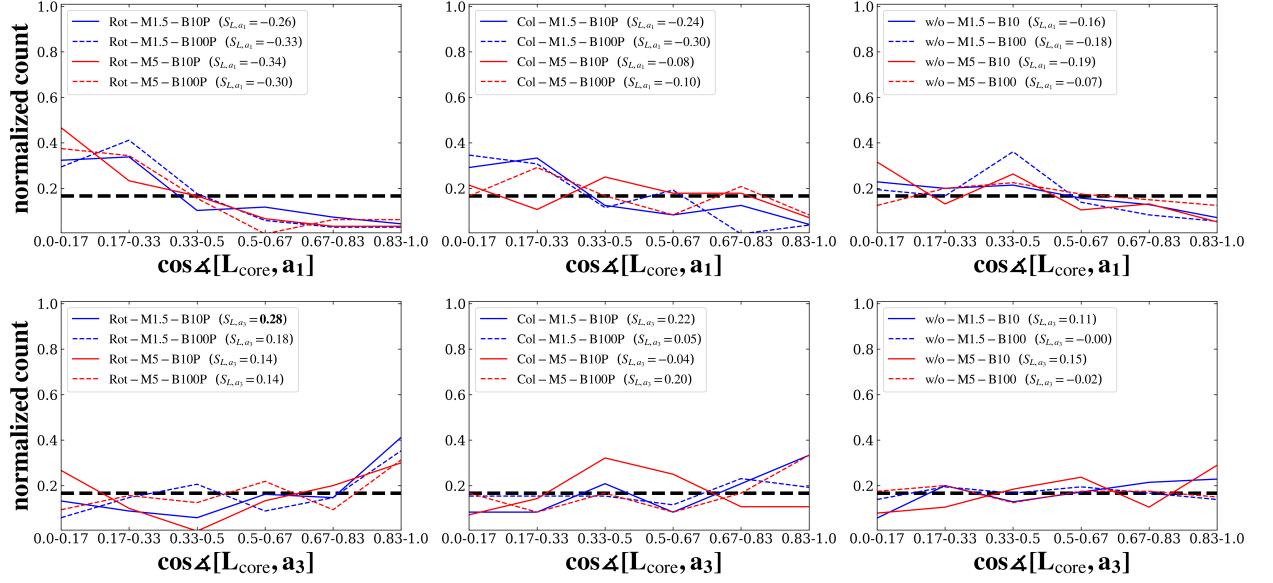


Figure 2.23: Histograms of the cosine of the relative angle between \mathbf{L}_{core} and its major (\mathbf{a}_1 , top) and minor (\mathbf{a}_3 , bottom) axes. In most models, \mathbf{L}_{core} tends to align perpendicular to \mathbf{a}_1 . On the other hand, \mathbf{L}_{core} has no preferred direction with respect to \mathbf{a}_3 except for models of Rotation Setup with $\mathcal{M} = 1.5$.

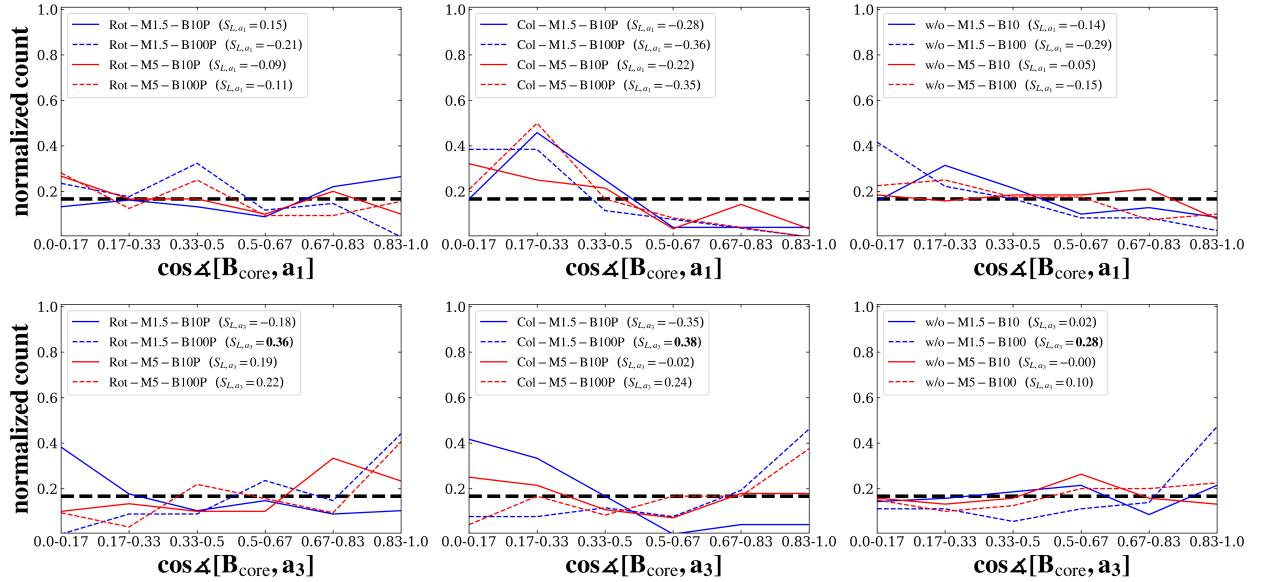


Figure 2.24: Histograms of the cosine of the relative angle between \mathbf{B}_{core} and its major (\mathbf{a}_1 , top) and minor (\mathbf{a}_3 , bottom) axes. In most models, \mathbf{B}_{core} tends to align perpendicular to \mathbf{a}_1 and parallel to \mathbf{a}_3 .

Table 2.3. Geometry of identified cores

Model name	S_{L,a_1}^a	p-value ^b ($\cos^2\angle[\mathbf{L}_{\text{core}}, \mathbf{a}_1]$)	S_{L,a_3}^c	p-value ^d ($\cos^2\angle[\mathbf{L}_{\text{core}}, \mathbf{a}_3]$)	S_{B,a_1}^e	p-value ^f ($\cos^2\angle[\mathbf{B}_{\text{core}}, \mathbf{a}_1]$)	S_{B,a_3}^g	p-value ^h ($\cos^2\angle[\mathbf{B}_{\text{core}}, \mathbf{a}_3]$)
Rotation Setup								
Rot-M1.5-B10P	-0.26	8.0×10^{-8}	0.28	4.4×10^{-5}	0.15	1.0×10^{-2}	-0.18	2.6×10^{-5}
Rot-M1.5-B100P	-0.33	7.0×10^{-6}	0.18	3.6×10^{-2}	-0.21	8.2×10^{-3}	0.36	6.5×10^{-5}
Rot-M5-B10P	-0.34	8.2×10^{-6}	0.14	1.0×10^{-1}	-0.09	3.8×10^{-1}	0.19	4.5×10^{-2}
Rot-M5-B100P	-0.30	2.6×10^{-6}	0.14	3.0×10^{-1}	-0.11	1.7×10^{-1}	0.22	2.4×10^{-2}
w/o Setup								
w/o-M1.5-B10	-0.16	7.8×10^{-3}	0.11	5.3×10^{-2}	-0.14	8.3×10^{-3}	0.02	9.4×10^{-1}
w/o-M1.5-B100	-0.18	1.3×10^{-2}	0.00	9.5×10^{-1}	-0.29	9.7×10^{-5}	0.28	5.7×10^{-4}
w/o-M5-B10	-0.19	2.7×10^{-2}	0.15	1.7×10^{-1}	-0.05	6.8×10^{-1}	0.00	8.8×10^{-1}
w/o-M5-B100	-0.07	5.1×10^{-1}	-0.02	9.9×10^{-1}	-0.15	7.0×10^{-2}	0.10	2.2×10^{-1}
Collision Setup (fast)								
Col-M1.5-B10P	-0.24	6.9×10^{-3}	0.22	8.9×10^{-2}	-0.28	3.8×10^{-4}	-0.35	3.4×10^{-5}
Col-M1.5-B100P	-0.30	2.8×10^{-4}	0.05	7.6×10^{-1}	-0.36	9.1×10^{-6}	0.38	4.4×10^{-4}
Col-M5-B10P	-0.08	4.6×10^{-1}	-0.04	3.5×10^{-1}	-0.22	3.0×10^{-4}	-0.02	2.5×10^{-1}
Col-M5-B100P	-0.10	2.7×10^{-1}	0.20	5.9×10^{-1}	-0.35	3.3×10^{-4}	0.24	6.1×10^{-1}

Note. — ^a The orientation parameter $S_{L,a_1} = (3\langle\cos^2\angle[\mathbf{L}_{\text{core}}, \mathbf{a}_1]\rangle - 1)/2$. ^b The p-value from comparing the $\cos^2\angle[\mathbf{L}_{\text{core}}, \mathbf{a}_1]$ distribution against a uniform distribution. ^c The orientation parameter $S_{L,a_3} = (3\langle\cos^2\angle[\mathbf{L}_{\text{core}}, \mathbf{a}_3]\rangle - 1)/2$. ^d The p-value from comparing the $\cos^2\angle[\mathbf{L}_{\text{core}}, \mathbf{a}_3]$ distribution against a uniform distribution. ^e The orientation parameter $S_{B,a_1} = (3\langle\cos^2\angle[\mathbf{B}_{\text{core}}, \mathbf{a}_1]\rangle - 1)/2$. ^f The p-value from comparing the $\cos^2\angle[\mathbf{B}_{\text{core}}, \mathbf{a}_1]$ distribution against a uniform distribution. ^g The orientation parameter $S_{B,a_3} = (3\langle\cos^2\angle[\mathbf{B}_{\text{core}}, \mathbf{a}_3]\rangle - 1)/2$. ^h The p-value from comparing the $\cos^2\angle[\mathbf{B}_{\text{core}}, \mathbf{a}_3]$ distribution against a uniform distribution. P-values below 0.05 are shown in bold.

setups. This trend is due to the turbulence induced by the collision, which was transferred to the cores. These results are consistent with the previous work by [Hsu et al. \(2023\)](#) and support their findings.

In the second row, we present the ratio between magnetic and gravitational energies, $E_{\text{mag}}/|E_{\text{grav}}|$, indicating that the contribution of E_{mag} is significant in the Collision Setup. As shown in Section 2.3.1.2, the gas is compressed perpendicular to the magnetic field in the Collision Setup, and the magnetic field is amplified inside the core while remaining aligned. This compression strengthens the magnetic field more than other models where gas contracts isotropically (see Appendix B.8). A common trend in all models is that the contribution of E_{mag} decreases with increasing core radius. In other words, the larger the core, the smaller the contribution of E_{mag} to E_{grav} and E_{kin} . In Appendix B.3, we show energies for gravitationally bound cores. A common trend for all models is that in most cores, the strength of magnetic energy E_{mag} is a fraction or an order of magnitude smaller than that of kinetic energy E_{kin} . Within bound cores, generally, E_{mag} is not dominant. This lowness of the magnetic energy contribution is qualitatively consistent with the result that \mathbf{B}_{core} does not limit \mathbf{L}_{core} as discussed in Section 2.4.2.

In the third row, we show histograms of the energy ratio of the sum of turbulent, thermal, and magnetic field energies to the absolute value of self-gravitational energy. As mentioned above, the contribution of turbulent and magnetic energies is significant in the Collision Setup, resulting in a higher proportion of unbound cores (see also Table 2.4). In summary, the formation of small-sized cores with a significant contribution of E_{kin} and E_{mag} is a characteristic unique to the Collision Setup.

Next, we will consider the contribution of the rotational energy of the bound cores. We investigated the ratio between the rotational energy and the gravitational potential energy, $\beta \equiv E_{\text{rot}}/|E_{\text{grav}}|$. The first row of Figure 2.26 confirms that β has a fairly large scatter and no clear dependence on radius. In the Rotation Setup, the scatter of larger cores is relatively small, and β is high, but as with other models, the typical value is $\beta \sim 0.05$ (see also Table 2.4). This value is roughly consistent with observations (e.g., [Goodman et al., 1993](#); [Caselli et al., 2002](#); [Tobin et al., 2011](#); [Chen et al., 2019](#)). The second row of Figure 2.26 shows the ratio between rotational and kinetic energies, $E_{\text{rot}}/E_{\text{kin}}$. In Collision and w/o Setups, this ratio exhibits significant variation, with the median ranging from a few percent to several tens of percent. In Rotation Setup, although the variation for larger cores is relatively low, $E_{\text{rot}}/E_{\text{kin}}$ is at most around

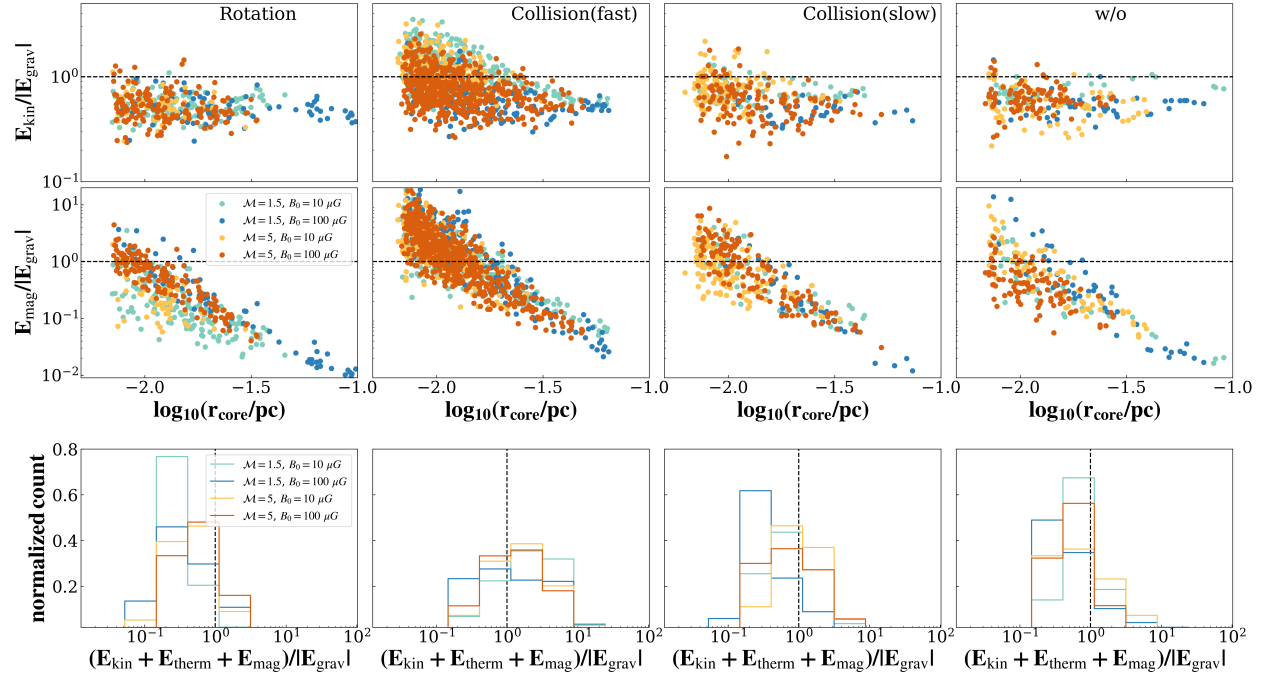


Figure 2.25: Top row: Ratio between kinetic and gravitational energies, $E_{\text{kin}}/|E_{\text{grav}}|$, as a function of core radius. The models with $\theta_0 = 0^\circ$ and 45° are presented together. Note that, unlike the other figures, this plot includes the unbound ($E_{\text{thermal}} + E_{\text{kin}} + E_{\text{mag}} + E_{\text{grav}} > 0$) core. Results of Rotation Setup, Collision Setup(fast), Collision Setup(slow), and w/o Setup are shown from left to right. Middle row: Ratio between magnetic and gravitational energies, $E_{\text{mag}}/|E_{\text{grav}}|$, plotted against the core radius. Bottom row: Histograms of the energy ratio of the sum of turbulent, thermal field, and magnetic field energies to the absolute value of self-gravitational energy. In the Collision Setup, the magnetic fields and kinetic energy have a relatively larger impact on smaller cores, resulting in a higher ratio of unbound cores.

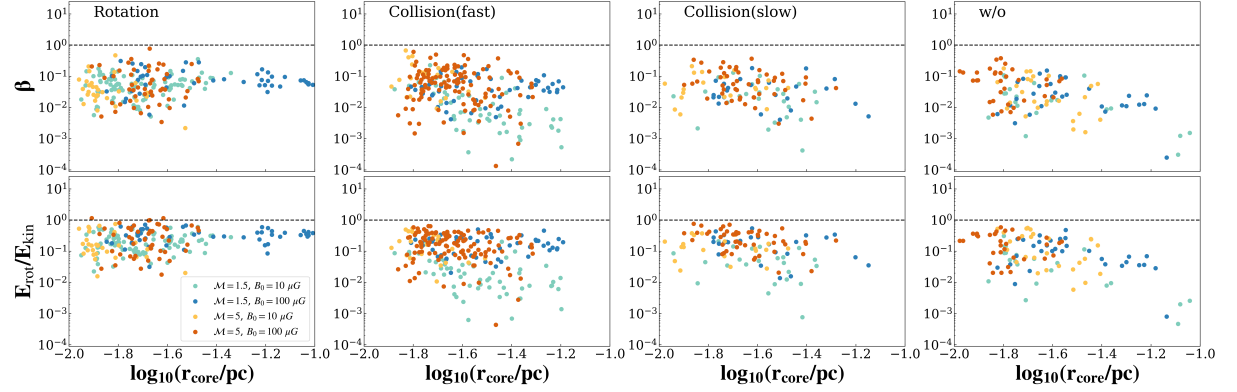


Figure 2.26: Top row: Rotational parameter β as a function of bound core radius. The models with $\theta_0 = 0^\circ$ and 45° are presented together. Results of Rotation Setup, Collision Setup(fast), Collision Setup(slow), and w/o Setup are shown from left to right. Bottom row: Ratio between rotational and total kinetic energies, $E_{\text{rot}}/E_{\text{kin}}$, plotted against the core radius. The distribution of β exhibits a large scatter with a typical value of $\beta \sim 0.05$, and there is also a large scatter in the distribution of $E_{\text{rot}}/E_{\text{kin}}$. The Rotation Setup model tends to have a lower scatter and slightly larger $E_{\text{rot}}/E_{\text{kin}}$ values than other setups. However, it is concluded that rotation is not the dominant motion in the dense core for any model.

several tens of percent, indicating that the contribution of rotation is not significant (see also Table 2.2). We can conclude that rotational motion is not dominant within bound dense cores, even if the parental clump is rotating or colliding. However, a characteristic feature of cores in Rotation Setup is that the contribution of E_{rot} is higher than that of other Setups, and the variance of $E_{\text{rot}}/E_{\text{kin}}$ and $E_{\text{rot}}/E_{\text{grav}}$ is relatively smaller for larger cores.

2.4.5 Specific Angular Momentum

The total specific angular momentum of cores, $j = L_{\text{core}}/M_{\text{core}}$ have important implications. As described in § 1.2, early observations have shown that j are correlated with the core size r , following a power-law $j \propto r^\alpha$ (Goodman et al., 1993; Caselli et al., 2002; Pirogov et al., 2003; Tatematsu et al., 2016). The correlation $j \propto r^{1.5}$ suggests that the rotation velocity inside the core is inherited from a turbulent cascade (Chen & Ostriker, 2018), while $j \propto r^2$ is expected for solid body rotation. Punanova et al. (2018) showed $j \propto r^{1.8-2.4}$ for the core in the L1495 filament in the Taurus molecu-

Table 2.4. Energetic properties of bound and unbound cores

Model name	$E_{\text{kin}}/ E_{\text{grav}} ^{\text{a}}$ /10 ⁻²	$E_{\text{mag}}/ E_{\text{grav}} ^{\text{b}}$ /10 ⁻²
Rotation Setup		
Rot-M1.5-B10P	26.1 (18.5–35.9)	10.5 (6.2–23.9)
Rot-M1.5-B100P	18.9 (14.9–24.7)	18.3 (1.8–55.8)
Rot-M5-B10P	29.7 (21.5–36.5)	20.0 (12.3–32.0)
Rot-M5-B100P	23.4 (16.7–45.4)	47.1 (20.5–94.4)
Rot-M1.5-B10D	26.2 (21.0–32.3)	13.8 (8.4–26.6)
Rot-M1.5-B100D	29.2 (24.3–38.4)	23.3 (3.8–47.9)
Rot-M5-B10D	34.3 (23.1–45.6)	27.3 (14.1–46.5)
Rot-M5-B100D	22.9 (17.1–36.0)	60.0 (29.0–95.8)
w/o Setup		
w/o-M1.5-B10	51.28 (39.6–65.8)	30.9 (13.8–99.1)
w/o-M1.5-B100	26.9 (20.8–35.3)	30.4 (11.2–96.3)
w/o-M5-B10	38.7 (29.7–53.4)	39.3 (22.6–60.5)
w/o-M5-B100	25.5 (18.0–40.6)	64.8 (18.3–141.9)
Collision Setup		
Col-M1.5-B10P	107.6 (65.1–248.5)	168.6 (61.1–351.3)
Col-M1.5-B100P	29.6 (23.4–48.0)	85.1 (18.1–340.1)
Col-M5-B10P	135.0 (84.7–227.3)	135.0 (67.3–281.9)
Col-M5-B100P	56.3 (31.7–92.1)	135.0 (52.1–286.1)
Col-M1.5-B10D	143.5 (76.1–287.5)	130.8 (55.0–266.1)
Col-M1.5-B100D	46.9 (26.1–83.4)	146.0 (42.2–390.1)
Col-M5-B10D	101.9 (68.5–184.1)	110.1 (64.2–218.6)
Col-M5-B100D	58.0 (32.5–100.5)	117.5 (55.1–243.1)
Col-S-M1.5-B10P	50.7 (41.1–72.7)	60.2 (14.5–121.0)
Col-S-M1.5-B100P	23.9 (16.0–28.5)	17.8 (8.9–60.8)
Col-S-M5-B10P	60.1 (39.0–88.6)	72.3 (38.4–154.6)
Col-S-M5-B100P	34.5 (20.4–53.5)	67.1 (23.1–158.9)

Note. — The values in this table are calculated including both bound and unbound cores. ^a The median and upper/lower quartiles of $E_{\text{kin}}/|E_{\text{grav}}|$ for each parameter set. ^b The median and upper/lower quartiles of $E_{\text{mag}}/|E_{\text{grav}}|$ for each parameter set.

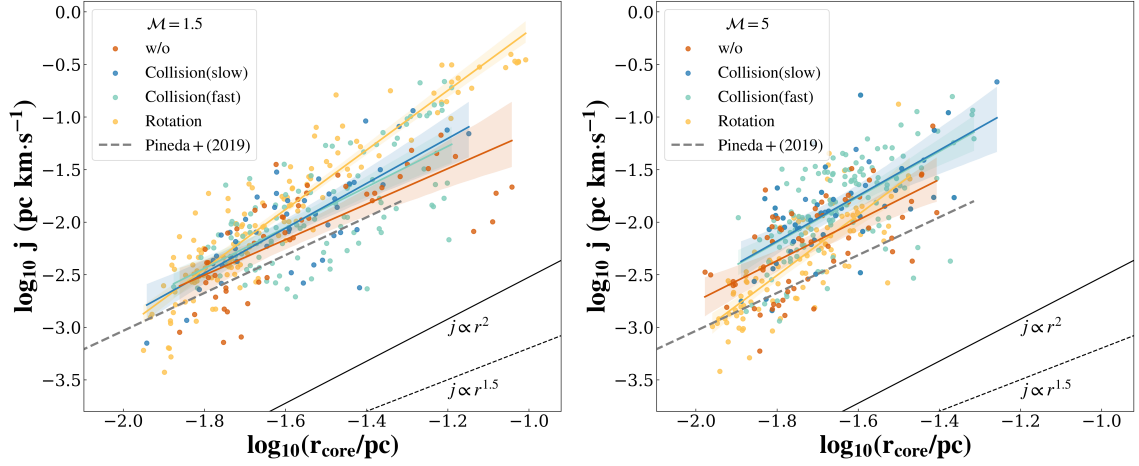


Figure 2.27: Specific angular momentum, $j \equiv L_{\text{core}}/M_{\text{core}}$, plotted against the core radius for all $\mathcal{M} = 1.5$ models (left) and $\mathcal{M} = 5$ (right) models, showing the best-fit power law relation with 95% confidence bands for each setup. The black solid and dashed lines are $j \propto r^2$ and $j \propto r^{1.5}$ respectively. For $\mathcal{M} = 1.5$, the slopes have fits of 2.83 (Rotation), 1.94 (collision (fast)), 2.13 (collision (fast)), and 1.69 (w/o). For $\mathcal{M} = 5$, the slopes have fits of 2.88 (Rotation), 2.16 (collision (fast)), 2.17 (collision (fast)), and 1.93 (w/o). When $\mathcal{M} = 1.5$, j and the best-fit slope in the Rotation Setup is relatively large. However, in $\mathcal{M} = 5$, although the slope is large, j in the rotation setup is not significantly different from the core in other setups. The gray dashed lines indicate the observed radial profile (Pineda et al., 2019).

lar cloud. More recently, Pandhi et al. (2023) found $j \propto r^{1.82 \pm 0.10}$ for cores in some star forming regions, suggesting that velocity gradients within cores originate from a combination of solid body rotation and turbulent motions.

Figure 2.27 shows the $j - r$ relation. In the Collision Setup, for both $\mathcal{M} = 1.5$ and 5, j is slightly higher than w/o Setup. This is due to the injection of turbulence during the collision, which increases the total kinetic energy of the core and, consequently, its specific angular momentum. However, the slope index does not differ much, and the fitting curves are within the confidence intervals of w/o Setup. On the other hand, in the Rotation Setup models for weak turbulence $\mathcal{M} = 1.5$, the $j - r$ relation is different from other setup models. Especially in larger cores, j takes relatively large values with smaller variations, resulting in a steeper slope. As discussed earlier, in the Rotation Setup models with $\mathcal{M} = 1.5$, the overall rotation of the clump is transferred to the core and significantly impacts its angular momentum. This process of rotation inheritance

may be reflected in the $j - r$ relation. For strong turbulence $\mathcal{M} = 5$, since the rotation of the clump is not transferred, there is no significant difference in the magnitude and variation of j compared to other models.

However, due to the large scatter from the fitting curve in the data points in Figure 2.27, we can not conclusively determine the extent of the significant difference among models in $j - r$ relation. Also, Misugi et al. (2023) showed that the $j - r$ slope changes depending on the evolutionary stage of the core. Further studies considering the evolutionary stages deserve.

2.4.6 Caveats

We identified cores for each simulation run and analyzed their properties when the most evolved core collapsed. We do not directly follow the evolution of each core. However, as shown in previous works (e.g., Kuznetsova et al., 2019; Misugi et al., 2023), time evolution of core properties such as angular momentum and magnetic fields, etc., are also important and debatable.

Our study focuses primarily on the early prestellar stage of bound cores, excluding the impact of stellar feedback. Although the protostellar core, where feedback is present, is outside the scope of this study, feedback is critical in determining the local core-to-star efficiency and driving turbulence across various scales within clumps (e.g., Cunningham et al., 2011). Feedback is expected to alter the physical core properties and the clump environment. Further research on the protostellar phase is valuable. Non-ideal MHD effects we neglect can also affect the properties of protostellar cores. We have mainly focused on gravitationally bound cores destined to form stars. However, unbound cores initially supported by magnetic fields can also eventually collapse, losing magnetic flux due to ambipolar diffusion. Investigating the fates of such magnetically supported cores considering non-ideal MHD effects is interesting.

Also, the range of parameters investigated in this study, such as clump mass, initial gas density, magnetic field strength, turbulence intensity, collision velocity, etc., is limited, which may introduce biases in our results. The number of cores identified is also limited. Therefore, the statistical trends observed in each model are not definitive.

Despite these limitations, our findings provide important insights into the physical properties of prestellar cores, i.e., the initial conditions for star formation.

2.5 Summary of this Chapter

We have investigated the properties of dense cores, including angular momentum \mathbf{L}_{core} and inner magnetic fields \mathbf{B}_{core} in the cluster-forming clump using isothermal MHD simulations with self-gravity. Three different setups were examined, including a single rotating clump (Rotation Setup), colliding clump (Collision Setup), and non-rotating/non-colliding clump (w/o Setup). Our main results are summarized as follows:

1. The transfer of the global angular momentum of the clump to each core

In the Rotation Setup, for $E_{\text{clump,rot}}/E_{\text{clump,tur}} > 1$ cases, \mathbf{L}_{core} inherit the rotation of parental clump. \mathbf{L}_{core} tends to align with the rotational axis of the clump. However, in $E_{\text{clump,rot}}/E_{\text{clump,tur}} \sim 1$ cases, there is no clear tendency for alignment. The turbulence intensity is an important parameter that determines whether or not the rotation of the parental clump is transferred to bound cores. On the other hand, in the Collision Setup and w/o Setup, \mathbf{L}_{core} does not show the trend of alignment irrespective of the collision speed, turbulence strength, and initial magnetic field properties. Only when a single clump is rotating and weakly turbulent, \mathbf{L}_{core} inherit the rotation of the parental clump.

2. The correlation between magnetic fields at the clump-scale and the core-scale

Generally, \mathbf{B}_{core} inherits the initial orientation of the clumps field, which leads to a tendency for \mathbf{B}_{core} to align parallel to the initial magnetic field \mathbf{B}_0 . The stronger the magnetic field, the less likely it is for the orientations of \mathbf{B}_{core} and \mathbf{B}_0 to deviate, resulting in a stronger tendency for them to align. Especially in the Collision setup, the magnetic field tends to bend globally along the shock-compressed layer, which is then inherited by the core, making \mathbf{B}_{core} , align with the shocked layer. The collision axis is crucial in determining the direction of \mathbf{B}_{core} .

3. Relative angle between the angular momentum of the core and core-scale magnetic field

Generally, \mathbf{B}_{core} and \mathbf{L}_{core} are not aligned, and distributions of $\angle[\mathbf{L}_{\text{core}}, \mathbf{B}_{\text{core}}]$ is random.

\mathbf{B}_{core} does not constrain the direction of \mathbf{L}_{core} . Since misalignment between a core's angular momentum and magnetic field may be critical in solving magnetic braking catastrophe, this result is important to understanding protostellar disk formation.

In addition, the following results are found.

- Analyses of the momentum of inertia within cores indicate that cores are more prolate than oblate. \mathbf{L}_{core} and \mathbf{B}_{core} are not necessarily perpendicular to major axes \mathbf{a}_1 or parallel to minor axes \mathbf{a}_3 contradicting the simple pictures. Especially, there is no correlation between \mathbf{L}_{core} and \mathbf{a}_3 except in Rotation Setup models with $\mathcal{M} = 1.5$.
- Regardless of the setups, the contribution of the core's rotational energy is small, accounting for $\sim 5\%$ of the gravitational energy. However, in the Rotation Setup, compared to other setups, the values of $E_{\text{rot}}/E_{\text{kin}}$ and $E_{\text{rot}}/E_{\text{grav}}$ are higher, and their variances are smaller for larger cores.
- In the Rotation Setup models for weak turbulence $\mathcal{M} = 1.5$, the $j - r$ relation is different from other models. Especially in larger cores, j takes relatively large values with smaller variations, resulting in a steeper slope. Clump rotation may be reflected in the $j - r$ relation of cores. A study with a larger number of samples that considers the time evolution of the core is desired.

Chapter 3

Collision between Prestellar Cores

3.1 Introduction of this Chapter

3.1.1 Collisions at Core-Scale

There have been increasing observational evidence that cloud-cloud collisions trigger star and star cluster formation in the Milky Way (e.g., [Loren, 1976](#); [Scoville et al., 1986](#); [Hasegawa et al., 1994](#); [Torii et al., 2011](#); [Kinoshita et al., 2021b](#)). Theoretical calculations have also demonstrated that cloud-cloud collisions can provide a viable mechanism for triggering star formation (e.g., [Tan, 2000](#)). High-velocity converging flows can produce dense gas clumps that tend to be gravitationally unstable and are the potential precursors to massive stars and star clusters. Observational evidence of triggered star formation by cloud-cloud collisions comes mainly from relatively giant molecular cloud-scale events that produce massive stars and clusters (see review by [Fukui et al., 2021](#)). Therefore, many numerical studies to date have been concerned with collisions between high mass clouds with supersonic speeds (e.g., [Inoue & Fukui, 2013](#); [Wu et al., 2015](#); [Takahira et al., 2018](#); [Abe et al., 2021](#); [Sakre et al., 2023](#)).

Meanwhile, as stated in § 1.5, collisions between smaller gas structures can also occur in regions with a dense distribution of cores. In Appendix C.1, we estimated the probability of collision between prestellar cores using identified cores for w/o Setup models discussed in Chapter 2. Although this is a rough estimate, the collision probability P_{col} is approximately 10 to 40%, suggesting that the interaction between cores is a

significant process that cannot be ignored. These collisions have profound implications on the physical state of prestellar cores, impacting the accretion rate, multiplicity, and CMF. Evaluating collisions of prestellar cores is thus essential.

Collisions between dense clumps or cores have been studied numerically for decades (e.g., [Chapman et al., 1992](#), [Whitworth et al., 1995](#); [Marinho & Lépine, 2000](#) [Marinho et al., 2001](#)). These studies have investigated the evolution of several orders of magnitude in density and protostellar fragmentation on small scales. In recent years, more precise numerical calculations have been performed. For instance, [Kitsionas & Whitworth \(2007\)](#) investigated the colliding gravitationally stable clumps ($\geq 10M_{\odot}$) using smoothed particle hydrodynamic (SPH) simulations. They showed that collisions produce shock-compressed layers that fragment into filaments depending on offset parameter b and core speed. [Arreaga-García & Klapp \(2015\)](#) presented 3D hydrodynamic simulations of two rotating-core ($8M_{\odot}$) collisions. In their simulation, high-density objects that could evolve into protostars were formed. Previous studies, primarily using hydrodynamic simulations, have demonstrated that core collisions have a significant impact on the star formation process.

3.1.2 Content of this Chapter

As described in § 1.3, observations have suggested that magnetic field significantly influences the dynamic evolution of cores. However, previous numerical studies on dense core collisions have not considered magnetic fields. In this Chapter, we consider the effect of magnetic fields on the prestellar core collision process. We perform a MHD simulation of collisions between $\sim 4M_{\odot}$ prestellar cores moving at speeds close to the sound speed, immersed in magnetic fields. The simulation ingredients include gas self-gravity and use the sink particle technique. The novelty of this work is to consider the effect of magnetic fields.

We will mainly examine the following two points.

1. The accretion rate of protostars (represented by sink particles)
2. Multiplicity (the number of sink particles)

The remainder of this Chapter is organized as follows. In Section 3.2.1, we describe the numerical, model, and analysis methods used. In Section 3.3, we present important

features of our simulation results. In Section 3.4, the results are discussed. Section 3.5 summarizes our main results.

3.2 Methods

3.2.1 Numerical Code

The numerical code is essentially the same as Chapter 2. Simulations were conducted using **Enzo**. The ideal MHD equations were solved using a Runge–Kutta second-order-based MUSCL solver, including Dedner MHD. The Riemann problem was solved using the Harten–Lax–van Leer (HLL) method, while the reconstruction method for the MUSCL solver was a piecewise linear model (PLM). We assumed a mean molecular weight of $\mu = 2.3$, and the adiabatic index was set to $\gamma = 1.00001$ for an approximate isothermal assumption.

Our simulation volume was ~ 0.6 pc sided cubic. The simulation had a top-level root grid of 256^3 with five additional levels of refinement, corresponding to a maximum resolution of $8,192^3$. We used the jeans criterion and adopted the limit in which the jeans length does not fall below eight cells: $\Delta x < \lambda_j/8$. Refinement was allowed until the finest resolution reached $\Delta x_{\min} = L_{\text{box}}/8,192 \simeq 6.7 \times 10^{-5}$ pc, where the local density reached $n_{\text{crit}} \simeq 3.2 \times 10^9 \text{ cm}^{-3}$. When the jeans length became unresolved, instead of creating another AMR level, we used the sink particle technique. When sink particles are formed, their density is assigned to the finest grids using a second-order cloud-in-cell interpolation technique (Hockney & Eastwood, 1988), and they move through the grid via gravitational interactions with the surrounding gas and other particles (see Bryan et al., 2014 for detail).

3.2.2 Initial Conditions

We considered the collision between two prestellar cores. For the initial core, we set a stable Bonnor–Ebert (BE) sphere (see Appendix A.1).

The BE sphere has a radius of $r_c = 0.1$ pc, the central density of $\rho_c = 10^5 \text{ cm}^{-3}$, and a sound speed $c_s \simeq 0.27 \text{ km s}^{-1}$, giving a dimensionless radius of $\xi \equiv (4\pi G \rho_c / c_s^2)^{1/2} r_c =$

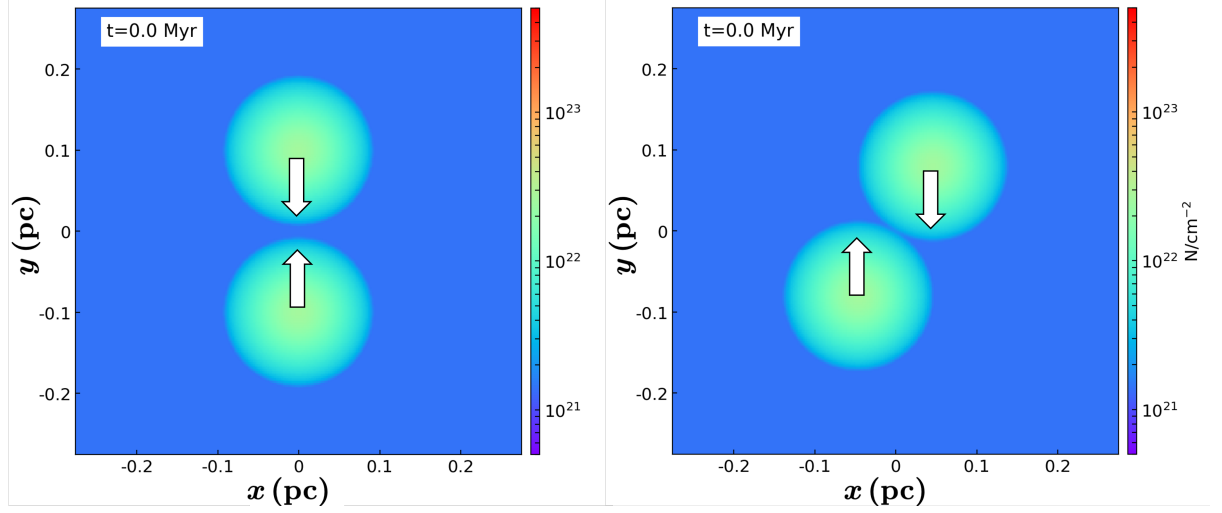


Figure 3.1: Initial conditions with the mass surface density shown. White arrows indicate the direction of each core’s motion. *Left panel*: Head-on collision ($b = 0$). *Right panel*: off-center collision ($b = 1$).

$6.0 < \xi_{\text{crit}}$ and mass of $M_c = 3.7 M_\odot$. The free-fall time of the center is $t_{\text{ff}} = (3\pi/[32G\rho_c])^{1/2} \simeq 0.1$ Myr. The density contrast between the cloud surface and ambient ISM gas was $\chi_c = 10$. The ambient medium was uniform and initialized to satisfy the pressure balance at the core boundary.

A summary of models is presented in Table 3.1. We considered both head-on and off-center collisions. Here, we defined the offset parameter b as the ratio of the impact parameter of the collision to r_c . Figure 3.1 shows the initial setup. For head-on collisions, they had no separations ($b = 0$) in the x direction, while for off-center collisions, the colliding cores were displaced by $b = 1$. For both cases, the two cores had pre-collision speeds v_c along the y -direction. We explored $v_c = 1.0 c_s$ and $v_c = 3.0 c_s$ cases corresponding to $\mathcal{M}_c \equiv v_c/c_s = 1$ and 3, respectively¹. Typically, the simulations were performed for $\sim 10 t_{\text{ff}} \simeq 1$ Myr. However, it will be terminated prematurely when the core material touches the boundary of the simulation box.

The simulation box is initialized with a uniform magnetic field directed at an angle θ relative to the collision axis of the cores². We considered the initial magnetic fields

¹Note that this definition of \mathcal{M}_c is different from \mathcal{M} in Chapter 2. \mathcal{M} means the Mach number of turbulence in Chapter 2, while in this Chapter, \mathcal{M}_c is a measure of the core’s velocity.

² θ represents the angle between the collision velocity and the collision axis, and its definition is different from θ_0 discussed in Chapter 2.

parallel to the y -direction ($\theta = 0^\circ$) and parallel to the z -direction ($\theta = 90^\circ$) to explore the effects of magnetic field orientations. For models with $b = 1$ and $\mathcal{M}_c = 1$, we additionally considered models with an angle $\theta = 45^\circ$.

We selected three magnetic field strengths: $B_0 = 10 \mu\text{G}$, $B_0 = 30 \mu\text{G}$, and $B_0 = 50 \mu\text{G}$, corresponding to the normalized mass-to-flux ratio $\mu_\Phi \equiv (M/\Phi)/(M/\Phi)_{\text{crit}} = 6.0$, 2.0, and 1.2, respectively. Such a parameter range is reasonable given that in the observational results (see § 1.3) and in the simulation results of Chapter 2 (see Appendix B.4). For $B_0 = 10 \mu\text{G}$ cases, the magnetic field has little effect, whereas for $B_0 = 50 \mu\text{G}$ cases, the magnetic energy is comparable to the gravitational energy of cores.

3.2.3 Analysis

3.2.3.1 Color Variable

To quantitatively follow the evolution of the core material, we solved the following additional advection equation (Xu & Stone, 1995) :

$$\frac{(\partial \rho C_i)}{\partial t} + \nabla \cdot (\rho C_i \mathbf{v}) = 0, \quad (3.1)$$

where C_i represents the set of two Lagrangian tracers. The subscript i denotes the two initial core materials: $i = 1$ and 2. In any zone, the density of the core material was $\rho_i = \rho C_i$. Initially, for one core, we defined $C_1 = 1$ and $C_2 = 0$, whereas for the other core, we defined $C_1 = 0$ and $C_2 = 1$. The ambient gas was labeled $C_1, C_2 = 0$. During the core-core collision, the core material is mixed with the ambient gas, resulting in regions with $0 < C_i < 1$. This analysis is essentially the same as that used in Kinoshita et al. (2021a). Mainly in § 3.4.3, we discuss the mixing of material using this color variable.

3.2.3.2 Derivation of Polarized Emissions

To visualize the influence of collisions on magnetic field structures, we derived the polarized emissions \mathbf{p} using a method in previous works (e.g., Chen et al., 2016; Wu et al., 2017).

Table 3.1. Explored parameter space

Model name ^a	b ^b (r_c)	\mathcal{M}_c ^c (degrees)	θ ^d (μG)	B_0 ^e	μ_Φ ^f	β ^g
b0-M1-By10	0	1.0	0	10	6.0	7.0
b0-M1-By30	0	1.0	0	30	2.0	0.8
b0-M1-By50	0	1.0	0	50	1.2	0.3
b0-M1-Bz10	0	1.0	90	10	6.0	7.0
b0-M1-Bz30	0	1.0	90	30	2.0	0.8
b0-M1-Bz50	0	1.0	90	50	1.2	0.3
b0-M3-By10	0	3.0	0	10	6.0	7.0
b0-M3-By30	0	3.0	0	30	2.0	0.8
b0-M3-By50	0	3.0	0	50	1.2	0.3
b0-M3-Bz10	0	3.0	90	10	6.0	7.0
b0-M3-Bz30	0	3.0	90	30	2.0	0.8
b0-M3-Bz50	0	3.0	90	50	1.2	0.3
b1-M1-By10	1	1.0	0	10	6.0	7.0
b1-M1-By30	1	1.0	0	30	2.0	0.8
b1-M1-By50	1	1.0	0	50	1.2	0.3
b1-M1-Bz10	1	1.0	90	10	6.0	7.0
b1-M1-Bz30	1	1.0	90	30	2.0	0.8
b1-M1-Bz50	1	1.0	90	50	1.2	0.3
b1-M1-Bob10	1	1.0	45	10	6.0	7.0
b1-M1-Bob30	1	1.0	45	30	2.0	0.8
b1-M1-Bob50	1	1.0	45	50	1.2	0.3
b1-M3-By10	1	3.0	0	10	6.0	7.0
b1-M3-By30	1	3.0	0	30	2.0	0.8
b1-M3-By50	1	3.0	0	50	1.2	0.3
b1-M3-Bz10	1	3.0	90	10	6.0	7.0
b1-M3-Bz30	1	3.0	90	30	2.0	0.8
b1-M3-Bz50	1	3.0	90	50	1.2	0.3

Note. — ^a Model names. ^b Impact parameter. ^c Mach number at which initial core moves. ^d Angle between the initial magnetic field and the collision axis. ^e Initial magnetic field strength. ^f Mass-to-flux ratio normalized to the critical value: $\mu_\Phi \equiv (M/\Phi)/(M/\Phi)_{\text{crit}}$. ^g Thermal-to-magnetic pressure ratio of the initial core surface: $\beta = 8\pi\rho_0 c_0^2/B^2$.

Using a Cartesian coordinate system, where the y -axis corresponds to the north, and the z -axis is parallel to the line of sight, the pseudo-vector \mathbf{p} is defined as

$$\mathbf{p} = (p \sin \chi) \hat{\mathbf{x}} + (p \cos \chi) \hat{\mathbf{y}}, \quad (3.2)$$

where p is the polarization fraction and χ is the polarization angle. We assumed a constant polarization fraction of $p = 0.1$. The χ is derived from Stokes parameters; the relative Stokes parameters were calculated as follows:

$$q = \int n \frac{B_y^2 - B_x^2}{B^2} ds \quad (3.3)$$

$$u = \int n \frac{2B_x B_y}{B^2} ds, \quad (3.4)$$

where B is the magnetic field and n is the number density. The inferred polarization angle on the plane of the sky is given by the four-quadrant inverse tangent

$$\chi = \frac{1}{2} \arctan 2(u, q). \quad (3.5)$$

The polarization angle χ was measured clockwise from north.

3.3 Results

We analyzed 27 simulation models listed in Table 3.1. Table 3.2 summarizes accretion rates and multiplicity (see also Figure 3.19). Section 3.3.1 shows the results of head-on collisions, whereas Section 3.3.2 shows the result of an off-center collision.

3.3.1 Head-On Collisions

In this Section, we present the results for the head-on ($b = 0$) collision models. In all $b = 0$ models, a single protostar (sink particle) was formed at the center of the compressed layer. In Section 3.3.1.1, we describe the general picture of the head-on collision using the evolution of the model **b0-M1-Bz10** as an example. In Section

3.3.1.2–3.3.1.4, we show how variations in the collision parameters affect the properties of protostars, i.e., accretion rate and multiplicity.

3.3.1.1 Head-On Collision Overview

Figure 3.2 displays the column density, velocity, and magnetic field distributions for the model b0-M1-Bz10. During the collision process, a compressed layer formed parallel to the x -axis at the interface between two cores. Gas motion at this front changed direction, aligning parallel to the x -axis, leading some gas toward the center. The central material continued to accrete into the center, forming a high-density point where a sink particle formed. Table 3.2 lists the core-to-sink efficiency (SFE) at 0.1 Myr after sink formation³. For the model b0-M1-Bz10, the end mass reached $5.1 M_{\odot}$, with a SFE of 70 %. Most of the core material accreted onto the central particle during collision.

The second row of Figure 3.2 shows the mass-weighted plane-of-sky magnetic field strength of the cloud material. White pseudovectors indicate the normalized magnetic polarization field, \mathbf{p} , calculated from Equations 3.2–3.5. A noticeable hourglass-shaped magnetic field with a stronger field is observed around the central region. As gas accreted, it pulled the magnetic field lines towards densely contracted regions, amplifying the field’s strength. At the edge of the compressed layer, some gas is accelerated outward along the x -direction. This acceleration is due to the pressure gradient between compressed gas via core collisions and the diffuse ambient gas around the core.

3.3.1.2 $\mathcal{M}_c = 1$ and $\theta = 0^\circ$

$\mathcal{M}_c = 1$ and $\theta = 0^\circ$ cases were explored in models b0-M1-By10, b0-M1-By30, and b0-M1-By50. Figure 3.3 depicts the temporal evolution of the mass accretion rate of sink particles. Comparing the three models indicated by green lines, the higher the B_0 , the lower the accretion rate. Models b0-M1-By10, b0-M1-By30, and b0-M1-By50 had SFEs of 67%, 61%, and 56%, respectively. Figure 3.4 shows the temporal evolution of maximum density. There is a mild retardation in the growth rate of density as B_0 rises.

³As in Kitsionas & Whitworth (2007), we assume, very crudely, that the Class 0 phase last about 0.1 Myr, after which the mass accretion rate drops sharply to negligible levels.

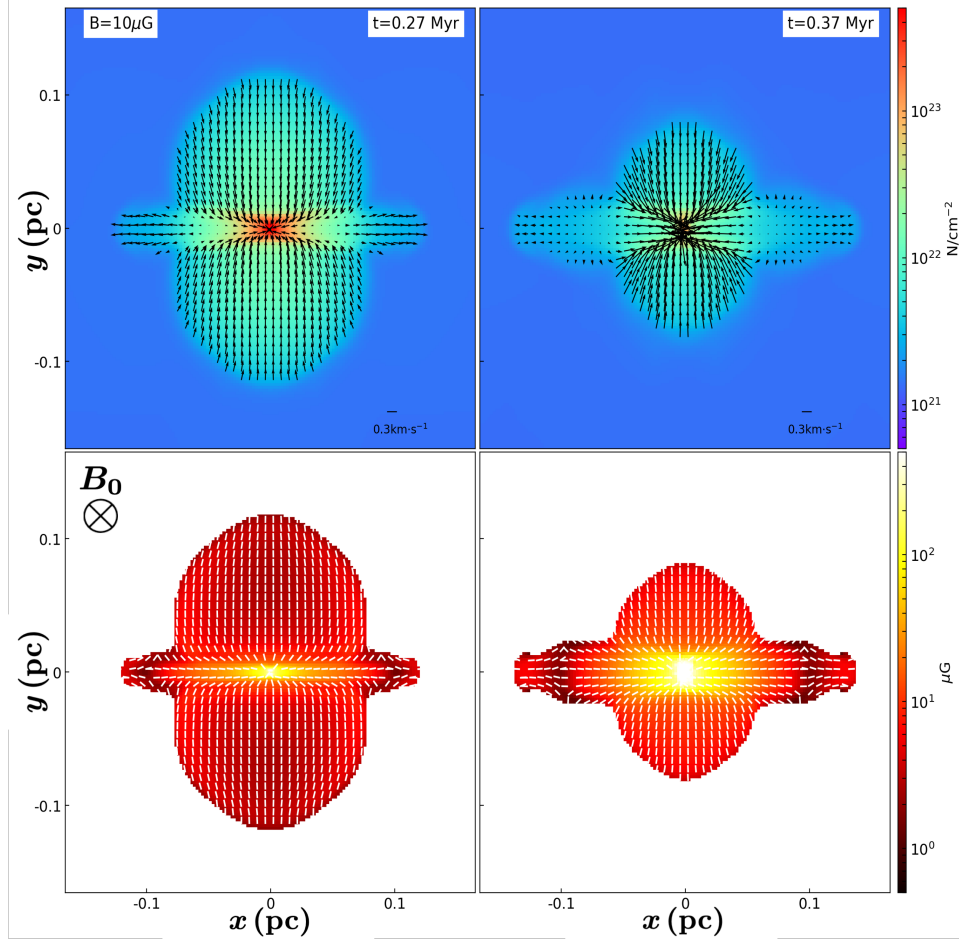


Figure 3.2: Column density, magnetic field, and velocity distributions of the model **b0-M1-Bz10**. *First row*: column density maps. The black vectors indicate the mass-weighted velocity field. Velocity arrows scale linearly with respect to the reference velocity shown in the bottom right of the panel and corresponding to $0.3 \text{ km} \cdot \text{s}^{-1}$. *Second row*: mass-weighted plane-of-sky magnetic field strength of cloud material are shown directly below their corresponding column-density maps. White pseudovectors indicate the normalized plane-of-sky magnetic polarization field, \mathbf{p} .

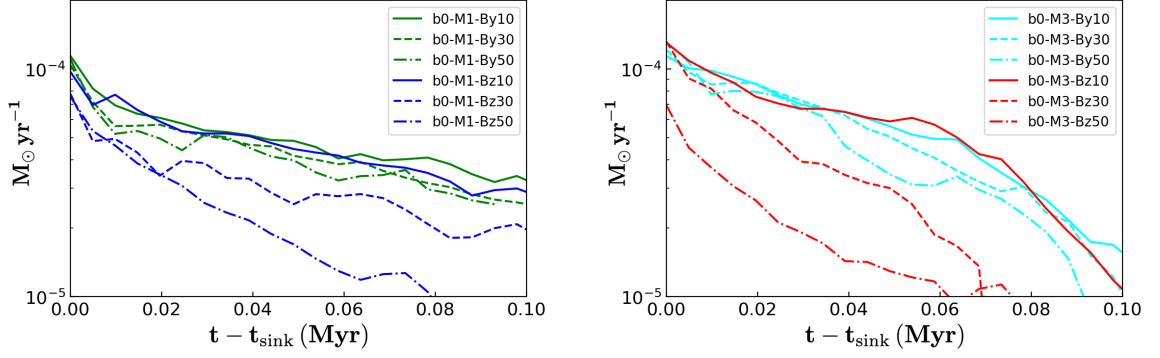


Figure 3.3: Temporal evolution of mass accretion rate of sink particles for head-on ($b = 0$) cases. *Left panel:* $\mathcal{M}_c = 1$ models. *Right panel:* $\mathcal{M}_c = 3$ models.

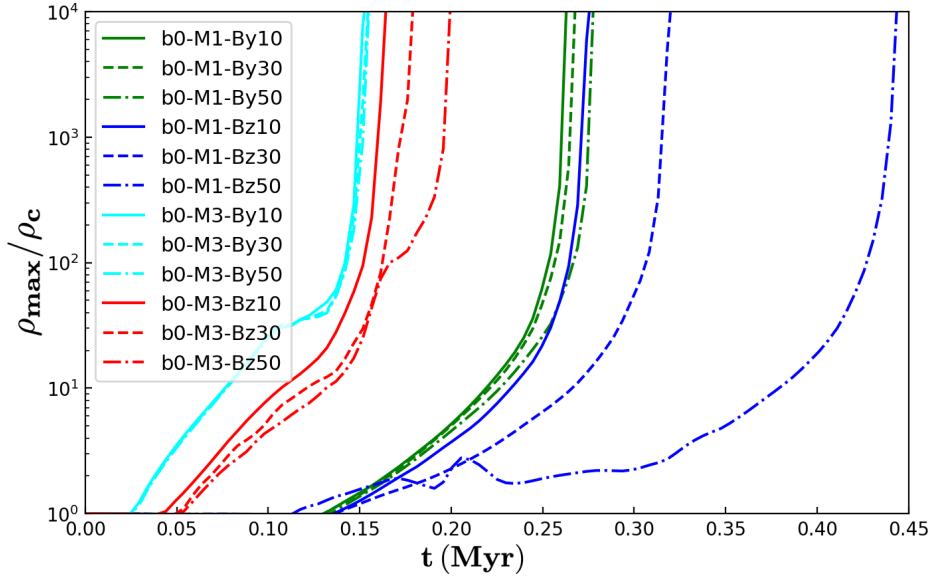


Figure 3.4: Temporal evolution of the maximum density normalized to the initial central core density for head-on ($b = 0$) cases.

3.3.1.3 $\mathcal{M}_c = 1$ and $\theta = 90^\circ$

The $\mathcal{M}_c = 1$ and $\theta = 90^\circ$ cases were explored in models b0-M1-Bz10, b0-M1-Bz30, and b0-M1-Bz50. Figure 3.3 implies that the higher the magnetic field strength, the lower the accretion rate. Differences in accretion rate among these three models (indicated by blue lines) were larger than those of $\theta = 0^\circ$ counterparts (indicated by green lines). In other words, when $\theta = 90^\circ$, the impact of differences in B_0 on the accretion rate is more substantial. However, when $\theta = 0^\circ$, the accretion rate's variation in response to B_0 is lower.

As illustrated in Figure 3.4, among the three models depicted with blue lines, an increase in magnetic field strength corresponds to a decrease in the density growth rate. Therefore, the sink formation time t_{sink} also became later in the stronger B_0 model (see Table 3.2). The component of the magnetic field perpendicular to the collision axis greatly influences the t_{sink} and accretion rates. A stronger magnetic field impedes accretion, delaying star formation.

3.3.1.4 $\mathcal{M}_c = 3$ and $\theta = 0^\circ$

Models b0-M3-By10, b0-M3-By30, and b0-M3-By50 explored the case of a faster pre-collision velocity $\mathcal{M}_c = 3$ and $\theta = 0^\circ$. As shown in Figure 3.4, the density increased more rapidly than $\mathcal{M}_c = 1$ models. This is because of the stronger compression over a short period. In addition, Table 3.2 shows that the mass accretion rates and SFEs were higher than their $\mathcal{M}_c = 1$ counterparts. While, for $\mathcal{M}_c = 3$ models b0-M3-By10, b0-M3-By30, and b0-M3-By50, SFEs were 85%, 80%, and 71%, respectively, for $\mathcal{M}_c = 1$ models b0-M1-By10, b0-M1-By30, and b0-M1-By50, SFEs were 67%, 61%, and 56%, respectively. The faster the collision speed, the quicker the star formation and the higher the accretion rate.

3.3.1.5 $\mathcal{M}_c = 3$ and $\theta = 90^\circ$

Models b0-M3-Bz10, b0-M3-Bz30, and b0-M3-Bz50 explored the case of $\mathcal{M}_c = 3$ and $\theta = 90^\circ$. Figure 3.4 shows that the density increased more rapidly than $\mathcal{M}_c = 1$ models. As in 3.3.1.4, the faster the collision speed, the quicker the star formation.

Figure 3.3 shows that the difference in accretion rate among these models (indicated by red lines) was larger than that of the $\theta = 0^\circ$ counterparts (indicated by cyan lines). For $\theta = 0^\circ$ models **b0-M3-By10**, **b0-M3-By30**, and **b0-M3-By50**, SFEs were 85%, 80%, and 71%, respectively. On the other hand, for $\theta = 90^\circ$ models **b0-M3-Bz10**, **b0-M3-Bz30**, and **b0-M3-Bz50**, SFEs were 85%, 54%, and 35%, respectively. That is, when $\theta = 90^\circ$, the impact of differences in B_0 on the accretion rate is higher than that of $\theta = 0^\circ$ counterparts.

3.3.2 Off-Center Collisions

In this Section, we present the results of the off-center ($b = 1$) collision models. As shown below, the multiplicity of protostars and accretion rates highly depend on the B_0 and θ .

3.3.2.1 $\mathcal{M}_c = 1$, and $\theta = 0^\circ$

Figure 3.5 shows snapshots of the $B_0 = 10 \mu G$ model **b1-M1-By10**. Initially, at $t \sim 0.21$ Myr, a compressed slab layer formed between the two cores. The gas and magnetic fields were bent parallel to the slab. The gas rotated clockwise because of the orbital angular momentum. By $t_{\text{sink}} = 0.31$ Myr, the compressed layer fragmented, and two sink particles were created; that is, binary forms. The separation between the particles was ~ 0.01 pc, and they were gravitationally bound. The gas was accreting onto the particles with an increasing specific angular momentum. The circumbinary disc developed, and the two protostars grew to $\sim 1 M_\odot$. The average mass accretion rates were $\sim 1.4 \times 10^{-5} M_\odot \text{ yr}^{-1}$ and the SFE was 38%.

In the $B_0 = 30 \mu G$ model **b1-M1-By30**, a single star is formed, rather than a binary system. Figure 3.6 presents snapshots of the model **b1-M1-By30**. Initially, a compressed layer was formed. Owing to the orbital angular momentum, clockwise rotational movement began. Subsequently, at $t = 0.36$ Myr, the compressed layer contracted gravitationally, and a single sink particle was formed. The gas was accreting onto the particles with an increasing specific angular momentum. At $t = 0.46$ Myr, a two-armed spiral developed. The average mass accretion rate was $2.4 \times 10^{-5} M_\odot \text{ yr}^{-1}$ and SFE was 33%.

In the $B_0 = 50 \mu G$ model **b1-M1-Bz50**, a single star formed with a two-armed spiral.

Table 3.2. Simulation results

Model name	$t_{\text{sink}}^{\text{a}}$ (Myr)	$\langle \dot{M} \rangle^{\text{b}}$ ($M_{\odot} \cdot \text{yr}^{-1}$)	M_{*}^{c} (M_{\odot})	SFE ^d (%)	Results
b0-M1-By10	0.26	5.3×10^{-5}	4.9	67	single star
b0-M1-By30	0.26	4.7×10^{-5}	4.4	61	single star
b0-M1-By50	0.27	4.4×10^{-5}	4.1	56	single star
b0-M1-Bz10	0.27	4.9×10^{-5}	5.1	70	single star
b0-M1-Bz30	0.32	3.3×10^{-5}	3.6	50	single star
b0-M1-Bz50	0.44	2.4×10^{-5}	2.5	34	single star
b0-M3-By10	0.15	6.0×10^{-5}	6.2	85	single star
b0-M3-By30	0.15	5.7×10^{-5}	5.8	80	single star
b0-M3-By50	0.15	5.1×10^{-5}	5.2	71	single star
b0-M3-Bz10	0.16	6.1×10^{-5}	6.2	85	single star
b0-M3-Bz30	0.18	3.7×10^{-5}	4.0	54	single star
b0-M3-Bz50	0.20	2.5×10^{-5}	2.5	35	single star
b1-M1-By10	0.31	1.4×10^{-5}	1.4	38	binary
	0.31	1.4×10^{-5}	1.4		
b1-M1-By30	0.36	2.5×10^{-5}	2.4	33	single star
b1-M1-By50	0.53	2.5×10^{-5}	2.4	33	single star
b1-M1-Bz10	0.30	1.4×10^{-5}	1.4	39	binary
	0.30	1.4×10^{-5}	1.4		
b1-M1-Bz30	0.40	1.7×10^{-5}	1.8	49	binary
	0.40	1.7×10^{-5}	1.8		
b1-M1-Bz50	—	—	0	0	merge
b1-M1-Bob10	0.30	1.3×10^{-5}	1.4	36	binary
	0.30	1.3×10^{-5}	1.4		
b1-M1-Bob30	0.46	1.7×10^{-5}	1.8	45	binary
	0.46	1.6×10^{-5}	1.8		
b1-M1-Bob50	—	—	0	0	merge
b1-M3-By10	—	—	0	0	destruction
b1-M3-By30	—	—	0	0	destruction
b1-M3-By50	—	—	0	0	destruction
b1-M3-Bz10	—	—	0	0	destruction
b1-M3-Bz30	—	—	0	0	destruction
b1-M3-Bz50	—	—	0	0	destruction

Note. — ^a Time interval from collision start until sink particles formed. ^b Mean mass accretion rate within 0.1 Myr after sink formation. ^c Sink particle mass 0.1 Myr after sink formation. ^d Core-to-sink efficiency 0.1 Myr after sink formation. See also Figure 3.19

The SFE and the structure formed was almost the same as that of the $B_0 = 30 \mu G$ counterpart **b1-M1-By30**.

3.3.2.2 $\mathcal{M}_c = 1$, and $\theta = 90^\circ$

For the $B_0 = 10 \mu G$ model **b1-M1-Bz10**, binary formed with a mean accretion rate of $\dot{M} = 1.4 \times 10^{-5} M_\odot \text{ yr}^{-1}$ and SFE of 39%. Figure 3.7 shows the snapshots. The separation between the particles was ~ 0.04 pc and wider than that of the $\theta = 0^\circ$ counterpart **b1-M1-By10**.

For the $B_0 = 30 \mu G$ model **b1-M1-Bz30**, the multiplicity differed from that of the $\theta = 0^\circ$ counterpart (**b1-M1-By30**). In the model **b1-M1-Bz30**, a binary system formed rather than a single star as shown in Figure 3.8. Figure 3.9 shows the evolution of the accretion rates. Most of the time, the accretion rate was higher than that of $B_0 = 10 \mu G$ counterpart **b1-M1-Bz10**. For the model **b1-M1-Bz30**, SFE was 49%, whereas for the model **b1-M1-Bz10**, SFE was 39%.

Figure 3.10 shows snapshots of the $B_0 = 50 \mu G$ model **b1-M1-Bz50**. The density increased in the compressed layer at approximately $t = 0.21$ Myr. However, unlike the $B_0 = 10 \mu G$ and $30 \mu G$ counterparts **b1-M1-Bz10** and **b1-M1-Bz30**, no structures dense enough for the formation of sink particles were observed (see also Figure 3.11). Two cores exhibited the rotational motion and eventually coalesced into a singular longitudinal structure. Tracking the evolution up to approximately $t \sim 1.0$ Myr ($\simeq 10t_{\text{ff}}$), no structures with sufficient density for gravitational collapse were identified.

3.3.2.3 $\mathcal{M}_c = 1$, and $\theta = 45^\circ$

In models where $\mathcal{M}_c = 1$, and $\theta = 45^\circ$, the results are similar to those of models where $\mathcal{M}_c = 1$, and $\theta = 90^\circ$ with respect to the multiplicity. For the $B_0 = 10 \mu G$ model **b1-M1-Bob10**, the binary formed with mean accretion rates of $\dot{M} = 1.3 \times 10^{-5} M_\odot \text{ yr}^{-1}$ and SFE of 36%. This accretion rate is almost the same as that of **b1-M1-By10** and **b1-M1-Bz10**. For the $B_0 = 30 \mu G$ model **b1-M1-Bob30**, a binary system formed with a mean accretion rate of $\dot{M} = 1.7 \times 10^{-5} M_\odot \text{ yr}^{-1}$ and SFE of 45%. For the $B_0 = 50 \mu G$ model **b1-M1-Bob50**, similar to the $\theta = 90^\circ$ counterpart **b1-M1-Bz50**, star formation was not triggered. The two cores merged gradually without collapse.

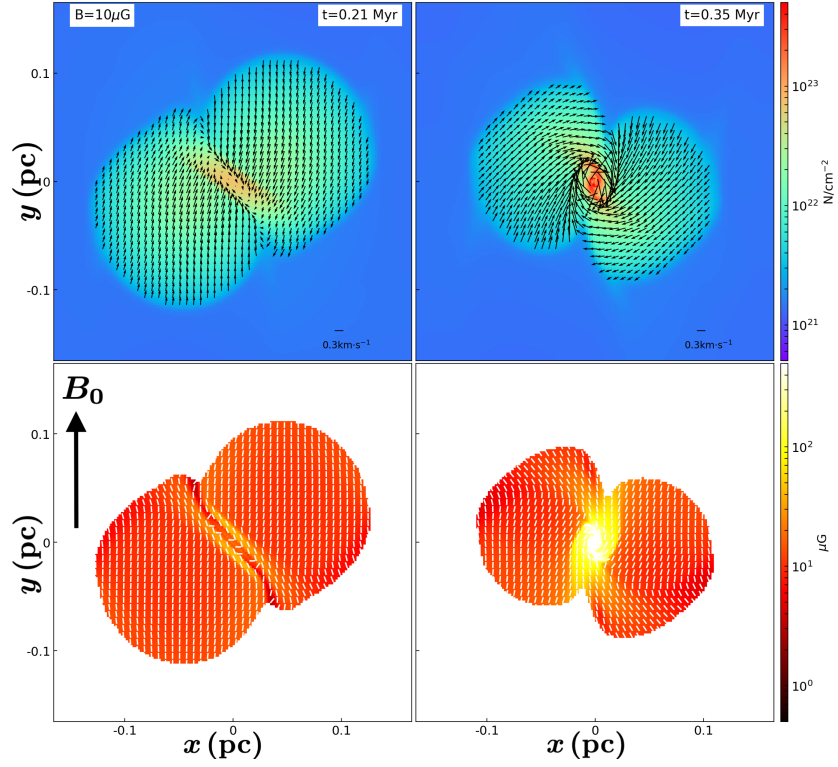


Figure 3.5: As in Figure 3.2 except for the model b1-M1-By10. Snapshots at 0.21, 0.3, and 0.4 Myr are shown. Binary systems are formed with the separation of ~ 0.01 pc.

3.3.2.4 $\mathcal{M}_c = 3$

In all $b = 1$ and $\mathcal{M}_c = 3$ models, star formation was not triggered. As an example, Figure 3.12 shows the temporal evolution of model b1-M3-Bz10. For this collision, no significant shock-compressed layer was formed, and the two cores passed each other. As the cores progressed, the Kelvin-Helmholtz (K-H) instability between the cores and the ambient gas was excited, leading to the ablation of the cores (Murray & Lin, 2004). At $t \sim 0.5$ Myr, the two cores touched the boundary of the simulation box and were mixed with the ambient gas. No significant shock-compressed layer was formed, and star formation was not triggered during the collision process. These results are consistent with those of Kitsionas & Whitworth (2007), who investigated clump collisions using hydrodynamic simulations. Kitsionas & Whitworth (2007) showed that large- b and high- \mathcal{M}_c collisions reduced clump collisions, and no shock-compressed layer was formed.

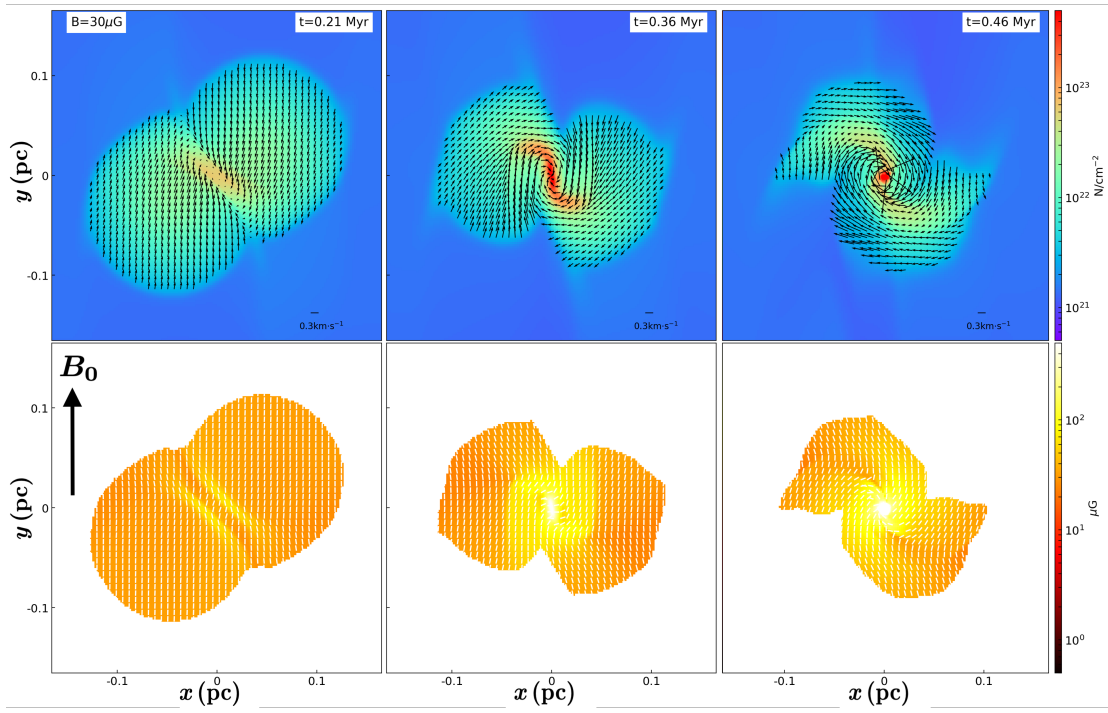


Figure 3.6: As in Figure 3.2 except for the model b1-M1-By30. Snapshots at 0.21, 0.36, and 0.46 Myr are shown. A single star is formed in the central region.

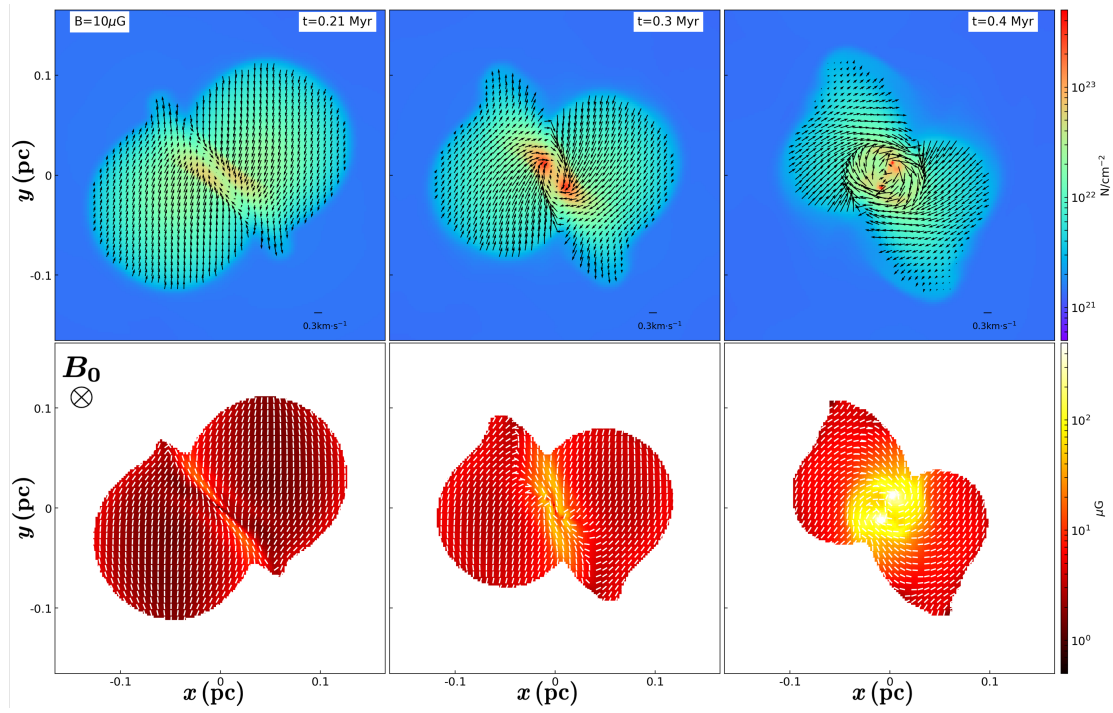


Figure 3.7: As in Figure 3.2 for the model b1-M1-Bz10. Snapshots at 0.21, 0.3, and 0.4 Myr are shown. Binary systems are formed with the separation of ~ 0.04 pc.

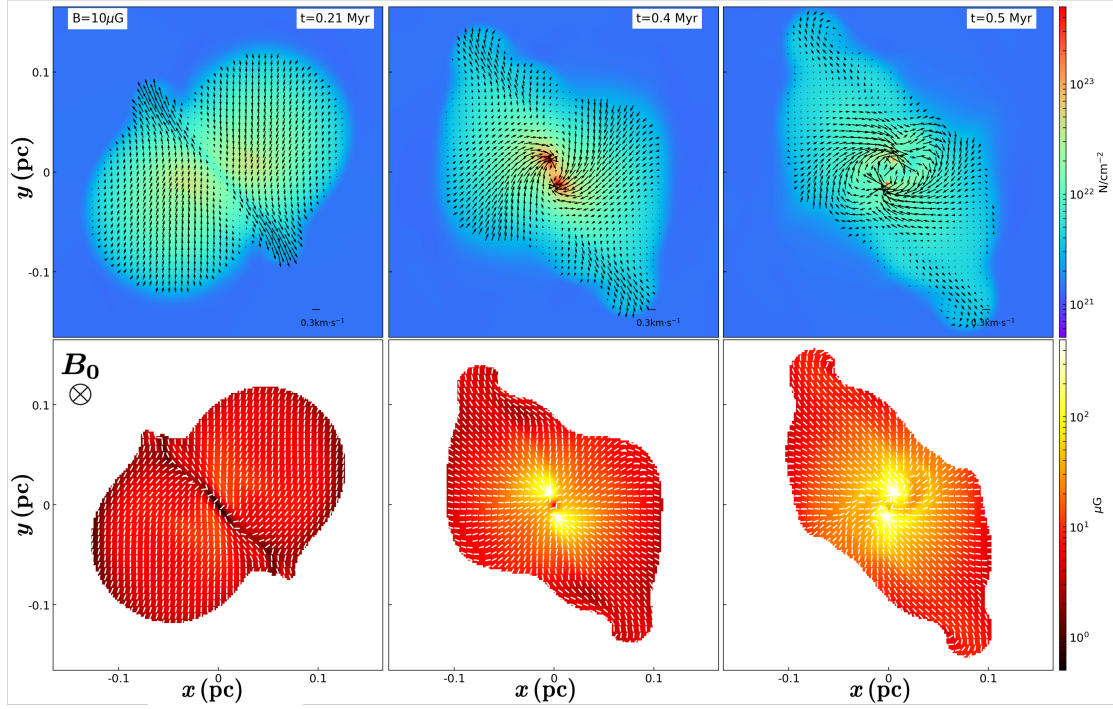


Figure 3.8: As in Figure 3.2 except for the model b1-M1-Bz30. Snapshots at 0.21, 0.4, and 0.5 Myr are shown. Binary systems are formed with the separation of ~ 0.04 pc.

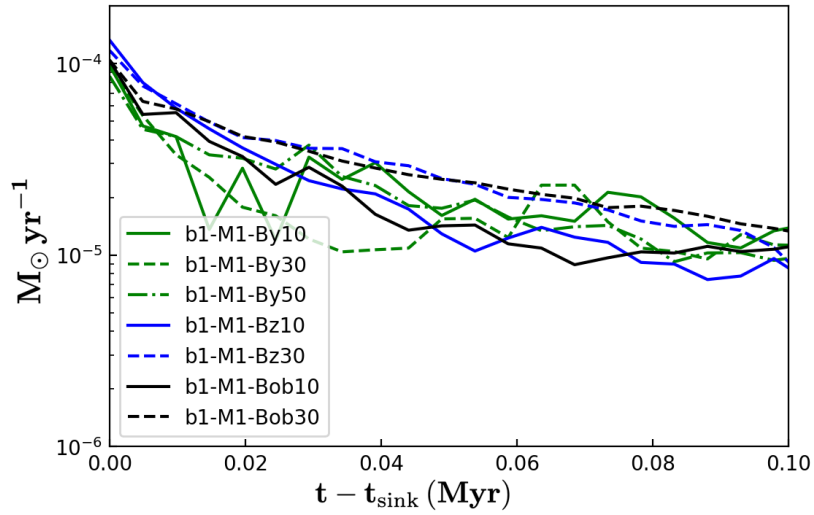


Figure 3.9: Temporal evolution of the mass accretion rate of sink particles for off-center ($b = 1$) cases. In cases where the binary is formed, the total accretion rates of two sinks are shown.

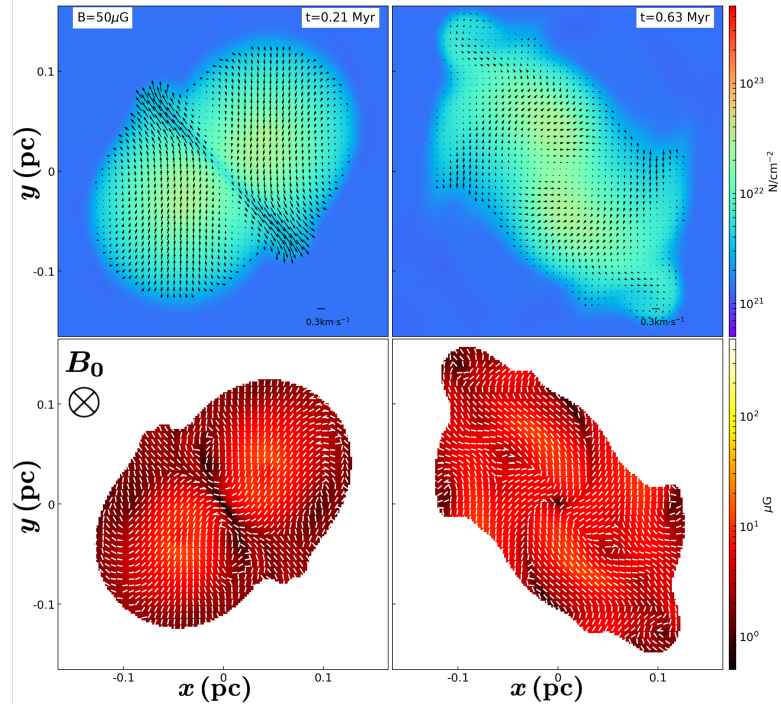


Figure 3.10: As in Figure 3.2 for the model b1-M1-Bz50. Snapshots at 0.21 and 0.63 Myr are shown. No structures with sufficient density for gravitational collapse were identified.

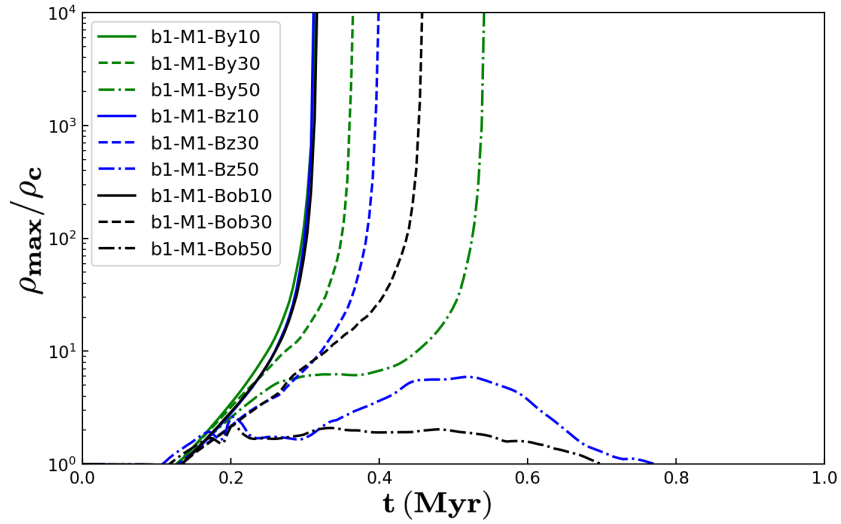


Figure 3.11: As in Figure 3.4 except for off-center ($b = 1$) cases.

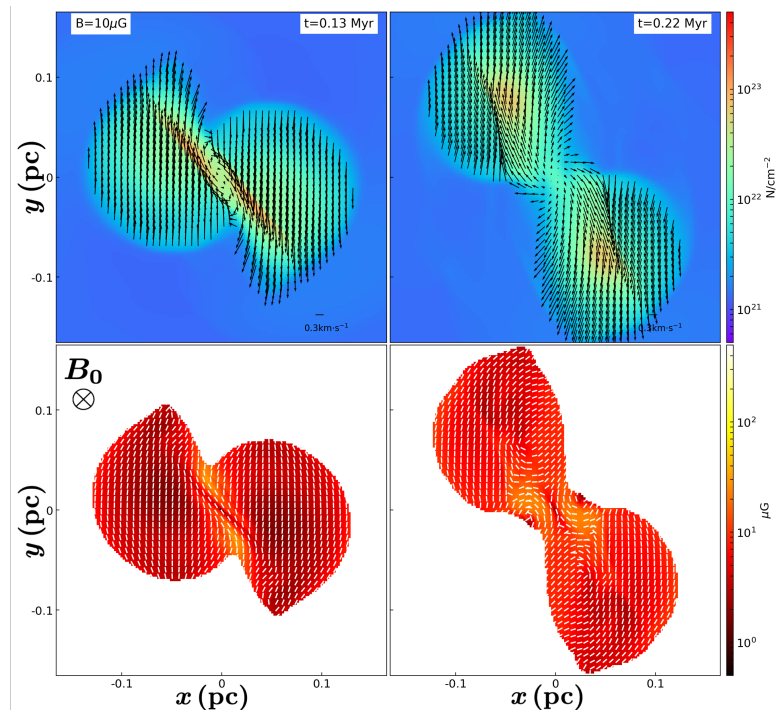


Figure 3.12: As in Figure 3.2 except for the model b1-M3-Bz10. Snapshots at 0.13 and 0.22 Myr are shown. Cores passed each other without contracting gravitationally.

3.4 Discussion

We performed a set of MHD simulations to follow the dense core collision process and the role of magnetic fields. As shown in Section 3.3, there is some dependence of the accretion rate and multiplicity on the magnetic field parameter. In this Section, we discuss the role of the magnetic field. Section 3.4.1 covers head-on collision cases, and Section 3.4.2 covers off-center cases. In Section 3.4.3, we supplementarily discuss gas mixing.

3.4.1 Discussion of Head-On Collision

As shown in § 3.3.1.3, for $\mathcal{M}_c = 1$ and $\theta = 90^\circ$ models, two primary trends were observed as B_0 increased. First, the density growth rate decreased, leading to a delayed sink particle formation time t_{sink} . Second, the accretion rate on the protostar decreased, resulting in a reduced protostar mass. From these results, we can conclude that the magnetic field perpendicular to the collision axis hinders the formation of high-density regions and reduces accretion. On the other hand, for the $\mathcal{M}_c = 1$ and $\theta = 0^\circ$ models, the dependence of the accretion rate on the field strength B_0 was lower (see § 3.3.1.2).

As magnetic pressure acts in directions perpendicular to the field lines, models in which B_0 were parallel to the pre-collision velocity ($\theta = 0^\circ$) resulted in less inhibited flow and higher accretion rates. On the other hand, for cases where the B_0 were perpendicular to the pre-collision velocity ($\theta = 90^\circ$), the magnetic pressure effectively prevents gas flow. Therefore, in $\theta = 90^\circ$ models, the higher B_0 is, the lower the accretion rate conspicuously. These differences between models with $\theta = 0^\circ$ and $\theta = 90^\circ$ are also consistently seen in models with $\mathcal{M}_c = 3$. Even in a simple process, such as a head-on collision, the accretion rate on the protostar strongly depends on the direction of the magnetic field. The initial direction of the magnetic field is crucial for the accretion rate and the end mass of protostars.

We will make these arguments a bit more quantitative, taking the models with $\mathcal{M}_c = 3$ as examples. Fast isothermal MHD shock waves were induced in $\mathcal{M}_c = 3$ models. For $\theta = 90^\circ$ models in which B_0 is parallel to the shock plane, the compression ratio of this fast shock can be estimated by the following shock jump condition (see Appendix A.40):

$$\frac{\rho_2}{\rho_1} = \frac{v_1}{v_2} = - \left\{ \frac{1}{2} + \left(\frac{c_s}{c_{A,1}} \right)^2 \right\} + \left[\left\{ \frac{1}{2} + \left(\frac{c_s}{c_{A,1}} \right)^2 \right\}^2 + 2 \left(\frac{v_1}{c_{A,1}} \right)^2 \right]^{1/2}, \quad (3.6)$$

where $c_{A,1} = B_1 / \sqrt{4\pi\rho_1}$.

The pre-shock velocity in the shock frame v_1 is equivalent to the shock velocity in the upstream rest frame. The relation between the core speed v_c and the post-shock velocity in the shock frame v_2 is given by

$$v_1 = v_c + v_2. \quad (3.7)$$

Therefore, we can write

$$\frac{\rho_2}{\rho_1} = \frac{v_1}{v_2} = \frac{v_1}{v_1 - v_c}. \quad (3.8)$$

Combining the right-hand sides of Equations 3.6 and 3.8, we can find the compression ratio ρ_2/ρ_1 . Additionally, we assume that the collapsing time of the post-shock layer is proportional to the freefall time $t_{\text{ff}} \propto \rho_2^{-1/2} \sim t_{\text{sink}}$. If we plug $B_1 = B_0$, $\rho_1 = \rho_c$ and $v_c = 3c_s$, for $B_0 = 10, 30$ and $50 \mu G$ models (**b0-M1-Bz10**, **b0-M1-Bz30** and **b0-M1-Bz50**), t_{ff} comparison among these three models is roughly $t_{\text{ff},10\mu G} : t_{\text{ff},30\mu G} : t_{\text{ff},50\mu G} = 0.7 : 0.9 : 1.0$. Assuming accretion rate $\dot{M} \propto t_{\text{ff}}^{-1}$, the ratio of \dot{M} among the three models is $\dot{M}_{10\mu G} : \dot{M}_{30\mu G} : \dot{M}_{50\mu G} = 1.4 : 1.2 : 1.0$. Using $\rho_1 = \rho_0$, we obtain $t_{\text{ff},10\mu G} : t_{\text{ff},30\mu G} : t_{\text{ff},50\mu G} = 0.6 : 0.9 : 1.0$ and $\dot{M}_{10\mu G} : \dot{M}_{30\mu G} : \dot{M}_{50\mu G} = 1.7 : 1.2 : 1.0$. Either way, as B_0 increases, \dot{M} decreases significantly, and when substituting $\rho_1 = \rho_0$, $\dot{M}_{50\mu G}$ becomes about half of $\dot{M}_{10\mu G}$. These estimates of a decrease in accretion rate are roughly consistent with our results shown in § 3.3.1.3.

On the other hand, for models with $\theta = 0^\circ$ in which B_0 is perpendicular to the shock plane, the shock jump condition becomes almost the same as for a purely hydrodynamical shock ($\rho_2/\rho_1 \propto (v_1/c_s)^2$), and the magnetic field plays no role in determining the shock properties.

Though the fast shock is not induced in $\mathcal{M}_c = 1$ models ($v_1 < (c_{A,1}^2 + c_s^2)^{1/2}$), dependence of t_{sink} and \dot{M} on B_0 can also be explained by the compression degree of the

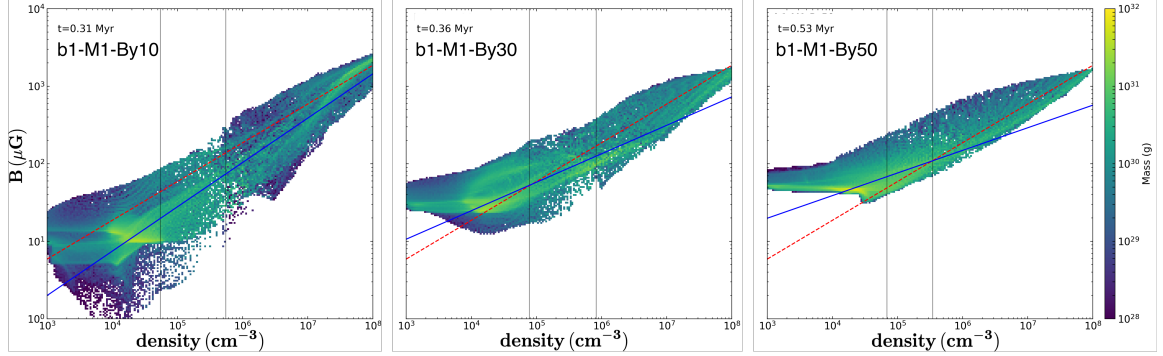


Figure 3.13: Phase plot of the magnetic field strength and gas density for models **b1-M1-By10**, **b1-M1-By30**, and **b1-M1-By50** at t_{sink} for each model. The color bar displays the total gas mass at each point. Two black lines show that the total mass of the gas located to the right of these lines accounted for 50% and 25% of the total mass of the two cores. The red dashed line represents the Alfvén speed, $v_A = c_s$. Blue lines are the results of least-square fits with a power-law $B \propto n^j$. The derived j for the models **b1-M1-By10**, **b1-M1-By30**, and **b1-M1-By50** are 0.57, 0.37, and 0.29 respectively.

central layer. While in $\theta = 0^\circ$ models, the magnetic field plays no role in determining the compression degree, in $\theta = 90^\circ$ models, higher B_0 decreases the growth of density within the compression layer leading to the longer t_{sink} and lower \dot{M} .

3.4.2 Discussion of Off-Center Collision

3.4.2.1 Effect of the Initial Magnetic Field Strength

As shown in § 3.3.2.1, for the $\mathcal{M}_c = 1$ and $\theta = 0^\circ$ models, the multiplicity of protostars depended on the magnetic field strength B_0 . The binary system formed for the $B_0 = 10\mu G$ model **b1-M1-By10**. On the other hand, a single sink particle formed for $B_0 = 30\mu G$ and $B_0 = 50\mu G$ counterparts **b1-M1-By30** and **b1-M1-By50**. The magnetic field strength significantly affects the multiplicity of protostars in the collision process.

To assess the magnetic field effect, we investigated the density-field relation. Figure 3.13 shows the magnetic field and density relationship for the **b1-M1-By10**, **b1-M1-By30**, and **b1-M1-By50** models at $t = t_{\text{sink}}$. We also drew constant Alfvén velocities of $1.0 c_s$ (red dashed line) for comparison with the sound speed and pre-collision velocity

($v_c = 1.0 c_s$). We fit the $B - n$ relation with the power law $B \propto n^j$. The blue lines indicate the results of the least-squares fit. The power-law index of the $B - n$ relation can be used to verify the dynamic importance of a magnetic field (see Appendix A.5). The left-hand panel of Figure 3.13 shows the results for the $B_0 = 10\mu G$ model **b1-M1-By10**. The alfvén speed of most gases in the core was less than the sound speed (pre-collision speed). Therefore, the magnetic fields have a minor effect on the gas motion within the core. Gas mass generally exhibits a positive correlation between B and n . The derived power-law index was 0.57. The middle and right panels show the results of the $B_0 = 30\mu G$ and $B_0 = 50\mu G$ models **b1-M1-By30** and **b1-M1-By50**, respectively. The estimated power-law indices were 0.37 and 0.12, respectively. For these models, the Alfvén speed of the gas in the core was comparable to the sound speed. Hence, the magnetic fields have a crucial effect on gas motion in cores. The power-law index also demonstrates the major dynamic importance of the magnetic field.

For **b1-M1-By30** and **b1-M1-By50**, unlike the weak magnetic model **b1-M1-By10**, only one star formed. This can be explained from the perspective of magnetic Jeans mass (e.g., Krumholz & Federrath, 2019):

$$M_{J,\text{mag}} = M_J(1 + \beta^{-1})^{3/2}, \quad (3.9)$$

where M_J and β are the purely thermal Jeans mass and the plasma β , respectively. As shown in Figure 3.13, for **b1-M1-By30** and **b1-M1-By50** models, Alfvén speeds of the gas were an order of magnitude higher than those of model **b1-M1-By10**. These higher Alfvén speeds mean higher β and magnetic Jeans mass; therefore, the compressed layer did not fragment into the binary like the model **b1-M1-By10**. Magnetic fields within cores restrict gas fragmentation, and their strength determines the multiplicity.

3.4.2.2 Effect of Initial Magnetic Field Orientation

For off-center collisions, owing to angular momentum, the direction of the magnetic field became complicated, and the gas flow was significantly affected. Figure 3.14 shows the simulation results in the B_0 vs. θ plane for the models with $b = 1$ and $\mathcal{M}_c = 1$. For the $\theta = 0^\circ$ or $B_0 < 50 \mu G$ cases, sink particles formed, whereas when the magnetic field was $B_0 = 50 \mu G$ and $\theta \geq 45^\circ$, star formation was not induced, and the cores merged.

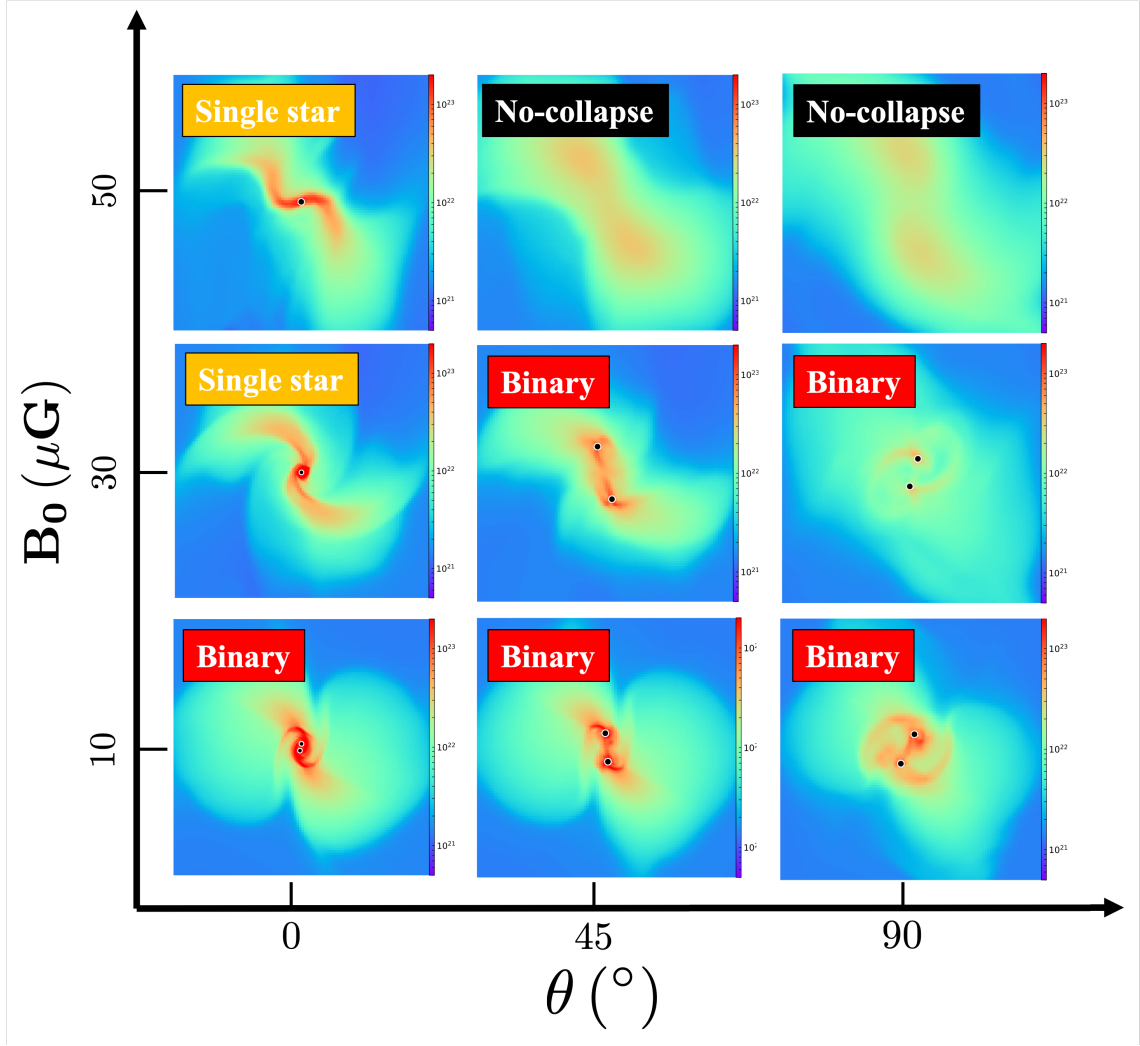


Figure 3.14: Simulation results in the B_0 vs. θ plane for models with $b = 1$ and $\mathcal{M}_c = 1$. In models where sink particles are formed, the column density at $t = t_{\text{sink}} + 0.1\text{Myr}$ is shown, while models without sink particles show the states at $t \sim 1\text{Myr}$. The black points show the sink particles.

In other words, when the magnetic field component perpendicular to the collision axis is stronger, star formation is not induced. The initial magnetic field orientation is important in the collision and star formation.

For the $\theta = 0^\circ$ model, the magnetic field was parallel to the xy plane. As shown in Figure 3.6, the magnetic field was bent parallel to the compressed layer. The magnetic pressure does not work parallel to the magnetic field. Hence, the dense gas in the compressed layer flowed into the center region along the direction of the magnetic field unimpeded by the magnetic pressure. A single star formed in the central region for models **b1-M1-By30** and **b1-M1-By50**.

In contrast, for $\theta = 45^\circ$ and $\theta = 90^\circ$ models, the initial magnetic field was nearly perpendicular to the collision axis. As shown in Figure 3.8, for the model **b1-M1-Bz30**, the gas flow along the compressed layer was more restricted than that in the $\theta = 0^\circ$ counterpart. A large amount of gas did not accumulate in the center region and formed binary gradually. For the $B_0 = 50 \mu G$ model **b1-M1-Bz50**, the gas did not accumulate (see Figure 3.10), and the magnetic Jeans mass was higher. Therefore, star formation was not triggered. These trends are true for $\theta = 45^\circ$ counterparts.

To quantitatively investigate how the direction of the B-field correlated with gas motion, we quantified the degree of alignment of the magnetic field with respect to the gas velocity pixel-by-pixel. Figure 3.15 shows a histogram of the relative angle between the magnetic field B and velocity of dense gas ($> 10^5 \text{ cm}^{-3}$) pixel-by-pixel in models **b1-M1-By50**, **b1-M1-Bz50**, and **b1-M1-Bob50**. Histograms peaking at $\phi = 0^\circ$ indicate that B-fields were preferentially aligned parallel to the gas flow, whereas peaks at $\phi = 90^\circ$ indicate preferentially perpendicular alignment. We show the histograms at 0.21, 0.36, and 0.64 Myr. Throughout the simulation time, the gas flow in the $\theta = 0^\circ$ model **b1-M1-By50** was preferentially aligned parallel to the magnetic field. Therefore, gas movement was relatively unimpeded by the magnetic pressure, and gas tended to accumulate quickly, leading to protostar formation. In contrast, the gas flow in the $\theta = 90^\circ$ model **b1-M1-Bz50** was firmly perpendicular to the B-fields. Hence, magnetic pressure inhibited gas flow, and higher-density gas did not easily yield. In the $\theta = 45^\circ$ model **b1-M1-Bob50**, the histogram initially peaked between 0° and 90° , but eventually peaked at approximately 90° ; therefore, the magnetic field pressure acts in directions parallel to the gas flow and hinders dense gas formation. A strong magnetic field perpendicular to the collision axis inhibits gas flow and suppresses star formation.

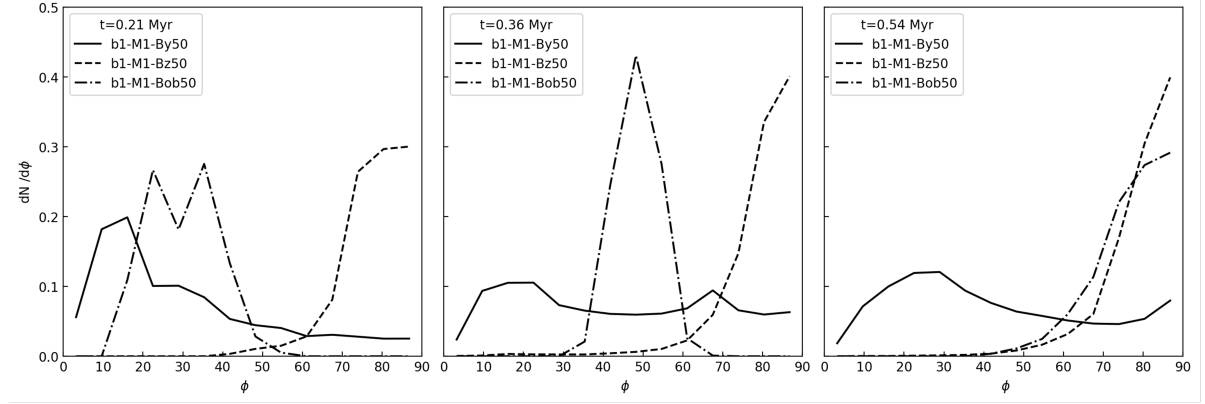


Figure 3.15: Histogram of the relative angle between the magnetic field B and the velocity of dense gas ($> 10^5 \text{ cm}^{-3}$) pixel-by-pixel in models **b1-M1-By50**, **b1-M1-Bz50**, and **b1-M1-Bob50**. Histograms at 0.21, 0.36, and 0.64 Myr are shown. Histograms with peaks at 90° correspond to B predominantly perpendicular to the dense gas flow.

3.4.3 Mixing of Gas

In some models, star formation is triggered by dense core collisions. However, sometime after protostar formation, the two cores did not retain their original shapes. In actual observation, it would be difficult to distinguish whether star formation is caused by core collision or contraction of a single core based only on the characteristics of the density distribution.

Currently, it is well known that the chemical compositions of low-mass protostellar cores show significant diversity (Sakai & Yamamoto, 2013). If pre-collision cores have different chemical compositions, we might observe the relics of the collision observationally, even after star formation. The left panel in Figure 3.16 shows the ratio of integration in the line of sight, represented by:

$$\text{integrated mixing rate} = \frac{\int_{C_1+C_2>0.5} \rho C_1 dx}{\int_{C_1+C_2>0.5} \rho (C_1 + C_2) dx}, \quad (3.10)$$

for model **b1-M1-By30** at $t = 0.45 \text{ Myr}$. This integration is a barometer of how much gas from each core is mixed (see section 3.2.3.1); values close to 0 indicate a large amount of gas originating from one core, while a value close to 1 indicates a large amount originating from the other core; values around 0.5 means that the two are equally mixed. At the collision interface, the two gases mixed well, whereas, in

spiral arm structures, the contribution of one gas was more significant. The arms and discs around the protostar had almost the same gas composition as in the initial state. The right panel of Figure 3.16 shows the time evolution of gas mass fraction. As the collision proceeded, the fraction of mixed gas increased; however, for approximately 0.1 Myr after particle formation, the gas mass with $C_1 > 0.9$ or $C_2 > 0.9$ was large. Thus, if we observe a notable abundance anomaly in the molecular envelope surrounding a star, it could suggest that the system was formed by the collision process of the two cores with different abundances.

To investigate the gas mixing process further, we examined additional models of the collision of unequal mass cores. In these models, we initially prepared two stable BE spheres at a mass ratio of 4:1. The first was the same condition as the previous models, with a radius of $r_{c1} = 0.1$ pc, central density of $\rho_{c1} = 10^5 \text{ cm}^{-3}$, temperature of $T_{c1} = 20$ K, and mass of $M_{c1} = 3.7 M_\odot$. The other was smaller with a radius of $r_{c2} = 0.05$ pc, central density of $\rho_{c2} = 2.0 \times 10^5 \text{ cm}^{-3}$, temperature of $T_{c2} = 10$ K, and mass of $M_{c2} = 1.9 M_\odot$. The gas components initially contained in the smaller and larger cores are labeled with color variables $(C_1, C_2) = (1, 0)$ and $(0, 1)$, respectively. By contrast, the ambient gas is labeled $(C_1, C_2) = (0, 0)$. For both cores, the pressure balance at the core boundary was satisfied. The cores had a pre-collision velocity of $v_c = 0.19 \text{ km s}^{-1}$, which corresponds to the sound speed in the smaller core with the impact parameter $b = r_{c2}$. Initially, we imposed a uniform magnetic field $B_y = 10 \mu\text{G}$, parallel to the collision direction. Figure 3.17 shows snapshots of the collision. Figure 3.18 shows the evolution of the mass and mass accretion rates of the sink particle. The contribution from each core is indicated based on an analysis using color variables. Initially, the smaller core plunged into the larger core, and a compressed layer formed in front of the core. At $t = 0.22$ Myr, the sink particle formed, and the gas components of the smaller core accreted onto the particle with $\dot{M} \sim 10^{-5} M_\odot \text{ yr}^{-1}$. Larger core components proceeded in the y -positive direction. At approximately $t = 0.3$ Myr, the accretion rate from the smaller core components decreased to $\dot{M} \sim 10^{-6} M_\odot \text{ yr}^{-1}$, followed by secondary accretion from the larger core components. Larger core components accreted and rotated around the particle. As shown in the rightmost panel, a one-arm spiral pattern resembling a whirlpool formed. The polarization vectors followed this spiral stream. In this way, for the collision of unequal mass, one core collapsed first, and the gas from the other core accreted next.

Such two-stage accretion we found suggests that gases with different chemical com-

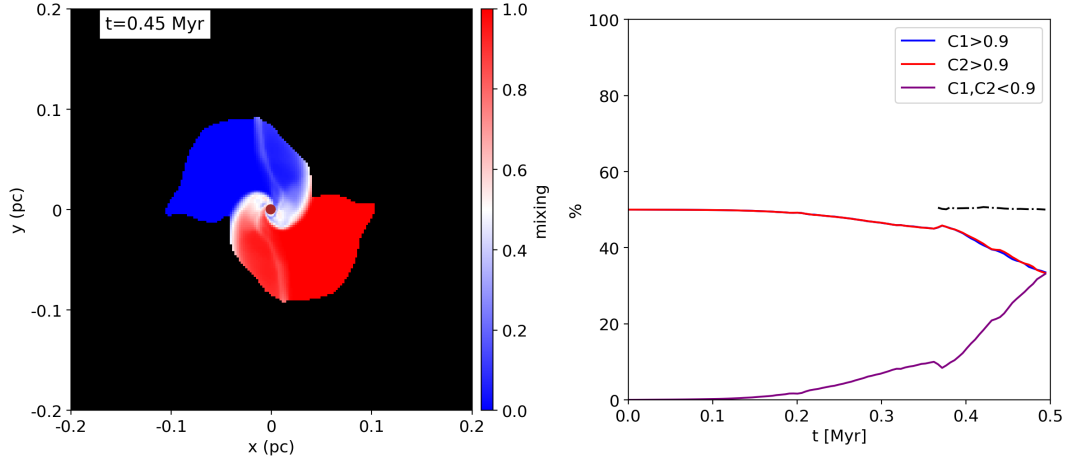


Figure 3.16: *Left:* Ration of the integration in the line of sight represented by $\int_{C_1+C_2>0.5} \rho C_1 dx / \int_{C_1+C_2>0.5} \rho(C_1 + C_2) dx$ for model **b1-M1-By30** at $t = 0.45$ Myr. For cells with $C_1 + C_2 > 0.5$, the integration in the line of sight of ρC_1 was divided by that of $\rho(C_1 + C_2)$. This is an indicator of how much gas is being mixed. The purple point represents the sink particle. The black region indicates where $\int_{C_1+C_2>0.5} \rho(C_1 + C_2) dx = 0$ *Right:* Mass fraction of the gas. The blue line indicates the mass fraction of the gas where $C_1 > 0.9$ in the whole gas. The red line indicates the mass fraction of gas where $C_2 > 0.9$. The purple line indicates that of the gas where both $C_1 < 0.9$ and $C_2 < 0.9$. The black dashed-dot lines indicate the mass fraction in the sink particle of the gas that is initially labeled $C_1 = 1.0$.

positions may accrete at different times, which could significantly affect the chemical evolution of a stellar system. Previous works have reported the dichotomy between non-carbonaceous and carbonaceous meteorites in our solar system (Nanne et al., 2019). The differences between different meteorites could be explained by considering that a second phase accretion occurred during planet formation and injected material into the disk ⁴.

In Appendix C.2, we briefly examine another collision model between unequal-mass cores and compare it with the observed spiral structure in one of the star forming regions.

⁴Pineda et al. (2020) proposed that the streamer structure could be the origin of the differences between different meteorites. Yano et al. (2023 submitted to ApJ) pointed out that this streamer structure could be formed by a core-core collision.

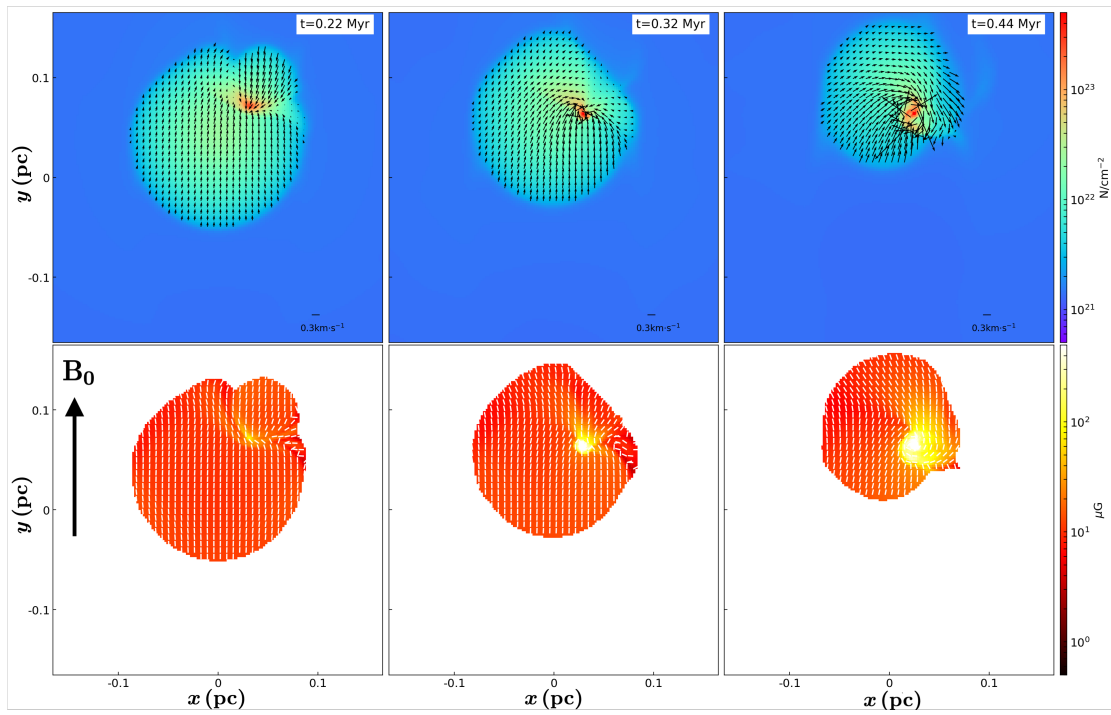


Figure 3.17: As in Figure 3.2 except for the collision of unequal-mass cores. Snapshots at 0.22, 0.32, and 0.44 Myr are shown.

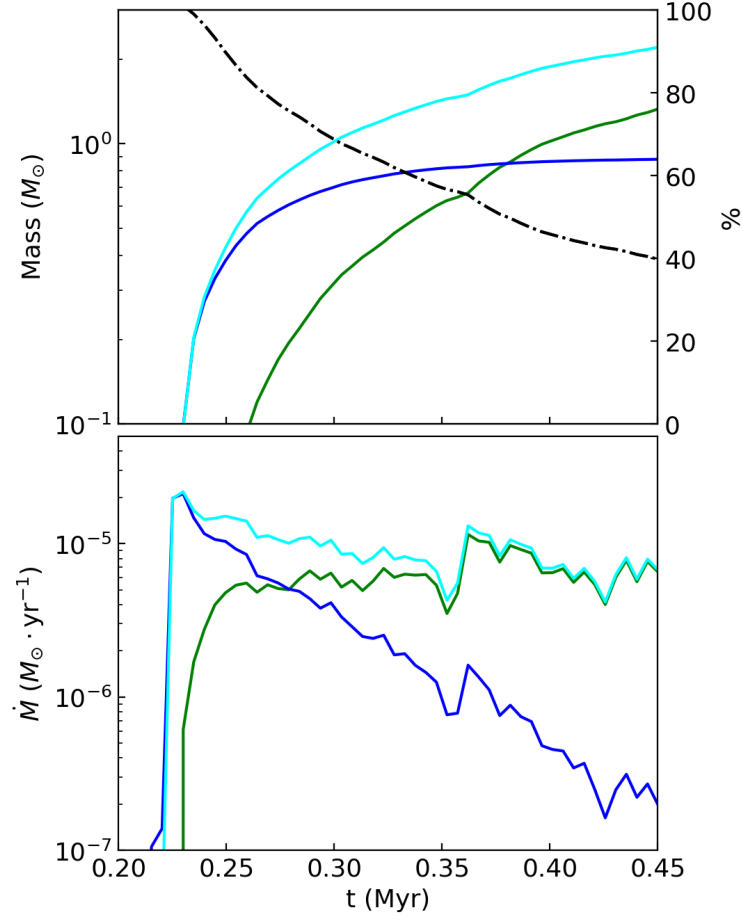


Figure 3.18: Evolution of mass (top) and mass accretion rate (bottom) of the sink particle for the collision of unequal-mass cores. The blue lines correspond to the contribution from gas initially labeled $C_1 = 1.0$. The green lines correspond to that from gas labeled $C_2 = 1.0$. The cyan lines indicate the total amount. In the top row, the black dashed-dot lines indicate the mass fraction of gas initially labeled $C_1 = 1.0$ for the sink particle.

3.4.4 Caveats

In our simulation, we do not take into account the effects of stellar feedback. However, feedback is critical in determining the local core-to-star efficiency. Estimated SFEs in our study is the rough indicator of the total accretion. More research is needed on the protostellar phase, considering the stellar feedback effect. Our results are helpful in the early stages before outflow is outstanding.

As a simple initial condition, we set a BE sphere and uniform magnetic fields. However, as presented in Chapter 2, dynamics, geometry, and inner structure of prestellar cores are more complex and various. Studies investigating core interactions under more realistic initial conditions might be worthwhile. Also, the range of parameters investigated in this study, such as core mass, initial gas density, magnetic field strength, collision velocity, etc., is limited, possibly introducing biases in our results. In [Kitsonas & Whitworth \(2007\)](#), collisions between low-mass clumps are simulated with various combinations of clump mass, impact parameter, and collision velocity. [Kitsonas & Whitworth \(2007\)](#) indicated that the efficiency of star formation is found to vary significantly in the different collision parameters. In this study, we focused on the effect of the magnetic field, but it would be useful to conduct a more detailed parameter search with the magnetic field, exploring the relationship with other parameters such as clump mass, impact parameter, and collision velocity.

Despite above limitations, our findings provide important insights into the physical properties of prestellar cores after the collision process. We find that not only \mathcal{M}_c and b , as shown in previous studies, but also the strength and direction of the magnetic field are important factors in determining the stellar fate.

3.5 Summary of this Chapter

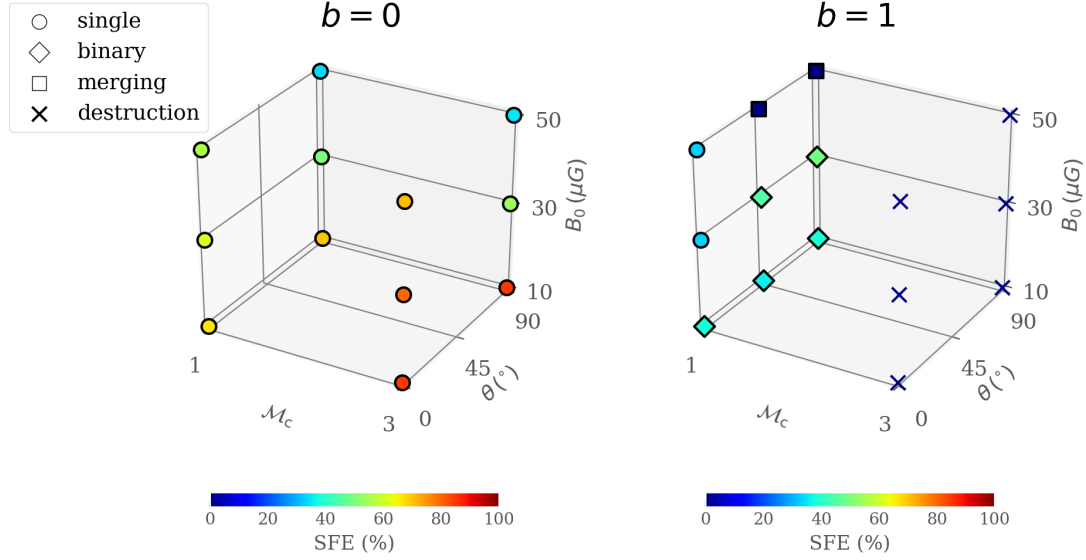


Figure 3.19: Results for all models shown in a 3D parameter space. *Left panel:* Head-on collision ($b = 0$). *Right panel:* off-center collision ($b = 1$). Red circles represent single star formation, red diamonds represent binary formation, and black squares represent the merging of cores without collapsing. Cross marks represent models in which cores ablate without collapsing. The color of marks corresponds to SFEs.

We conducted a series of 3D MHD simulations to study the evolution of prestellar core collisions in a magnetic field. Adaptive mesh refinement and sink-particle techniques were used to follow the evolution of colliding cores. We explored the parameter space of dense core collisions, including the offset parameter b , Mach number of the initial core \mathcal{M}_c , magnetic field strength B_0 , and angle θ between the initial magnetic field and collision axis. Figure 3.19 shows results for all models. Our main findings are summarized as follows:

1. Head-On Collision

For the case of a head-on ($b = 0$) collision, one protostar is formed. As the initial magnetic field strength was higher (with \mathcal{M}_c and θ held constant), the growth rate of density and the accretion rate onto the protostar decreased. As magnetic pressure acts in directions perpendicular to the field lines, for models with $\theta = 90^\circ$, the accretion rate was more dependent on the initial magnetic field strength, as compared with $\theta = 0^\circ$ models. The initial state of the magnetic field had a strong effect on the mass growth of the protostar.

2. Off-Center Collision

In the case of an off-center ($b = 1$) collision, the whole system had an angular momentum, and therefore the structures were complicated. The motion of gas and the number of protostars strongly depended on the initial magnetic field strength and orientation. The dynamic importance of the magnetic field determined the magnetic Jeans mass, and therefore, the initial magnetic field strength affected the fragmentation of dense gas and the number of protostars. Besides, the evolution of the collision process depended on θ , because the magnetic field orientation influences gas motion. The initial state of the magnetic field affected the accretion rate and multiplicity of protostars.

We also supplementarily investigate gas mixing. We use the color variable in our simulations to track the gas mixing. We found that the gas components of two cores mixed well at the collision interface, while in the arm structures, the mixing rate was meager, 0.1 Myr after star formation. Moreover, for the collision of unequal mass, we observed that one core collapsed first, and the gas from the other core accreted next. If pre-collision cores have different chemical compositions, we may find observational relics of the collision by investigating the differences in abundance.

Chapter 4

Conclusions and Future Prospects

4.1 Summary of this Dissertation

Understanding the properties of prestellar cores is crucial for a comprehensive grasp of star formation, as prestellar cores are the direct progenitors to stars. Recent observational studies suggest that the clumps from which prestellar cores form may exhibit rotational dynamics or collide with other clumps. Moreover, collisions between prestellar cores have also been implied by observations. Therefore, assessing the effects of these dynamic physical environments on core properties is vital.

Using 3D MHD simulations, we investigated the properties of prestellar cores. Figure 4.1 summarizes the position and discoveries of this paper. In Chapter 2, we examined the nature of prestellar cores formed within single rotating clump and colliding clump, with particular focus on the extent to which angular momentum and magnetic fields are inherited from the parent clumps. We found that cores inherit the angular momentum from their parent clump effectively when a single clump rotates, and its rotational is higher than its turbulent energy. However, when the contribution of the clump's rotational energy is lower, the direction of the angular momentum \mathbf{L}_{core} becomes random. Furthermore, when clumps collide, cores form rapidly within dense compressed layers that acquire little angular momentum, resulting in a random direction of \mathbf{L}_{core} . We also found that a stronger magnetic field in the parent clump tends to imprint its orientation onto the core's internal field \mathbf{B}_{core} . Alignment of \mathbf{B}_{core} is particularly notable in cases where clumps collide; the global magnetic field aligns along the compressed

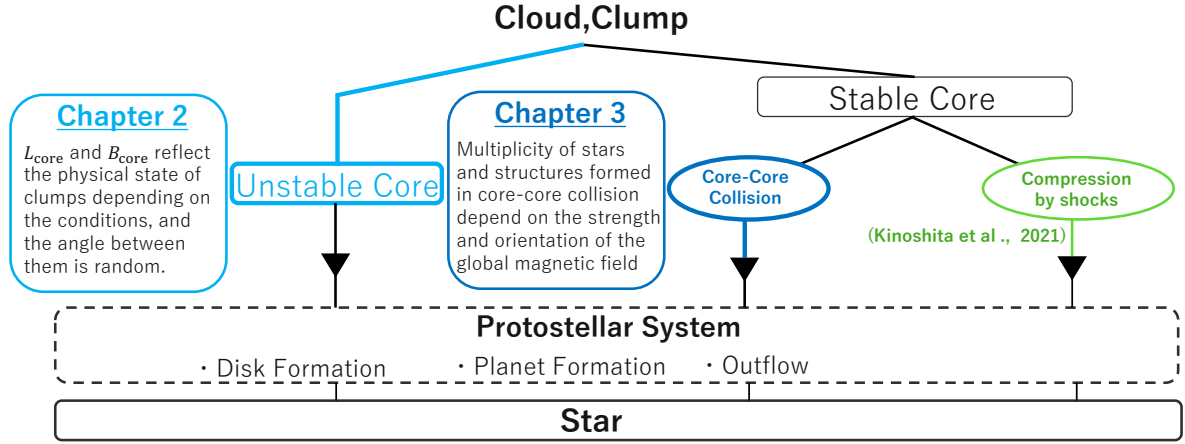


Figure 4.1: The position and discoveries of this paper. In Chapter 2, we explored the links between the gravitationally bound prestellar cores and the parental clumps. In Chapter 3, we investigated the collisions between stable cores. In the research I conducted during my master’s course, I explored the interactions between cores and the shock waves caused by supernova explosions using HD simulations (Kinoshita et al., 2021a).

layer, and consequently, B_{core} is well aligned. Our intriguing finding is that the angle between L_{core} and B_{core} is random in most cases. This general misalignment between L_{core} and B_{core} has significant implications for resolving the “magnetic braking catastrophe” and validating the disk formation. In this study, we expanded upon previous research, which dealt with simple clumps and clouds, by setting rotating and colliding clumps as initial conditions. This allowed us to newly elucidate the inheritance and correlation of L_{core} and B_{core} .

In Chapter 3, we investigated the impact of collisions between prestellar cores on their physical properties and subsequent stellar evolution, focusing on how the orientation and strength of magnetic fields affect the collision. We confirmed that stronger magnetic fields inhibit gas motion due to magnetic pressure, reducing accretion rates and fewer stars. Moreover, we discovered that the multiplicity of stars and the structures formed heavily depend on the angle between the collision axis and the initial magnetic field. Our findings extend beyond previous research that considered only the core velocity and impact parameter, showing that magnetic field strength and orientation are also critical during the collision process.

4.2 Discussion and Conclusions throughout this Dissertation

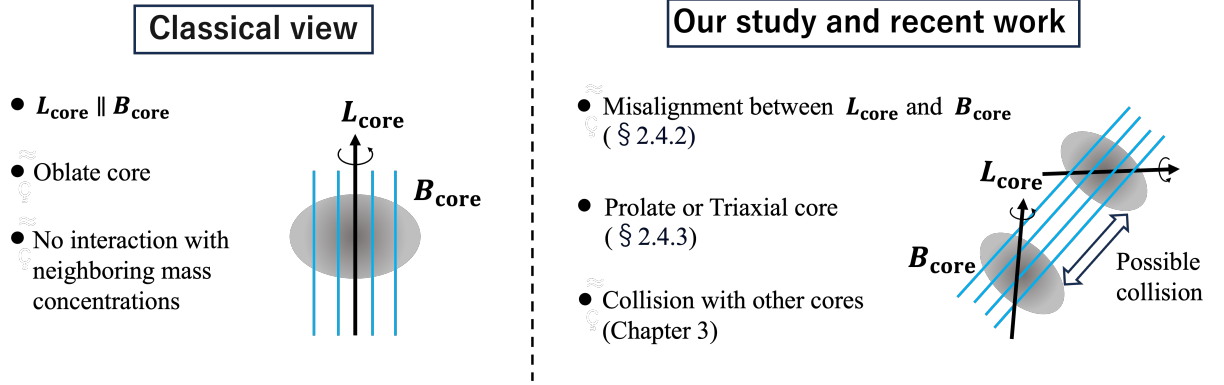


Figure 4.2: Comparison between classical views and pictures obtained from our study and recent research.

Our study demonstrates that the depiction of idealized prestellar cores in classical theory differs significantly from the actual prestellar cores formed within clumps or clouds. Figure 4.2 compares classical views and pictures obtained from our study and recent research. In the classical pictures, the core was assumed to be in a simple physical state, and its correlation with the surrounding gas was not properly considered. The standard depiction was of an oblate core, contracting with its long axis perpendicular to the magnetic field and angular momentum, which are parallel. On the other hand, recent research and our study have presented new and realistic pictures. L_{core} is misaligned with B_{core} (see § 2.4.2) and cores are prolate or triaxial rather than oblate generally (see § 2.4.3). Besides, collisions between cores can occur in regions with a dense distribution of cores, and the subsequent stellar evolution is greatly affected. These depictions can only be obtained by tracing the formation of cores from their parent clumps or cloud scales and by studying the interactions between cores. Rather than focusing solely on the prestellar core, it is essential to consider its correlation with the parental clump and interactions with surrounding mass concentration. Our study highlights the significance of considering the effects of the physical environment

surrounding the core. Especially, the points newly clarified in our study are as follows:

- In single rotating clumps, irrespective of the magnetic field's physical state, when the global rotational energy exceeds the turbulent energy, \mathbf{L}_{core} inherits the rotation of parental clump. The global orientation of the magnetic field does not influence the orientation of \mathbf{L}_{core} at least within the range of parameters investigated in our study (see § 2.4.1).
- In colliding clumps, even if the entire system is strongly rotating, the initial cores formed in the central compressed layer do not inherit the global rotation (see § 2.4.1).
- In the shocked layer within colliding clumps, the magnetic field is bent and compressed from both sides. As a result, many cores with high magnetic energy are formed, and \mathbf{B}_{core} pairs become strongly aligned (see § 2.3.2.2).
- Within clumps that are colliding or strongly rotating, the relative angle between \mathbf{L}_{core} and \mathbf{B}_{core} generally displays a random distribution (see § 2.4.2).
- In the core-core collision process, not only core speed and impact parameters but also the strength and direction of the magnetic field are essential factors in determining the stellar fate (see § 3.4).

Furthermore, our study can provide significant insights into the following topics.

Initial Mass Function

The stellar initial mass function (IMF), representing the mass distribution of stars at their birth, is of fundamental importance across various fields of astrophysics. In many regions, the cores' mass function (CMF) appears to resemble IMF. Therefore, it is believed that the IMF inherits characteristics from the CMF. To understand IMF, it is first necessary to grasp the CMF and its evolution.

Our simulation results have significant implications for CMF. To explore the evolution of the CMF, Huang et al. (2013) constructed a numerical method to consider the coagulation between the cores and their ablation due to K-H instability. They demonstrated the importance of balancing ablation and coagulation for CMF evolution, yet

they ignored the impact of magnetic fields in their analysis. Meanwhile, our research in Chapter 3 suggested that initial magnetic field properties are crucial in determining stellar evolution during core collision processes. Especially when B_0 is perpendicular to the collision axis in a head-on collision ($b = 0$), accretion rates highly depend on the magnetic field strength (see § 3.4.1). Furthermore, for off-center collisions ($b = 1$) where the collision velocity is approximately the sound speed ($\mathcal{M}_c = 1$), the initial magnetic field strength and orientation are key parameters determining the multiplicity and accretion rates (see § 3.4.2). Our study emphatically indicates that considering the effects of magnetic fields is essential in understanding the evolution of CMFs.

In Chapter 2, we explored the core’s angular momentum and magnetic field, and these properties are also critical to the CMF. The angular momentum of cores is one of the critical parameters for the multiplicity of a stellar system and their separation (e.g., Machida et al., 2008). The relation between \mathbf{L}_{core} and \mathbf{B}_{core} affects the outflow drive efficiency and thus the accretion rate. Our results on angular momentum, magnetic field, and the relationship between them are helpful in discussing the final mass of the star and, thus, the CMF. As we will discuss later in § 4.3, it would be meaningful to compare our results with simulations that follow the formation of protostars on smaller scales.

Observational studies

Our results help to estimate the nature of the core’s parental clump or cloud observationally. As shown in § 2.4.1, clear alignment of core rotation is realized only if the single clump rotates strongly. Conversely speaking, if a strong alignment of \mathbf{L}_{core} is observed, it suggests that the rotational motion of the parental clump is strong. Moreover, if a clump exhibits such strong rotation, it is also possible that the cloud structures encompassing the clump may also display strong rotational movement. Alternatively, it is also plausible that clumps are formed in regions with anisotropic accretion, such as in the centers of hub-filament structures, and consequently acquire significant angular momentum (e.g., Treviño-Morales et al., 2019).

4.3 Future Prospects

In Chapter 2, we have clarified the properties of \mathbf{L}_{core} and \mathbf{B}_{core} at a certain point just before the collapse of prestellar cores. Meanwhile, Misugi et al. (2023) suggested that the mean angular momentum and profile within cores change during the initial stage of their formation process. Kuznetsova et al. (2020) indicated that the relative angle between \mathbf{L}_{core} and \mathbf{B}_{core} also could change due to the time variability in the direction of the angular momentum. One of the future prospects of our research is a more intricate investigation into the mechanisms of angular momentum acquisition by cores and their relationship with magnetic fields, achieved by directly tracking the temporal evolution of the cores. This necessitates the accurate identification and differentiation of each core. Employing the *dendrogram* algorithm for identification (e.g., Offner et al., 2022), as well as the analysis of simulations using SPH (e.g., Misugi et al., 2023), can be considered as practical approaches. Additionally, tracking the temporal evolution of cores in clump/cloud scale simulations could shed light on the frequency and conditions of core collisions. As indicated in Chapter 3, the outcomes of collisions, such as boundness, accretion rate, and multiplicity, significantly depend on collision parameters (\mathcal{M}_c , b , B_0 , θ). Since off-center collisions can provide angular momentum to cores, it is also important to clarify the initial conditions of core collisions through clump/cloud scale simulations to better understand the origins of core angular momentum. In summary, research that connects the content of Chapter 2 with Chapter 3 is desirable for understanding the origins of the physical state of prestellar cores.

There is also room for improvement in the numerical code. In our simulations, the HLL scheme was used as in Sakre et al. (2023), which explored cloud-cloud collision using *Enzo*. The HLL scheme approximates two out of the seven waves by collapsing the full structure of the Riemann fan into a single average state. On the other hand, the Harten-Lax-Van Leer with multiple discontinuities (HLLD, Miyoshi & Kusano, 2005) is a five-wave Riemann solver and can accurately solve contact discontinuities, rotation (Alfven) discontinuities, and tangent discontinuities in the MHD equations. HLL is simpler and faster than HLLD but more dissipative. It is meaningful to employ the HLLD method for our simulation to capture and discuss local-scale structures more accurately. In our calculations, we also assume isothermal conditions, as is done in many previous simulations investigating star formation within supersonic turbulent clouds (Bonnell et al., 2003; Inoue & Fukui, 2013; Chen & Ostriker, 2018; Mocz & Burkhart, 2018; Kuznetsova et al., 2019; Abe et al., 2021). This assumption is considered a rea-

sonable approximation for the low-mass star-forming regions on the scales we explored. However, it is also significant to implement heating and cooling processes to reproduce more realistic gas conditions especially for regions strongly compressed by shocks.

Considering non-ideal MHD effects is also interesting. Especially in the scale of gas we studied, the effect of Ambipolar Diffusion (AD) is crucial (e.g., [Kunz & Balbus, 2004](#)). In Chapter 2 and 3, we found some unbound cores supported by magnetic fields. For example, in 2, dense but unbound cores with high magnetic energies are detected especially for Collision Setup models (see § 2.4.4). In Chapter 3, for the model **b1-M1-Bz50** and **b1-M1-Bob50**, colliding cores merge without gravitational collapse (see § 3.3.2.2 and § 3.3.2.3). Given the influence of AD, magnetic flux may escape from these cores, eventually leading to gravitational contraction. It is intriguing to explore the behavior of such cores initially supported by magnetic fields.

Furthermore, it is also critical to track the progression after forming the first core. Our studies reveal the initial conditions of star formation, i.e., the physical states of prestellar cores. Based on our findings, it is highly meaningful to examine the mechanisms of disk formation and feedback through sub-core scale simulations.

Appendix A

Key Terms and Concepts

This appendix describes some terms or concepts used in this paper.

A.1 Bonnor-Ebert Sphere

Bonnor-Ebert sphere is an isothermal gas sphere remaining in hydrostatic equilibrium ([Ebert, 1955](#); [Bonnor, 1956](#)).

Assuming a thermally supported gas sphere, the equation for hydrostatic equilibrium becomes

$$\frac{dP(r)}{dr} = -\frac{GM(r)\rho(r)}{r^2}, \quad (\text{A.1})$$

where $P(r)$ is the pressure, $\rho(r)$ is the density, and

$$M(r) = 4\pi \int_0^r \rho(r')r'^2 dr'. \quad (\text{A.2})$$

The equation of state of the isothermal gas is

$$P(r) = \rho(r)c^2, \quad (\text{A.3})$$

where c is the sound speed. Combining equation [A.1](#) and [A.3](#), we have

$$\frac{\rho(r)}{\rho_c} = \exp \left[-\frac{1}{c^2} \int_0^r \frac{GM(r')}{r'^2} dr' \right], \quad (\text{A.4})$$

where ρ_c is the central density of sphere. By putting dimensionless radius $\xi = (r/c)\sqrt{4\pi G\rho_c}$ and $\rho = \rho_c \exp(-\psi)$, the radial density profile is described by the modified equation of Lane-Emden:

$$\frac{1}{\xi^2} \frac{d}{d\xi} \left(\xi^2 \frac{d\psi}{d\xi} \right) = \exp(-\psi). \quad (\text{A.5})$$

Ignoring singularity at $r = 0$, the Lane-Emden equation has the solution:

$$\frac{\rho}{\rho_c} = \exp(-\psi) = 2\xi^{-2} = \frac{c^2}{2\pi G r^2}, \quad (\text{A.6})$$

which is called Singular isothermal sphere (SIS).

On the other hand, we can get a numerical solution with the boundary conditions

$$\psi(0) = \frac{d\psi(0)}{d\xi} = 0. \quad (\text{A.7})$$

Figure A.1 shows the radial density profile of the Bonnor-Ebert sphere (i.e. the numerical solution of equation A.5 and A.7) and the SIS. Around the inner side, the density of the numeric solution is almost flat, whilst the density falls off with r^{-2} to the outside.

The mass of a Bonnor-Ebert sphere is

$$M_c = \int_0^r 4\pi \rho(r') r'^2 dr' \quad (\text{A.8})$$

$$= 4\pi \rho_c \left(\frac{c^2}{4\pi \rho_c} \right)^{3/2} \int_0^\xi \exp(-\psi) \xi'^2 d\xi'. \quad (\text{A.9})$$

Plugging in the Equation A.5, we can get

$$\int_0^\xi \exp(-\psi) \xi'^2 d\xi' = \xi^2 \frac{d\psi}{d\xi}, \quad (\text{A.10})$$

which gives the mass

$$M_c = 4\pi \rho_c \left(\frac{c^2}{4\pi G \rho_c} \right)^{3/2} \xi^2 \frac{d\psi}{d\xi}. \quad (\text{A.11})$$

We now define the dimensionless mass as

$$m \equiv \frac{P_0^{1/2} G^{3/2} M_c}{c^4}, \quad (\text{A.12})$$

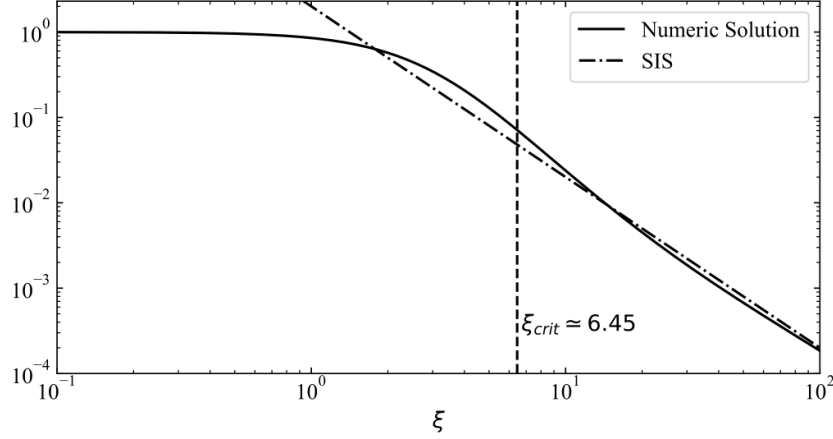


Figure A.1: The density profile of Bonnor-Ebert sphere. The abscissa is the dimensionless radius ξ , and the ordinate is the density ratio ρ/ρ_c . The vertical dashed line indicates the critical dimensionless radius above which the Bonnor-Ebert sphere is unstable.

where P_0 is an external pressure. For an outer boundary $\xi = \xi_0$, dimensionless mass can be rewritten as

$$m = \left(4\pi \frac{\rho_c}{\rho_0}\right)^{-1/2} \left(\xi^2 \frac{d\psi}{d\xi}\right)_{\xi_0}, \quad (\text{A.13})$$

where ρ_0 is the boundary density of sphere.

Figure A.2 shows the dimensionless mass as a function of ρ_c/ρ_0 . The function has a maximum value at $\rho_c/\rho_0 \simeq 14.1$. The corresponding $\xi_{\text{crit}} (\simeq 6.45)$ is the critical dimensionless radius for the Bonnor-Ebert sphere. The Bonnor-Ebert sphere is unstable when its dimensionless radius exceeds this critical dimensionless radius. The Bonnor-Ebert critical mass and pressure corresponding to these critical values are

$$M_{\text{crit}} = 1.18 \frac{c_s^4}{G^{3/2} P_0^{1/2}} \quad (\text{A.14})$$

$$P_{\text{crit}} = 1.40 \frac{c_s^8}{G^3 M_c^2}. \quad (\text{A.15})$$

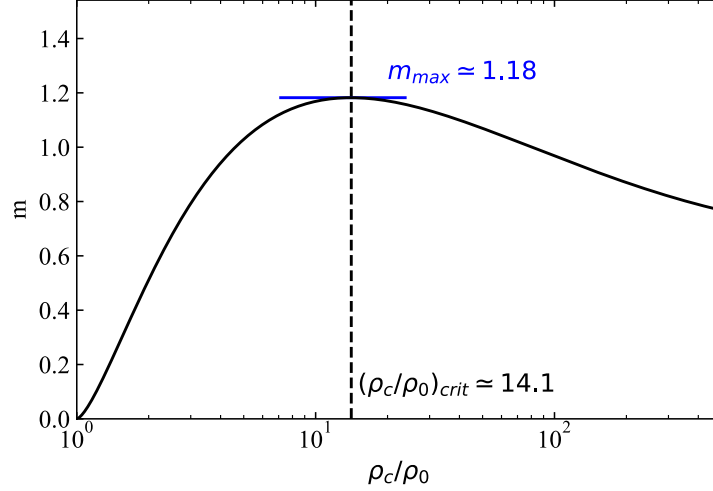


Figure A.2: Dimensionless mass as a function of ρ_c/ρ_0 . The vertical dashed line indicates the critical density ratio. The blue horizontal line indicates the maximum dimensionless mass.

A.2 Mach number

Turbulence is an inherently nonlinear, multiscale process and not amenable to simple analytical description. Therefore, turbulence is often treated as a non-thermal, isotropic pressure. The non-thermal pressure can be written as $P_{nt} = \rho \sigma_{v,nt}^2$, where ρ is the gas density and $\sigma_{v,nt}$ is the one-dimensional velocity dispersion of the non-thermal random motion. If turbulence is isotropic, the amount of turbulence can be parameterized by the gas Mach number:

$$\mathcal{M} = \frac{\sqrt{3}\sigma_{v,nt}}{c_s}, \quad (\text{A.16})$$

where c_s is sound speed.

A.3 Alfven Mach Number

Alfven wave is a MHD wave propagating along magnetic field lines, for which magnetic tension is a restoring force. Its velocity, the Alfven velocity v_A , is defined as

$$v_A = \frac{B}{\sqrt{4\pi\rho}}, \quad (\text{A.17})$$

where ρ is the gas density.

The relative importance of magnetism and non-thermal motion is parameterized by the Alfven Mach number:

$$\mathcal{M}_A = \frac{\sqrt{3}\sigma_{v,\text{nt}}}{v_A}, \quad (\text{A.18})$$

For $\mathcal{M}_A < 1$ (sub-Alfvenic), magnetic fields predominantly govern gas dynamics. $\mathcal{M}_A > 1$ (super-Alfvenic) indicates the converse.

A.4 Mass-to-Flux Ratio

Magnetic energy is given by

$$E_{\text{mag}} = \frac{B^2 V}{8\pi}, \quad (\text{A.19})$$

where B is the magnetic field strength and V is volume. E_{mag} can be compared to the other energy terms, typically gravitational potential energy and kinetic energy.

To ascertain the significance of magnetic fields, one can calculate the ratio of magnetic energy to gravitational energy. Consider a homogenous, spherically symmetrical cloud with mass M , volume V , and radius R . In ideal MHD, where the field is frozen into gas, the magnetic flux Φ remains constant and is represented by $\pi R^2 B$. In this case,

$$\frac{E_{\text{mag}}}{E_{\text{grav}}} = \frac{B^2 V}{8\pi} \times \frac{3R}{5GM^2} \propto \frac{B^2 R^4}{M^2} \propto \left(\frac{\Phi}{M}\right)^2. \quad (\text{A.20})$$

It is clear from Equation A.20, that there is a critical value of the magnetic intensity for which the gravitational collapse is impeded. For an isothermal gaseous disk, the critical mass-to-flux ratio is

$$\left(\frac{M}{\Phi}\right)_{\text{crit}} = \frac{1}{2\pi\sqrt{G}}, \quad (\text{A.21})$$

(Nakano & Nakamura, 1978), where G is the gravitational constant. For an isolated cloud, it is roughly $0.126/\sqrt{G}$ (Mouschovias & Spitzer, 1976). It is usual to define $\mu_\Phi = (M/\Phi)/(M/\Phi)_{\text{crit}}$. A core with $\mu_\Phi > 1$ can collapse and is called supercritical; a core with $\mu_\Phi < 1$ is stabilized by the magnetic field and called subcritical. In the subcritical core, gravitational collapse to form a stellar can only happen over long timescales due to diffusion mechanisms that can remove the magnetic flux from the central region of the core, for example by ambipolar diffusion (e.g., Shu, 1983).

A.5 Magnetic Field-Density Relation

The relationship between the magnetic field B and the density ρ is stated in the form of a power law

$$B \propto n^\kappa \quad (\text{A.22})$$

If the magnetic field is unimportant throughout the collapse of a spherical cloud, magnetic flux conservation ($\Phi_B = \pi R^2 B$) implies $B \propto R^{-2}$ and mass conservation ($M = 4\pi R^3 \rho/3$) dictates $\rho^{2/3} \propto R^{-2}$; thus $\kappa \approx 2/3$ (Mestel, 1966). Spherical collapse requires a weak magnetic field, while a strong field would constrain collapsing perpendicular to field lines and lead to clouds flattened along B and $\kappa \leq 0.5$ (Lada & Kylafis, 1999). Ambipolar diffusion models predict $0 < \kappa < 0.5$, evolving from $\kappa \sim 0$ initially (indicating collapse along field lines) to $\kappa \sim 0.5$ in the later stages of collapse.

The observed results generally follow the Equation A.22, and are well-known as the "Crutcher relation" (Crutcher et al., 2010):

$$B = \begin{cases} 10 \mu G & (n < 300 \text{ cm}^{-3}) \\ 10 \left(\frac{n}{300 \text{ cm}^{-3}}\right)^{\frac{2}{3}} \mu G & (n > 300 \text{ cm}^{-3}) \end{cases}. \quad (\text{A.23})$$

A.6 The Timescale of Magnetic Braking

In a magnetized core, due to the magnetic tension, angular momentum can be exchanged between fluid particles. Typically, this exchange occurs between a cloud and an outer envelope and happens through torsional Alfvén waves.

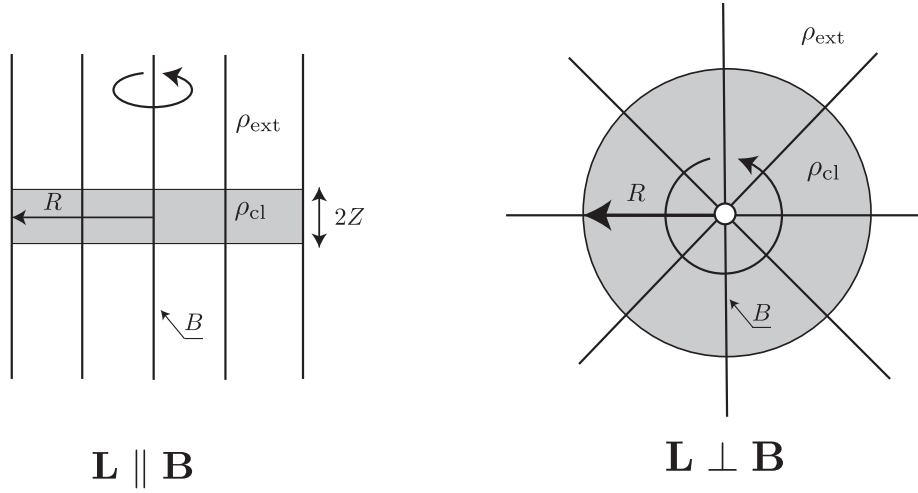


Figure A.3: The geometries employed for discussing the magnetic braking of aligned (left) and perpendicular (right) rotators in Appendix A.6. Originally made by Mouschovias (1985).

Mouschovias & Paleologou (1979, 1980) showed that the magnetic braking timescale τ_b of a central region with a moment of inertia I_c can be estimated as the time over which Alfvén waves sweep through an amount of gas in the outer envelope with a moment of inertia $I_{\text{ext}}(\tau_b)$ equal to I_c . That is,

$$I_{\text{ext}}(\tau_b) = I_c. \quad (\text{A.24})$$

In the case of the aligned rotator (disk or cylinder) with the configuration of Figure A.3 (left), the moments of inertia of the central region with a radius R and outer envelope are given by $I_c = \pi \rho_{\text{cl}} R^4 Z$ and $I_{\text{ext}}(\tau_b) = \pi \rho_{\text{ext}} R^4 v_A \tau_b$, respectively, where v_A is the Alfvén velocity in the outer envelope. By solving Equation A.24, τ_b is given by

$$\tau_{b,\parallel} = \frac{\rho_{\text{cl}}}{\rho_{\text{ext}}} \frac{Z}{v_A} \quad (\text{A.25})$$

For the perpendicular rotator of Figure A.3 (right), the braking timescale corresponds to the time it takes for the Alfvén waves to reach R_{ext} , the radius at which Equation A.24 holds. The Alfvén waves propagate in the equatorial plane, thus $\rho_{\text{cl}} R^4 = \rho_{\text{ext}} (R_{\text{ext}}^4 - R^4)$. Considering that the magnetic field is such that $B(r) \propto r^{-1}$, so that $v_A(r) = v_A(R) \times R/r$, the magnetic braking timescale is then

$$\tau_{b,\perp} = \int_R^{R_{\text{ext}}} \frac{dr}{v_A(r)} \quad (\text{A.26})$$

$$= \frac{1}{2} \left[\left(1 + \frac{\rho_{\text{cl}}}{\rho_{\text{ext}}} \right)^{1/2} - 1 \right] \frac{R}{v_A(R)} \quad (\text{A.27})$$

Equations A.25 and A.26 show that if $\rho_{\text{cl}} \gg \rho_{\text{ext}}$ and $Z \simeq R$ the braking is more efficient when the magnetic field is perpendicular to the rotation axis than when it is parallel.

Matsumoto & Tomisaka (2004) estimated the magnetic braking timescale of a collapsing cloud by a similar method to that employed in Mouschovias & Paleologou (1980). For the center region of the collapsing cloud, the density distribution can be approximated as

$$\rho \simeq \begin{cases} \rho_{\text{cen}}, & (r < \lambda_{\text{J,cl}}) \\ \rho_{\text{cen}} (r/\lambda_{\text{J,cl}})^{-2}, & (r \geq \lambda_{\text{J,cl}}) \end{cases} \quad (\text{A.28})$$

where ρ_{cen} is the central density and $\lambda_{\text{J,cl}} = c_s (\pi/G\rho_{\text{cen}})^{1/2}$ is the Jeans length within the cloud. The cloud has a central plateau, which is enveloped by an outer layer. The plateau maintains its scale length to be roughly equal to the Jeans length. The z component of the moment of inertia of the plateau is calculated as

$$I_c = \int_{r < \lambda_{\text{J,cl}}} \rho (x^2 + y^2) d\mathbf{r} \quad (\text{A.29})$$

$$= \frac{8}{15} \pi \rho_{\text{cen}} \lambda_{\text{J,cl}}^5 \quad (\text{A.30})$$

the moment of inertia of the outer envelope is estimated as

$$I_{\text{ext}}(\tau_{\text{b,col}}) = \int_{\lambda_{\text{J,cl}} \leq r \leq v_a \tau_{\text{b,col}}} \rho (x^2 + y^2) d\mathbf{r} \quad (\text{A.31})$$

$$= \frac{8}{9} \pi \rho_{\text{cen}} \lambda_{\text{J,cl}}^5 \left[\left(\frac{v_a \tau_{\text{b,col}}}{\lambda_{\text{J,cl}}} \right)^3 - 1 \right], \quad (\text{A.32})$$

By the condition of Equation A.24, the braking time $\tau_{\text{b,col}}$ for the collapsing cloud is estimated as

$$\tau_{\text{b,col}} = \left(\frac{8}{5} \right)^{1/3} \frac{\lambda_{\text{J,cl}}}{v_a}. \quad (\text{A.33})$$

A.7 Triaxiality

Examining the ratio of the axes helps evaluate the geometry of a structure that an ellipsoid with three axes can approximate. The triaxiality of an ellipsoid can be quantified by the parameter T (Franx et al., 1991):

$$T = \frac{a_1^2 - a_2^2}{a_1^2 - a_3^2}, \quad (\text{A.34})$$

where a_1, a_2 and a_3 are the semi-axes, with $a_1 \geq a_2 \geq a_3$. Purely prolate ellipsoids have $T = 1$, while purely oblate ellipsoids have $T = 0$ (see also Figure A.4).

A.8 Position-Position-Velocity Data Cube

Position-position-velocity (PPV) space is a way of visualizing data. Instead of three dimensions of physical space, it uses two spatial dimensions on the sky and one for radial velocity. This creates a 3D data cube, where the first two dimensions represent physical positions in the sky, and the third represents the speed at which material is moving toward or away from us. It's beneficial for studying structures like molecular clouds in star-forming regions, where internal movement and distribution are important.

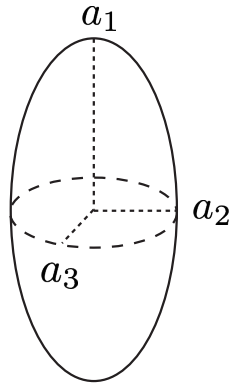
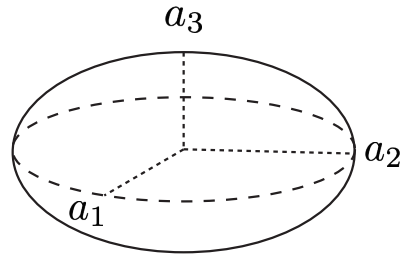
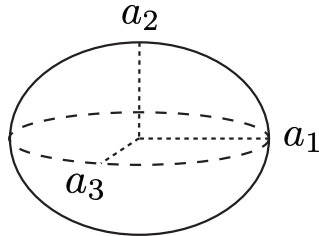
Prolate ($a_1 > a_2 = a_3$)Oblate ($a_1 = a_2 > a_3$)Triaxial ($a_1 > a_2 > a_3$)

Figure A.4: Schematic depiction of prolate, oblate, and triaxial ellipsoids. The three orthogonal axes in each case correspond to the maximum (a_1), intermediate (a_2) and minimum (a_3).

Previous works of 3D simulations obtain a PPV data cube from the simulated three-dimensional density and velocity fields at each position (x, y) (e.g., [Miville-Deschênes et al., 2003](#)). This is done assuming optically thin emission. If we set the line of sight parallel to the z -axis, the PPV cube $N_v(x, y, v)$, which is the column density along the line of sight at a given position (x, y) and the velocity v within δv , can be computed using the following equation,

$$N_v(x, y, v) = \sum_z \frac{n(x, y, v)\delta z}{\sqrt{2\pi}\sigma(x, y, z)} \exp \left\{ -\frac{[v - v_{\text{los}}(x, y, z)]^2}{2\sigma(x, y, z)^2} \right\}, \quad (\text{A.35})$$

where $v_{\text{los}}(x, y, z)$ is the line of sight velocity component. The dispersion of the Gaussian is

$$\sigma(x, y, z) = \sqrt{\frac{k_B T}{m}}, \quad (\text{A.36})$$

where k_B is the Boltzmann constant, T is the gas kinetic temperature, and m is the mass of the emitting species.

A.9 Shock-Compression Ratio for the Isothermal MHD equations

Here, we calculate the shock-compression ratio for the isothermal MHD equations under the simplified case. We assume that fluid flows perpendicular to the wavefront and neglect the component of the magnetic field that is parallel to the shock normal (see [Figure A.5](#)). Under this assumption, the conservation of mass and momentum gives the jump conditions for the isothermal MHD equations :

$$\rho_1 v_1 = \rho_2 v_2 \quad (\text{A.37})$$

$$\rho_1 (v_1^2 + c_s^2) + \frac{B_1^2}{8\pi} = \rho_2 (v_2^2 + c_s^2) + \frac{B_2^2}{8\pi}, \quad (\text{A.38})$$

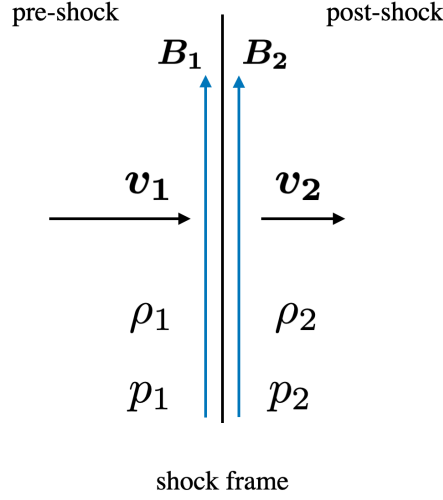


Figure A.5: The geometry of a plane parallel MHD shock. We are in the shocks frame of reference, with pre-shocked gas flowing in from the left side.

where the subscripts 1 and 2, respectively, denote the pre-shock and post-shock variables. Additionally, when the time derivative of the magnetic field is zero, the induction equation gives

$$v_1 B_1 = v_2 B_2. \quad (\text{A.39})$$

By solving these equations, we can get the compression ratio (see e.g., [Fukui et al., 2021](#)):

$$\frac{\rho_2}{\rho_1} = \frac{v_1}{v_2} = \frac{B_2}{B_1} = - \left\{ \frac{1}{2} + \left(\frac{c_s}{c_{A,1}} \right)^2 \right\} + \left[\left\{ \frac{1}{2} + \left(\frac{c_s}{c_{A,1}} \right)^2 \right\}^2 + 2 \left(\frac{v_1}{c_{A,1}} \right)^2 \right]^{1/2}, \quad (\text{A.40})$$

where $c_{A,1} = B_1 / \sqrt{4\pi\rho_1}$ is the pre-shock Alfven velocity.

Appendix B

Appendix of Chapter 2

B.1 Verification of Prograde Rotation

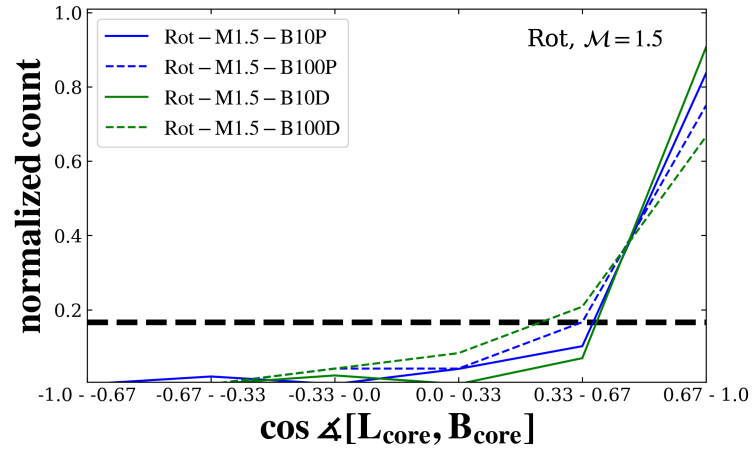


Figure B.1: Histograms of the cosine of the relative angles between parental clump rotation axis Ω_0 and the integrated angular momentum \mathbf{L}_{core} , for bound cores formed in $\mathcal{M} = 1.5$ models. The histogram ranges from -1 to 1 to distinguish between prograde and retrograde rotations. The black dashed line shows the expected distribution for an isotropic orientation of \mathbf{L}_{core} . The peak of the distribution is located in the range of 0.67-1.0, indicating that \mathbf{L}_{core} aligns with a prograde rotation rather than a retrograde rotation.

In Section § 2.3.1.1, we showed that in $\mathcal{M} = 1.5$ models of Rotation Setups, \mathbf{L}_{core} tends to align with the rotational axis of the clump $\mathbf{\Omega}_0$. To distinguish between prograde and retrograde rotation, Figure 2.4 displays the histogram of $\cos \angle[\mathbf{L}_{\text{core}}, \mathbf{B}_{\text{core}}]$ in these models, ranging from -1 to 1 ($0^\circ \leq \angle[\mathbf{L}_{\text{core}}, \mathbf{B}_{\text{core}}] \leq 180^\circ$) instead of 0 to 1 ($0^\circ \leq \angle[\mathbf{L}_{\text{core}}, \mathbf{B}_{\text{core}}] \leq 90^\circ$). The histogram has a pronounced peak in the 0.67-1.0 range, indicating that these models are aligned with a prograde rotation rather than a retrograde rotation. The direction of $\mathbf{\Omega}_0$ is inherited by the core without reversal.

B.2 Dispersion of the Magnetic Field within Cores

As an indicator of the degree of dispersion in magnetic field orientations, We calculated the mean of the relative angle between \mathbf{B}_{core} and the magnetic field of a simulation cell \mathbf{B}_i within each core:

$$\langle \theta_B \rangle = \frac{\sum_i \angle[\mathbf{B}_{\text{core}}, \mathbf{B}_i] \Delta V_i}{V_{\text{core}}}, \quad (\text{B.1})$$

where $\angle[\mathbf{B}_{\text{core}}, \mathbf{B}_i]$ is the relative angle between \mathbf{B}_{core} and \mathbf{B}_i . Figure B.2 shows histograms of $\langle \theta_B \rangle$ for various models. The model with a higher B_0 ($100\mu G$) has a lower $\langle \theta_B \rangle$ compared to the model with a lower B_0 ($10\mu G$). That is, the stronger the initial magnetic field strength, the more aligned the directions of the magnetic fields within the core.

B.3 Energies within Cores.

In Figure B.3, we show energies of the gravitationally bound cores for models of Rotation Setups and w/o Setups. Similarly, Figure B.4 depicts the energies for models of Collision Setups. A common trend in most cores is that the strength of magnetic energy E_{mag} is a fraction or an order of magnitude smaller than that of kinetic energy E_{kin} . Furthermore, it can be observed that the ratio of E_{mag} to either $|E_{\text{grav}}|$ or E_{kin} is smaller for cores with larger radii. Within bound cores, generally, E_{mag} is not dominant.

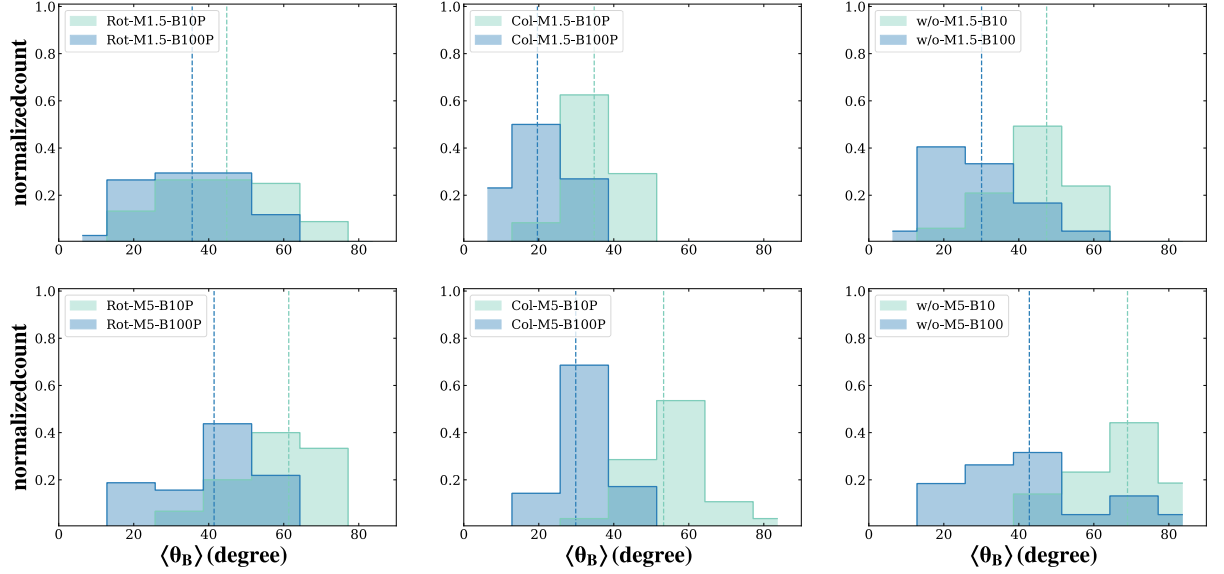


Figure B.2: Histograms of $\langle \theta_B \rangle$ for various models. The vertical dashed lines represent the mean of $\langle \theta_B \rangle$ for each model. Generally, the model with higher B_0 (with setup and \mathcal{M} held constant) has lower $\langle \theta_B \rangle$ than that of that model with lower B_0 .

B.4 Mass-to-Flux Ratio

Figure B.5 shows histograms of the estimated mass-to-flux ratio $\mu_\Phi = (M/\Phi)/(M/\Phi)_{\text{crit}}$ for each model. We estimate M/Φ as $M_{\text{core}}/(\pi R_{\text{core}}^2 |B_{\text{core}}|)$ and adopt $(M/\Phi)_{\text{crit}} = 1/2\pi\sqrt{G}$ (see Appendix A.4). Median values of μ_Φ are in the range 2-5, which are about the same or twice those derived from Zeeman effect measurements (Crutcher, 2012, see also § 1.3) except for the model Rot-M1.5-B100P. Identified cores in the model Rot-M1.5-B100P have a relatively larger mass, the median of μ_Φ is around 10. Note that our estimation is rough as it uses $\pi R_{\text{core}}^2 |B_{\text{core}}|$ to approximate the magnetic flux Φ .

B.5 Rotation-Magnetic Field Relation and Energies

Figure B.6 shows the correlation between $\angle[\mathbf{L}_{\text{core}}, \mathbf{B}_{\text{core}}]$ and energies of bound cores for Rotation and w/o Setup models. The first row of Figure B.6 presents the scatter plots

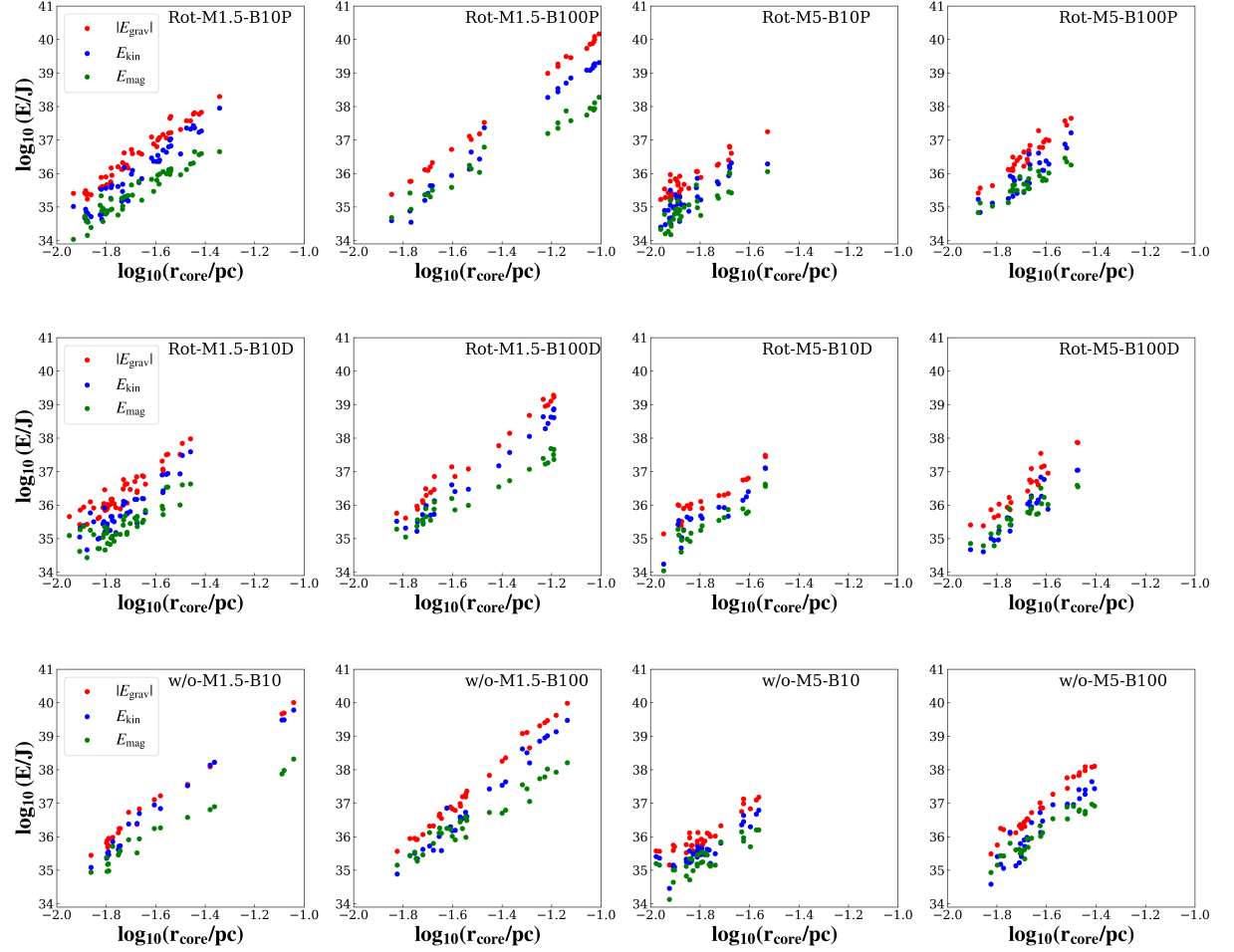


Figure B.3: Energies of the self-gravity (absolute value) $|E_{\text{grav}}|$ (red), kinetic E_{kin} (blue), and magnetic field E_{mag} (green) of the gravitationally bound cores for models of Rotation Setups and w/o Setups. For most cores, the strength of magnetic energy E_{mag} is a fraction or an order of magnitude smaller than that of kinetic energy E_{kin} .

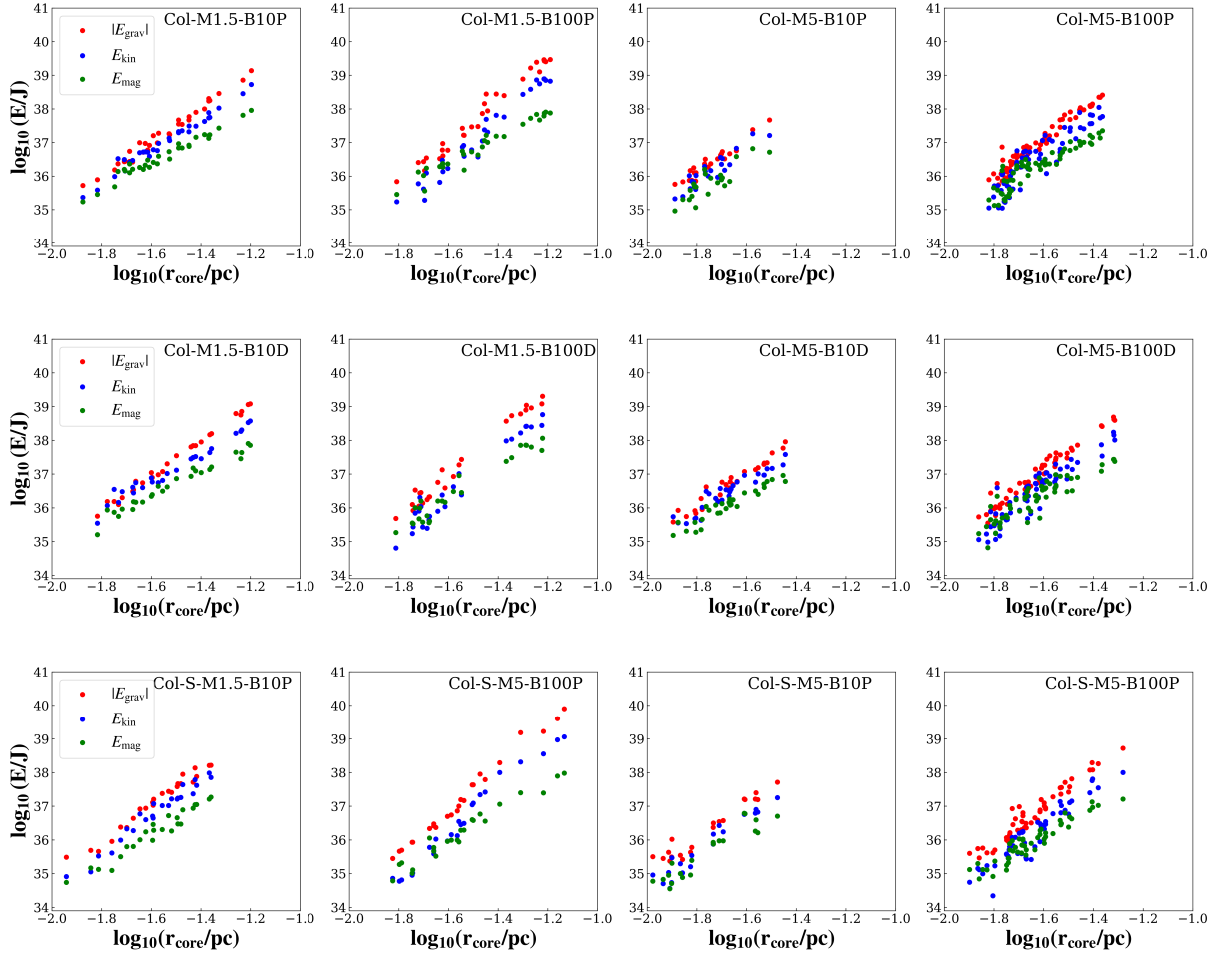


Figure B.4: Same as Figure B.3 except for models of Collision Setups. For most cores, the strength of magnetic energy E_{mag} is a fraction or an order of magnitude smaller than that of kinetic energy E_{kin} .

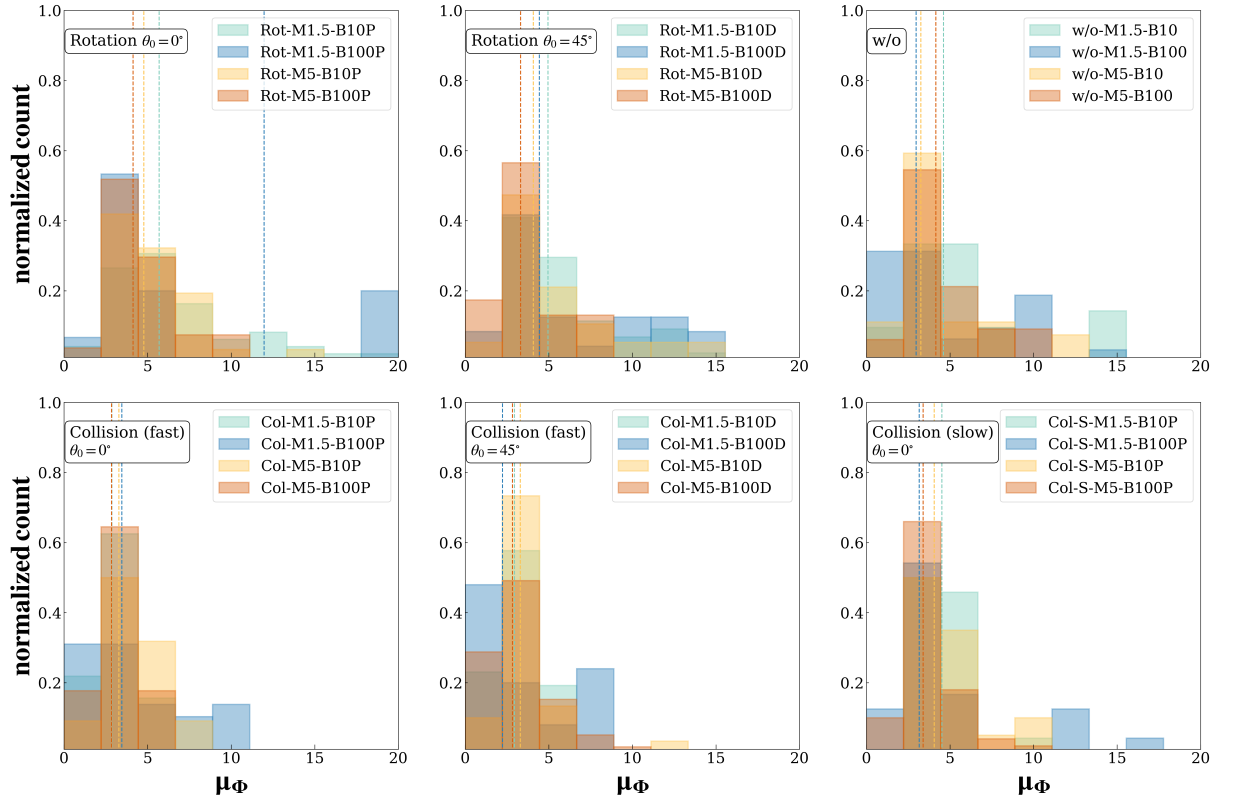


Figure B.5: Histograms of the estimated mass-to-flux ratio $\mu_\Phi = (M/\Phi)/(M/\Phi)_{\text{crit}}$ for each model. Vertical dashed lines indicate the median value. We estimate M/Φ as $M_{\text{core}}/(\pi R_{\text{core}}^2 |B_{\text{core}}|)$ and adopt $(M/\Phi)_{\text{crit}} = 1/2\pi\sqrt{G}$.

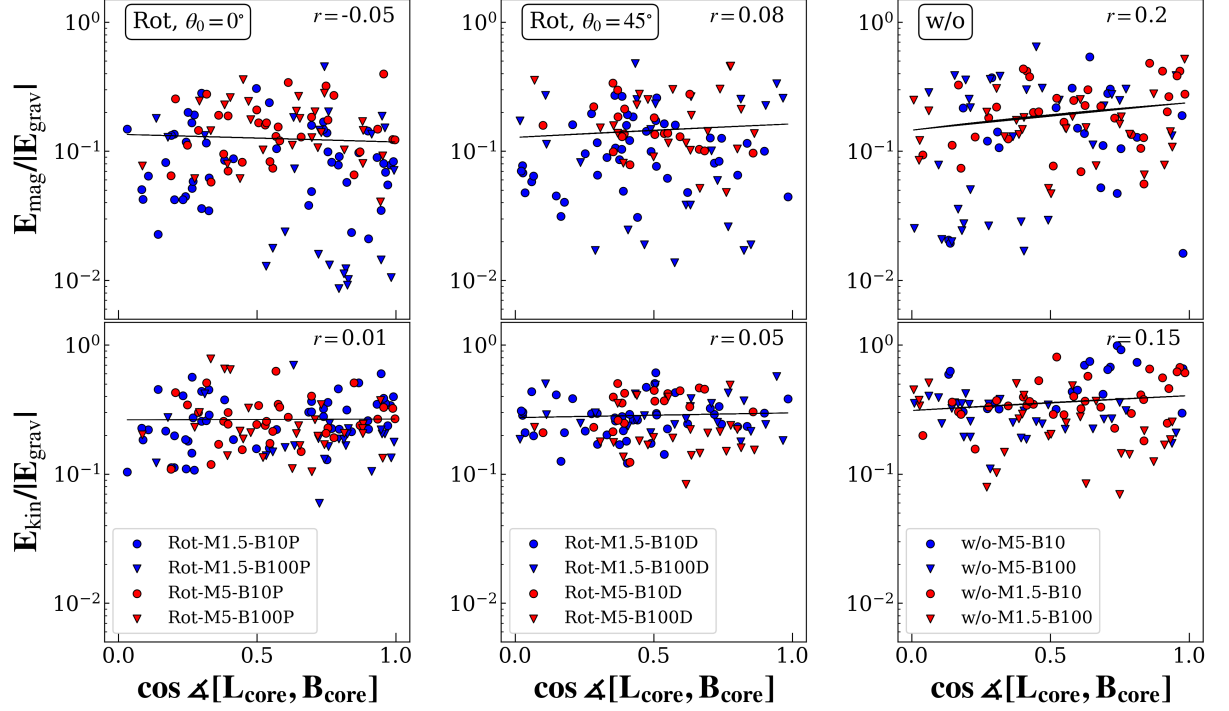


Figure B.6: Top row: Scatter plots (and correlation coefficients r) of $E_{\text{mag}}/|E_{\text{grav}}|$ vs. $\cos \angle[\mathbf{L}_{\text{core}}, \mathbf{B}_{\text{core}}]$ (cosine of the relative angle between \mathbf{L}_{core} and \mathbf{B}_{core}). Rotation Setup models with $\theta_0 = 0^\circ$ are shown in the left panel, while $\theta_0 = 45^\circ$ models are shown in the middle panel. The right panel shows the results of w/o Setup. Bottom row: Scatter plots of $E_{\text{kin}}/|E_{\text{grav}}|$ vs. $\cos \angle[\mathbf{L}_{\text{core}}, \mathbf{B}_{\text{core}}]$. The independence of $\angle[\mathbf{L}_{\text{core}}, \mathbf{B}_{\text{core}}]$ with $E_{\text{mag}}/|E_{\text{grav}}|$ is confirmed. $\angle[\mathbf{L}_{\text{core}}, \mathbf{B}_{\text{core}}]$ is also independent of $E_{\text{kin}}/|E_{\text{grav}}|$.

(and correlation coefficients r) of $E_{\text{mag}}/|E_{\text{grav}}|$ vs. $\cos \angle[\mathbf{L}_{\text{core}}, \mathbf{B}_{\text{core}}]$. Generally, the correlation between $\angle[\mathbf{L}_{\text{core}}, \mathbf{B}_{\text{core}}]$ and $E_{\text{mag}}/|E_{\text{grav}}|$ is weak. The second row shows the scatter plots of $E_{\text{kin}}/|E_{\text{grav}}|$ vs. $\cos \angle[\mathbf{L}_{\text{core}}, \mathbf{B}_{\text{core}}]$. $\angle[\mathbf{L}_{\text{core}}, \mathbf{B}_{\text{core}}]$ does not depend on $E_{\text{kin}}/|E_{\text{grav}}|$ either. As Figure B.6, Figure B.7 shows $E_{\text{mag}}/|E_{\text{grav}}|$ and $E_{\text{kin}}/|E_{\text{grav}}|$ for Collision Setup models. Even in Collision Setup models, $\angle[\mathbf{L}_{\text{core}}, \mathbf{B}_{\text{core}}]$ is independent of $E_{\text{mag}}/|E_{\text{grav}}|$ or $E_{\text{kin}}/|E_{\text{grav}}|$.

B.6 Shape of identified cores

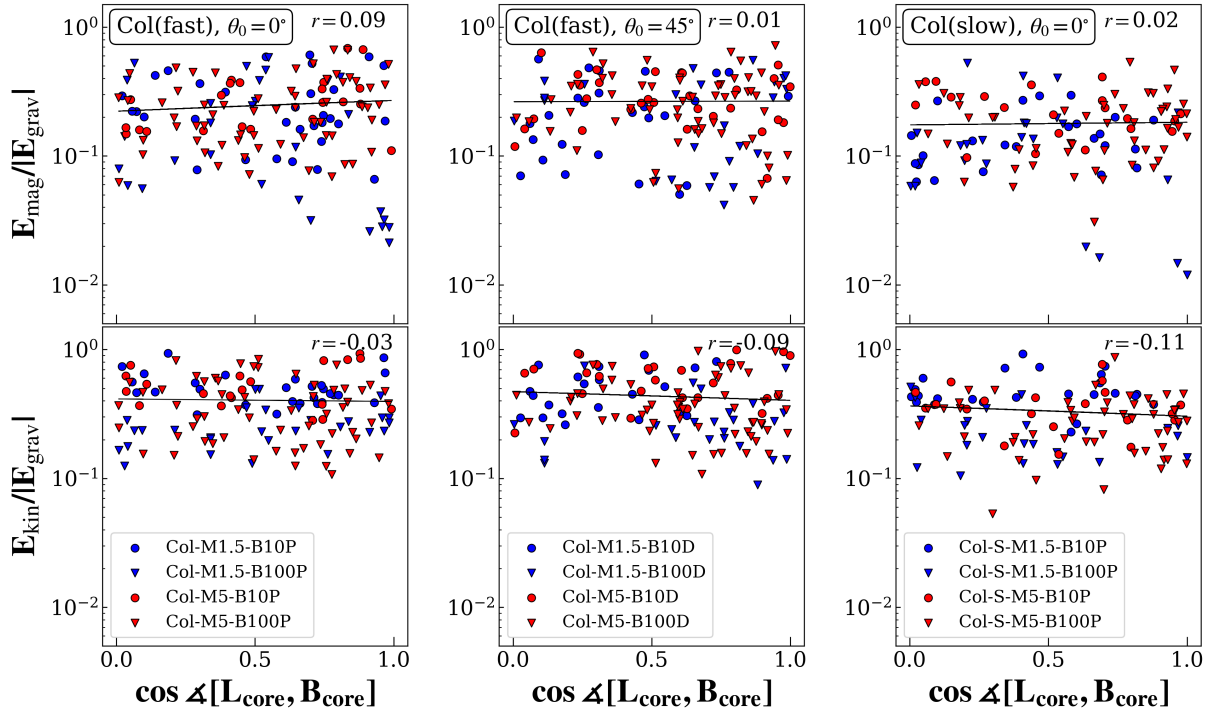


Figure B.7: Same as Figure B.6 except for Collision Setup models. Fast collision velocity cases with $\theta_0 = 0^\circ$ are shown in the left panel, and those of $\theta_0 = 45^\circ$ are shown in the middle panel. Slow collision velocity cases are shown in the right panel. $\angle[\mathbf{L}_{\text{core}}, \mathbf{B}_{\text{core}}]$ does not depend on either $E_{\text{mag}}/|E_{\text{grav}}|$ and $E_{\text{kin}}/|E_{\text{grav}}|$.

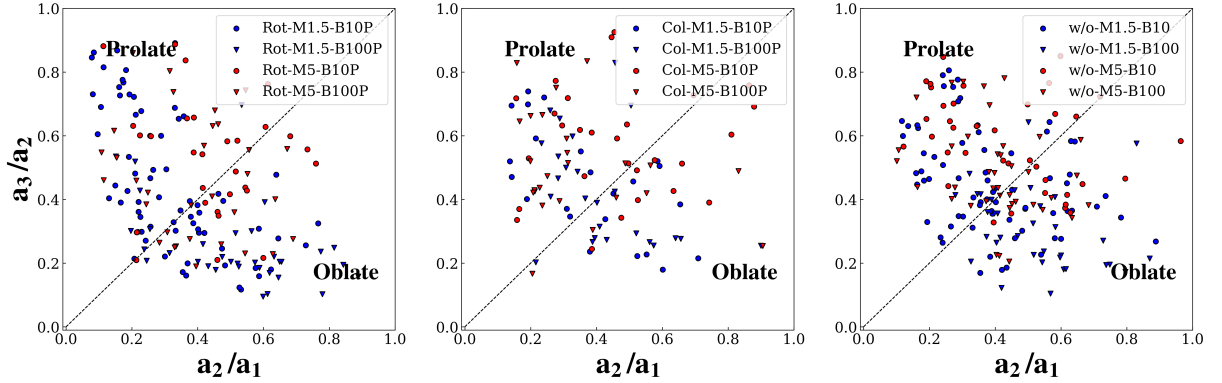


Figure B.8: The a_3/a_2 vs. a_2/a_1 plot. The dashed line is the locus of the pure triaxial core. The line separates prolate and oblate cores, which lie in the top left and bottom right of the plane, respectively.

Figure B.8 displays the core aspect ratios. Unlike Figure 2.22, this figure is displayed in the plane of a_3/a_2 and a_2/a_1 . The dashed line separates prolate and oblate cores, which lie in the top left and bottom right of the plane, respectively. Generally, identified cores are distributed more in the prolate plane than in the oblate plane. Table B.1 summarizes the classification of the core shape. The proportions of prolate and oblate determined by the comparison of $a_1 a_3$ and a_2^2 (If $a_1 a_3 > a_2^2$, then prolate; if $a_1 a_3 < a_2^2$, then oblate), and the proportions of prolate, triaxial, and oblate determined by the triaxiality T , are shown for each model. Except for models of Rot-M1.5-B100P and w/o-M1.5-B100, the proportion of prolate cores is higher than that of oblate cores regardless of the classification method. Rot-M1.5-B100P and w/o-M1.5-B100 are models with weak turbulence and strong magnetic fields, which could lead to the formation of oblate cores due to the stronger influence of the magnetic field.

B.7 Core-Scale and Clump-Scale Field Relation and Energies of Cores.

Figure B.9 shows the correlation between $\angle[\mathbf{B}_{\text{core}}, \mathbf{B}_0]$ and energies of bound cores for Rotation and w/o Setup models. The first row of Figure B.9 presents the scatter plots (and correlation coefficients r) of $E_{\text{mag}}/|E_{\text{grav}}|$ vs. $\cos \angle[\mathbf{B}_{\text{core}}, \mathbf{B}_0]$. The second row shows the scatter plots of $E_{\text{kin}}/|E_{\text{grav}}|$ vs. $\cos \angle[\mathbf{B}_{\text{core}}, \mathbf{B}_0]$. As Figure B.9, Figure

Table B.1. Shape of identified cores

Model name	Axial ratio comparison		Triaxiality		
	Prolate (%)	Oblate (%)	Prolate (%)	Triaxial (%)	Oblate (%)
Rotation Setup					
Rot-M1.5-B10P	61.8	38.2	91.2	8.8	0.0
Rot-M1.5-B100P	20.6	79.4	61.8	32.2	5.9
Rot-M5-B10P	56.7	43.3	86.7	13.3	0.0
Rot-M5-B100P	50.0	50.0	87.5	12.5	0.0
w/o Setup					
w/o-M1.5-B10	58.6	41.4	90.0	8.6	1.4
w/o-M1.5-B100	19.4	80.6	72.2	25.0	2.8
w/o-M5-B10	68.4	31.6	78.9	18.4	2.6
w/o-M5-B100	60.0	40.0	90.0	10.0	0.0
Collision Setup (fast)					
Col-M1.5-B10P	54.2	45.8	87.5	12.5	0.0
Col-M1.5-B100P	50.0	50.0	88.5	7.7	3.8
Col-M5-B10P	60.7	39.3	78.6	21.4	0.0
Col-M5-B100P	70.8	29.2	91.7	4.2	4.2

Note. — The proportions of prolate and oblate determined by the comparison of $a_1 a_3$ and a_2^2 , and the proportions of prolate, triaxial, and oblate determined by the triaxiality T , are shown for each model.

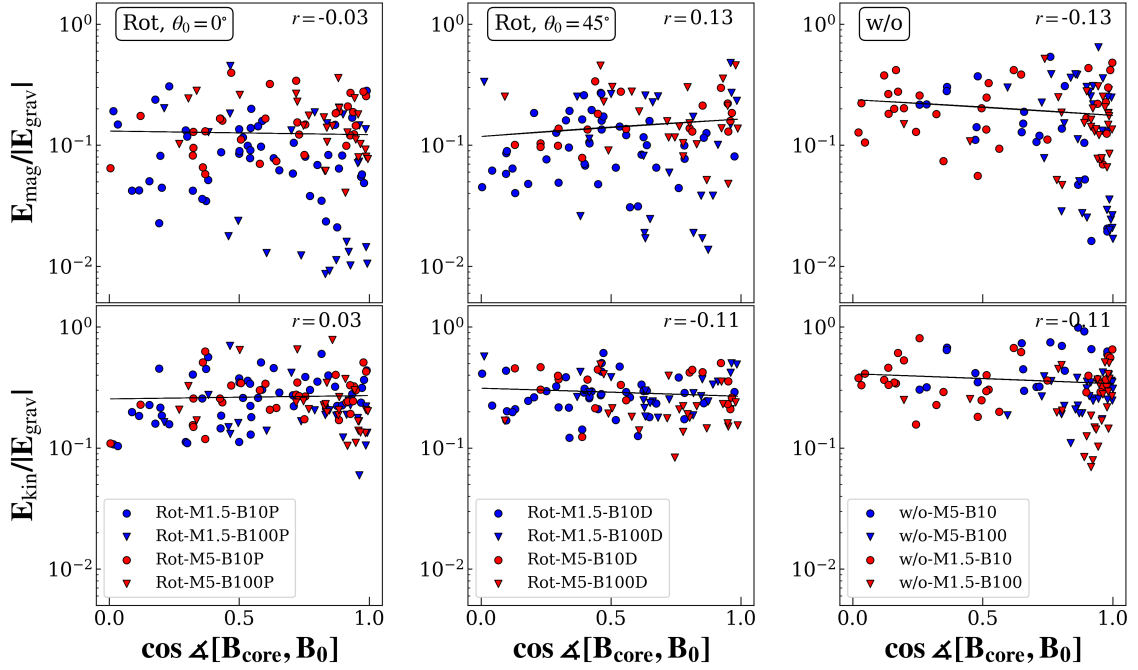


Figure B.9: Top row: Scatter plots (and correlation coefficients r) of $E_{\text{mag}}/|E_{\text{grav}}|$ vs. $\cos \angle[\mathbf{B}_{\text{core}}, \mathbf{B}_0]$. Rotation Setup models with $\theta_0 = 0^\circ$ are shown in the left panel, while $\theta_0 = 45^\circ$ models are shown in the middle panel. The right panel shows the results of w/o Setup. Bottom row: Scatter plots of $E_{\text{kin}}/|E_{\text{grav}}|$ vs. $\cos \angle[\mathbf{B}_{\text{core}}, \mathbf{B}_0]$. The independence of $\angle[\mathbf{B}_{\text{core}}, \mathbf{B}_0]$ with $E_{\text{mag}}/|E_{\text{grav}}|$ is confirmed. $\angle[\mathbf{B}_{\text{core}}, \mathbf{B}_0]$ is also independent of $E_{\text{kin}}/|E_{\text{grav}}|$.

B.10 shows $E_{\text{mag}}/|E_{\text{grav}}|$ and $E_{\text{kin}}/|E_{\text{grav}}|$ for Collision Setup models. As a whole, the correlation between $\angle[\mathbf{B}_{\text{core}}, \mathbf{B}_0]$ and $E_{\text{mag}}/|E_{\text{grav}}|$ is weak. The correlation between $\angle[\mathbf{B}_{\text{core}}, \mathbf{B}_0]$ and $E_{\text{kin}}/|E_{\text{grav}}|$ is also not strong.

It is conceivable that as the core evolves, \mathbf{B}_{core} becomes misaligned with \mathbf{B}_0 , that is $\angle[\mathbf{B}_{\text{core}}, \mathbf{B}_0]$ might simply reflect the core's evolution (the steeper gravitational potential could become dominant over the magnetic tension, causing the local magnetic field direction to twist relative to \mathbf{B}_0). However, this interpretation is not plausible because the correlation between $\angle[\mathbf{B}_{\text{core}}, \mathbf{B}_0]$ and $E_{\text{mag}}/|E_{\text{grav}}|$ is weak.

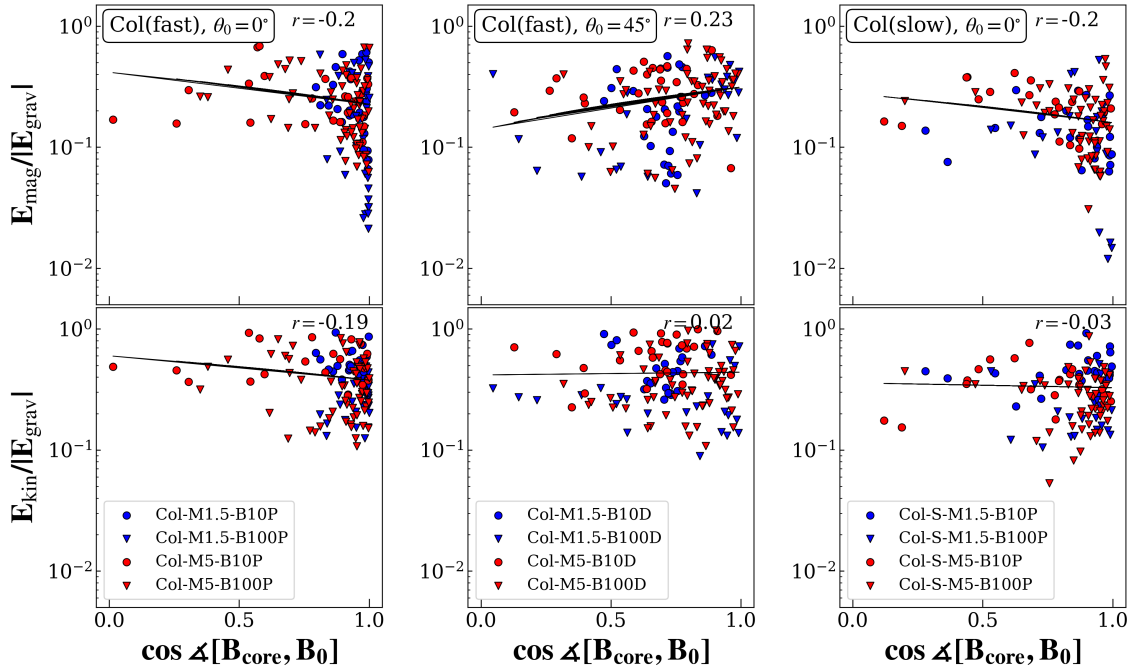


Figure B.10: Same as Figure B.6 except for Collision Setup models. Fast collision velocity cases with $\theta_0 = 0^\circ$ are shown in the left panel, and those of $\theta_0 = 45^\circ$ are shown in the middle panel. Slow collision velocity cases are shown in the right panel. $\angle[\mathbf{B}_{\text{core}}, \mathbf{B}_0]$ does not depend on either $E_{\text{mag}}/|E_{\text{grav}}|$ and $E_{\text{kin}}/|E_{\text{grav}}|$.

B.8 Magnetic Field-Density Relation for Simulated Cluster-Forming Clumps

Figure B.11 - B.14 show the phase plots of B versus the number density n_{H} (see Appendix A.5). In each figure, models with the same initial turbulence strength \mathcal{M} and magnetic field intensity B_0 are compared.

For models of Collision Setup, the slope of B versus n_{H} relation is steeper than other Setups. Collision generally produces stronger field strengths for a given density. In the gas compression perpendicular to the magnetic field, the power law indexes of $n_{\text{H}} - B$ relation are expected to approach 1, which is steeper than in an isotropic contraction (e.g., Li, 2021). In Collision Setups, we observe the gas compression perpendicular to the magnetic field (see § 2.3.2.2). Therefore, such compression forms stronger field strengths for a given density in the Collision Setups.

Comparing the models with the same setup and \mathcal{M} , we can see that the overall distribution of B is narrower when B_0 is higher. The power law index in the B versus n_{H} relation decreases as B_0 increases.

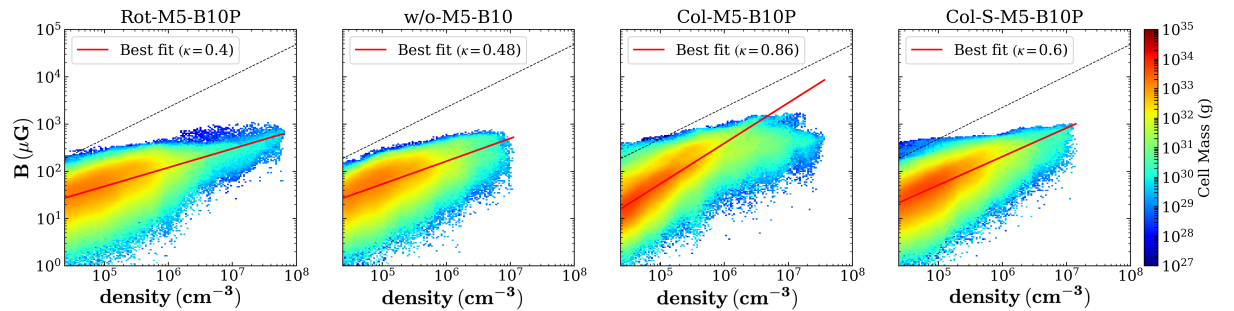


Figure B.11: Phase plots of B versus n_{H} among models with $\mathcal{M} = 5$, $B_0 = 10\mu\text{G}$, and $\theta = 0^\circ$. From left to right are Rotation, w/o, Collision(fast), and Collision(slow) Setups, respectively, for cell mass distributions. The realization of the input turbulence is common. Results are displayed when gas over a number density of 10^6cm^{-3} is exactly 10% of the total clump mass M_{total} . Red lines indicate the best-fit power law relation, $B \propto n_{\text{H}}^\kappa$. Black dashed lines show the "Crutcher relation" (see Appendix A.5).

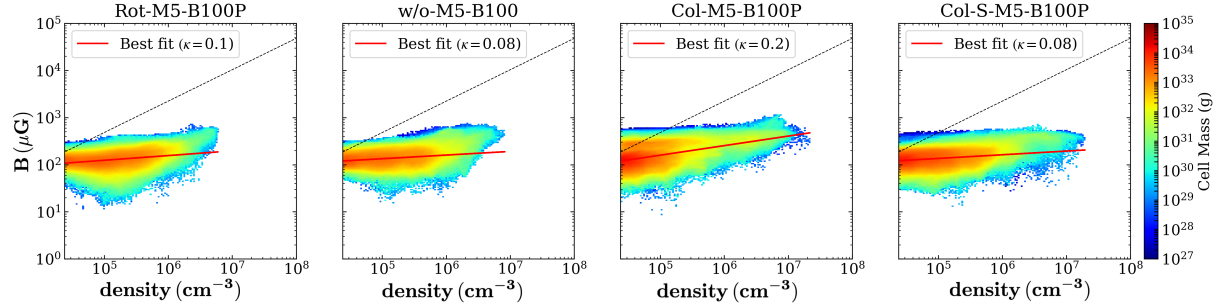


Figure B.12: Same as Figure B.11 except for models with $\mathcal{M} = 5$, $B_0 = 100 \mu\text{G}$, and $\theta = 0^\circ$.

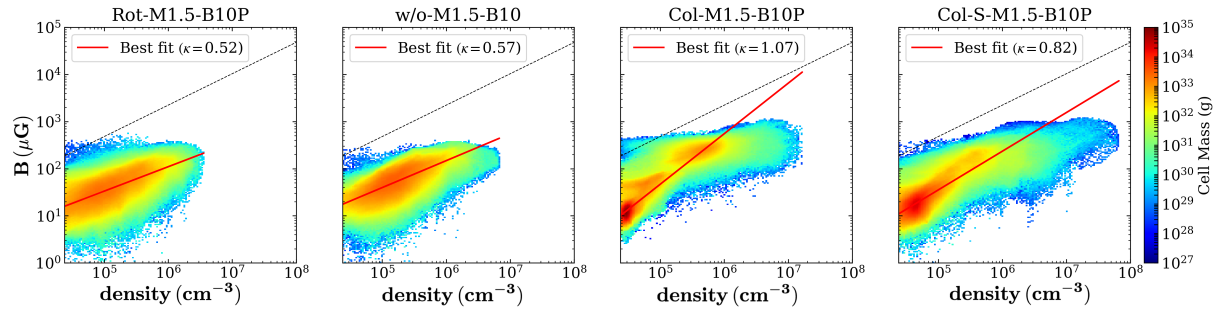


Figure B.13: Same as Figure B.11 except for models with $\mathcal{M} = 1.5$, $B_0 = 10 \mu\text{G}$, and $\theta = 0^\circ$.

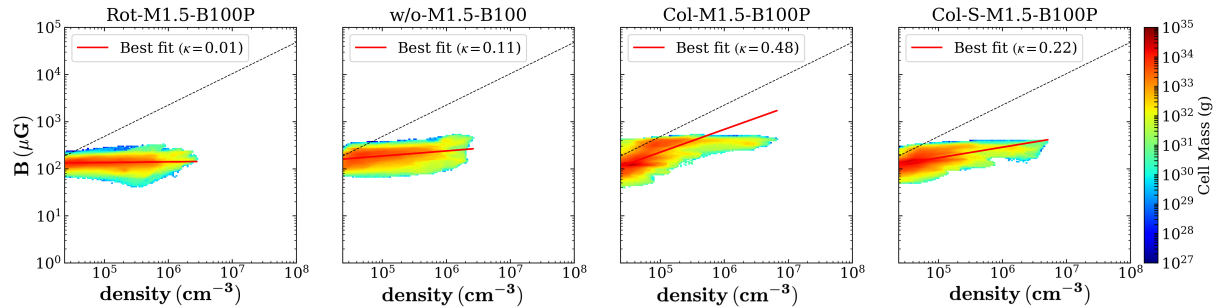


Figure B.14: Same as Figure B.11 except for models with $\mathcal{M} = 1.5$, $B_0 = 100 \mu\text{G}$, and $\theta = 0^\circ$.

B.9 High-Resolution Runs

As outlined in Section 2.2.2, our simulations employ a refinement criterion that resolves the Jeans length with 8 cells, and a maximum refinement level of 5. For select models, we have also conducted high-resolution runs with a more stringent refinement criterion that resolves the Jeans length with 16 cells ($\Delta x \leq \lambda_J/16$) and extends the maximum refinement level to 6 (therefore, n_{crit} does not change). Table B.2 lists the explored parameter space for high-resolution runs. Except for the refinement criterion and the maximum refinement level, the high-resolution simulations maintain the same initial conditions and core identification methods as described in Section 2.2. In this section, we will demonstrate that key trends observed in the simulated cores we have presented so far are also evident in high-resolution runs.

B.9.1 Angular Momentum for High-Resolution Runs

Here, we examine trends of the relative angle between the angular momentum of the core, \mathbf{L}_{core} , and the global rotational axis of the clump, $\mathbf{\Omega}_0$ ($\mathbf{\Omega}_{\text{col}}$). Figure B.15 shows histograms of the cosine of the relative angles between $\mathbf{\Omega}_0$ and \mathbf{L}_{core} for high-resolution runs of Rotation Setup models. For all models with weak turbulence (indicated by blue lines), the distribution of $\cos \angle[\mathbf{L}_{\text{core}}, \mathbf{\Omega}_0]$ has clear peak in the range of 0.83-1.0 and the null hypothesis that “the distribution is uniform” is rejected at a significance level of 5% using the K-S test. Therefore, in models with weak turbulence, the rotation of the parental clump is passed down to the bound cores. On the other hand, in models with strong turbulence (indicated by red lines), the distribution of spin axes is close to isotropic, and the null hypothesis that “the distribution is uniform” cannot be rejected. This uniform distribution suggests that strong turbulence disturbs the inheritance of clump rotation to bound cores. These trends are consistent with the findings in § 2.3.1.1.

Figure B.16 illustrates histograms of $\cos \angle[\mathbf{L}_{\text{core}}, \mathbf{\Omega}_{\text{col}}]$ for high-resolution runs of Collision (fast) Setup models. As shown in § 2.3.2.1, for all models of Collision (fast) Setup, distributions of $\cos \angle[\mathbf{L}_{\text{core}}, \mathbf{\Omega}_{\text{col}}]$ are almost uniform. In these models, the null hypothesis that “the distribution is uniform” is not rejected. Such random distribution of the angle between \mathbf{L}_{core} and $\mathbf{\Omega}_{\text{col}}$ is consistent with results in § 2.3.2.1.

Table B.2. Summary of simulation results and explored parameter space for high-resolution runs

Model name	V_0^a (km s ⁻¹)	\mathcal{M}^b	B_0^c (μG)	θ_0^d ($^\circ$)	$S_{L,\Omega}^e$	S_{B,B_0}^f	$S_{L,B}^g$	N_{core}^h
Rotation Setup								
HR-Rot-M1.5-B10P	...	1.5	10	0	0.45	0.07	0.02	65
HR-Rot-M1.5-B100P	...	1.5	100	0	0.43	0.56	0.25	36
HR-Rot-M5-B10P	...	5	10	0	0.18	0.14	0.03	30
HR-Rot-M5-B100P	...	5	100	0	0.10	0.48	-0.02	34
HR-Rot-M1.5-B10D	...	1.5	10	45	0.58	-0.08	-0.05	49
HR-Rot-M1.5-B100D	...	1.5	100	45	0.37	0.36	0.03	40
HR-Rot-M5-B10D	...	5	10	45	0.14	0.15	-0.06	22
HR-Rot-M5-B100D	...	5	100	45	0.02	0.34	0.09	26
w/o Setup								
HR-w/o-M1.5-B10	...	1.5	10	0	...	0.34	0.01	70
HR-w/o-M1.5-B100	...	1.5	100	0	...	0.76	-0.14	36
HR-w/o-M5-B10	...	5	10	0	...	0.17	0.05	38
HR-w/o-M5-B100	...	5	100	0	...	0.66	-0.01	40
Collision Setup (fast)								
HR-Col-M1.5-B10P	2.8	1.5	10	0	-0.08	0.85	0.00	21
HR-Col-M1.5-B100P	2.8	1.5	100	0	0.20	0.92	0.19	26
HR-Col-M5-B10P	2.8	5	10	0	0.08	0.58	0.03	28
HR-Col-M5-B100P	2.8	5	100	0	-0.06	0.69	0.09	29
HR-Col-M1.5-B10D	2.8	1.5	10	45	-0.12	0.26	-0.12	24
HR-Col-M1.5-B100D	2.8	1.5	100	45	-0.04	0.43	0.05	37
HR-Col-M5-B10D	2.8	5	10	45	0.04	0.17	-0.15	20
HR-Col-M5-B100D	2.8	5	100	45	0.04	0.40	0.07	26

Note. — ^a The pre-collision velocity of the clump. ^b The Mach number of turbulence. ^c The strength of initial magnetic field. ^d The angle between the initial magnetic field \mathbf{B}_0 relative to the $\mathbf{\Omega}_0$ ($\mathbf{\Omega}_{\text{col}}$). ^e The orientation parameter $S_{L,\Omega} = (3\langle \cos^2 \angle[\mathbf{L}_{\text{core}}, \mathbf{\Omega}_0(\mathbf{\Omega}_{\text{col}})] \rangle - 1)/2$. ^f The orientation parameter $S_{B,B_0} = (3\langle \cos^2 \angle[\mathbf{B}_{\text{core}}, \mathbf{B}_0] \rangle - 1)/2$. ^g The orientation parameter $S_{L,B} = (3\langle \cos^2 \angle[\mathbf{L}_{\text{core}}, \mathbf{B}_{\text{core}}] \rangle - 1)/2$. ^h The total number of identified bound cores.

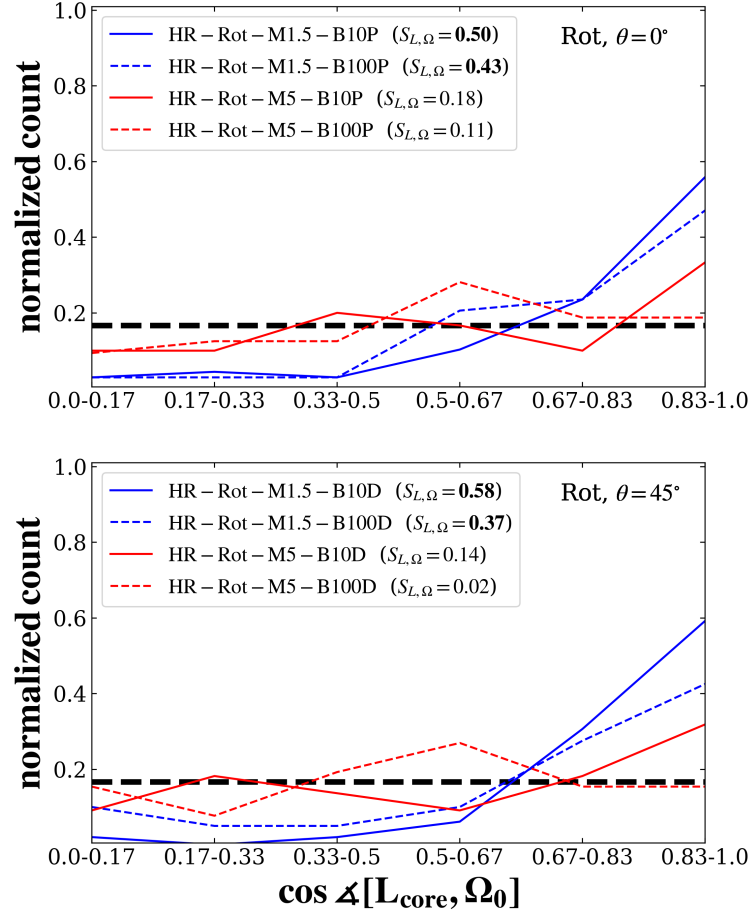


Figure B.15: Same as Figure 2.4 except for high-resolution runs of Rotation Setup models. As in Figure 2.4, there is a clear tendency for \mathbf{L}_{core} and $\mathbf{\Omega}_0$ to align for all models with weak turbulence (indicated by blue lines), while no tendency for alignment is observed for the strong turbulence models (indicated by red lines).

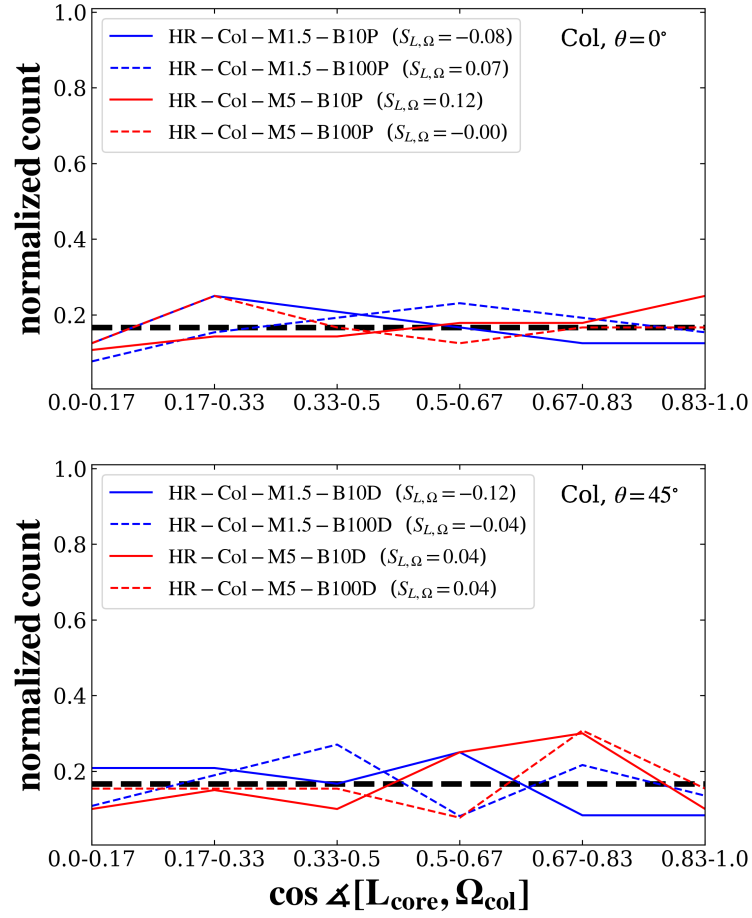


Figure B.16: Same as Figure 2.10 except for high-resolution runs of Collision Setup models. As in Figure 2.10, for all models in the Collision Setup, the angles are close to being isotropically distributed, and no tendency for alignment is observed.

B.9.2 Magnetic Field for High-resolution Runs

We explore the correlation between the mean magnetic field within the core, \mathbf{B}_{core} , and the initial magnetic field of the clump, \mathbf{B}_0 . Figure B.17 shows the histograms of the cosine of the angle between \mathbf{B}_{core} and \mathbf{B}_0 for high-resolution runs of Rotation Setup and w/o Setup models. All models with strong B_0 (indicated by dashed lines) indicate a tendency for \mathbf{B}_{core} to align with \mathbf{B}_0 . The null hypothesis that “the distribution is uniform” is rejected at a significance level of 5% for all models with strong B_0 . That is, with strong B_0 , \mathbf{B}_{core} inherits the initial orientation of the clump’s field. For models with weak B_0 , the degree of alignment between \mathbf{B}_{core} and \mathbf{B}_0 is weaker compared to models of strong B_0 . The relationship between \mathbf{B}_{core} and \mathbf{B}_0 is heavily influenced by the initial magnetic field strength B_0 . This tendency matches with results in § 2.3.1.2.

Figure B.18 illustrates the histograms of $\cos \angle[\mathbf{B}_{\text{core}}, \mathbf{B}_0]$ for high-resolution runs of Collision (fast) Setup models. In $\theta_0 = 0^\circ$ models (shown in the top panel), the alignment tendency between \mathbf{B}_{core} and \mathbf{B}_0 is strong in both weak and strong B_0 models. This clear alignment is considered to reflect the large-scale magnetic fields along the compressed layer, as shown in Figure 2.13. The bottom panel of Figure B.18 shows results of fast collision models with $\theta_0 = 45^\circ$. In these models with weak B_0 (indicated by solid lines), the peak of the distribution of $\cos \angle[\mathbf{B}_{\text{core}}, \mathbf{B}_0]$ is not within the range of 0.83-1.0. models. On the other hand, as shown in Figure B.19, weak B_0 models indicate the strong trend for \mathbf{B}_{core} to align with Ω_{col} . The collision-axis determines the direction of \mathbf{B}_{core} , particularly in models with a weak B_0 , similar to the results shown in § 2.3.2.2.

B.9.3 Rotation-Magnetic Field Relation for High-Resolution Runs

We investigate the relative angle between \mathbf{L}_{core} and \mathbf{B}_{core} . Figure B.20 depicts the CDF of the cosine of the relative angle between \mathbf{L}_{core} and \mathbf{B}_{core} for high-resolution runs of Rotation Setup and w/o Setup models. In models other than Rot-M1.5-B100P, the CDF appears to be a relatively straight line, and the null hypothesis that “the distribution is uniform” is not rejected at a significance level of 5 % using the K-S test. Figure B.21 similarly shows the CDF of $\cos \angle[\mathbf{L}_{\text{core}}, \mathbf{B}_{\text{core}}]$ for high-resolution runs of Collision (fast) Setup models. In all models of Collision (fast) Setup, the CDF

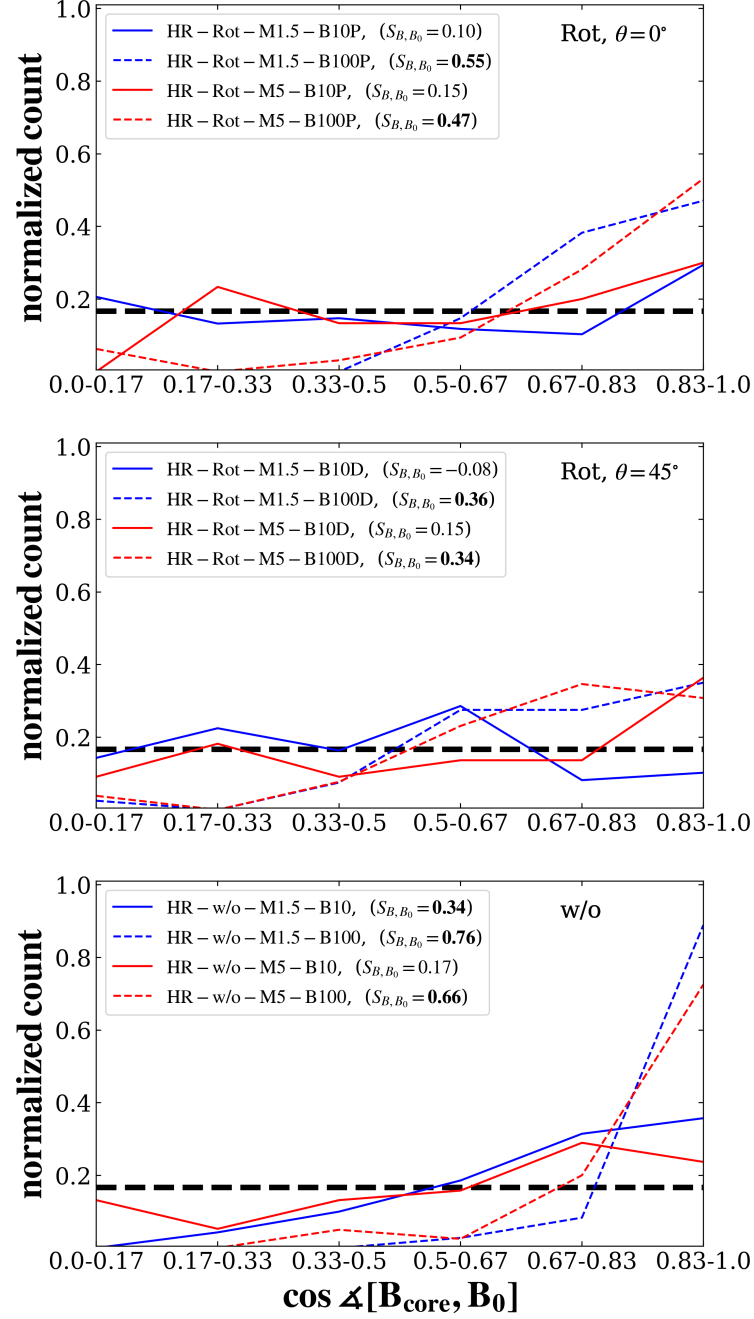


Figure B.17: Same as Figure 2.7 except for high-resolution runs of Rotation Setup and w/o Setup models. As in Figure 2.7, in models with strong magnetic fields (indicated by dashed lines), the strong alignment between B_{core} and B_0 is observed.

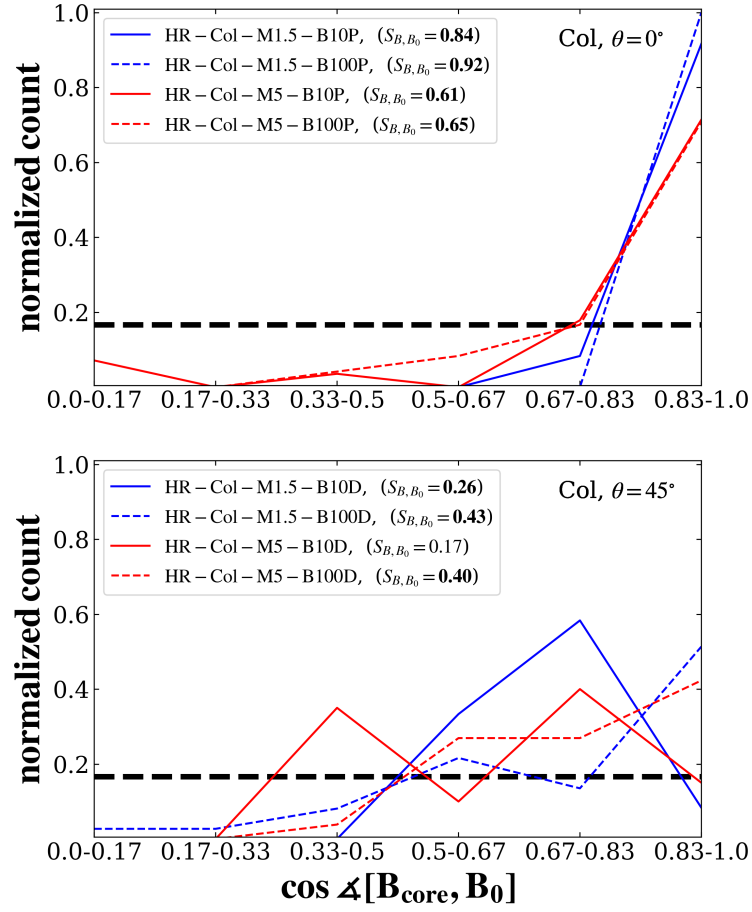


Figure B.18: Same as Figure 2.12 except for high-resolution runs of Rotation Setup models.

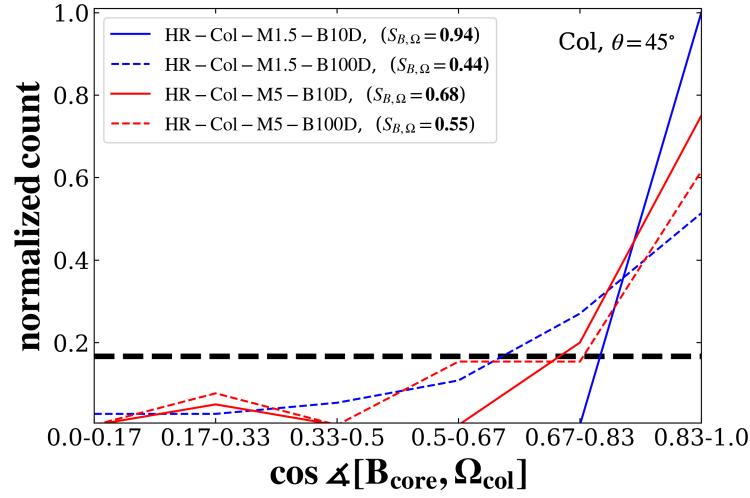


Figure B.19: Same as Figure 2.14 except for high-resolution runs. As in Figure 2.14, in models with weak magnetic fields (indicated by solid lines), the strong alignment of \mathbf{B}_{core} with $\boldsymbol{\Omega}_{\text{col}}$ is observed. In the weak magnetic field model, $S_{B,\Omega}$ is higher than S_{B,B_0} , indicating that the direction of \mathbf{B}_{core} is determined by the direction of collision axis.

appears close to a uniform distribution, and the null hypothesis that “the distribution is uniform” is not rejected. As discussed in § 2.4.2, except for limited initial conditions, the relative angle between \mathbf{L}_{core} and \mathbf{B}_{core} is randomly determined.

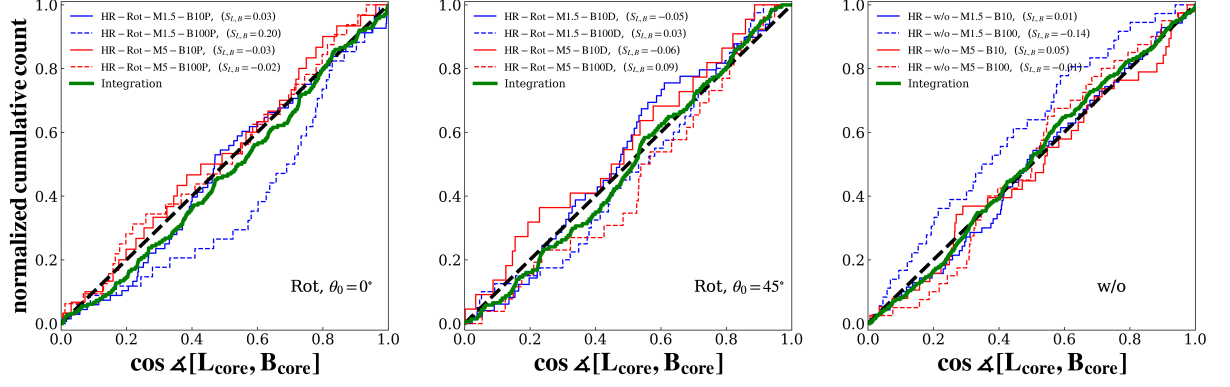


Figure B.20: Same as Figure 2.9 except for high-resolution runs of Rotation Setup and w/o Setup models. As in Figure 2.9, in most models, they suggest random distributions of $\Delta[\mathbf{L}_{\text{core}}, \mathbf{B}_{\text{core}}]$.

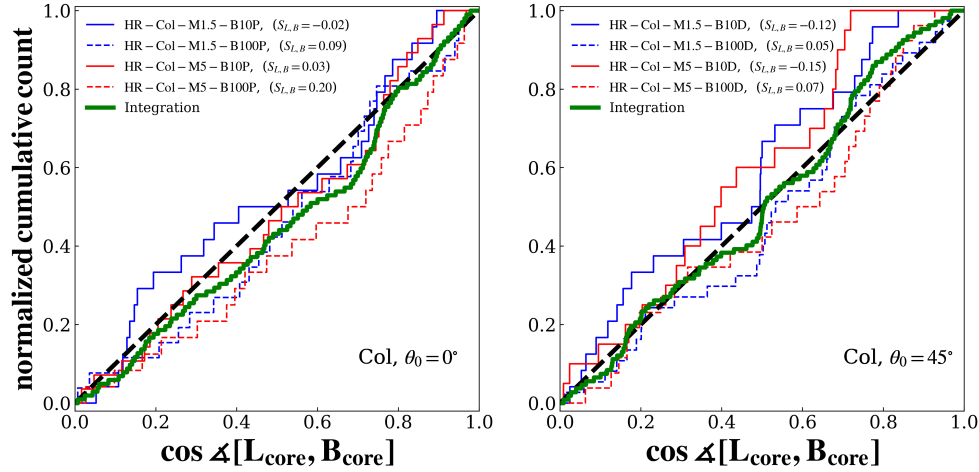


Figure B.21: Same as Figure 2.16 except for high-resolution runs of Collision Setup models. As in Figure 2.16, in most models, they suggest random distributions of $\Delta[\mathbf{L}_{\text{core}}, \mathbf{B}_{\text{core}}]$.

Appendix C

Appendix of Chapter 3

C.1 Estimation of Collision Rate

Here, we will roughly estimate the collision rate between prestellar cores using identified cores, including both bound and unbound ones for w/o Setup models in Chapter 2. As described in § 1.5, the collision timescale is calculated using the Equation 1.3, $\tau_{\text{coll}} = 1/(4\pi r_c^2 n_c v_c)$.

For each core, its mean velocity v_{core} is derived as follows:

$$v_{\text{core}} = \frac{|\sum_i \mathbf{v}_i \rho_i \Delta V_i|}{M_{\text{core}}}. \quad (\text{C.1})$$

The number density of cores is estimated using the separation distances between them, applying the minimum spanning tree (MST) method to calculate the nearest neighboring separations of identified cores. The MST is a graph theory technique that connects a set of points with a set of straight lines such that the total length of the lines is minimized. MST was initially introduced by (Barrow et al., 1985) for astrophysical applications and has since been widely utilized in the research of the spatial distribution of star-forming objects like dense cores (e.g., Wu et al. 2020; Zhang et al. 2021). The number density of cores is derived as:

Table C.1. Properties of cores in models of w/o Setups

Model Name	$\langle v_{\text{core}} \rangle$ (km s ⁻¹)	$\langle R_{\text{core}} \rangle$ (pc)	$\langle l_{\text{core}} \rangle$ (pc)	τ_{col} (Myr)	P_{col}
w/o-M1.5-B10	2.7	1.8×10^{-2}	0.10	0.06	0.44
w/o-M1.5-B100	2.3	2.5×10^{-2}	0.16	0.11	0.25
w/o-M5-B10	1.7	1.2×10^{-2}	0.11	0.28	0.11
w/o-M5-B100	1.3	1.4×10^{-2}	0.13	0.43	0.08

$$n_{\text{core}} = \left[\frac{4}{3} \pi \left(\frac{\langle l_{\text{core}} \rangle}{2} \right)^3 \right]^{-1} \quad (\text{C.2})$$

where $\langle l_{\text{core}} \rangle$ represents the average core MST separations.

Substituting $v_c = \langle v_{\text{core}} \rangle$, $r_c = \langle R_{\text{core}} \rangle$ ¹, and $n_c = n_{\text{core}}$ into Equation 1.3, we estimated the collision timescale τ_{col} . Additionally, the probability of a core experiencing one or more collisions with other cores is calculated using the formula provided by [Hills & Day \(1976\)](#):

$$P_{\text{col}} = 1 - \exp \left(-\frac{t_{\text{lf}}}{\tau_{\text{col}}} \right), \quad (\text{C.3})$$

where t_{lf} is the core lifetime. We adopt a typical value of $t_{\text{lf}} = t_{\text{ff}} \equiv (3\pi/[32G\mu_{\text{H}}n_{\text{th}}])^{1/2}$. Table C.1 summarizes the estimated P_{col} for each w/o Setup model.

We note that these estimates are approximate, based on mean values and assumptions. For a more precise understanding of the collision rate, tracking each core and accurately identifying collisions would be more effective.

¹The symbol $\langle \rangle$ denotes the average across all identified cores.

C.2 Comparison with Observed Magnetic Spirals

Recent ALMA observations of the high mass star-forming regions IRAS 18089-1732 (Sanhueza et al., 2021) found that the dense molecular envelope surrounding the high-mass star has a complex spiral pattern at the 0.003–0.1 pc scales. This spiral morphology is seen in the gas and dust as well as in the distribution of the linear polarization vectors. Sanhueza et al. (2021) suggested that the core gravitational energy dominates over the rotational energy and magnetic energy.

As shown in § 3.3.2, $b = 1$ models show rotational gas flows and magnetic fields presenting spiral features. Through the collision process, the rotational motion around the particles was generated, and magnetic field lines are twisted along the spiral arm. To further investigate the formation of such spiral arm and their observational features, we briefly examine additional models of the collision of unequal-mass cores. In these models, initially, we prepared two stable BE spheres with a mass ratio of 4:1. One has the radius $r_{c1} = 0.03$ pc, central density $\rho_{c1} = 10^5 \text{ cm}^{-3}$, temperature $T_{c1} = 10$ K, and mass $M_{c1} = 0.5 M_{\odot}$. The other is larger and heavier with $r_{c2} = 0.06$ pc, central density $\rho_{c2} = 5.0 \times 10^4 \text{ cm}^{-3}$, temperature $T_{c2} = 20$ K, and mass $M_{c2} = 2.0 M_{\odot}$. The gas components initially contained in the small and large cores are labeled with color variables $(C_1, C_2) = (1, 0)$ and $(0, 1)$, respectively. On the other hand, the ambient gas is labeled $(C_1, C_2) = (0, 0)$. For both cores, pressure balances at the core boundary are satisfied. The cores have the pre-collision speed $v_c = 0.19 \text{ km s}^{-1}$ in the y -direction, which corresponds to the sound speed in the smaller core. The colliding cores are displaced by an impact parameter r_{c2} along the x -direction. We initially impose a uniform magnetic field, which is parallel to the collision direction. We selected the $B_y = 1 \mu\text{G}$ which correspond to $\mu_{\Phi} = 43$.

Figure C.1 shows the column density maps and P-V diagrams of the collision of unequal-mass cores for $B_y = 1 \mu\text{G}$. In these visualizations, we use (x', y', z') , where the axes are rotated 30 degrees around the x -axis. We set the line of sight parallel to the z' -axis. P-V diagrams are created by PPV cube $N_u(x', y', u)$ (see Appendix A.8). Figure C.2 shows the evolution of mass and mass accretion rate of the sink particle. The contribution from each core is indicated based on the analysis using color variables. Initially, the smaller core plunged into the larger core, and a compressed layer formed in front of the core. On the P-V diagram, this compressed layer can be recognized as a bridge feature linking the two cores. This bridge feature is a characteristic of gas

collisional interaction (e.g., [Haworth et al., 2015](#)). At $t = 0.26$ Myr, a sink particle was created, and gas components of the smaller core accreted onto the particle. Larger core components proceeded toward the y' -positive direction. Around $t = 0.4$ Myr, accretion from smaller core components almost ended, and then secondary accretion from the larger core components took over. Larger core components accreted rotating anti-clockwise around the particle. As shown in the rightmost panel, a one-arm spiral pattern resembling a whirlpool was formed. The polarization vectors follow this spiral stream. In the P-V diagram, the black line delineates the spiral structures. The velocity increases closer to the sink particle, implying the infall and accelerating close to the particle. The ring-like structure with a large velocity range near $y' = 0$ corresponds to a rotating falling gas near a particle.

This geometry of the one-arm spiral streamer is similar to features of IRAS 18089-1732 ([Sanhueza et al., 2021](#)). We note that our models do not investigate massive star formation, and physical quantities such as magnetic field strength, mass, and gas velocities observed in [Sanhueza et al. \(2021\)](#) are different from those in our simulation. However, qualitatively, our model is consistent with observations. Our results and the observed regions share similar spiral patterns of gas and magnetic fields. Our simulations suggest that collisions of unequal-mass cores in the weak magnetic field can be one of the mechanisms that generate the spiral structure of gas and magnetic field, sometimes observed around protostars.

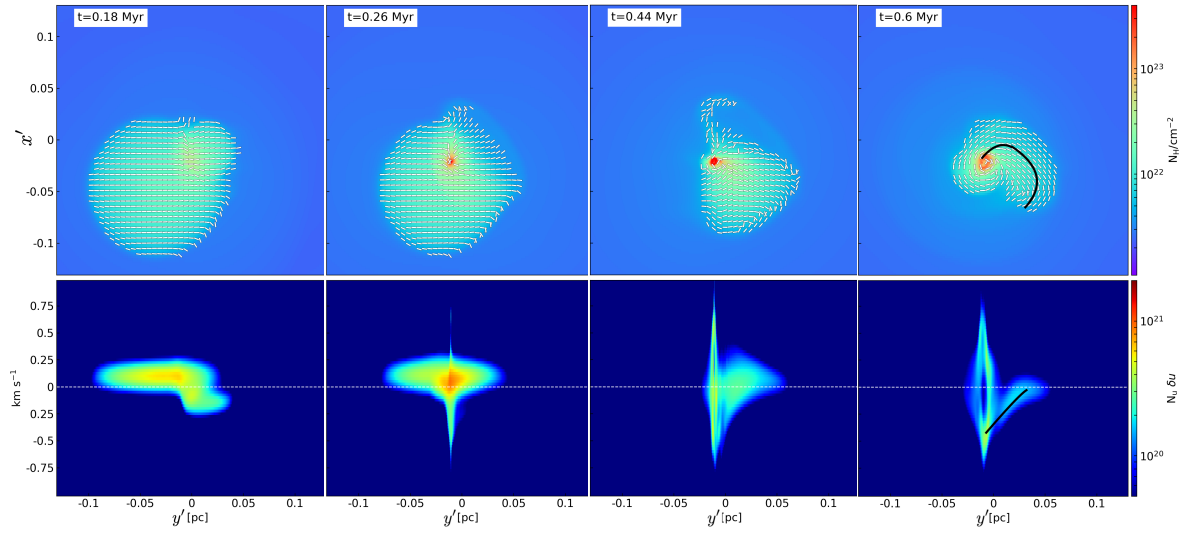


Figure C.1: Time evolution of the column density and position-velocity diagrams for the collision of unequal-mass cores. *Top*: time evolution of the column density. White pseudovectors indicate the normalized plane-of-sky magnetic polarization field, \mathbf{p} . In the rightmost panel, the black line delineates the spiral structures. *Bottom*: position-velocity diagrams are shown directly below their corresponding column density maps. In the rightmost panel, the spiral structure is indicated. In this visualization, we use (x', y', z') , where the axes are rotated 30 degrees around the x -axis. We set the line of sight parallel to the z' -axis. Snapshots at 0.18, 0.26, 0.44, and 0.6 are shown.

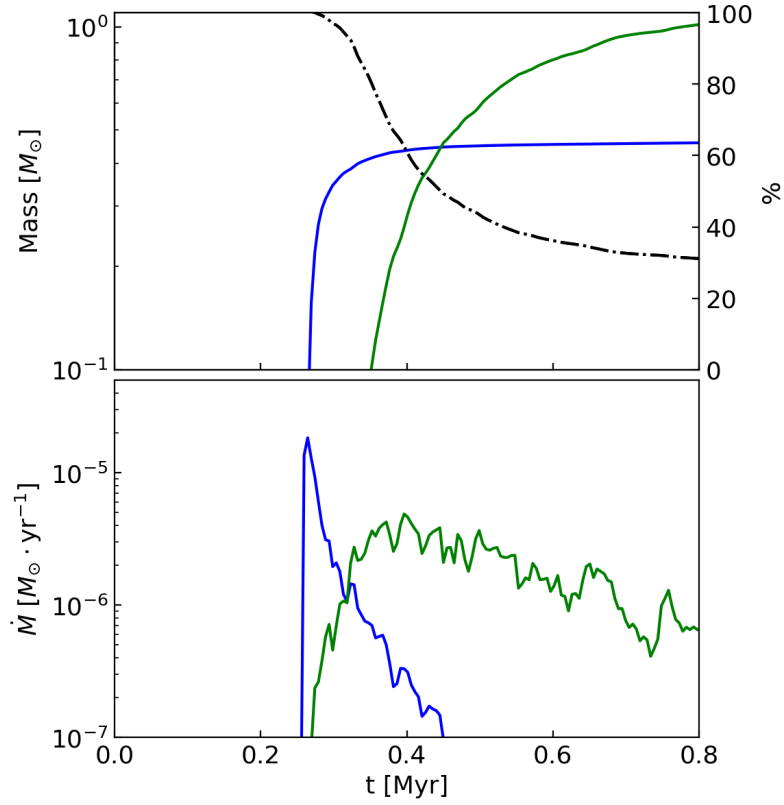


Figure C.2: Evolution of mass (top) and mass accretion rate (bottom) of the sink particle for the collision of unequal-mass cores. The blue lines correspond to the contribution from the gas that is initially labeled $C_1 = 1.0$. The green lines correspond to that of the gas that is initially labeled $C_2 = 1.0$. In the top row, the black dashed-dot lines indicate the fraction in the sink particle of the gas that is initially labeled $C_1 = 1.0$.

Bibliography

- Abe, D., Inoue, T., Inutsuka, S.-i., & Matsumoto, T. 2021, *ApJ*, 916, 83, doi: [10.3847/1538-4357/ac07a1](https://doi.org/10.3847/1538-4357/ac07a1)
- Allen, A., Li, Z.-Y., & Shu, F. H. 2003, *ApJ*, 599, 363, doi: [10.1086/379243](https://doi.org/10.1086/379243)
- Alves, F. O., Frau, P., Girart, J. M., et al. 2014, *A&A*, 569, L1, doi: [10.1051/0004-6361/201424678](https://doi.org/10.1051/0004-6361/201424678)
- Arreaga-García, G., & Klapp, J. 2015, *Astronomische Nachrichten*, 336, 695, doi: [10.1002/asna.201512204](https://doi.org/10.1002/asna.201512204)
- Barranco, J. A., & Goodman, A. A. 1998, *ApJ*, 504, 207, doi: [10.1086/306044](https://doi.org/10.1086/306044)
- Barrow, J. D., Bhavsar, S. P., & Sonoda, D. H. 1985, *MNRAS*, 216, 17, doi: [10.1093/mnras/216.1.17](https://doi.org/10.1093/mnras/216.1.17)
- Bate, M. R., Bonnell, I. A., & Bromm, V. 2003, *MNRAS*, 339, 577, doi: [10.1046/j.1365-8711.2003.06210.x](https://doi.org/10.1046/j.1365-8711.2003.06210.x)
- Bergin, E. A., & Tafalla, M. 2007, *ARA&A*, 45, 339, doi: [10.1146/annurev.astro.45.071206.100404](https://doi.org/10.1146/annurev.astro.45.071206.100404)
- Bhandare, A., Kuiper, R., Henning, T., et al. 2018, *A&A*, 618, A95, doi: [10.1051/0004-6361/201832635](https://doi.org/10.1051/0004-6361/201832635)
- Bonnell, I. A., Bate, M. R., & Vine, S. G. 2003, *MNRAS*, 343, 413, doi: [10.1046/j.1365-8711.2003.06687.x](https://doi.org/10.1046/j.1365-8711.2003.06687.x)
- Bonnor, W. B. 1956, *MNRAS*, 116, 351, doi: [10.1093/mnras/116.3.351](https://doi.org/10.1093/mnras/116.3.351)
- Boss, A. P., & Keiser, S. A. 2013, *ApJ*, 764, 136, doi: [10.1088/0004-637X/764/2/136](https://doi.org/10.1088/0004-637X/764/2/136)

- Bouvier, J., Cabrit, S., Fernandez, M., Martin, E. L., & Matthews, J. M. 1993, *A&A*, 272, 176
- Bryan, G. L., Norman, M. L., O'Shea, B. W., et al. 2014, *ApJS*, 211, 19, doi: [10.1088/0067-0049/211/2/19](https://doi.org/10.1088/0067-0049/211/2/19)
- Burkert, A., & Bodenheimer, P. 2000, *ApJ*, 543, 822, doi: [10.1086/317122](https://doi.org/10.1086/317122)
- Caselli, P., Benson, P. J., Myers, P. C., & Tafalla, M. 2002, *ApJ*, 572, 238, doi: [10.1086/340195](https://doi.org/10.1086/340195)
- Chandrasekhar, S., & Fermi, E. 1953, *ApJ*, 118, 113, doi: [10.1086/145731](https://doi.org/10.1086/145731)
- Chapman, S., Pongracic, H., Disney, M., et al. 1992, *Nature*, 359, 207, doi: [10.1038/359207a0](https://doi.org/10.1038/359207a0)
- Chen, C.-Y., King, P. K., & Li, Z.-Y. 2016, *ApJ*, 829, 84, doi: [10.3847/0004-637X/829/2/84](https://doi.org/10.3847/0004-637X/829/2/84)
- Chen, C.-Y., & Ostriker, E. C. 2018, *ApJ*, 865, 34, doi: [10.3847/1538-4357/aad905](https://doi.org/10.3847/1538-4357/aad905)
- Chen, C.-Y., Storm, S., Li, Z.-Y., et al. 2019, *MNRAS*, 490, 527, doi: [10.1093/mnras/stz2633](https://doi.org/10.1093/mnras/stz2633)
- Chen, C.-Y., Behrens, E. A., Washington, J. E., et al. 2020, *MNRAS*, 494, 1971, doi: [10.1093/mnras/staa835](https://doi.org/10.1093/mnras/staa835)
- Chen, H. H.-H., Pineda, J. E., Offner, S. S. R., et al. 2019, *ApJ*, 886, 119, doi: [10.3847/1538-4357/ab4ce9](https://doi.org/10.3847/1538-4357/ab4ce9)
- Chen, X., Launhardt, R., & Henning, T. 2007, *The Astrophysical Journal*, 669, 1058, doi: [10.1086/521868](https://doi.org/10.1086/521868)
- Ciardi, A., & Hennebelle, P. 2010, *MNRAS*, 409, L39, doi: [10.1111/j.1745-3933.2010.00942.x](https://doi.org/10.1111/j.1745-3933.2010.00942.x)
- Corsaro, E., Lee, Y.-N., García, R. A., et al. 2017, *Natas*, 1, 0064, doi: [10.1038/s41550-017-0064](https://doi.org/10.1038/s41550-017-0064)
- Crutcher, R. M. 2012, *ARA&A*, 50, 29, doi: [10.1146/annurev-astro-081811-125514](https://doi.org/10.1146/annurev-astro-081811-125514)
- Crutcher, R. M., & Kemball, A. J. 2019, *FrASS*, 6, 66, doi: [10.3389/fspas.2019.00066](https://doi.org/10.3389/fspas.2019.00066)

- Crutcher, R. M., Wandelt, B., Heiles, C., Falgarone, E., & Troland, T. H. 2010, *ApJ*, 725, 466, doi: [10.1088/0004-637X/725/1/466](https://doi.org/10.1088/0004-637X/725/1/466)
- Cunningham, A. J., Klein, R. I., Krumholz, M. R., & McKee, C. F. 2011, *ApJ*, 740, 107, doi: [10.1088/0004-637X/740/2/107](https://doi.org/10.1088/0004-637X/740/2/107)
- Dapp, W. B., Basu, S., & Kunz, M. W. 2012, *A&A*, 541, A35, doi: [10.1051/0004-6361/201117876](https://doi.org/10.1051/0004-6361/201117876)
- Davis, L. 1951, *PhRv*, 81, 890, doi: [10.1103/PhysRev.81.890.2](https://doi.org/10.1103/PhysRev.81.890.2)
- Dedner, A., Kemm, F., KrÄner, D., et al. 2002, *JCoPh*, 175, 645, doi: <https://doi.org/10.1006/jcph.2001.6961>
- Dib, S. 2023, arXiv e-prints, arXiv:2309.10842, doi: [10.48550/arXiv.2309.10842](https://doi.org/10.48550/arXiv.2309.10842)
- Dib, S., Hennebelle, P., Pineda, J. E., et al. 2010, *ApJ*, 723, 425, doi: [10.1088/0004-637X/723/1/425](https://doi.org/10.1088/0004-637X/723/1/425)
- Dobashi, K., Matsumoto, T., Shimoikura, T., et al. 2014, *ApJ*, 797, 58, doi: [10.1088/0004-637X/797/1/58](https://doi.org/10.1088/0004-637X/797/1/58)
- Doi, Y., Hasegawa, T., Furuya, R. S., et al. 2020, *ApJ*, 899, 28, doi: [10.3847/1538-4357/aba1e2](https://doi.org/10.3847/1538-4357/aba1e2)
- Ebert, R. 1955, *ZA*, 37, 217
- Falgarone, E., Troland, T. H., Crutcher, R. M., & Paubert, G. 2008, *A&A*, 487, 247, doi: [10.1051/0004-6361:200809577](https://doi.org/10.1051/0004-6361:200809577)
- Ferrière, K. M. 2001, *Reviews of Modern Physics*, 73, 1031, doi: [10.1103/RevModPhys.73.1031](https://doi.org/10.1103/RevModPhys.73.1031)
- Franx, M., Illingworth, G., & de Zeeuw, T. 1991, *ApJ*, 383, 112, doi: [10.1086/170769](https://doi.org/10.1086/170769)
- Fukui, Y., Habe, A., Inoue, T., Enokiya, R., & Tachihara, K. 2021, *PASJ*, 73, S1, doi: [10.1093/pasj/psaa103](https://doi.org/10.1093/pasj/psaa103)
- Gammie, C. F., Lin, Y.-T., Stone, J. M., & Ostriker, E. C. 2003, *ApJ*, 592, 203, doi: [10.1086/375635](https://doi.org/10.1086/375635)
- Gaudel, M., Maury, A. J., Belloche, A., et al. 2020, *A&A*, 637, A92, doi: [10.1051/0004-6361/201936364](https://doi.org/10.1051/0004-6361/201936364)

- Girart, J. M., Beltrán, M. T., Zhang, Q., Rao, R., & Estalella, R. 2009, *Sci*, 324, 1408, doi: [10.1126/Sci.1171807](https://doi.org/10.1126/Sci.1171807)
- Goodman, A. A., Benson, P. J., Fuller, G. A., & Myers, P. C. 1993, *ApJ*, 406, 528, doi: [10.1086/172465](https://doi.org/10.1086/172465)
- Hacar, A., & Tafalla, M. 2011, *A&A*, 533, A34, doi: [10.1051/0004-6361/201117039](https://doi.org/10.1051/0004-6361/201117039)
- Hasegawa, T., Sato, F., Whiteoak, J. B., & Miyawaki, R. 1994, *ApJL*, 429, L77, doi: [10.1086/187417](https://doi.org/10.1086/187417)
- Haworth, T. J., Shima, K., Tasker, E. J., et al. 2015, *MNRAS*, 454, 1634, doi: [10.1093/mnras/stv2068](https://doi.org/10.1093/mnras/stv2068)
- Hennebelle, P., & Ciardi, A. 2009, *A&A*, 506, L29, doi: [10.1051/0004-6361/200913008](https://doi.org/10.1051/0004-6361/200913008)
- Hennebelle, P., Commerçon, B., Joos, M., et al. 2011, *A&A*, 528, A72, doi: [10.1051/0004-6361/201016052](https://doi.org/10.1051/0004-6361/201016052)
- Hennebelle, P., & Fromang, S. 2008, *A&A*, 477, 9, doi: [10.1051/0004-6361:20078309](https://doi.org/10.1051/0004-6361:20078309)
- Higuchi, A. E., Kurono, Y., Saito, M., & Kawabe, R. 2010, *ApJ*, 719, 1813, doi: [10.1088/0004-637X/719/2/1813](https://doi.org/10.1088/0004-637X/719/2/1813)
- Hills, J. G., & Day, C. A. 1976, *Astrophys. Lett.*, 17, 87
- Hirano, S., Tsukamoto, Y., Basu, S., & Machida, M. N. 2020, *ApJ*, 898, 118, doi: [10.3847/1538-4357/ab9f9d](https://doi.org/10.3847/1538-4357/ab9f9d)
- Hockney, R. W., & Eastwood, J. W. 1988, *Computer simulation using particles* (crc Press)
- Hsu, C.-J., Tan, J. C., Christie, D., Cheng, Y., & O'Neill, T. J. 2023, *MNRAS*, 522, 700, doi: [10.1093/mnras/stad777](https://doi.org/10.1093/mnras/stad777)
- Huang, X., Zhou, T., & Lin, D. N. C. 2013, *ApJ*, 769, 23, doi: [10.1088/0004-637X/769/1/23](https://doi.org/10.1088/0004-637X/769/1/23)
- Hull, C. L. H., & Zhang, Q. 2019, *FrASS*, 6, 3, doi: [10.3389/fspas.2019.00003](https://doi.org/10.3389/fspas.2019.00003)
- Hull, C. L. H., Plambeck, R. L., Bolatto, A. D., et al. 2013, *ApJ*, 768, 159, doi: [10.1088/0004-637X/768/2/159](https://doi.org/10.1088/0004-637X/768/2/159)

- Hull, C. L. H., Mocz, P., Burkhart, B., et al. 2017, *ApJLetters*, 842, L9, doi: [10.3847/2041-8213/aa71b7](https://doi.org/10.3847/2041-8213/aa71b7)
- Inoue, T., & Fukui, Y. 2013, *ApJL*, 774, L31, doi: [10.1088/2041-8205/774/2/L31](https://doi.org/10.1088/2041-8205/774/2/L31)
- Inutsuka, S., & Miyama, S. M. 1997, *The Astrophysical Journal*, 480, 681, doi: [10.1086/303982](https://doi.org/10.1086/303982)
- Jackson, R. J., & Jeffries, R. D. 2010, *MNRAS*, 402, 1380, doi: [10.1111/j.1365-2966.2009.15983.x](https://doi.org/10.1111/j.1365-2966.2009.15983.x)
- Joos, M., Hennebelle, P., & Ciardi, A. 2012, *A&A*, 543, A128, doi: [10.1051/0004-6361/201118730](https://doi.org/10.1051/0004-6361/201118730)
- Joos, M., Hennebelle, P., Ciardi, A., & Fromang, S. 2013, *A&A*, 554, A17, doi: [10.1051/0004-6361/201220649](https://doi.org/10.1051/0004-6361/201220649)
- Karoly, J., Soam, A., Andersson, B.-G., et al. 2020, *ApJ*, 900, 181, doi: [10.3847/1538-4357/abad37](https://doi.org/10.3847/1538-4357/abad37)
- Kinoshita, S. W., Nakamura, F., & Wu, B. 2021a, *ApJ*, 921, 150, doi: [10.3847/1538-4357/ac1d4b](https://doi.org/10.3847/1538-4357/ac1d4b)
- Kinoshita, S. W., Nakamura, F., Nguyen-Luong, Q., et al. 2021b, *PASJ*, 73, S300, doi: [10.1093/pasj/psaa053](https://doi.org/10.1093/pasj/psaa053)
- Kirk, J. M., Ward-Thompson, D., & Crutcher, R. M. 2006, *MNRAS*, 369, 1445, doi: [10.1111/j.1365-2966.2006.10392.x](https://doi.org/10.1111/j.1365-2966.2006.10392.x)
- Kitsionas, S., & Whitworth, A. P. 2007, *MNRAS*, 378, 507, doi: [10.1111/j.1365-2966.2007.11707.x](https://doi.org/10.1111/j.1365-2966.2007.11707.x)
- Klessen, R. S., Heitsch, F., & Mac Low, M.-M. 2000, *ApJ*, 535, 887, doi: [10.1086/308891](https://doi.org/10.1086/308891)
- Kong, S., Arce, H. G., Maureira, M. J., et al. 2019, *ApJ*, 874, 104, doi: [10.3847/1538-4357/ab07b9](https://doi.org/10.3847/1538-4357/ab07b9)
- Kong, S., Arce, H. G., Feddersen, J. R., et al. 2018, *ApJS*, 236, 25, doi: [10.3847/1538-4365/aabafc](https://doi.org/10.3847/1538-4365/aabafc)

- Konigl, A., & Pudritz, R. E. 2000, in *Protostars and Planets IV*, ed. V. Mannings, A. P. Boss, & S. S. Russell, 759, doi: [10.48550/arXiv.astro-ph/9903168](https://doi.org/10.48550/arXiv.astro-ph/9903168)
- Kovacs, G. 2018, *A&A*, 612, L2, doi: [10.1051/0004-6361/201731355](https://doi.org/10.1051/0004-6361/201731355)
- Krasnopolsky, R., Li, Z.-Y., & Shang, H. 2011, *ApJ*, 733, 54, doi: [10.1088/0004-637X/733/1/54](https://doi.org/10.1088/0004-637X/733/1/54)
- Krumholz, M. R., Crutcher, R. M., & Hull, C. L. H. 2013, *ApJLetters*, 767, L11, doi: [10.1088/2041-8205/767/1/L11](https://doi.org/10.1088/2041-8205/767/1/L11)
- Krumholz, M. R., & Federrath, C. 2019, *FrASS*, 6, 7, doi: [10.3389/fspas.2019.00007](https://doi.org/10.3389/fspas.2019.00007)
- Kunz, M. W., & Balbus, S. A. 2004, *MNRAS*, 348, 355, doi: [10.1111/j.1365-2966.2004.07383.x](https://doi.org/10.1111/j.1365-2966.2004.07383.x)
- Kunz, M. W., & Mouschovias, T. C. 2010, *MNRAS*, 408, 322, doi: [10.1111/j.1365-2966.2010.17110.x](https://doi.org/10.1111/j.1365-2966.2010.17110.x)
- Kuznetsova, A., Hartmann, L., & Heitsch, F. 2019, *ApJ*, 876, 33, doi: [10.3847/1538-4357/ab12ce](https://doi.org/10.3847/1538-4357/ab12ce)
- . 2020, *ApJ*, 893, 73, doi: [10.3847/1538-4357/ab7eac](https://doi.org/10.3847/1538-4357/ab7eac)
- Lada, C. J., Bergin, E. A., Alves, J. F., & Huard, T. L. 2003, *ApJ*, 586, 286, doi: [10.1086/367610](https://doi.org/10.1086/367610)
- Lada, C. J., & Kylafis, N. D. 1999, *The origin of stars and planetary systems*, Vol. 540 (Springer Sci & Business Media)
- Larson, R. B. 1981, *MNRAS*, 194, 809, doi: [10.1093/mnras/194.4.809](https://doi.org/10.1093/mnras/194.4.809)
- Launhardt, R., Pavlyuchenkov, Y., Gueth, F., et al. 2009, *A&A*, 494, 147, doi: [10.1051/0004-6361:200810835](https://doi.org/10.1051/0004-6361:200810835)
- Lazarian, A. 2007, *JQSRT*, 106, 225, doi: [10.1016/j.jqsrt.2007.01.038](https://doi.org/10.1016/j.jqsrt.2007.01.038)
- Li, H.-B. 2021, *Galaxies*, 9, doi: [10.3390/galaxies9020041](https://doi.org/10.3390/galaxies9020041)
- Li, H.-b., Dowell, C. D., Goodman, A., Hildebrand, R., & Novak, G. 2009, *ApJ*, 704, 891, doi: [10.1088/0004-637X/704/2/891](https://doi.org/10.1088/0004-637X/704/2/891)

- Li, Z.-Y., Krasnopolsky, R., & Shang, H. 2013, *ApJ*, 774, 82, doi: [10.1088/0004-637X/774/1/82](https://doi.org/10.1088/0004-637X/774/1/82)
- Loren, R. B. 1976, *ApJ*, 209, 466, doi: [10.1086/154741](https://doi.org/10.1086/154741)
- Machida, M. N., Inutsuka, S.-i., & Matsumoto, T. 2011, *PASJ*, 63, 555, doi: [10.1093/pasj/63.3.555](https://doi.org/10.1093/pasj/63.3.555)
- Machida, M. N., Tomisaka, K., Matsumoto, T., & Inutsuka, S.-i. 2008, *ApJ*, 677, 327, doi: [10.1086/529133](https://doi.org/10.1086/529133)
- Marchand, P., Commerçon, B., & Chabrier, G. 2018, *A&A*, 619, A37, doi: [10.1051/0004-6361/201832907](https://doi.org/10.1051/0004-6361/201832907)
- Marinho, E. P., Andreazza, C. M., & Lépine, J. R. D. 2001, *A&A*, 379, 1123, doi: [10.1051/0004-6361:20011352](https://doi.org/10.1051/0004-6361:20011352)
- Marinho, E. P., & Lépine, J. R. D. 2000, *A&AS*, 142, 165, doi: [10.1051/aas:2000327](https://doi.org/10.1051/aas:2000327)
- Masson, J., Chabrier, G., Hennebelle, P., Vaytet, N., & Commerçon, B. 2016, *A&A*, 587, A32, doi: [10.1051/0004-6361/201526371](https://doi.org/10.1051/0004-6361/201526371)
- Matsumoto, T., & Hanawa, T. 2004, *Ap&SS*, 292, 273, doi: [10.1023/B:ASTR.0000045027.95992.fc](https://doi.org/10.1023/B:ASTR.0000045027.95992.fc)
- Matsumoto, T., Machida, M. N., & ichiro Inutsuka, S. 2017, *The Astrophysical Journal*, 839, 69, doi: [10.3847/1538-4357/aa6a1c](https://doi.org/10.3847/1538-4357/aa6a1c)
- Matsumoto, T., & Tomisaka, K. 2004, *ApJ*, 616, 266, doi: [10.1086/424897](https://doi.org/10.1086/424897)
- McKee, C. F. 1989, *ApJ*, 345, 782, doi: [10.1086/167950](https://doi.org/10.1086/167950)
- McKee, C. F., & Ostriker, E. C. 2007, *ARA&A*, 45, 565, doi: [10.1146/annurev.astro.45.051806.110602](https://doi.org/10.1146/annurev.astro.45.051806.110602)
- McKee, C. F., & Ostriker, J. P. 1977, *ApJ*, 218, 148, doi: [10.1086/155667](https://doi.org/10.1086/155667)
- Mellon, R. R., & Li, Z.-Y. 2008, *ApJ*, 681, 1356, doi: [10.1086/587542](https://doi.org/10.1086/587542)
- Mellon, R. R., & Li, Z.-Y. 2009, *ApJ*, 698, 922, doi: [10.1088/0004-637X/698/1/922](https://doi.org/10.1088/0004-637X/698/1/922)
- Mestel, L. 1966, *MNRAS*, 133, 265, doi: [10.1093/mnras/133.2.265](https://doi.org/10.1093/mnras/133.2.265)

- Mestel, L., & Spitzer, L., J. 1956, MNRAS, 116, 503, doi: [10.1093/mnras/116.5.503](https://doi.org/10.1093/mnras/116.5.503)
- Misugi, Y., Inutsuka, S.-i., & Arzoumanian, D. 2023, ApJ, 943, 76, doi: [10.3847/1538-4357/aca88d](https://doi.org/10.3847/1538-4357/aca88d)
- Miville-Deschênes, M. A., Levrier, F., & Falgarone, E. 2003, ApJ, 593, 831, doi: [10.1086/376603](https://doi.org/10.1086/376603)
- Miyama, S. M., Hayashi, C., & Narita, S. 1984, ApJ, 279, 621, doi: [10.1086/161926](https://doi.org/10.1086/161926)
- Miyoshi, T., & Kusano, K. 2005, Journal of Computational Physics, 208, 315, doi: [10.1016/j.jcp.2005.02.017](https://doi.org/10.1016/j.jcp.2005.02.017)
- Mocz, P., & Burkhardt, B. 2018, MNRAS, 480, 3916, doi: [10.1093/mnras/sty1976](https://doi.org/10.1093/mnras/sty1976)
- Mouschovias, T. C. 1979, ApJ, 228, 159, doi: [10.1086/156832](https://doi.org/10.1086/156832)
- . 1985, A&A, 142, 41
- Mouschovias, T. C., & Paleologou, E. V. 1979, ApJ, 230, 204, doi: [10.1086/157077](https://doi.org/10.1086/157077)
- . 1980, ApJ, 237, 877, doi: [10.1086/157936](https://doi.org/10.1086/157936)
- Mouschovias, T. C., & Spitzer, L., J. 1976, ApJ, 210, 326, doi: [10.1086/154835](https://doi.org/10.1086/154835)
- Murray, S. D., & Lin, D. N. C. 2004, ApJ, 615, 586, doi: [10.1086/424658](https://doi.org/10.1086/424658)
- Myers, P. C. 1978, ApJ, 225, 380, doi: [10.1086/156500](https://doi.org/10.1086/156500)
- Nakamura, F., & Li, Z.-Y. 2007, ApJ, 662, 395, doi: [10.1086/517515](https://doi.org/10.1086/517515)
- Nakano, T., & Nakamura, T. 1978, PASJ, 30, 671
- Nanne, J. A., Nimmo, F., Cuzzi, J. N., & Kleine, T. 2019, Earth and Planetary Science Letters, 511, 44, doi: <https://doi.org/10.1016/j.epsl.2019.01.027>
- Ntormousi, E., & Hennebelle, P. 2019, A&A, 625, A82, doi: [10.1051/0004-6361/201834094](https://doi.org/10.1051/0004-6361/201834094)
- Offner, S. S. R., Klein, R. I., & McKee, C. F. 2008, ApJ, 686, 1174, doi: [10.1086/590238](https://doi.org/10.1086/590238)
- Offner, S. S. R., Taylor, J., Markey, C., et al. 2022, MNRAS, 517, 885, doi: [10.1093/mnras/stac2734](https://doi.org/10.1093/mnras/stac2734)

- Padoan, P., Haugbølle, T., & Nordlund, Å. 2014, *ApJ*, 797, 32, doi: [10.1088/0004-637X/797/1/32](https://doi.org/10.1088/0004-637X/797/1/32)
- Pandhi, A., Friesen, R. K., Fissel, L., et al. 2023, *MNRAS*, doi: [10.1093/mnras/stad2283](https://doi.org/10.1093/mnras/stad2283)
- Pattle, K., Lai, S.-P., Francesco, J. D., et al. 2021, *ApJ*, 907, 88, doi: [10.3847/1538-4357/abcc6c](https://doi.org/10.3847/1538-4357/abcc6c)
- Pineda, J. E., Segura-Cox, D., Caselli, P., et al. 2020, *Nature Astronomy*, 4, 1158, doi: [10.1038/s41550-020-1150-z](https://doi.org/10.1038/s41550-020-1150-z)
- Pineda, J. E., Zhao, B., Schmiedeke, A., et al. 2019, *ApJ*, 882, 103, doi: [10.3847/1538-4357/ab2cd1](https://doi.org/10.3847/1538-4357/ab2cd1)
- Pirogov, L., Zinchenko, I., Caselli, P., Johansson, L. E. B., & Myers, P. C. 2003, *A&A*, 405, 639, doi: [10.1051/0004-6361:20030659](https://doi.org/10.1051/0004-6361:20030659)
- Price, D. J., & Bate, M. R. 2007, *Ap&SS*, 311, 75, doi: [10.1007/s10509-007-9549-x](https://doi.org/10.1007/s10509-007-9549-x)
- Punanova, A., Caselli, P., Pineda, J. E., et al. 2018, *A&A*, 617, A27, doi: [10.1051/0004-6361/201731159](https://doi.org/10.1051/0004-6361/201731159)
- Sakai, N., & Yamamoto, S. 2013, *Chemical Reviews*, 113, 8981, doi: [10.1021/cr4001308](https://doi.org/10.1021/cr4001308)
- Sakre, N., Habe, A., Pettitt, A. R., et al. 2023, *MNRAS*, 522, 4972, doi: [10.1093/mnras/stad1089](https://doi.org/10.1093/mnras/stad1089)
- Sanhueza, P., Contreras, Y., Wu, B., et al. 2019, *ApJ*, 886, 102, doi: [10.3847/1538-4357/ab45e9](https://doi.org/10.3847/1538-4357/ab45e9)
- Sanhueza, P., Girart, J. M., Padovani, M., et al. 2021, *ApJLetters*, 915, L10, doi: [10.3847/2041-8213/ac081c](https://doi.org/10.3847/2041-8213/ac081c)
- Scoville, N. Z., Sanders, D. B., & Clemens, D. P. 1986, *ApJL*, 310, L77, doi: [10.1086/184785](https://doi.org/10.1086/184785)
- Shimoikura, T., Dobashi, K., Hirano, N., et al. 2022, *ApJ*, 928, 76, doi: [10.3847/1538-4357/ac5327](https://doi.org/10.3847/1538-4357/ac5327)

- Shimoikura, T., Dobashi, K., Matsumoto, T., & Nakamura, F. 2016, *ApJ*, 832, 205, doi: [10.3847/0004-637X/832/2/205](https://doi.org/10.3847/0004-637X/832/2/205)
- Shimoikura, T., Dobashi, K., Nakamura, F., et al. 2015, *ApJ*, 806, 201, doi: [10.1088/0004-637X/806/2/201](https://doi.org/10.1088/0004-637X/806/2/201)
- Shimoikura, T., Dobashi, K., Nakamura, F., Matsumoto, T., & Hirota, T. 2018, *ApJ*, 855, 45, doi: [10.3847/1538-4357/aaaccd](https://doi.org/10.3847/1538-4357/aaaccd)
- Shu, F. H. 1983, *ApJ*, 273, 202, doi: [10.1086/161359](https://doi.org/10.1086/161359)
- Shu, F. H., Adams, F. C., & Lizano, S. 1987, *ARA&A*, 25, 23, doi: [10.1146/annurev.aa.25.090187.000323](https://doi.org/10.1146/annurev.aa.25.090187.000323)
- Shu, F. H., Galli, D., Lizano, S., & Cai, M. 2006, *ApJ*, 647, 382, doi: [10.1086/505258](https://doi.org/10.1086/505258)
- Shu, F. H., Najita, J. R., Shang, H., & Li, Z. Y. 2000, in *Protostars and Planets IV*, ed. V. Mannings, A. P. Boss, & S. S. Russell, 789–814
- Takahira, K., Shima, K., Habe, A., & Tasker, E. J. 2018, *PASJ*, 70, S58, doi: [10.1093/pasj/psy011](https://doi.org/10.1093/pasj/psy011)
- Takemura, H., Nakamura, F., Kong, S., et al. 2021, *ApJL*, 910, L6, doi: [10.3847/2041-8213/abe7dd](https://doi.org/10.3847/2041-8213/abe7dd)
- Tan, J. C. 2000, *ApJ*, 536, 173, doi: [10.1086/308905](https://doi.org/10.1086/308905)
- Tatematsu, K., Ohashi, S., Sanhueza, P., et al. 2016, *PASJ*, 68, 24, doi: [10.1093/pasj/psw002](https://doi.org/10.1093/pasj/psw002)
- Tobin, J. J., Hartmann, L., Chiang, H.-F., et al. 2011, *ApJ*, 740, 45, doi: [10.1088/0004-637X/740/1/45](https://doi.org/10.1088/0004-637X/740/1/45)
- Tokuda, K., Fujishiro, K., Tachihara, K., et al. 2020, *ApJ*, 899, 10, doi: [10.3847/1538-4357/ab9ca7](https://doi.org/10.3847/1538-4357/ab9ca7)
- Tomida, K., Okuzumi, S., & Machida, M. N. 2015, *ApJ*, 801, 117, doi: [10.1088/0004-637X/801/2/117](https://doi.org/10.1088/0004-637X/801/2/117)
- Tomida, K., Tomisaka, K., Matsumoto, T., et al. 2012, *ApJ*, 763, 6, doi: [10.1088/0004-637X/763/1/6](https://doi.org/10.1088/0004-637X/763/1/6)

- Tomisaka, K. 2002, *ApJ*, 575, 306, doi: [10.1086/341133](https://doi.org/10.1086/341133)
- Torii, K., Enokiya, R., Sano, H., et al. 2011, *ApJ*, 738, 46, doi: [10.1088/0004-637X/738/1/46](https://doi.org/10.1088/0004-637X/738/1/46)
- Treviño-Morales, S. P., Fuente, A., Sánchez-Monge, Á., et al. 2019, *A&A*, 629, A81, doi: [10.1051/0004-6361/201935260](https://doi.org/10.1051/0004-6361/201935260)
- Truelove, J. K., Klein, R. I., McKee, C. F., et al. 1997, *ApJL*, 489, L179, doi: [10.1086/310975](https://doi.org/10.1086/310975)
- Tsukamoto, Y., Okuzumi, S., Iwasaki, K., Machida, M. N., & Inutsuka, S. 2018, *ApJ*, 868, 22, doi: [10.3847/1538-4357/aae4dc](https://doi.org/10.3847/1538-4357/aae4dc)
- Tsuribe, T., & Inutsuka, S.-i. 1999, *ApJL*, 523, L155, doi: [10.1086/312267](https://doi.org/10.1086/312267)
- Vázquez-Semadeni, E., Banerjee, R., Gómez, G. C., et al. 2011, *MNRAS*, 414, 2511, doi: [10.1111/j.1365-2966.2011.18569.x](https://doi.org/10.1111/j.1365-2966.2011.18569.x)
- Virtanen, P., Gommers, R., Oliphant, T. E., et al. 2020, *Nature Methods*, 17, 261, doi: [10.1038/s41592-019-0686-2](https://doi.org/10.1038/s41592-019-0686-2)
- Wang, P., Abel, T., & Zhang, W. 2008, *ApJS*, 176, 467, doi: [10.1086/529434](https://doi.org/10.1086/529434)
- Ward-Thompson, D., Motte, F., & Andre, P. 1999, *MNRAS*, 305, 143, doi: [10.1046/j.1365-8711.1999.02412.x](https://doi.org/10.1046/j.1365-8711.1999.02412.x)
- Ward-Thompson, D., Scott, P. F., Hills, R. E., & Andre, P. 1994, *MNRAS*, 268, 276, doi: [10.1093/mnras/268.1.276](https://doi.org/10.1093/mnras/268.1.276)
- Whitworth, A. P., Chapman, S. J., Bhattal, A. S., et al. 1995, *MNRAS*, 277, 727, doi: [10.1093/mnras/277.2.727](https://doi.org/10.1093/mnras/277.2.727)
- Wu, B., Tan, J. C., Christie, D., & Nakamura, F. 2020, *ApJ*, 891, 168, doi: [10.3847/1538-4357/ab77b5](https://doi.org/10.3847/1538-4357/ab77b5)
- Wu, B., Tan, J. C., Nakamura, F., et al. 2017, *ApJ*, 835, 137, doi: [10.3847/1538-4357/835/2/137](https://doi.org/10.3847/1538-4357/835/2/137)
- Wu, B., Van Loo, S., Tan, J. C., & Bruderer, S. 2015, *ApJ*, 811, 56, doi: [10.1088/0004-637X/811/1/56](https://doi.org/10.1088/0004-637X/811/1/56)

- Xu, D., Offner, S. S. R., Gutermuth, R., & Tan, J. C. 2022, *ApJ*, 941, 81, doi: [10.3847/1538-4357/aca153](https://doi.org/10.3847/1538-4357/aca153)
- Xu, J., & Stone, J. M. 1995, *ApJ*, 454, 172, doi: [10.1086/176475](https://doi.org/10.1086/176475)
- Yen, H.-W., Koch, P. M., Takakuwa, S., et al. 2015, *ApJ*, 799, 193, doi: [10.1088/0004-637X/799/2/193](https://doi.org/10.1088/0004-637X/799/2/193)
- Yen, H.-W., Koch, P. M., Hull, C. L. H., et al. 2021, *ApJ*, 907, 33, doi: [10.3847/1538-4357/abca99](https://doi.org/10.3847/1538-4357/abca99)
- Young, A. K. 2023, Insights into the first and second hydrostatic core stages from numerical simulations. <https://arxiv.org/abs/2312.03039>
- Zhang, S., Zavagno, A., López-Sepulcre, A., et al. 2021, *A&A*, 646, A25, doi: [10.1051/0004-6361/202038421](https://doi.org/10.1051/0004-6361/202038421)
- Zhao, B., Caselli, P., Li, Z.-Y., & Krasnopolsky, R. 2018, *MNRAS*, 473, 4868, doi: [10.1093/mnras/stx2617](https://doi.org/10.1093/mnras/stx2617)
- Zhao, B., Caselli, P., Li, Z.-Y., et al. 2016, *MNRAS*, 460, 2050, doi: [10.1093/mnras/stw1124](https://doi.org/10.1093/mnras/stw1124)